

RAFAEL SALLES

**Experimental Analysis of the Vortex Self-Induced
Vibration of a Catenary Riser Model in the Modal Space**

São Paulo
2022

RAFAEL SALLES

**Experimental Analysis of the Vortex Self-Induced
Vibration of a Catenary Riser Model in the Modal Space**

Original version

Thesis presented to Escola Politécnica of
University of São Paulo in partial fulfill-
ment of the requirements for the Doctor of
Sciences degree.

São Paulo
2022

RAFAEL SALLES

**Experimental Analysis of the Vortex Self-Induced
Vibration of a Catenary Riser Model in the Modal Space**

Original version

Thesis presented to Escola Politécnica of
University of São Paulo in partial fulfill-
ment of the requirements for the Doctor of
Sciences degree.

Graduate Program:
Naval Architecture and Ocean Engineer-
ing

Supervisor:
Prof. Dr. Celso Pupo Pesce

São Paulo
2022

Catálogo-na-publicação

Salles, Rafael

Experimental Analysis of the Vortex Self-Induced Vibration of a Catenary Riser Model in the Modal Space / R. Salles -- São Paulo, 2022.

265 p.

Tese (Doutorado) - Escola Politécnica da Universidade de São Paulo. Departamento de Engenharia Naval e Oceânica.

1.Dinâmica de Estruturas 2.Tubos Flexíveis 3.Vórtices em Fluidos 4.Interação Fluido-Estrutura 5.Análise Modal I.Universidade de São Paulo. Escola Politécnica. Departamento de Engenharia Naval e Oceânica II.t.

Às vovós, aos vovôs e aos pais.

ACKNOWLEDGMENTS

Primeiramente, gostaria de agradecer ao meu orientador, Professor Celso Pupo Pesce, por ter me acolhido em seu grupo de pesquisa desde 2009, delegando-me tarefas que sempre me impulsionaram a um próximo patamar em minha vida profissional. Não poderia também deixar de agradecer ao Programa de Pós-Graduação em Engenharia Naval e Oceânica (PPGEN) por todo o apoio dado desde o início do meu doutoramento, provendo soluções para os mais variados problemas enfrentados.

Muitos anos já se passaram desde que iniciei meus trabalhos dentro do Laboratório de Mecânica Offshore (LMO), que à época ainda era Laboratório de Interação Fluido-Estrutura e Mecânica Offshore (LIFE&MO) ainda como aluno de graduação em Engenharia Mecânica, e seria impossível agradecer a todos os companheiros com quem tive o prazer de trabalhar durante estes 13 anos; porém gostaria de mencionar: Marcos Rabello, Flávia Soares, Caio Cesar, Heloísa Guedes, Dra. Fernanda Takafuji, e também a equipe técnica com Larissa, Cristiano e a sempre presente Dona Edith. Um agradecimento especial à equipe do TPN, IPT e NDF, especialmente ao Dr. Pedro Mello por sua infundável ajuda em tudo.

Este trabalho também não seria possível sem o auxílio e patrocínio da Petrobras por meio do projeto USP no. 21056/09.1.2874.3.2, Dinâmica Não-Linear de Risers, através do qual eu tive meu primeiro contato com mecânica offshore experimental, criando modelos e realizando diversos ensaios de caracterização mecânica, bem como a participação durante os experimentos aqui analisados. O presente trabalho foi realizado com apoio da Coordenação de Aperfeiçoamento de Pessoal de Nível Superior - Brasil (CAPES) - Código de Financiamento 001, através de bolsa de doutorado no Brasil e com estágio no exterior, através do Programa PRInt/USP.

Agradeço aos professores que durante estes últimos anos ajudaram-me a crescer profissionalmente, especialmente: ao Prof. Gustavo Assi por sempre ter paciência comigo; ao Prof. Raúl Gonzalez por sempre inspirar-me a aprender e refletir mais sobre a natureza das coisas; ao Prof. Guilherme Franzini por ter-me auxiliado em muitos momentos; ao Prof. Renato Orsino por ser um ótimo companheiro de trabalho.

También me gustaría agradecer al Prof. Francisco Huera-Huarte por darme la bienvenida a su grupo de investigación en la URV y al compañero de laboratorio Javier. Un saludo especial a los amigos que hice durante mi estancia en Catalunya. Fueron grandes momentos que siempre quedarán en mi memoria.

Finalmente, reconheço a imprescindível acolhida de meus pais, Niluza Diaz e Ronaldo Salles, durante o período de doutoramento: sem vocês e o privilégio que me foi oferecido, eu não poderia ter chegado até aqui. Um especial agradecimento à minha mãe, ao Hugo Diaz, ao Henrique Polverini e à Miriam Teodoro por me terem recebido com enorme carinho em Portugal durante um período de pandemia. Sem esquecer da minha avó, com quem eu estive nestes últimos meses durante a redação da tese, sempre me enchendo de quitutes.

Por último, gostaria de agradecer infinitamente a todos os amigos que me acom-

panharam até aqui, dando apoio e força para levar e sacudir a poeira em momentos mais difíceis. Nomeadamente, um enorme salve à Lara Neville (ou seu alterego Larissa Ihara), à Bella Moschkovich, à Natália Ishikawa (Mozikawa), ao Danilo Polidoro, ao César Vieira e à Esther Morel. Inclusive, obrigado Larissa, eu não teria conseguido sem sua constante ajuda com redação.

*“E vós, Tágides minhas, pois criado
tendes em mim um novo engenho ardente,
se sempre em verso humilde celebrado
foi de mim vosso rio alegremente,
dai-me agora um som alto e sublimado,
um estilo grandíloquo e corrente,
por que de vossas águas Febo ordene
que não tenham inveja às de Hipocrene.”*

– Camões, L. de, *Os Lusíadas*. Canto I,
estrofe 4

RESUMO

O fenômeno de Vibração Auto-Induzida por Vórtices (VSIV) ainda é pouco explorado nos projetos de risers em catenária na exploração de hidrocarbonetos em águas profundas e ultra-profundas. O VSIV é causado pelo movimento imposto ao riser pela unidade flutuante, que é sujeita à ação de ondas de gravidade, induzindo vibrações no plano da catenária e assim liberando vórtices que provocam movimento oscilatório em direção a ele perpendicular. Estudos fundamentais com cilindros rígidos, montados em base elástica em uma direção e forçados a se movimentar na direção a ela perpendicular, desvelam uma fenomenologia rica e complexa, mostrando diversos padrões de sincronização e picos de resposta em função da amplitude e frequência do movimento imposto. Contrário ao fenômeno observado em cilindros rígidos, o caso em catenária não apresenta uma clara relação de causalidade, e os movimentos no plano e fora deste são respostas daquela excitação primária. Além disto, cilindros flexíveis assumem respostas multimodais, dificultando a compreensão fenomenológica do VSIV. Utilizando um modelo em escala reduzida de “riser” em catenária, deslocamentos medidos opticamente ao longo da linha foram utilizados em um processo de decomposição de Galerkin, levando à obtenção de séries modais de movimento do modelo sujeito ao VSIV. A partir da consideração de causalidade entre a resposta de vibração do plano e fora deste, foi possível obter um Modelo de Ordem Reduzida (MOR) contendo um número finito de modos. Além disto, os grupos adimensionais tipicamente utilizados em análise de VSIV foram reinterpretados na forma de parâmetros equivalentes modais dos quais se percebeu a necessidade de se substituir a velocidade reduzida pela relação entre a frequência dominante do movimento no plano e a frequência natural de cada modo analisado, em seu movimento fora deste plano. Finalmente, adotando-se uma hipótese de que o mecanismo responsável pelo movimento fora do plano é causado pelo modo dominante no plano, foi possível obter relações de similaridade entre os resultados da dinâmica multimodal e os apresentados para o caso do cilindro rígido.

Palavras-Chave – Dinâmica das Estruturas; Tubos Flexíveis; Vórtices em Fluidos; Interação Fluido-Estrutura; Análise Modal.

ABSTRACT

The phenomenon of Vortex Self-Induced Vibration (VSIV) is still little explored in the design and analysis of catenary risers used in the production of hydrocarbons in deep and ultra-deep waters. The VSIV is driven by the movement imposed to the top extremity due to the vessels oscillations caused by the action of gravity waves, inducing vibrations in the catenary plane and, therefore, shedding vortices which provoke oscillatory motions perpendicular to this plane. Fundamental studies with rigid cylinders, mounted on an elastic apparatus and forced to oscillate in the direction perpendicular to the springs, reveal a rich and complex phenomenology, showing diverse patterns of synchronization and amplitude peaks as function of amplitude and frequency of the imposed motion. Contrary to the case in rigid cylinders, the phenomenon in catenary models is not characterized by a clear causality relation, since the only imposed movement is at the upper-extremity and the movements in-plane and out-of-plane are both responses to that excitation. In addition, flexible cylinders assume multimodal responses, making the phenomenological understanding of the VSIV difficult. Using a small-scale model of a catenary riser, displacements optically measured along the line were used in a Galerkin's decomposition process to obtain modal motion series of the model subjected to VSIV. Considering a causality relation between the in-plane and out-of-plane vibration responses, it was possible to obtain a Reduced Order Model (MOR) decomposed into a finite number of modes. In addition, the dimensionless groups typically used in VSIV analysis were reinterpreted, leading to the proposition of a set of equivalent modal parameters. Then, it was observed that a redefinition of the reduced velocity parameter should be made, replacing it with the ratio between the in-plane mode measured dominant frequency with the out-of-plane natural frequency of the mode under analysis. Finally, a hypothesis was adopted that the driving mechanism responsible for the out-of-plane movement was caused by the dominant mode in the plane, making it possible to obtain similarity relations between the the VSIV multimodal dynamic results and those from the rigid cylinder case.

Keywords – Structural Dynamics; Flexible Pipes; Fluid Vortex; Fluid-Structure Interaction; Modal Analysis.

LIST OF FIGURES

1.1	Schematic configuration of typical offshore structures use to exploit and store hydrocarbons.	1
1.2	Different risers configurations used in deep-waters exploitation and drilling process.	2
1.3	Some nonlinear phenomena acting on different risers and floating vessels.	3
2.1	Inertia force coefficient, C_M , of a rigid cylinder subjected to oscillatory flow.	18
2.2	Drag force coefficient, C_D , of a rigid cylinder subjected to oscillatory flow.	18
2.3	Lift force coefficient and lateral motion amplitude with respect to reduced velocity for a sand-roughened cylinder in harmonic flow ($k/D = 0.01$).	20
2.4	Temporal variation on the vortex shedding frequency during a cycle for some reduced velocity values.	21
2.5	Elastic mounted cylinder subjected to harmonic displacement in water: experimental system sketch.	21
2.6	Frequency and amplitude response. Exp. I.	23
2.7	SCR normalized fatigue damage in 1 year.	26
2.8	Selected targets spectra and trajectories.	27
2.9	Fatigue damage due to VSIV for different sea conditions. Comparison between in-plane (magenta) and out-of-plane (blue) contributions to accumulate damage.	29
2.10	Petrobras Platform P18 SCR <i>in-situ</i> , $KC_{max} = 10$	29
2.11	Petrobras Platform P18 SCR <i>in-situ</i> : in-plane vs. out-of-plane trajectories.	30
2.12	Vortex Self-Induced Vibration amplitude and frequency responses for several KC conditions.	31
2.13	Trajectories found in the VSIV in-plane and out-of-plane response synchronization for several experimental conditions.	32

2.14 Vortex patterns measurements (PIV) in VSIV motion for $KC = 10$ and $V_R = 4.65$	33
2.15 Typical VSIV response in high KC regime with its proposed division.	35
2.16 Hysteresis showed in the VSIV amplitude response during an imposed movement cycle.	35
2.17 VSIV experimental response in two different KC . The first column corresponds to $KC = 31$ and the second, $KC = 178$; top-to-down indicate a decrease on the period (or increase on frequency) of imposed movement.	37
2.18 Distribution of $KC(s)$ throughout the model span for two different tested conditions.	38
2.19 Traction variation evaluated in the VSIV presence (model test) and in the VSIV absence (quasi-static and Orcaflex [®]).	39
2.20 Experimental responses in two different conditions.	40
2.21 Fatigue damage estimated in several conditions.	41
2.22 Local analysis of the target 29.	44
2.23 Frequency ratio, relative frequency and amplitude responses with respect to $2\pi A_i^* \frac{f_i}{f_3}$ for different input amplitude conditions at the top.	45
2.24 Cartesian displacement trajectories for input test $2\pi A_i^* = 10$ and $f_i = 0.72Hz$; $f_i/f_3 = 1$	47
2.25 Analyses of the Cartesian displacements for input test $2\pi A_i^* = 10$ and $f_i = 0.72Hz$; $f_i/f_3 = 1$	48
2.26 VSIV response in the top point of a cantilever subjected to oscillatory flow.	49
2.27 Added mass coefficient evaluated using FF-LS methodology for a SCR model ($m^* = 1.53$) subjected to oscillatory flow ($A_i = 0.105m$ and $T_i = 5.96s$).	50
3.1 Prototype used to measure in air the model equivalent linear structural damping.	56
3.2 Sketch of the experimental arrangement used in the longitudinal catenary model.	60

3.3	Testing model monitored span both under and out of water. The sketch also shows the planar catenary-like 3D geometric configuration in all Cartesian planes.	61
3.4	Group of optical target tracking cameras used to capture 3D displacement of the model at each sampled instant.	62
3.5	Aerial portion of the longitudinal catenary-like model showing in detail the imposing heave motion actuator and the load cell installed at the hang-off point.	63
3.6	Vertical model testing set-up carried out in TPN facility.	64
3.7	Optical target tracking cameras used in the vertical riser model tests in air.	65
3.8	Some normal normalized eigenvectors for catenary-shaped riser obtained by Pesce and Martins using the WKB approximation.	68
3.9	Structural modal shapes obtained by Chatjigeorgiou's complete and simplified models using the WKB approximation.	69
3.10	Structural II mode (1 st in-plane mode), $f_{N,n}^{(1)} = 0.7113\text{Hz}$, obtained with the numerical model on Orcaflex [®]	73
3.11	Typical experimental normal displacement spectrogram and scalogram found in the present work. Case: $A_i = 70\text{mm}$ and $f_i = 0.42\text{Hz}$, alternatively At70-ID16.	76
3.12	Motion spectra in the global reference coordinates of the cases A17-ID04 and A105-ID24.	80
3.13	Schematic experimental arrangement depicting the adopted reference frames.	83
3.14	Motion scalogram in the global reference coordinates of the cases A17-ID04 and A35-ID09.	84
3.15	Motion scalograms in the global reference coordinates of the cases A70-ID16 and A105-ID24.	85
3.16	Flowchart on the evaluation of the local reference frame, TNB, at each monitored target.	87
3.17	Interpolations on the catenary-like model static configuration obtained as to evaluate the arclength and the local reference frame (TNB).	90

3.18	Plane catenary-like model static configuration depicting the TNB frame.	92
3.19	Flowchart on the algorithm used in the measured data projection into the TNB reference frame.	93
3.20	Motion scalograms and spectra in the local reference coordinates considering the case A105-ID24.	95
3.21	Normal displacement and absolute scalograms regarding the previous case, A105-ID24, depicting in detail the TDP variation within a vibration cycle.	95
3.22	Causality between normal and binormal responses depicted as a block diagram.	103
3.23	Out-of-plane spectrum response attainment of a mid-span target (18) considering the testing case whose amplitude is $A_i = 17.5\text{mm}$ and $f^* = 1$ (A17-ID04).	105
3.24	Block diagram showing the simplified modal hydroelastic ROMs.	112
4.1	Modal functions, $\varphi_n(\hat{s})$ (dotted black), and their orthonormal counterparts used in Galerkin's decomposition, $\hat{\varphi}_n(\hat{s})$ (solid orange).	117
4.2	Frequency and amplitude response with respect to f^* . Exp. I.	120
4.3	Vortex Self-Induced Vibration amplitude and frequency responses for several KC conditions with respect to f^*	122
4.4	Examplng the synchronization displayed using orbits in the space of configuration between normal and binormal displacements measured at specific points selected in the model span considering the testing group $A_i = 105\text{mm}$	125
4.5	Modal orbits for out-of-plane modes against dominant in-plane mode; out-of-plane modes: 1 st to 5 th	128
4.6	Modal orbits and their local reference frame orientation.	128
4.7	Modal response of the first and second out-of-plane modes with respect to the modal frequency ratio parameter: $45.2 \leq KC^{(d)} \leq 48$	130
4.8	Modal response of the third and fourth out-of-plane modes with respect to the modal frequency ratio parameter: $45.2 \leq KC^{(d)} \leq 48$	131

4.9	Modal peak-to-peak amplitude response, considering all out-of-plane modes with respect to the dominant plane modal displacement $45.2 \leq KC^{(d)} \leq 48$.	133
4.10	Exampling the synchronization displayed using orbits in the space of configuration between normal and binormal displacements measured at specific points selected in the model span considering the testing group $A_i = 70\text{mm}$.	134
4.11	Modal orbits for out-of-plane modes against dominant in-plane mode; out-of-plane modes: 1 st to 5 th .	137
4.12	Modal orbits and their local reference frame orientation.	137
4.13	Modal response of the first and second out-of-plane modes with respect to the modal frequency ratio parameter: $30.1 \leq KC^{(d)} \leq 33.9$.	139
4.14	Modal response of the third and fourth out-of-plane modes with respect to the modal frequency ratio parameter: $30.1 \leq KC^{(d)} \leq 33.9$.	140
4.15	Modal peak-to-peak amplitude response, considering all out-of-plane modes with respect to the dominant plane modal displacement and $30.1 \leq KC^{(d)} \leq 33.9$.	141
4.16	Exampling the synchronization displayed using orbits in the space of configuration between normal and binormal displacements measured at specific points selected in the model span considering the testing group $A_i = 35\text{mm}$.	143
4.17	Modal orbits for out-of-plane modes against dominant in-plane mode; out-of-plane modes: 1 st until 5 th .	146
4.18	Modal orbits and their local reference frame orientation.	146
4.19	Modal response of the first and second out-of-plane modes with respect to the modal frequency ratio parameter: $13 \leq KC^{(d)} \leq 18$.	147
4.20	Modal response of the third and fourth out-of-plane modes with respect to the modal frequency ratio parameter: $13 \leq KC^{(d)} \leq 18$.	149
4.21	Modal response of the fifth out-of-plane mode with respect to the modal frequency ratio parameter: $13 \leq KC^{(d)} \leq 18$.	150

4.22	Modal peak-to-peak amplitude response, considering all out-of-plane modes with respect to the dominant plane modal displacement and $13 \leq KC^{(d)} \leq 18$.	151
4.23	Examplng the synchronization displayed using orbits in the space of configuration between normal and binormal displacements measured at specific points selected in the model span considering the testing group $A_i = 17.5\text{mm}$.	152
4.24	Modal orbits for out-of-plane modes against dominant in-plane mode; out-of-plane modes: 1 st until 5 th .	157
4.25	Modal orbits and their local reference frame orientation.	157
4.26	Modal response of the first and second out-of-plane modes with respect to the modal frequency ratio parameter: $7 \leq KC^{(d)} \leq 10.6$.	159
4.27	Modal response of the third and fourth out-of-plane modes with respect to the modal frequency ratio parameter: $7 \leq KC^{(d)} \leq 10.6$.	160
4.28	Modal orbits for out-of-plane modes against dominant in-plane mode; out-of-plane modes: 6 th until 10 th .	162
4.29	Modal orbits and their local reference frame orientation.	162
4.30	Modal response of the fifth and sixth out-of-plane modes with respect to the modal frequency ratio parameter: $7 \leq KC^{(d)} \leq 10.6$.	163
4.31	Modal response of the seventh and eighth out-of-plane modes with respect to the modal frequency ratio parameter: $7 \leq KC^{(d)} \leq 10.6$.	164
4.32	Modal peak-to-peak amplitude response, considering all out-of-plane modes with respect to the dominant plane modal displacement and $7 \leq KC^{(d)} \leq 10.6$.	165
4.33	Effect of imposed amplitude and exciting frequency range on the modal intrasimilarities.	167
A.1	Small-scale model axial stiffness experimental evaluation.	198
A.2	Small-scale model bending stiffness experimental evaluation.	199
C.1	Normal and binormal dynamics in the space of configuration obtained from the testing case ID 06 of the group $A_i = 105\text{mm}$.	207

C.2	Modal orbits obtained from all testing cases in the group $A_i = 105\text{mm}$.	208
C.3	Second mode normal displacement series and correspondent spectral contents from testing cases IDs 01 until 10 in the group $A_i = 105\text{mm}$.	210
C.4	Second mode binormal displacement series and correspondent spectral contents from testing cases IDs 01 until 10 in the group $A_i = 105\text{mm}$.	211
C.5	Modal frequency response of the second out-of-plane modes with respect to the modal reduced velocity parameter: $45.2 \leq KC^{(d)} \leq 48$.	212
C.6	Normal and binormal dynamics in the space of configuration obtained from the testing case ID 09 of the group $A_i = 70\text{mm}$.	214
C.7	Modal orbits obtained from all testing cases in the group $A_i = 105\text{mm}$.	215
C.8	Second mode normal displacement series and correspondent spectral contents from testing cases IDs 01 until 10 in the group $A_i = 70\text{mm}$.	217
C.9	Second mode binormal displacement series and correspondent spectral contents from testing cases IDs 01 until 10 in the group $A_i = 70\text{mm}$.	218
C.10	Modal frequency response of the second out-of-plane modes with respect to the modal reduced velocity parameter: $30.1 \leq KC^{(d)} \leq 33.9$.	219
C.11	Normal and binormal dynamics in the space of configuration obtained from the testing case ID 04 of the group $A_i = 105\text{mm}$.	221
C.12	Modal orbits obtained from all testing cases in the group $A_i = 35\text{mm}$.	222
C.13	First mode normal displacement series and correspondent spectral contents from testing cases IDs 01 until 10 in the group $A_i = 35\text{mm}$.	224
C.14	First mode binormal displacement series and correspondent spectral contents from testing cases IDs 01 until 10 in the group $A_i = 35\text{mm}$.	225
C.15	Modal frequency response of the first out-of-plane modes with respect to the modal reduced velocity parameter: $13 \leq KC^{(d)} \leq 18$.	226
C.16	Normal and binormal dynamics in the space of configuration obtained from the testing case ID 06 of the group $A_i = 17.5\text{mm}$.	228
C.17	Modal orbits obtained from all testing cases in the group $A_i = 17.5\text{mm}$.	229
C.18	third mode normal displacement series and correspondent spectral contents from testing cases IDs 01 until 10 in the group $A_i = 17.5\text{mm}$.	231

C.19 third mode binormal displacement series and correspondent spectral contents from testing cases IDs 01 until 10 in the group $A_i = 17.5\text{mm}$.	232
C.20 Modal frequency response of the third out-of-plane modes with respect to the modal reduced velocity parameter: $7 \leq KC^{(d)} \leq 10.6$.	233

LIST OF TABLES

2.1	Experimental system parameters used in which test case.	22
2.2	Cylinder subjected to oscillatory flow main control parameters.	28
2.3	VSIV references chronological guide. Nomenclature: Steel Catenary Riser (SCR); Scaled Catenary Riser (ScCR); Rigid Right Cylinder (RRC); and Scaled Flexible Horizontal Cylinder (SFHC).	53
3.1	Main nondimensional parameters related to the hydroelastic dynamics of a catenary-like riser model subjected to the imposed motion at the top due to the action of gravitational waves on a floating unit.	57
3.2	Mechanical properties of the chosen operational riser, the small-scale and the “as-built” models.	58
3.3	Experimental natural frequencies obtained from free decay tests in water and their correspondent mode occurrence plane.	66
3.4	Natural frequencies and modal shapes obtained from Orcaflex [®] numerical model.	71
3.5	Out-of-plane modes natural frequencies, $f_{N,b} (Hz)$, obtained in free-decay tests and numerically using Orcaflex [®]	74
3.6	In-plane modes natural frequencies, $f_{N,n} = f_{N,in-plane} (Hz)$, obtained in free-decay tests and numerically using Orcaflex [®]	75
3.7	Test matrix for the longitudinal catenary-like model subjected to imposed movement at the top, in which $v_i = 2\pi A_i^* f_i^*$, $f_i^* = f_i/f_{N,b}^{(1)}$ and $f_{N,b}^{(1)} = 0.4265Hz$	78
3.8	Fitting curves coefficients used in each experimental group in order to evaluate model arclength and local reference frames.	88
3.9	Targets with poorly measured temporal displacement series and evaluated total length, L , for each testing group using the correspondent interpolation coefficients.	89

3.10	Orthogonality index evaluated using the Orcaflex [®] binormal modes, $\varphi_n(s)$. Each mode norm is in the diagonal.	98
3.11	Orthogonality index evaluated using the Orcaflex [®] binormal modes after orthonormalization process.	99
3.12	Illustration on the modal nomenclature used in the present work.	102
4.1	Dominant modal Keulegan-Carpenter ($KC^{(d)}$) evaluated for all testing groups and the correspondent dominant in-plane normal mode occur- rence.	118
4.2	Modal Keulegan-Carpenter, $KC^{(j)}$, evaluated for all relevant modes in the $A_i = 105\text{mm}$ testing group.	126
4.3	Ratio $f^{(j,k)*} = f_{n,dom}^{(j)} / f_{b,N}^{(k)}$ for all tests with imposed movement at the top $A_i = 105\text{mm}$	128
4.4	Modal Keulegan-Carpenter, $KC^{(j)}$, evaluated for all relevant modes in the $A_i = 70\text{mm}$ testing group.	136
4.5	Ratio $f^{(j,k)*} = f_{n,dom}^{(j)} / f_{b,N}^{(k)}$ for all test with imposed movement at the top $A_i = 70\text{mm}$	137
4.6	Modal Keulegan-Carpenter, $KC^{(j)}$, evaluated for all relevant modes in the $A_i = 35\text{mm}$ testing group	144
4.7	Ratio $f^{(j,k)*} = f_{n,dom}^{(j)} / f_{b,N}^{(k)}$ for all tests with imposed movement at the top $A_i = 35\text{mm}$	146
4.8	Modal Keulegan-Carpenter, $KC^{(j)}$, evaluated for all considered modes in the $A_i = 17.5\text{mm}$ testing group along with the correspondent nondi- mensional frequency parameter, $f^{(j,k)*} = f_{n,dom}^{(j)} / f_{b,N}^{(k)}$ and $f^* = f^{(n,n)*}$	155
4.9	Ratio $f^{(j,k)*} = f_{n,dom}^{(j)} / f_{b,N}^{(k)}$ for all tests with imposed movement at the top $A_i = 17.5\text{mm}$	157
4.10	Ratio $f^* = f_{n,dom}^{(d)} / f_{b,N}^{(k)}$ for all test with imposed movement at the top $A_i =$ 17.5mm , regarding dominant in-plane mode; out-of-plane modes: 6 th until 10 th	162
5.1	Comparison of the frequency ratio parameter values in which could be observed amplitude peak response between the rigid straight cylinder model and the present flexible catenary-like one.	173

A.1	Scaling factor for selected physical quantities using the Froude scale. . .	194
A.2	Mechanical properties of the chosen full scale riser and the scaled model.	196
A.3	Mechanical properties of the designed and “as-built” models.	197
C.1	Modal KC for imposed movement at the top $A_{top} = 105\text{mm}$. Dominant modal KC is colored with respect to the modal color scheme.	209
C.2	Modal KC for imposed movement at the top $A_{top} = 70\text{mm}$. Dominant modal KC is highlighted in red.	216
C.3	Modal KC for imposed movement at the top $A_{top} = 35\text{mm}$. Dominant modal KC is highlighted in red.	223
C.4	Modal KC for imposed movement at the top $A_{top} = 17.5\text{mm}$. Dominant modal KC is highlighted in red.	230

LIST OF ABBREVIATIONS

Abbreviation	Meaning
CAPES	Coordination for the Improvement of Higher Education Personnel
CNPq	National Council for Scientific and Technological Development
FAPESP	São Paulo Research Foundation
FFT	Fast Fourier Transform
FINEP	Brazilian Innovation Agency
FIV	Flow Induced Vibration
HHT	Hilbert-Huang Transform
IPT	Institute for Technological Research
LIFE&MO	Laboratory of Fluid-Structure Interaction and Offshore Mechanics
LMO	Laboratoy of Offshore Mechanics
NDF	Fluid & Dynamics Research Group
NLDR	Non-Linear Dynamics of Risers
TPN	Numerical Offshore Tank
URV	Universitat Rovira i Virgili
USP	University of São Paulo
VIV	Vortex Induced Vibration
VSIV	Vortex Self-Induced Vibration

LIST OF SYMBOLS

Roman letters	Description
A	Local displacement vector
A_i	Imposed amplitude
A_t, A_n, A_b	Local displacement measured in $(\hat{t}, \hat{n}, \hat{b})$, respectively
$A_t^{(k)}, A_n^{(k)}, A_b^{(k)}$	Modal displacements measured in $(\hat{t}, \hat{n}, \hat{b})$, respectively
\mathcal{B}	Modal functions basis (finite)
$\hat{\mathcal{B}}$	Orthonormalized modal functions basis
\mathcal{B}_∞	Modal functions basis (infinite)
C_a, a	Added mass
C_D	Drag coefficient
C_L	Lift coefficient
C_M	Inertial coefficient
D	Diameter
$\hat{e}_x, \hat{e}_y, \hat{e}_z$	Global Cartesian unit vectors
EA	Axial rigidity
EI	Bending rigidity
f	Frequency
f_i	Exciting imposed frequency
f_n, f_b	Normal and binormal motion frequencies
f_N	Natural frequency
f_r	Response frequency
f_s	Shedding frequency
f^*	Frequency ratio
$f^{(j,k)*}$	Modal frequency ratio (j -th in-plane and k -th out-of-plane modes)
KC	Keulegan-Carpenter's number
$KC^{(j)}$	Modal Keulegan-Carpenter's number (j -th in-plane mode)
L	Length
m_s	Linear mass
m^*	Reduced mass
N	Synchronization number
$N^{(k)}$	Modal synchronization number (k -th out-of-plane mode)
O	Anchor point
\vec{P}_j	Arbitrary point

Roman letters	Description
Re	Reynolds' number
$Re^{(j)}$	Modal Reynolds's number (j -th in-plane mode)
s	Arclength
\hat{s}	Normalized arclength with respect to L
Σ	Reference frame
St	Strouhal's number
$St^{(j)}$	Modal Strouhal's number (j -th in-plane mode)
$\hat{t}, \hat{n}, \hat{b}$	Local TNB unit vectors
V_R	Reduced velocity
$V_R^{(j,k)}$	Modal reduced velocity (j -th in-plane and k -th out-of-plane modes)
x, y, z	Global displacements measured in $(\hat{e}_x, \hat{e}_y, \hat{e}_z)$, respectively
XY, XZ, YZ	Cartesian reference planes

Greek letters	Description
λ_f	Flexural length
φ_n	Eigenfunction (n -th mode)
ψ_n	Eigenfunction (n -th mode)
θ_t	Plane angle at the top with respect to the horizontal
ξ	Normalized arclength with respect to L
ζ	Linear structural damping coefficient

Superscripts	Description
\square^c	Centered position
$\square^{(d)}$	Associated with dominant mode
$\square^{(j)}$	Associated with j -th in-plane mode
$\square^{(k)}$	Associated with k -th out-of-plane mode
$\square^{(n)}$	Associated with n -th mode
$\square^{(s)}$	Associated with subdominant mode
\square^s	Static position
\square^*	Normalized with respect to D

Subscripts	Description
\square_b	Associated with binormal direction
f_{dom}	Dominant frequency
\square_i	Associated with imposed motion
\square_n	Associated with normal direction
$f_{n,N}, f_{b,N}$	Normal and binormal natural frequencies
\square_t	Associated with tangent direction

PREFACE

The Laboratory of Offshore Mechanics (LMO) is a large group composed by a few research groups, among them the Fluid-Structure Laboratory, originally named LIFE&MO (Laboratório de Interação Fluido-Estrutura e Mecânica Offshore). The LIFE&MO has dedicated its lifetime to study fluid-structure interaction phenomena and many other aspects of offshore mechanics since 1990, such as: structural mechanics of risers, pipes and mooring lines, dynamic positioning of floating ocean systems, non-linear dynamics and hydrodynamics.

The LIFE&MO main research field has been Offshore Engineering, mainly sponsored by Prysmian, Petrobras, the São Paulo Research Foundation (FAPESP), the National Council for Scientific and Technological Development (CNPq), the Coordination for the Improvement of Higher Education Personnel (CAPES) and the Brazilian Innovation Agency (FINEP). Some pioneer works developed by the LMO group are, among others:

- The Steel Catenary Riser (SRC) pioneer design that was installed in the Petrobras semi-submersible platform P18 (PESCE et al., 1994);
- The methodology used for designing SCRs (PESCE; ARANHA; MARTINS, 1996);
- Analytical treatment of riser dynamics (PESCE, 1997; ARANHA; MARTINS; PESCE, 1997; PESCE; FUJARRA, 1997; FUJARRA, 1997; PESCE et al., 1998, 1999; RAMOS; PESCE, 2003; PESCE; FUJARRA; KUBOTA, 2006; SILVEIRA et al., 2007).

Concerning experimental activities, LMO and LIFE&MO were pioneers in using some new sensing methods and acquisition systems as to measure Vortex-Induced Vibration (VIV) acting on flexible cylinders and riser models since 1997.

For instance, some of these methods and systems use accelerometry and conventional extensometers installed and distributed along the cylinder span (FUJARRA, 1997; FUJARRA; PESCE; PARRA, 1998; PESCE; FUJARRA, 2000; FUJARRA et al., 2001; FUJARRA, 2002).

The Laboratory of Offshore Mechanics carried out many experimental campaigns using small-scale models in several prestigious facilities, such as: the Institute for

Technological Research (IPT), Michigan University and Cornell University. The distributed extensometry method was considered pioneer by the international community (PESCE; FUJARRA, 2000; FUJARRA et al., 2001; WILLIAMSON; GOVARDHAN, 2004).

These sensing methods are still present in recent studies carried out at LMO, e.g. Franzini et al. (2008, 2009, 2011), and other research groups (MOROOKA et al., 2009). Later, the use of high speed optical tracking targets techniques were employed in order to measure spatial displacement series with minimal interference (RATEIRO et al., 2013; FRANZINI et al., 2016a; FRANZINI et al., 2016c; PESCE et al., 2017; SALLES; PESCE, 2019).

Leading and always innovating, LMO also introduced the use of Hilbert-Huang Transform (HHT) as to analyze VIV (PESCE; FUJARRA; KUBOTA, 2006; SILVEIRA et al., 2007; FRANZINI et al., 2008, 2010, 2011). The HHT allows the realization of time-frequency spectral analysis for extremely non-ergodic signals, specially the ones that exhibit instantaneous variation on frequency; thus, showing to be essential in state-of-the-art analyses executed with offshore platforms subjected to Vortex-Induced Motion (VIM) (GONÇALVES et al., 2012b).

More recently, the R&D project entitled “Non-Linear Dynamics of Risers: non-linear interactions of hydro-elastic and contact nature (NLDR)”¹ was commissioned to the Universidade de São Paulo (USP) by Petrobras in late 2009, under the Offshore Structures Thematic Network. Its scope was based on four complementary activities, as follows:

- Mathematical modeling of risers dynamics with reduction techniques, using non-linear modes representation;
- Parametric excitation and internal resonant responses, arising from dynamical interaction in several time and space scales, such as heave imposed movement, VIV, or both;
- Analysis of typical cases, focusing on non-linear dynamics of risers;
- Design methodology and experimental tests with riser small-scale model.

It is noteworthy that the Non-Linear Dynamics of Risers (NLDR) project assisted

¹The original title (in Portuguese): “Dinâmica não-linear de Risers: Interações não-lineares de natureza hidro-elástica e de contato”.

LIFE&MO to advance in the state-of-the-art analysis of VIV and riser dynamics, improving technical and scientific topics related to theoretical models, and modeling and monitoring techniques.

Additionally, a multitude of experiments carried out with small-scale riser models were possible due to the NLDR project scope, which comprised topics as:

- Small-scale modeling and monitoring techniques:
 - Development of new methodology for designing small-scale riser models, using a silicon hose filled with stainless steel micro spheres, keeping some degree of similitude with an operational riser (LIFE&MO, 2012b; RATEIRO et al., 2012);
 - Use of high speed optical tracking cameras as to measure spatial displacements with minimal interference carried out at several facilities, e.g. Water Channel of the Fluid & Dynamics Research Group (NDF), Hydrodynamic Calibrator of the Numerical Offshore Tank (TPN) and Towing Tank (IPT) (LIFE&MO, 2012a,b; GONÇALVES et al., 2012a; FRANZINI et al., 2013; RATEIRO et al., 2013).

- Experimental analysis techniques:
 - Consolidation of diverse analysis methodology, combining different approaches, such as: statistical methods, spectrum and time-domain analyses (LIFE&MO, 2012c,d);
 - Time-frequency spectrum analysis using the HHT (LIFE&MO, 2012b; GONÇALVES et al., 2012a; FRANZINI et al., 2013; RATEIRO et al., 2013; FRANZINI et al., 2015, 2016b);
 - Modal decomposition methods applied to Flow Induced Vibration (FIV) phenomena (LIFE&MO, 2012d; FRANZINI et al., 2014).

Particularly, the nonlinear dynamics of risers project produced a huge experimental database that is further detailed in LIFE&MO (2011a,b,c,d,e, 2012a,b,c,d). Finally, quoting the preface of LIFE&MO (2012d):

The specific results obtained [and reported in the technical reports LIFE&MO (2012c,d)] [...] are unique, since they came from thorough planning and experimental tests that were conducted systematically with a great degree of comprehensiveness and completeness.

The reader will be able to verify that the huge experimental data base [...] will serve not only to technical and scientific insights of experimental nature, but also primarily to the verification of different models, turning it possible to be an important source for benchmarking with consequent impact assessments on risers design methodology. (LIFE&MO (2012d), p. 12, own translation.)

The provided experimental database made it possible the present work realization. It is hoped that more works could come to fruition from such an amazing source.

CONTENTS

List of Abbreviations	xxii
List of Symbols	xxiii
Preface	xxvi
1 Introduction	1
1.1 Motivation	1
1.2 Contextualization	3
1.3 Main goals and achievements	7
1.4 Text organization	8
2 Literature review	12
2.1 The Vortex Self-Induced Vibration	12
2.2 Phenomenological aspects, analysis and modeling of VSIV	15
2.2.1 Cylinder subjected to oscillatory flow	15
2.2.2 Vortex Self-Induced Vibration: chronology & idiosyncrasies	25
2.2.3 Other numerical models	51
3 Experimental arrangement and analysis methodology	55
3.1 Experimental description	55
3.1.1 Small-scale riser model: concept, design and characterization	56
3.1.2 Experimental arrangements	59
3.2 Longitudinal catenary-like model: modal characterization	65
3.2.1 Test matrix and selected cases	76
3.2.2 Real riser paradigm and the experimental methodology motivation	79

3.3	Experimental analysis methodology: modal approach to the VSIV	82
3.3.1	Raw data pre-processing	86
3.3.2	Modal space and Galerkin's decomposition	96
3.3.3	Results post-processing	100
3.3.4	Governing parameters and their modal counterparts	106
3.3.5	Structural and hydrodynamic oscillators	114
4	VSIV modal response analysis	116
4.1	Rigid straight cylinders	119
4.2	VSIV response in a catenary-like cylinder	123
4.2.1	Testing group $A_i = 105mm$	124
4.2.1.1	Modal orbits, synchronization and amplitude results	125
4.2.1.2	Modal similarity	132
4.2.2	Testing group $A_i = 70mm$	133
4.2.2.1	Modal orbits, synchronization and amplitude results	134
4.2.2.2	Modal similarity	141
4.2.3	Testing group $A_i = 35mm$	142
4.2.3.1	Modal orbits, synchronization and amplitude results	142
4.2.3.2	Modal similarity	150
4.2.4	Testing group $A_i = 17.5mm$	151
4.2.4.1	Modal orbits, synchronization and amplitude results	153
4.2.4.2	Modal similarity	165
4.3	Intra and intersimilarities	166
5	Conclusions and further works	170
5.1	Considerations on the modal methodology approach	170
5.2	VSIV multi-modal response	172

5.3	Final thoughts on the VSIV modal approach	176
5.4	Further works	178
References		179
A – Testing model design		193
A.1	Froude scale	193
A.2	Riser scaling	195
A.3	Mechanical characterization	198
B – Experimental analysis methodology: algorithms		200
B.1	Orthonormalization - Modified Gram-Schmidt	200
B.2	Numerical differentiation	201
B.2.1	Arbitrary step	201
B.2.2	Fixed step differentiation	202
B.3	Filter design	204
C – VSIV: modal analysis complementary results		206
C.1	$A_i = 105mm$	206
C.2	$A_i = 70mm$	213
C.3	$A_i = 35mm$	220
C.4	$A_i = 17.5mm$	227

1 INTRODUCTION

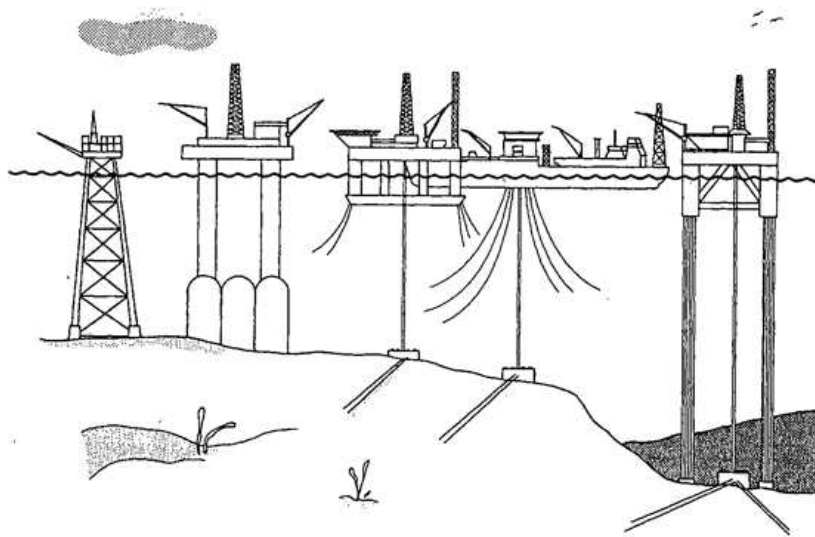


MAHLER, G., Symphony no. 8, Part II: Schlußszene aus Goethes Faust (excerpt)

1.1 Motivation

Currently, the use of commodities as oil and gas is still intrinsically connected to the world development, participating in industrial processes or in daily civilian activities, such as fossil fuel used in vehicles and heating source. Thus, the exploitation of hydrocarbons in the marine environment was responsible for nearly 2.1 billions dollars annual revenues in 2021¹.

Figure 1.1: Schematic configuration of typical offshore structures use to exploit and store hydrocarbons.



Source: Extracted from [Faltinsen \(1993\)](#).

¹According to IBISWorld.

In the XX century, the majority of risers employed in the oil and gas exploitation were rigid and the use of such structure was possible due to their prospecting in shallow waters basins; see the first and second examples in Figure 1.1. Additionally, a vast amount of oil and gas could be exploited onshore, specially in the Middle East, providing the commodity at low price.

Notwithstanding, the historical events that occurred in the last century, *e.g.* the Gulf War, showed that, in order to maintain the progressing zeitgeist, it was necessary to find new markets from where the commodity could be obtained.

The discovery of hydrocarbons basins in deep and ultra-deep waters changed how the offshore industry should approach the designing and projecting methodologies, taking into consideration new solutions, such as the Highly Compliant Rigid (HCR) riser and the flexible Steel Catenary Riser (SCR); see Figures 1.1-1.2.

Figure 1.2: Different risers configurations used in deep-waters exploitation and drilling process.



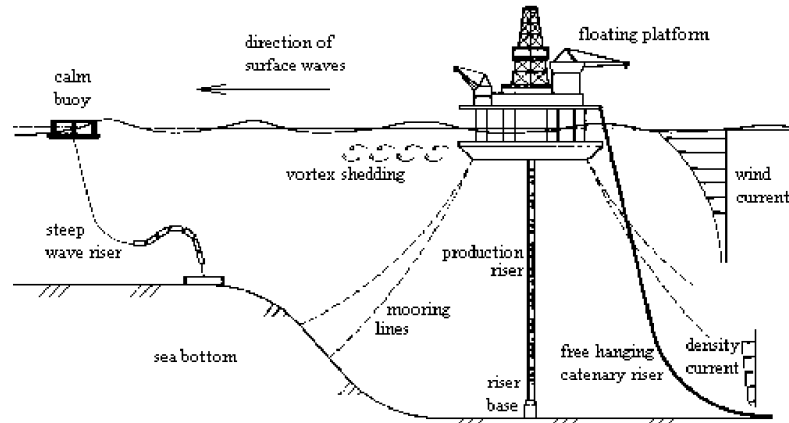
Source: Extracted from 4subsea - Flexible Pipeline Engineering. All rights reserved.

Although rigid risers in shallow water also experience fluid-structure interaction phenomena, the dynamics observed in flexible marine structure due to Fluid Induced Vibration (FIV) is highly nonlinear and assorted; see Figure 1.3.

The nonlinearities arise from a multitude of sources, such as: incident current; imposed motion in the marine platforms or Floating Production Storage Offloading (FPSO) systems due to the incidence of gravitational waves; nonlinear contact in the

Touch Down-Zone (TDZ) with the seabed; structural materials composition; internal multi phase flow; amid others.

Figure 1.3: Some nonlinear phenomena acting on different risers and floating vessels.



Source: Extracted from Hoffman et al. (1991).

Such hydroelastic systems are so complex that it is difficult to fully comprehend and predict its dynamics considering all possible phenomena to which it could be subjected at once, not even by the current computational methods and hardware available.

Thus, the use of small-scale prototypes experimental results are more and more necessary in order to calibrate prediction models that are tailor made for some real case scenarios. The goal of the present work is to unveil some interesting behaviors observed from the dynamics of a SCR small-scale model, considering just a snippet of the real scenario in which there is the imposition of movement at the upper extremity due to floating vessel oscillations.

1.2 Contextualization

The experimental data available for the present work was obtained during the “Non-linear Dynamics of Risers” project sponsored by Petrobras which is presented in the Preface. The project had a huge scope and experimental campaigns were carried out in several facilities.

As to partially replicate the real structural dynamics in a laboratory facility, a testing prototype was designed using scaling methods, typically used in experimental marine applications regarding floating structures, in order to obtain a small-scale model that could be as representative as possible to a real scale flexible riser.

The small-scale prototype does not exhibit full similarity with the real scale riser; however, there is some degree of similitude between them; see Appendix A. The experimental model is composed of a silicon hose filled with stainless steel micro spheres and it is launched in still water from a fixed structure on top of a towing vehicle at the IPT facility, located in São Paulo, Brazil.

Tests were carried out using the small-scale model and subjecting it to incident flow, imposed movement at the top, or both concomitantly. The testing models were arranged in-plane with the incident flow or perpendicular to it. Additionally, the incident flow were imposed intrados or extrados with respect to the catenary plane.

The water depth was about 3.5m deep, considering the fake floor used to anchoring the slender model. Due to the structural relative weight, a plane half catenary-like static configuration was achieved successfully. The upper extremity, also known as the hang-off point, was fixated in an actuator that could impose vertical movement at it.

The acquisition system was composed of high speed tracking target cameras and a typical traction cell at the upper extremity. Special reflecting tape strips were placed along the cylinder span in order to the tracking cameras measure the 3D Cartesian instantaneous position of each monitored section.

The vertical movement could be harmonic, specified using an amplitude and exciting frequency values, or it could even emulate a typical JONSWAP sea condition spectrum. The present works deals only with the experimental arrangement in which harmonic movement is imposed at the upper extremity.

Hence, the imposed vertical motion was used to experimentally simulate the effect due to gravitational waves in floating vessels where real scale flexible risers are installed in order to exploit hydrocarbons, typically oil and gas, or inject substances, such as water or carbon-dioxide, in oil wells.

The vertical plane motion acting on the plane catenary-like structure induces vortex shedding that produces lift forces pointing in the out-of-plane direction. As a result, the in-plane dynamics induced lateral motion through the structural span. This phenomenon here named Vortex Self-Induced Vibration (VSIV), after [Fernandes et al. \(2008\)](#).

Whereas it is not fully understood the VSIV role on the general fatigue life of a SCR, lateral displacement at the Touch Down Zone (TDZ) can induce a snaking movement at the seabed trenches where the structure rests. This motion could cause collapse

of the trenches walls due to the excavation process induced by the lateral motion. Consequently, the boundary condition change at the Touch Down Point (TDP) to a cantilever-like one would have a great fatigue impact locally.

The phenomenon of out-of-plane movement due to in-plane harmonic oscillation in a viscous fluid was already reported occurring in straight rigid cylinders models (SARPKAYA, 1976, 1986; SUMER; FREDSSØE, 1988). Sarpkaya and Rajabi (1979) reported an early model to predict the transversal amplitude response of circular rigid cylinders subjected to harmonic oscillations.

Sumer and Fredsøe (1988) presented a thorough study using a couple of rigid cylinders mounted in an elastic structure free to vibrate in the plane orthogonal to the forced harmonic oscillation movement. The results reported showed that the cross-flow dynamics exhibits several amplitude peaks, depending on the forced movement velocity, and the existence of a synchronicity between both movements.

The name Vortex Self-Induced Vibrations (VSIV) was firstly introduced in Fernandes et al. (2008) when early experimental data obtained in a real scale structure append to Petrobras P18 platform evidenced lateral motions due to imposed movement at the floating unit.

Later, Fernandes, Mirzaei Sefat, and Cascão (2014) also carried out experimental studies using a rigid straight cylinder, finding more evidences on the kinematic and dynamic characteristic responses exhibited by the structure.

Laboratory observations of flexible pipes subjected to VSIV can be find in Le Cunff, Biolley, and Damy (2005), Rateiro et al. (2013), Wang et al. (2014), and Pesce et al. (2017), to cite a few. These former references are also characterized by analyses in the state of configuration, *i.e.* regarding the 3D Cartesian displacements of each monitored section.

The multimodal vibrating intrinsic behavior of flexible structures oscillations poses big challenges in the experimental analysis, limiting itself to some selected cases in which a certain mode dominates the general structural dynamics.

The modal characterization would benefit the experimental analysis by spatially filtering the structural motion, unveiling fewer Degrees of Freedom (DOF), *i.e.* the vibrating eigenfunctions, in which the majority of the system energy is distributed. Thus, the modal representation is also a form of obtaining Reduced Order Models (ROM) for the hydroelastic system.

Additionally, the coupled 3D hydroelastic responses are highly nonlinear, exhibiting internal and parametric resonances. There is also a fundamental difference on the kinematics of the VSIV acting on a plane slender structure when compared to the rigid straight cylinder case.

The latter is elastic mounted and the forced oscillations are an input of the system, whilst in the former the input is characterized by the imposed motion at the hang-off point and both the in-plane and out-of-plane dynamics are hydroelastic responses.

Thus, the present work uses Galerkin's decomposition and modal analysis methods as to study how the VSIV acts on each modal parcel present in the multimodal responses. Accordingly, some ansatzes are also needed in order to turn the phenomenon treatable from the modal hydroelastic system characterization perspective.

The methodology to be devised later, albeit conventional, is pioneer, providing a fully linear modal representation of the VSIV acting of a catenary-like cylinder. Modal analysis methods were used formerly in order to characterize the structural response with respect to its dominant mode information, which can be regarded as a proto analysis in the modal space.

For instance, [Wang et al. \(2015\)](#) used wavelet analysis so as to obtain instantaneous representation of the out-of-plane response. The use of strain data in the aforementioned work also revealed that there are consistent differences in the catenary-like response within the imposed movement oscillation period.

This may be attributable to the asymmetry exhibited in the catenary-like static configuration due to the curvature caused by the structural own weight. [Wang et al. \(2015\)](#) also studied the hydroelastic response considering the local Keulegan-Carpenter (KC) parameter distribution along the structural span.

Typically, the KC is measured with respect to the vertical motion experienced by floating units, or, in the rigid straight cylinder, the forced harmonic movement; nonetheless, should the in-plane motion be considered as an proper input to the out-of-plane motion in the catenary-like case, then each in-plane section will be subjected to a different KC value.

Contrarily to the characterization reported in [Wang et al. \(2015\)](#), the current modal methodology dwelves deeper in the modal realm, carrying out a modal reinterpretation of the govern parameters typically found in the VSIV analysis.

Moreover, compared to the previous references, the present work suggests a new

set of governing parameters, taking into account that the modal reduced velocity ought to be replaced by the frequency ratio parameter.

This normalized frequency is evaluated as the ratio between the response frequency with the system natural one, which is commonly employed in the analysis of driven damped linear oscillators.

1.3 Main goals and achievements

Rigid straight cylinder subjected to VSIV exhibits a clear causality input/output relation. Regarding this particular structure, the input is the driving oscillation in one direction, presenting fixed amplitude, and the output is the response measured in the perpendicular direction with respect to the imposed movement.

Considering the catenary-like structure, the only true input in the system is the forced motion at the upper-extremity and both in-plane and out-of-plane oscillations are responses of the hydroelastic oscillator.

Thus, it should be necessary to assume a causality relation between the in-plane and out-of-plane responses, which is characterized by the hypothesis that the out-of-plane response is solely caused by the in-plane one; additionally, the out-of-plane oscillations has a second order effect in the in-plane one. Such causality assumption would make the problem physically treatable, establishing an input/output relation determined by a given experimental analysis methodology.

Taking into consideration that the VSIV is characterized by multimodal response in the catenary-like case, modal analysis could allow to reduce the system order by specifying in which modes the structure responds.

Modal decomposition carried out using Galerkin's method would be a linear approximation of the highly nonlinear phenomenon. Furthermore, the linearization process should be executed around the structural static configuration as to simplify the geometric nonlinearities presented by the catenary-like configuration.

One big challenge is that the in-plane motion presents different amplitudes along the cylinder span and it is not possible to determine an unique characteristic value. Moreover, even considering the modal approach, the in-plane modal response depends on the imposed amplitude and exciting frequency at the top extremity, not being achievable fixed values.

However, it could be possible to conjecture whether the dominant mode amplitude should be used to characterize the out-of-plane one, finding a clear causality relation between in-plane and out-of-plane dynamics. Together with the dominant mode amplitude, one should also consider the dominant frequency obtained in its movement.

Undoubtedly, this is considered a fundamental assumption in the present work in order to seek similarities with the rigid cylinder cases using the dominant in-plane mode as the driving mechanism for the multimodal out-of-plane response.

It is certainly true that the hydrodynamic oscillator is generally characterized by a group of governing parameters, such as the Keulegan-Carpenter's, Reynolds' and Strouhal's numbers, among others. Notwithstanding, as a result of the varying in-plane amplitude, these parameters cannot assume fixed values, varying along the cylinder span.

These parameters are typically presented for the rigid cylinder model and, when needed, they can be used in the strip theory context. Regarding the modal representation, one could wonder how these parameter would be included in the experimental analysis and if there is the necessity of adapting them in some modal degree.

These are some considerations that will be addressed in the following chapters. The present work main question to be answered is whether there is similarities between the complex multimodal response observed in the catenary-like case with the fundamental results obtained using a rigid cylinder.

As a result of these considerations, modal analysis could unveil that it is possible to attain similarities between the rigid cylinder experimental results with the ones obtained using catenary-like model. Achieving this was possible considering the in-plane dominant mode as driving mechanism for the out-of-plane response.

More importantly, the reinterpretation of Buckingham's Π theorem, obtaining a set of modal governing parameters, was a fundamental step in order to achieve the main results. It is also the case that modal intra and intersimilarities could be found during analysis of the VSIV multimodal responses.

1.4 Text organization

The modal experimental analysis carried out during the last years produced a total amount of 60GB data, distributed in a multitude of graphics, several databases and a

proto numerical solver with thousands lines using MATLAB[®].

Consequently, the current work is organized considering the multitude of experimental results that were obtained in the previous years, aiming to provide a concise text that is accessible to the reader, without losing the rigorous foundations used to devise the experimental methodology.

Thus, the writer tried to limit the text insofar as containing only the most fundamental results, considering only the modal analysis. Space of configuration findings and complimentary modal results are avoided in the main text, being presented in Appendixes when necessary.

The present work is organized in five different chapters that are advisable to be read in order. The current chapter is the introduction in which a brief contextualization was given in order to situate the reader in the context of multimodal responses of a catenary-like flexible cylinder subjected to VSIV.

The main goals and results were also summarized in the previous section, providing the reader a black box perspective, in which it is possible to understand the inputs and outputs present in this work. Hence, the work itself would be a thorough description on the black box contents, *i.e.* the experimental methodology devised.

The second chapter, entitled “Literature review”, contains a concise presentation on the VSIV history and a summary of the results reported in the technical literature. Currently, no review paper was solely written about the VSIV; thus, the second chapter tries to partially fill this gap, showing a brief time line on the previous findings about the VSIV reported in several papers.

The literature review chapter also presents a critical evaluation of the multitude of terminologies used in technical publications in order to refer to the VSIV. The lack of consensus and the adoption of a name that describes the phenomenon was a challenge to be overcome when searching for references and, consequently, the present review is to be considered as thorough as possible, but not complete.

Following, the third chapter is the present work core, acquainting the reader with a detailed characterization of the experimental model and arrangement used. Besides, the modal space and a modal characterization of the structural system is carried out using analytic results and a discrete model simulated using Orcaflex[®].

The modal characterization is comprised of free decay tests from which the structural natural frequencies are computed. Then, the numerical model is used as to obtain

the structure eigenfunctions, *i.e.* vibrating modes. The Orcaflex[®] results are discussed and comparison of the natural frequencies obtained numerically with the ones in free decay tests is carried out.

Furthermore, analytic results concerning the catenary cylinder eigenfunctions reported in [Chatjigeorgiou \(2008\)](#) and [Pesce and Martins \(2005\)](#) are used in order to specify the modal basis used in the Galerkin's decomposition.

A thorough description on the processing methods used in the experimental analysis is then provided. These tools are not innovative *per se*, being based on classical methods of averaging oscillating series, basic concepts of signal and spectral analysis, and differential geometry.

A more complex and fundamental discussion about the VSIV governing parameters is carried out using Buckingham's Π theorem. A reinterpretation of the usual parameter is executed, achieving their modal counterparts that are going to be used in the experimental analysis.

The assumption that the in-plane motion be considered as an input for the out-of-plane response is revisited at the end of the third chapter. Finally, it is presented a new ansatz that tries to incorporate the concept of dominant KC, *i.e.* the modal KC evaluated to the dominant mode (largest modal amplitude), into the modal ROMs formulation.

It is noteworthy to note that the present work does not formulate a modal ROM explicitly, but it tests the hypothesis that such ROM could be written as a function of the in-plane dominant mode dynamics in a first approximation. The experimental results obtained later would serve as a calibration tool to other models, benchmarking, or both.

The fourth chapter presents the results obtained using the proposed experimental methodology in the previous chapter. Firstly, the results reported in [Sumer and Fredsøe \(1988\)](#) and [Fernandes, Mirzaei Sefat, and Cascão \(2014\)](#) are reinterpreted using the frequency ratio parameter in lieu of the reduced velocity.

These results are used to propose a simple tool to predict possible candidates that will present some sort of resonant peak response. The candidates are the group of modal amplitudes obtained from the Galerkin's decomposition method, average using Root Mean Square (RMS).

The modal results are displayed in a similar fashion of the ones reported in [Sumer and Fredsøe \(1988\)](#) and [Fernandes, Mirzaei Sefat, and Cascão \(2014\)](#). The set of

results for each mode is comprised of a peak-to-peak amplitude graphic, in which it is possible to check for peak responses, and a set of spectral amplitude graphics from which the synchronization presented in a given amplitude peak can be identified.

The candidates predicted are compared with the peaks evidenced in the peak response graphic for each mode. Then, if they are indeed a resonant peak, they are classified accordingly. Other peaks that are not predicted by the frequency relations are also addressed.

Considering the experimental testing groups presented in the third chapter, it is argued that the first group to be analyzed is the $A_i = 105\text{mm}$, followed by 70mm, 35mm and 17.5mm. The analysis follows that order due to the actuator power limitation, which is responsible for higher imposed amplitude cases be subjected to a exciting frequency whose values are lower.

It is observed that, when higher driven frequencies are used in the imposed motion, the VSIV modal response is richer in higher modes responses, being more complex to analyze.

A modal intersimilarity test is carried out by plotting the amplitude peak responses for all modes in the same graphic. This analysis is carried out for each testing group and later the results as recollected and reanalyzed in a modal intrasimilarity test.

The main text finishes with the fifth chapter, in which it is summarized the results obtained using the proposed methodology. Frequency ratios reported to the rigid straight cylinder tests are compared to the values found in the multimodal analysis. Moreover, it is presented a brief discussion on possible further works.

The reader will find three Appendixes that are complementary to the main text. The first appendix carries a detailed discussion on the design of the small-scale testing model and its mechanical characterization in order to obtain rigidity moduli, specific mass, structural damping coefficient, to cite just a few.

The second appendix contains a description of all numerical algorithms and methods used in the experimental analysis. Filtering approaches are also introduced. The final and third appendix contains complementary experimental results. These additional results were not added in the fourth chapter due to the vast amount of results already included there.

This ends the introduction chapter. The author hopes for a good appreciation of the present work.

2 LITERATURE REVIEW

*(...) Sem tangibilidade, ver humilhava a memória,
que nunca recuperaria a completude de coisa
alguma. A memória era o resto da realidade. Uma
sobra que mutava para a ilusão com facilidade.*

MÃE, V.H., *In: Homens imprudentemente poéticos.*

The Vortex Self-Induced Vibration (VSIV) belongs to the class of Flow Induced Vibration (FIV) phenomena in fluid-structure nonlinear dynamics study field. Generally, the VSIV occurs always on slender flexible structures, as risers and umbilical cables, that are launched in catenary-like configuration, so that an imposed movement at their top end, as those due to the action of gravitational waves on a floating vessel, causes an oscillating movement at their configuration plane (henceforth called in-plane). As a result of such in-plane oscillations, vortex shedding is established and it induces lift forces that causes out-of-plane oscillating vibrations.

At a first glance, the VSIV and the Vortex Induced Vibration (VIV) seem to bare a great deal of similarity: in-plane flow induces vortex shedding which causes lateral movement. Nonetheless, this impression is misleading from the actual VSIV phenomenology. Firstly, the in-plane flow in VSIV is a response from imposed oscillatory movement at the structure upper end, which differs from the VIV in which there is an incident current flow. In addition, the VSIV phenomenology differs in almost every aspects from the VIV, displaying a closer similarity with the response of a rigid cylinder subjected to oscillatory flow. The VSIV phenomenology will be further discussed later in this chapter.

2.1 The Vortex Self-Induced Vibration

Now that the VSIV was briefly introduced, one ought to dive deeper in its origins, terminologies and other aspects of interest. The VSIV has a strong dependence on the structural configuration, occurring in cases that the geometrical configuration has any horizontal displacement with respect to the structural suspension point fixed at the

floating unit.

At the present work only planar structural configurations are considered, *i.e.* when it is possible to define a set of osculating planes spanned by tangent and normal vectors evaluated at each point of the structural material curve so that these planes are equivalent to each other (henceforth called vertical plane). Under this consideration, the VSIV is caused by any oscillatory movement at the upper end in the vertical plane due to the floating unit dynamics.

Besides, although the floating unit can display rigid body motion, *e.g.* heave, surge and pitch, the same terminology is not conceptually correct to describe the structural hang-off point motion, for there is a causality relationship between the latter onto the former.

One typical structural configuration found in offshore applications is the catenary-like. The terminology catenary-like (or “catenary”) is conceptually more precise for the catenary shape is obtained in the context of an inextensible string subjected to its own weight. In other words, the catenary dynamics is due to the geometrical stiffness variation, *i.e.* reaction variation at each section.

Not only offshore structures launched in catenary-like configuration are extensible, they are also subjected to bending stiffness effects near both lower and upper ends, regions where the curvature changes substantially. On the other hand, the structural dynamics at mid-span is dictated by the geometrical stiffness.

Although “catenary shape” in the context of real structures is an improper terminology usage, one acknowledges that it is impossible to go against the current terminology fashion and advises the reader to think of catenary-like (or “catenary”) every time it is read catenary in the following work.

In VIV literature, specially regarding elastic mounted rigid cylinders, the incident flow direction is referred as In-Line (IL) and the response is measured on the Cross-Flow (CF) direction. The same terminology becomes less accurate in the VSIV context for the self-incident flow is approximately within the “catenary” plane¹, reinforcing the *in-plane* terminology usage in the present work.

The other way around, the CF direction is perpendicular to the self-imposed flow, coinciding with the out-of-plane direction. Nonetheless, such terminologies, IL and CF,

¹ Considering that the out-of-plane motion is of lesser order than the in-plane one, so the instantaneous and local osculating planes, spanned by the tangent and normal to the curve unit vectors, $\hat{i}(s,t)$ and $\hat{n}(s,t)$, are somehow bounded around the static configuration plane.

will not be used within the present work.

In the technical literature, there is little consensus on how the VSIV as a phenomenon should be named and there are some culprits to be considered in this lack of terminology precision. Firstly, the VSIV chronology shows its first (and accidental) observation dating from the late '90s², being a recent study field. Secondly, the VIV technical literature is very proliferous, causing a direct influence on studies regarding the VSIV and, sometimes, an amalgamation of both phenomena into two faces of the same coin. Lastly, the usual terminology fashion in this field can lack of precision sometimes, as discussed previously.

Juxtaposed with which has been discussed, the VSIV can be found in the technical literature as: Intermittent Vortex-Induced Vibration Lateral Response³; Heave-Induced Intermittent Vortex-Induced Vibration⁴; Heave Induced Lateral Motion (HILM)⁵; Vortex Self-Induced Vibration⁶; Vortex-Induced Vibration in Oscillatory Flow⁷; Vortex-Induced Vibration caused by Vessel Motions⁸; Unsteady Flow Vortex-Induced Vibration⁹; Modulated Vortex-Induced Vibration¹⁰; among others.

Some of those terminologies are redundant, show improper usage of terms, or just consider VIV and VSIV as the same phenomena. Two of them, “Vortex Self-Induced Vibration” and “Modulated Vortex-Induced Vibration”, seem to be the most appropriate in this context. The justification for the usage of “VSIV” over “Modulated VIV” in the present work is purely phenomenological: the VSIV shows a persistent response, with no post-critical regime, nor the “lock-in” phenomenon as in the VIV. So, the choice is based on avoiding the acronym “VIV” that carries much of the VIV phenomenology within.

²Grant, Litton, and Mamidipudi (1999).

³Grant, Litton, and Mamidipudi.

⁴Mark Chang and Isherwood (2003).

⁵Le Cunff, Biolley, and Damy (2005); and Le Cunff et al. (2009).

⁶Fernandes et al. (2008), Rateiro et al. (2013); and Pesce et al. (2017).

⁷Fu et al. (2013a).

⁸Wang et al. (2014).

⁹Lu et al. (2019).

¹⁰Liu et al. (2020).

2.2 Phenomenological aspects, analysis and modeling of VSIV

This literature review aims at a brief contextualization of the VSIV since its first observation in Grant, Litton, and Mamidipudi (1999). The main purpose is to present a historical point of view of how the VSIV has been reported for the last two decades. Besides, the fundamental references that have been used to support the current analyses or served as paradigms to them will be thoroughly discussed along the text, when needed. This approach was adopted to avoid letting the text too tedious to the reader.

This section is organized in order to introduce fundamental studies on the rigid cylinder subjected to oscillatory flow, before taking the VSIV as main subject. This particular order is due to the existence of parallels between both phenomena, as it was pointed out in several VSIV references that will be duly discussed later.

2.2.1 Cylinder subjected to oscillatory flow

Experimental tests of structures subjected to steady incident flow have been a matter of interest for several centuries. Initially, the æolian harp, as the name suggests, was a mythical instrument powered by the god of winds himself, a common godly explanation rule mankind has been following as to accept what rational thinking can not resolve yet.

The mystery around the æolian harp could only be explained fairly recently by Lord Rayleigh in the early XX century, observing that the tones would be a response to an aeroelastic phenomenon, VIV, characterized by the detachment of a von Kármán vortex street which occurred with a certain shedding frequency, f_s , with respect to the incoming velocity, U_∞ .

Surprisingly, the shedding frequency was not purely proportioned to the incoming air velocity, inasmuch as there was a special range in which the vortex shedding frequency would assume a constant value, corresponding to one of the harp string natural frequency. This particular feature of the VIV response would later be called “lock-in”.

Previously, other studies in the fluid dynamic field have already presented theoretical and experimental explanations on the von Kármán vortex street and the vortex shedding frequency in which parameters, such as the Reynolds' and Strouhal's numbers, Re and St respectively, were acknowledged to take a key role on the fluid behavior.

Nonetheless, little was known about the VIV fluid-elastic mechanism and much could be unveiled on this topic over the last centuries (PESCE; FUJARRA, 2000; FUJARRA et al., 2001; SARPKEYA, 2004; WILLIAMSON; GOVARDHAN, 2004; MA et al., 2022). Thus, the VIV is a very complex fluid-structure interaction phenomenon that still puzzles many researchers, specially with respect to flexible structural multi-modal responses (HUERA-HUARTE, 2006).

However complex the VIV response is, the presence of an unsteady incoming flow enriches and increases the structural response complexity to a whole new level. It is noteworthy that the current discussion will be restrained to the rigid cylinder case, which is submitted to a harmonic incident flow with zero mean velocity in one direction.

The cylinder dynamics depends on hydrodynamic loads that occur in the flow and also in the cross flow directions. The in-plane forces are mainly due to drag and added inertia, which can be evaluated considering a parcel that is in phase with the relative velocity (drag) and other with the relative acceleration (inertia).

Firstly with respect to the potential flow theory, a moving structure is subject to hydrodynamic loads that can be expressed as the Froude-Krylov force. Considering a circular cylinder, immersed in a viscous fluid flow, the in-line forces can be approximated as the Morison's formula,

$$F = \frac{1}{2}\rho DC_d \|U\| U + m_d C_M \frac{dU}{dt}, \quad (2.1)$$

in which ρ is the fluid density, D , the cylinder diameter, U , the incoming flow velocity and t , time. The force coefficients, C_d and C_M , are related to drag and added inertia terms, respectively, and the fluid displaced mass, $m_d = \pi\rho D^2/4$. Should the velocity of the ambient flow be harmonic, it will be possible to write it as $U(t) = U_m \cos(2\pi f_i t)$, assuming known the velocity amplitude, U_m , and the imposed motion frequency, f_i .

Generally, the imposed motion is supposed to be harmonic with zero mean velocity, which allows one to write $U_m = 2\pi f_i A_i$ with A_i being the imposed amplitude. In this configuration, the Keulegan's-Carpenter's and Reynold's numbers can be evaluated as

$$KC = \frac{U_m}{Df_i} = \frac{2\pi A_i}{D} = 2\pi A_i^*, \quad (2.2)$$

$$Re = \frac{U_m D}{\nu}, \quad (2.3)$$

in which ν is the fluid kinematic viscosity. Moreover, both drag and inertia coefficients also depends on the relative surface roughness, k/D , and they are supposed to assume different values at distinct phases of the oscillatory flow cycle.

Accordingly, any force coefficient, C_f , ought to be written with respect to these governing parameters,

$$C_f = f \left(KC, Re, \frac{k}{D}, f_{it} \right), \quad (2.4)$$

which would not be manageable even for simple geometries. In turn, time independent mean coefficient values are generally simpler and more feasible, *i.e.*

$$C_f = f \left(KC, Re, \frac{k}{D} \right), \quad (2.5)$$

to be carried out experimentally.

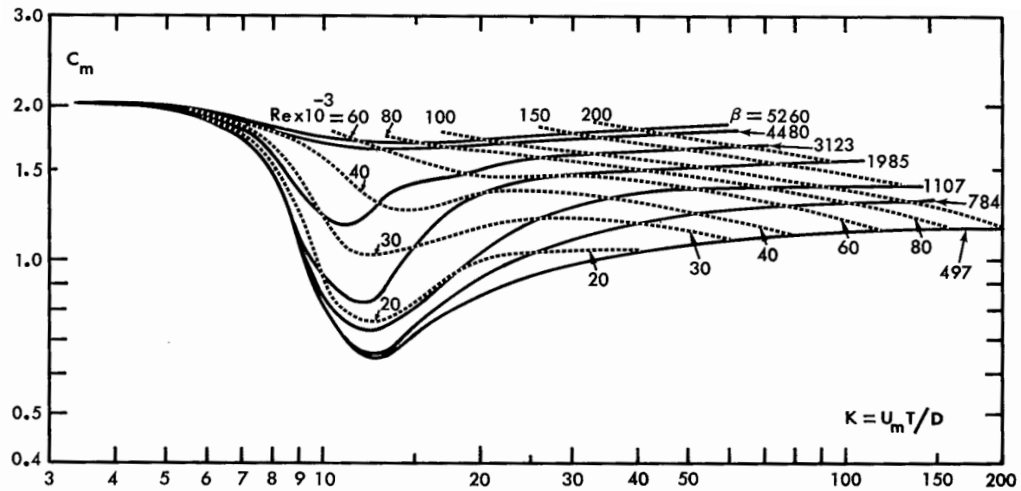
[Sarpkaya \(1976\)](#) argues that the choice of both KC and Re are not the best option available due to them be depended on the velocity amplitude, U_m . Consequently, it is suggested the frequency parameter instead

$$\beta = \frac{KC}{Re} = \frac{f_i D^2}{\nu}. \quad (2.6)$$

Thus far, there was a multitude of experimental data concerning a fixed cylinder subjected to oscillatory flow, measuring in-line and transverse forces by means of force transducers in each directions. Focusing on in-line forces, such as drag and fluid inertial force, there was no systematical experiment that could combine into a set of charts how the force coefficients would behave in the oscillatory flow regime.

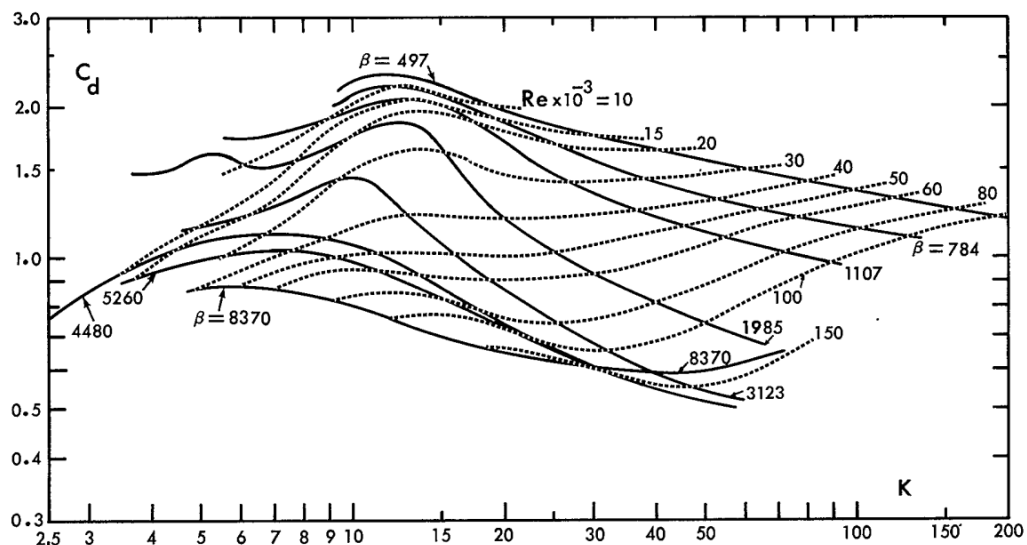
[Sarpkaya \(1976\)](#) overcame that issue using a novel experimental set-up, consisting of a U-shaped tube with a small section at the middle where a cylinder specimen was placed. The fixed cylinder was subjected to the incident oscillatory flow due to a pressure controlling system. By decomposing the measured in-line force into a parcel in phase to flow velocity and other to the relative acceleration, a direct measurement of drag and the inertial force could be accomplished.

Figure 2.1: Inertia force coefficient, C_M , of a rigid cylinder subjected to oscillatory flow.



Source: Extracted from Sarpkaya (1976).

Figure 2.2: Drag force coefficient, C_D , of a rigid cylinder subjected to oscillatory flow.



Source: Extracted from Sarpkaya (1976).

Undeniably, a great effort was made in Sarpkaya (1976) so as to exhibit a comprehensible set of experimental drag and added inertia coefficients; see Figures 2.1-2.2. Dissecting a bit further the added inertia chart, it is possible to identify that low KC regime displays a limit value, $C_M = 1 + C_a \rightarrow 2^+$ (SALLES; PESCE, 2019), coinciding with the potential added mass, $C_a = 1$.

More significantly, the vast majority of hydrodynamic studies on risers subjected to oscillatory flows uses $C_a = 1$ as known parameter, whereas Figure 2.1 shows that the

added mass varies depending on the amplitude and frequency of the imposed motion; the same occurs with the drag force coefficient. Moreover, those charts are evaluated using data from a fixed rigid circular cylinder, which means that other geometries and configurations need further investigations (SARPKAYA, 1976).

After the previous studies on the fixed cylinder, Sarpkaya and Rajabi (1979) exhibited results using a cylinder that is subjected to an oscillatory flow, however it is free to oscillate in the cross flow direction. Sumer and Fredsøe (1988) also carried out experiments in the same fashion, which were already cited in the context of Le Cunff, Biolley, and Damy (2005), dealing with the VSIV in a catenary-like cylinder.

Considering the elastic mounted cylinder subjected to harmonic flow, the controlling parameters differ from what was considered in the fixed cylinder case; Equation 2.5. Whence some parameters, such as mass ratio, damping coefficient and reduced velocity, are necessary to unveil the new dynamic behavior.

For instance, the lift force coefficient and the relative lateral amplitude could be considered as

$$C_L = f\left(KC, Re, \frac{k}{D}, V_R, m^*, \zeta\right) \text{ and} \quad (2.7)$$

$$Y^* = g\left(KC, Re, \frac{k}{D}, V_R, m^*, \zeta\right), \quad (2.8)$$

in which V_R is the reduced velocity,

$$V_R = \frac{U_m}{Df_N}, \quad (2.9)$$

m^* is the mass ratio,

$$m^* = \frac{m_s}{m_d} = \frac{4m_s}{\rho\pi D^2}, \quad (2.10)$$

and ζ is the damping coefficient. The system natural frequency is f_N ; the structural mass, m_s ; the displaced mass, m_d ; and the fluid density, ρ .

Sarpkaya and Rajabi (1979) evinced some interesting features within the lateral response. Firstly, they introduced a new controlling parameter,

$$R_P = \frac{m_s \zeta}{\rho L D^2 C_{LM}^{\circ}}, \quad (2.11)$$

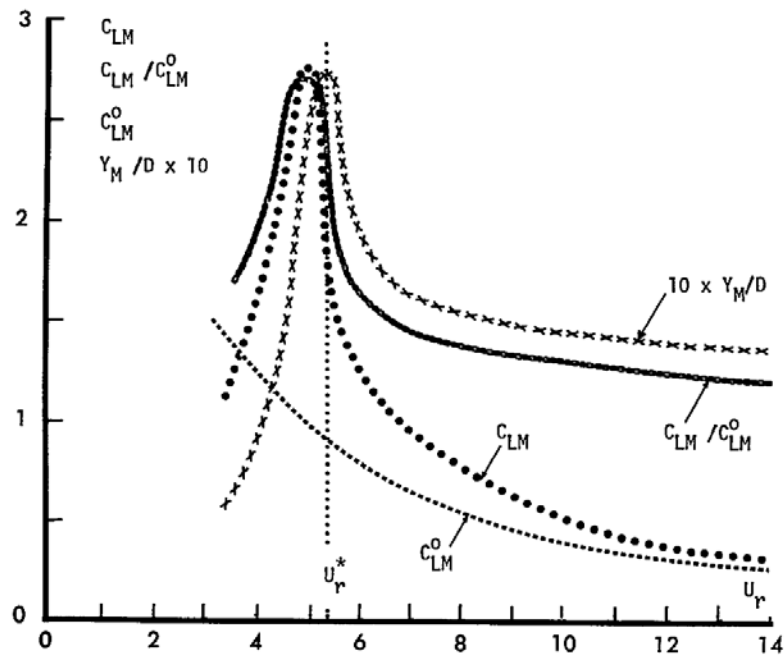
grouping the parameter $m^* \zeta$, commonly used in VIV analysis to characterize the amplitude response, and also the lift force coefficient, C_{LM}° in which C_{LM}° corresponds to the lift force coefficient relative to a fixed cylinder.

The ratio C_{LM}/C_{LM}° appears in the predicted cylinder lateral response,

$$Y_M^* = \frac{V_R^2}{32\pi^2 R_P} \frac{C_{LM}}{C_{LM}^{\circ}}, \quad (2.12)$$

as an amplification parameter to evaluate how the lift force magnitude of an oscillating cylinder can behave with respect to the fixed one; Y_M^* corresponds to the mean relative lateral amplitude.

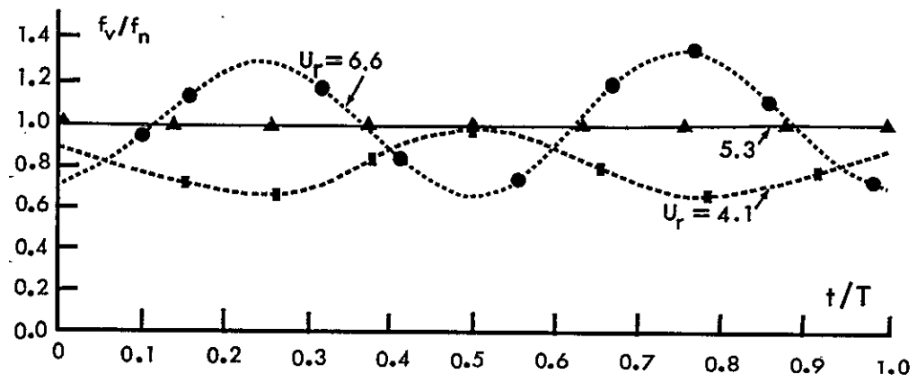
Figure 2.3: Lift force coefficient and lateral motion amplitude with respect to reduced velocity for a sand-roughened cylinder in harmonic flow ($k/D = 0.01$).



Source: Extracted from [Sarpkaya and Rajabi \(1979\)](#).

Interestingly, [Sarpkaya and Rajabi \(1979\)](#) could demonstrate that the perfect synchronization would occur when of $V_R^* = 5.4$ and the maximum of the lift force, C_{LM}/C_{LM}° , would happen to values slightly lower than V_R^* ; see [Figure 2.3](#).

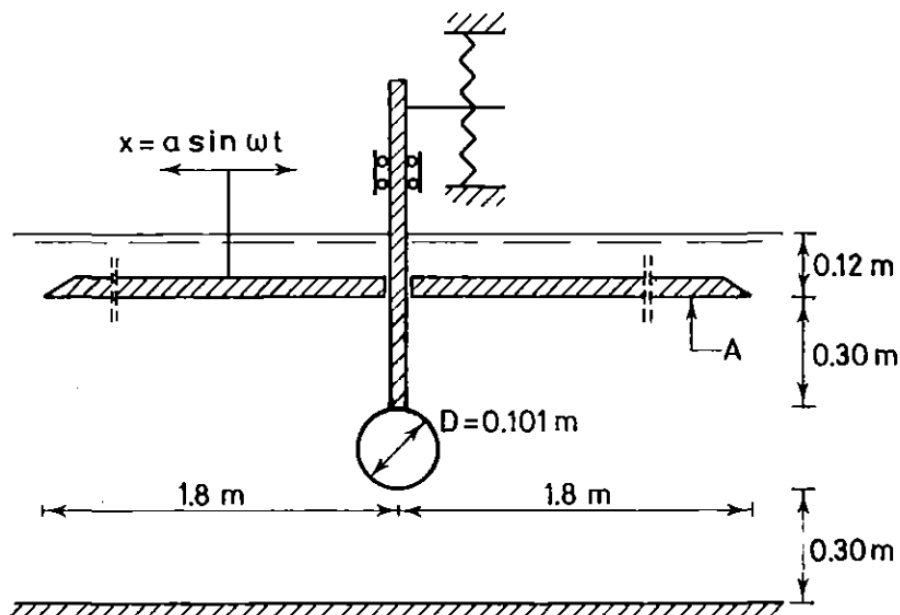
Figure 2.4: Temporal variation on the vortex shedding frequency during a cycle for some reduced velocity values.



Source: Extracted from [Sarpkaya and Rajabi \(1979\)](#).

The shedding frequency also unraveled that its value synchronizes with the system natural frequency in V_R^* , whereas it could assume an oscillating value close to the system natural frequency during the oscillation cycle, depending on the V_R value; see [Figure 2.4](#).

Figure 2.5: Elastic mounted cylinder subjected to harmonic displacement in water: experimental system sketch.



Source: Extracted from [Sumer and Fredsøe \(1988\)](#).

Whilst [Sarpkaya and Rajabi \(1979\)](#) were concerned with the lift force magnitude and its contribution on the lateral amplitude, [Sumer and Fredsøe \(1988\)](#) shed light on

the lift force spectral content, especially on the frequency ratio between lateral and imposed motion, N , with respect to KC and V_R .

Figure 2.5 shows the experimental set-up designed and used in order to carry out a thorough investigation on the lateral motion characteristics. Although fairly simple, the experimental arrange was capable to execute several tests within a broad KC range, including a typical VIV test and others varying parameters, such as: the spring stiffness, k , the system natural frequency (still water), f_n , the relative weight, $s = \rho_{cylinder}/\rho_{water}$, and the stability parameter, $K_s \propto m^* \zeta$; see Table 2.1.

Table 2.1: Experimental system parameters used in which test case.

Exp.	k/ρ (m^2/s^2)	f_n (Hz)	s	K_s
I	0.336	0.71	1	0.9
II	1.074	1.24	1	0.3
III	0.168	0.51	1	1.5
IV	0.336	0.61	1.8	1.2

Source: Extracted from [Sumer and Fredsøe \(1988\)](#).

Following the nomenclature used in [Sumer and Fredsøe \(1988\)](#), the imposed motion is due to a controlled displacement, $x(t) = A \sin(\omega_w t)$, and the velocity can be duly obtained through differentiation,

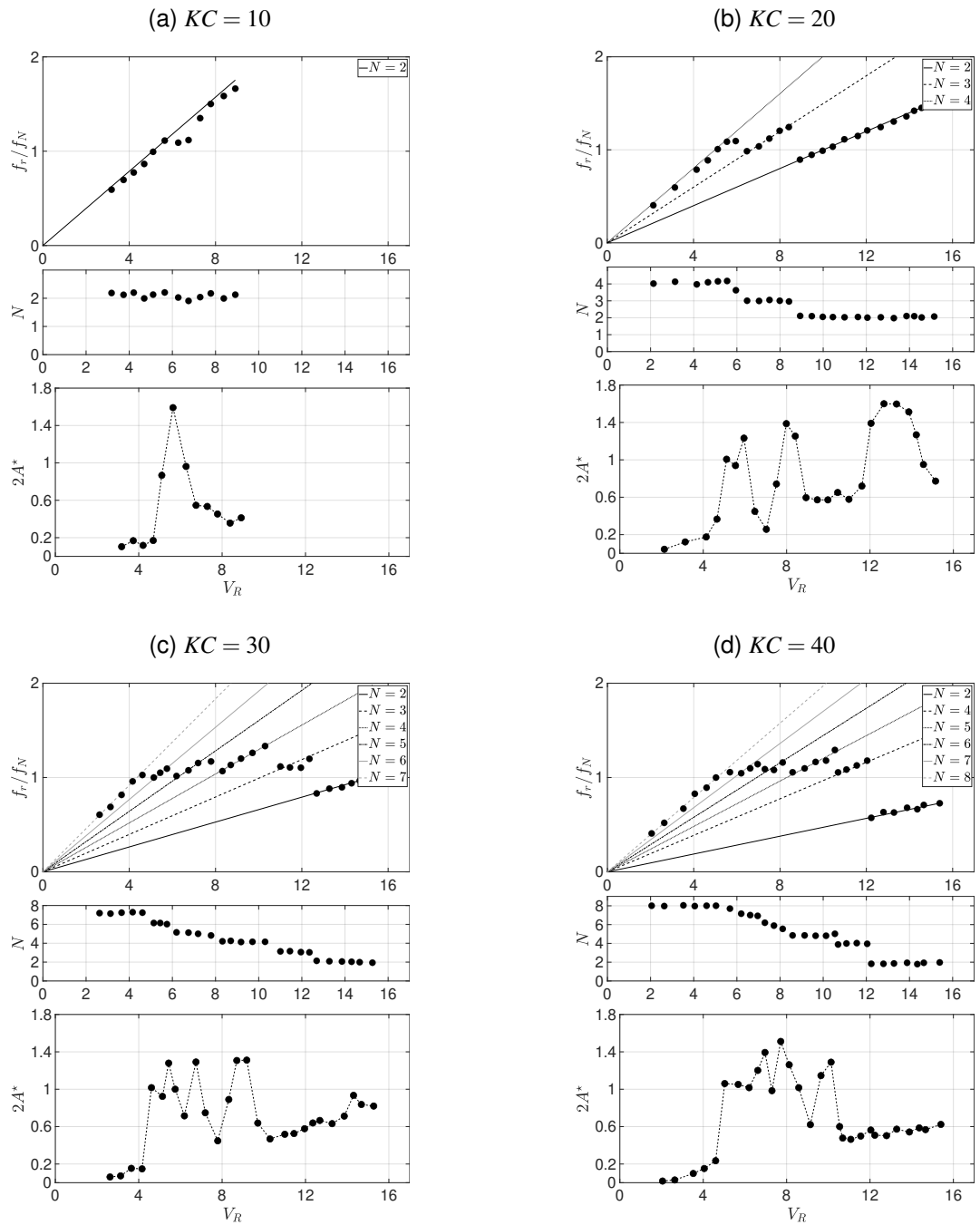
$$U = U_m \cos(\omega_w t) = 2\pi f_w A \cos(2\pi f_w t), \quad (2.13)$$

in which $\omega_w = 2\pi f_w$ is the driving frequency. The Keulegan-Carpenter number, KC , and reduced velocity, V_R , can be directly evaluated using U_m and f_n ,

$$KC = \frac{U_m}{f_w D} = \frac{2\pi f_w A}{f_w D} = 2\pi A^*, \quad (2.14)$$

$$V_R = \frac{U_m}{f_n D} = \frac{2\pi f_w A}{f_n D} = KC \frac{f_w}{f_n}. \quad (2.15)$$

Figure 2.6: Frequency and amplitude response. Exp. I.



Source: Adapted from [Sumer and Fredsøe \(1988\)](#).

Most importantly, the lateral response oscillates with dominant frequency, f , proportional to the driving one, which is computed within the number of vibrations per cycle (hereinafter called the cycle number),

$$N = \frac{f}{f_w}, \quad (2.16)$$

assuming integer values that decreases as the reduced velocity increases; see Figure 2.6. The cycle number shows an interesting behavior that can display an important role in the fatigue damage analysis.

Observing closely Figure 2.6, it is possible to infer that KC is a strong governing parameter and the lateral response shows greater complexity when the KC increases. Except from the $KC = 10$ test that keeps $N = 2$ within the whole run, Figure 2.6a, every other test exhibits a cascade of N values that decreases in a steadily manner until reaching a minimum value of $N = 2$; see Figures 2.6b-2.6d.

Recalling Equation 2.14, the KC is solely dependable on the imposed amplitude, which serves as an energy input to the system. Thus, higher the KC , larger the maximum number of vibration in on cycle can be, which can be verified observing Figure 2.6 where the maximum N can assume higher values as KC increases.

Figure 2.6a displays a typical VIV response, in which the lateral motion frequency follows the increase in the imposed one until it reaches a region near the system natural frequency. There, the “lock-in” causes an amplitude peak response that, passing a critical value, diminishes due to the loss of synchronization.

The other cases present a different response in which the lateral vibration starts with a maximum N until the response frequency reaches values close to the system natural frequency. Thus, a synchronization is achieved and an amplitude peak is observed; see Figures 2.6b-2.6d. Differently from the typical VIV lock-in, the system response usually does not assume the same frequency as the natural one.

Most significantly, the system jumps to a lower cycle number, N , every time the response reaches a peak. This jump phenomenon occurs until the minimum $N = 2$ is achieved. Then, the response does not mitigate, maintaining the relative peak-to-peak amplitude close to one diameter.

Although the $KC = 10$ case seems to display a typical VIV lock-in, the synchronization due to imposed oscillatory movement shows a different kinematics when the KC increases. Thus, this synchronization phenomenon is acknowledged as an unique feature on the lateral vibration due to the oscillatory flow, assuming some sort of “lock-in” behavior asymptotically when $KC \rightarrow 0$.

Sumer and Fredsøe (1988) argues that the cycle number never reaches the unity, $N = 1$, stating that

Note that N becomes unity only (i) in the case where KC is in the range

$4 < KC < 7$, as demonstrated in the following paragraphs; and (ii) in the case where f_w overlaps with f_n (SUMER; FREDSE, 1988, p. 390)

which seems to be the case in their work. It would be interesting to analyze what should occur when the imposed frequency reached the same value as the system natural frequency. In such case, given the aforementioned argument, the lateral response should admit $N = 1$.

2.2.2 Vortex Self-Induced Vibration: chronology & idiosyncrasies

The VSIV was firstly reported in Grant, Litton, and Mamidipudi (1999) during experimental studies using Highly Compliant Rigid (HCR) large-scale models. The experimental tests were conducted in the lake Pend Oreille, USA. The large-scale models were of several configurations, specially a catenary-like configuration launched in 800ft (~ 245 m) depth, using different soil configurations.

The SCR model showed lateral motion when subjected to imposed motion at the upper end. The lateral response was intermittent, displaying amplitude and frequency magnitudes increasing with respect to an increase in the top motion frequency. The lateral dynamics observed was highly nonlinear due to the nonlinear soil-riser contact at the Touch Down Point (TDP).

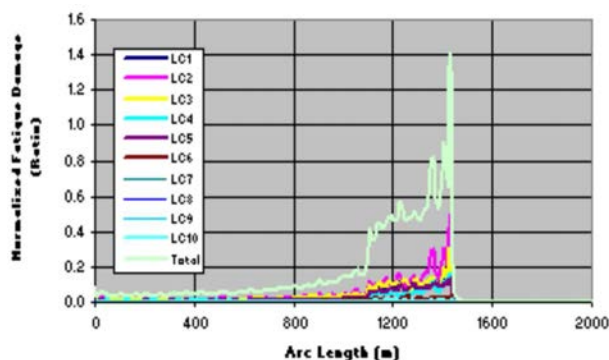
The effect of soil stiffness is of importance at the Touch Down Zone (TDZ), impacting the local dynamics. Although the global dynamics and fatigue life are not heavily affected by the soil stiffness itself (QUÉAU, 2015), the type of soil matters in real structures local analyzes. For instance, a softer soil allows the lateral response at the bottom to display a snaking motion that, over time, produces soil trenches where the riser rests. The event of a lateral trench side collapse could lead to a *quasi*-cantilever boundary condition at the TDZ that would have a great impact on the structural dynamics and fatigue life.

These nonlinear conditions impose a great limitation on frequency domain VIV numerical models and time domain algorithms, albeit slower, need to be employed as to capture the lateral motion observed in experimental data. The fluid-structure coupling is feasible for the hydrodynamic loads adapt to the complex in-plane and out-of-plane synchronous motion. Currently, none of the available commercial algorithms take into account the VSIV in their analyses because it is difficult to measure the VSIV isolated response *in-situ* structures, when a multitude of phenomena occurs concomitantly.

An early time domain model that aimed to capture the VSIV response can be found in [Grant et al. \(2000\)](#), a semi-empirical approach that approximates the lift and drag forces by using data from a Single Degree of Freedom (SDOF) cylinder subjected to steady flow. Then, the instantaneous frequency and amplitude observed in the lateral motion were fed into an algorithm that evaluates the instantaneous hydrodynamic forces that the elastic mounted cylinder would be subjected to. This procedure were tested using several geometrical configurations, including the catenary-like, and showed good agreement with predictions and observations.

Following [Grant, Litton, and Mamidipudi \(1999\)](#) and [Grant et al. \(2000\)](#), [Mark Chang and Isherwood \(2003\)](#) reported a thorough discussion on Computational Fluid Dynamics (CFD) techniques that could be employed into VSIV models. The main goal of [Mark Chang and Isherwood \(2003\)](#) was the fatigue assessment due to the VSIV, which was studied by considering a test matrix using a large-scale generic riser model and typical Brazilian sea conditions. The vortex tracking empirical model ([SARPKAYA; SCHOAFF, 1979a](#); [SARPKAYA; SCHOAFF, 1979b](#)) was chosen over other empirical models, such as wake oscillators, or CFD.

Figure 2.7: SCR normalized fatigue damage in 1 year.



Source: Extracted from [Mark Chang and Isherwood \(2003\)](#).

The outcomes categorically showed that the riser bottom part around the TDZ was subjected to the highest fatigue due to the VSIV; see [Figure 2.7](#). Although promising, the vortex tracking model missed calibration using field measurements, reinforcing the need of experimental tests to be used as paradigms to numerical models.

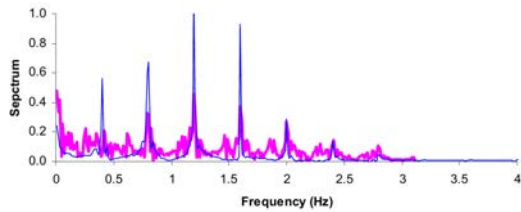
Whilst previous works focused on large-scale models, [Le Cunff, Biolley, and Damy \(2005\)](#) carried out experimental analyses aiming to isolate the VSIV response with a small-scale SCR model. The experimental tests were conducted at IFREMER located in Brest, France. It is noteworthy that the VSIV is difficult to measure *in-situ* due to

the concomitant effect of incident flow (VIV), amid others geophysical phenomena, (LE CUNFF; BIOLLEY; DAMY, 2005, p. 1 apud MARK CHANG; ISHERWOOD, 2003).

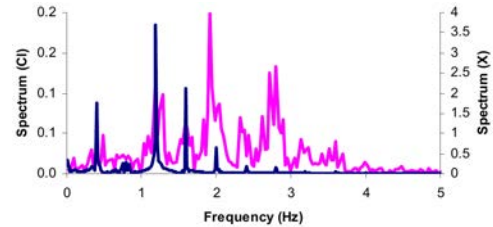
The planar small-scale SCR model was subjected to imposed sinusoidal vertical motion at the hang-off and its bottom sag bend was monitored using optical tracking cameras. The set of observed material points (henceforth called space of configuration) displayed complex and nonlinear dynamics, specially due to the TDP spacial (3D) motion. The lateral response showed to be intermittent and persistent when the imposed motion increased its magnitude and frequency, likewise the previous works.

Figure 2.8: Selected targets spectra and trajectories.

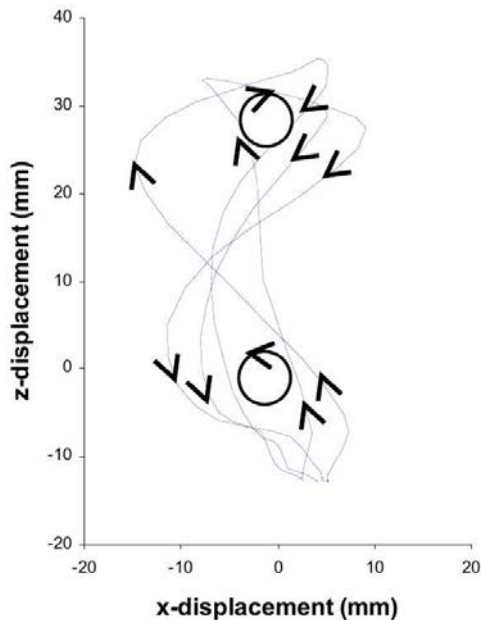
(a) 3D-1 target displacement spectra: experimental in magenta; deepflow in blue



(b) 3D-8 target: displacement spectrum in blue; lift coefficient spectrum in magenta



(c) 3D-8 target: in-plane vs. out-of-plane trajectory



Source: Extracted from Le Cunff, Biolley, and Damy (2005).

Le Cunff, Biolley, and Damy (2005) also introduced a *proto* modal analysis in which an out-of-plane dominant mode was determined by using the largest lateral displacement value measured in the bottom sag bend region. Additionally, a 2D numerical

model by slice (ETIENNE et al., 2001) was employed to obtain an iterative process that computes fluid forces coefficients using a Navier-Stokes solver and a structural coupling model; see Figures 2.8a-2.8b. The riser experimental and computed states showed good agreement.

One of the greatest achievements in Le Cunff, Biolley, and Damy (2005) is the parallel between the VSIV and the dynamics of rigid cylinders subjected to oscillatory flow (SARPKAYA, 1976; SARPKAYA; RAJABI, 1979; SARPKAYA, 1986; SUMER; FREDSSØE, 1988, 1989; KOZAKIEWICZ; SUMER; FREDSSØE, 1994). Consequently, the VSIV inherited a group of control parameters that plays an important role in its intrinsic behavior; see Equation 2.8 and Table 2.2.

Table 2.2: Cylinder subjected to oscillatory flow main control parameters.

Parameters	Definition
Reynolds	$Re = \frac{UD}{\nu}$
Keulegan-Carpenter	$KC = \frac{U}{f_w D} \sim \frac{2\pi A}{D}$
Reduced velocity	$V_R = \frac{U}{f_n D}$
Relative roughness	$\frac{k}{D}$
Stability parameter	$K_s \propto m^* \zeta = \frac{4m_s}{\rho \pi D^2} \zeta$

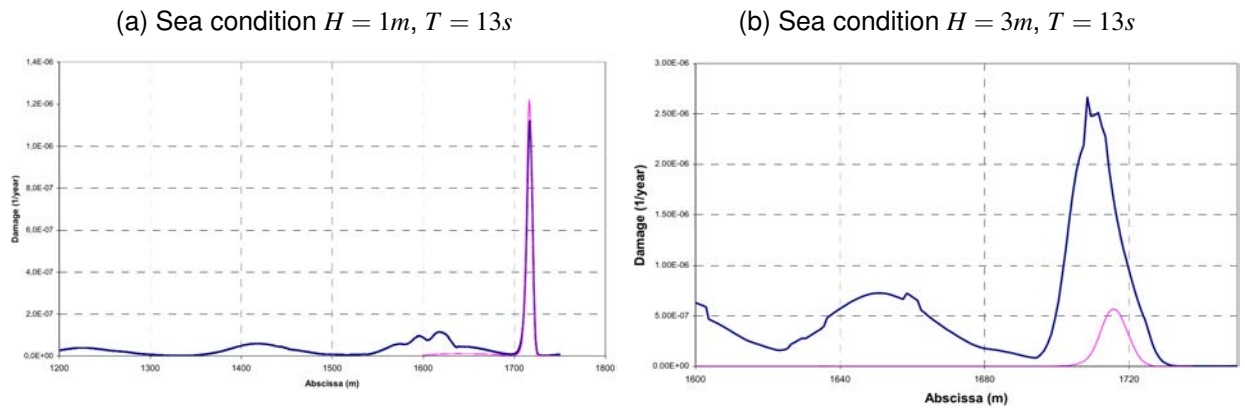
Source: Adapted from Sumer and Fredsøe (1988).

The VSIV also showed a synchronization ratio between in-plane and out-of-plane motions similar to the cycle number, N , in elastic mounted rigid cylinders subjected to oscillatory flow, which will be further detailed later in this chapter; see Figure 2.8c.

Following Grant et al. (2000) and Mark Chang and Isherwood (2003), Le Cunff et al. (2009) presented a simplified model to predict the VSIV dynamics. In contrast with the vortex tracking model (SARPKAYA; SCHOAFF, 1979a; MARK CHANG; ISHERWOOD, 2003), this particular model employed a fluid wake oscillator coupled to the structural model (FACCHINETTI; DE LANGRE; BIOLLEY, 2008).

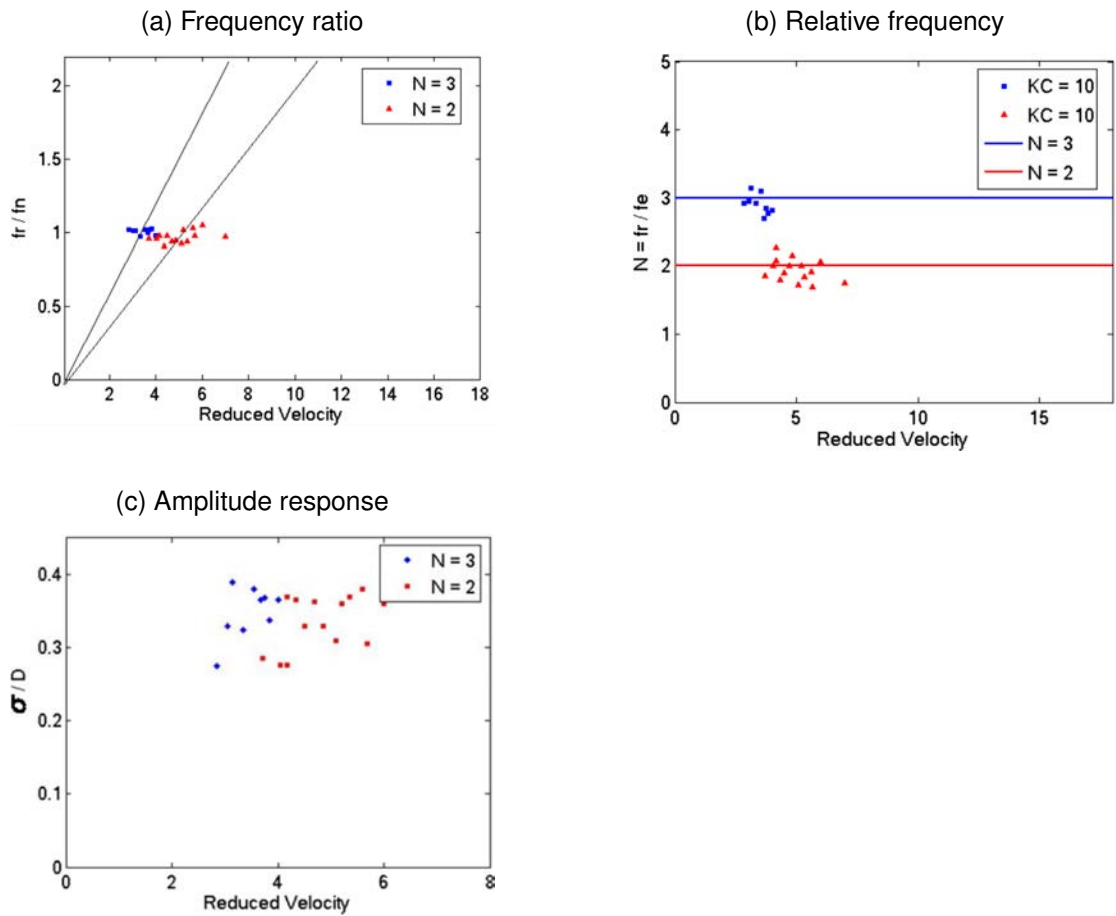
Additionally, the proposed simplified model (LE CUNFF et al., 2009) was used to assess fatigue damage of a real riser structure and it was possible to observe that the VSIV spreads the fatigue damage across the structure span, which, in the VSIV absence, would be restricted to the bottom sag and TDZ due to soil-riser interactions and in-plane movement; see Figure 2.9.

Figure 2.9: Fatigue damage due to VSIV for different sea conditions. Comparison between in-plane (magenta) and out-of-plane (blue) contributions to accumulate damage.



Source: Extracted from [Le Cunff et al. \(2009\)](#).

Figure 2.10: Petrobras Platform P18 SCR *in-situ*, $KC_{max} = 10$.



Source: Extracted from [Fernandes et al. \(2008\)](#).

Most importantly, depending on the sea condition, the VSIV accumulated damage

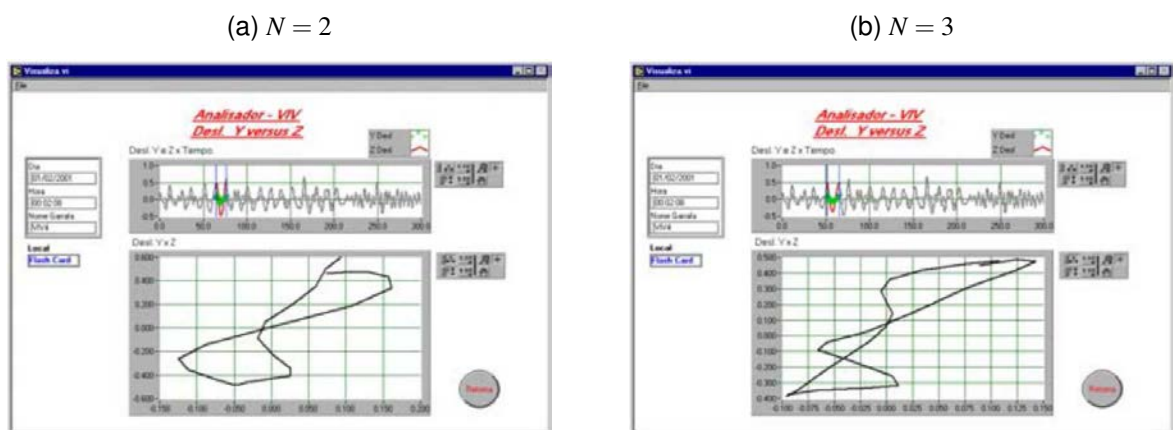
can overcome the fatigue due to in-plane movements, spreading considerably the damage throughout the riser span; see Figure 2.9b. About the fatigue due to the VSIV, [Le Cunff et al. \(2009\)](#) concludes that

[the] HILM [VSIV] generates out-of-plane motion and stresses in the pipe. The motion is not restricted to the TDZ and therefore will spread the fatigue. Another consequence is that the local drag coefficient is amplified due to the vibration. This reduces the dynamic in the TDZ and improves the life due to pipe/soil interaction, up to a point where the vibration in the lateral direction overcomes the vertical damage. ([LE CUNFF et al., 2009](#), p. 6)

Up to a point, the VSIV was thought of difficult observation *in-situ* conditions ([MARK CHANG; ISHERWOOD, 2003](#)), due to concomitant effects that would have greater impact than the VSIV isolated lateral motion. Juxtaposed with this previous assumption, [Fernandes et al. \(2008\)](#) reported the evidence of lateral motion due to VSIV measured in real risers structures installed in the Petrobras platform P18; see Figure 2.10.

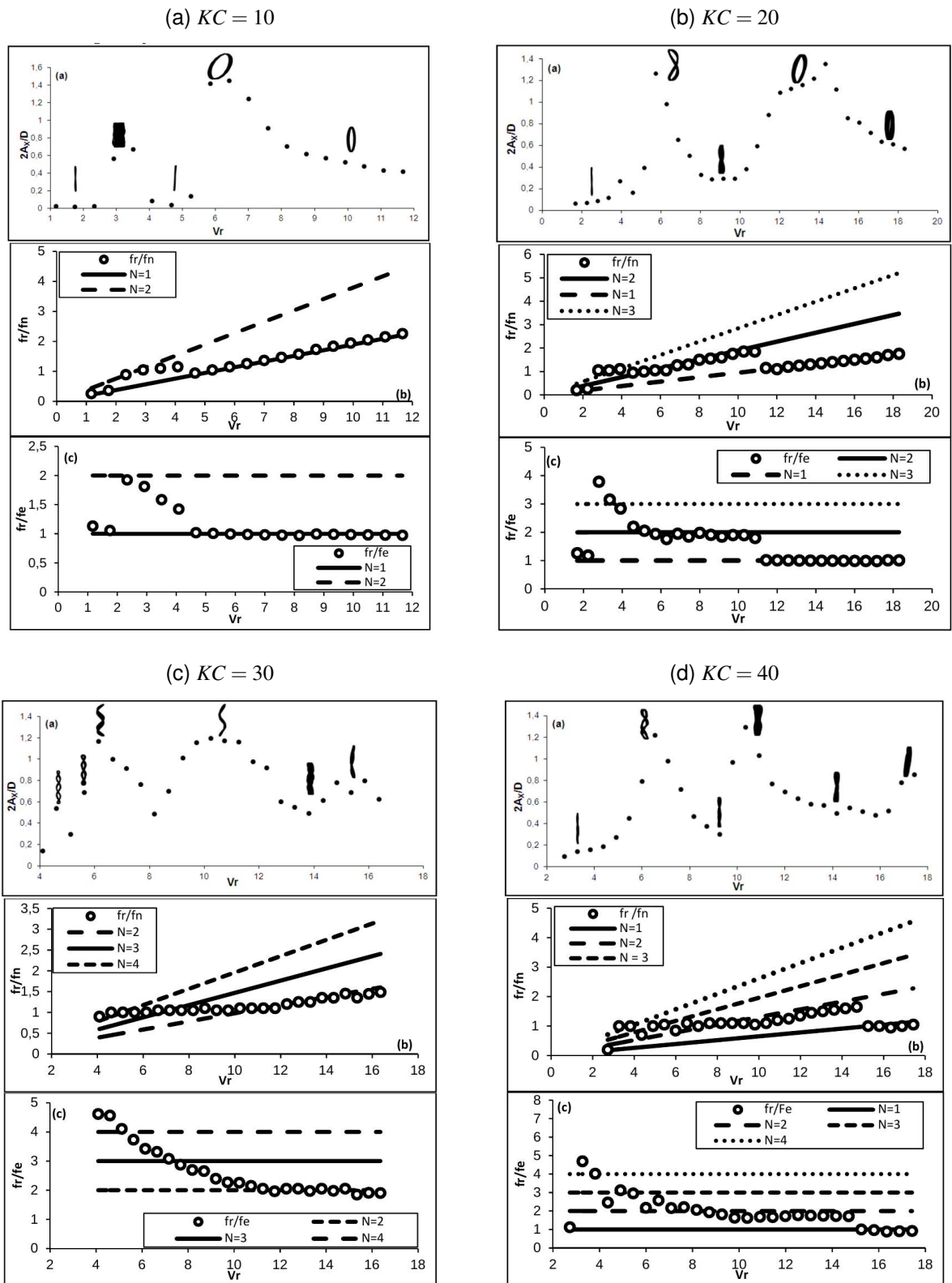
The *in-situ* observations displayed typical synchronization with two or three Lissajous rings and maximum $KC \sim 10$ spanwise; see Figure 2.11. The synchronization observed was coherent with previous experimental results ([LE CUNFF; BIOLLEY; DAMY, 2005](#)).

Figure 2.11: Petrobras Platform P18 SCR *in-situ*: in-plane vs. out-of-plane trajectories.



Source: Extracted from [Fernandes et al. \(2012\)](#).

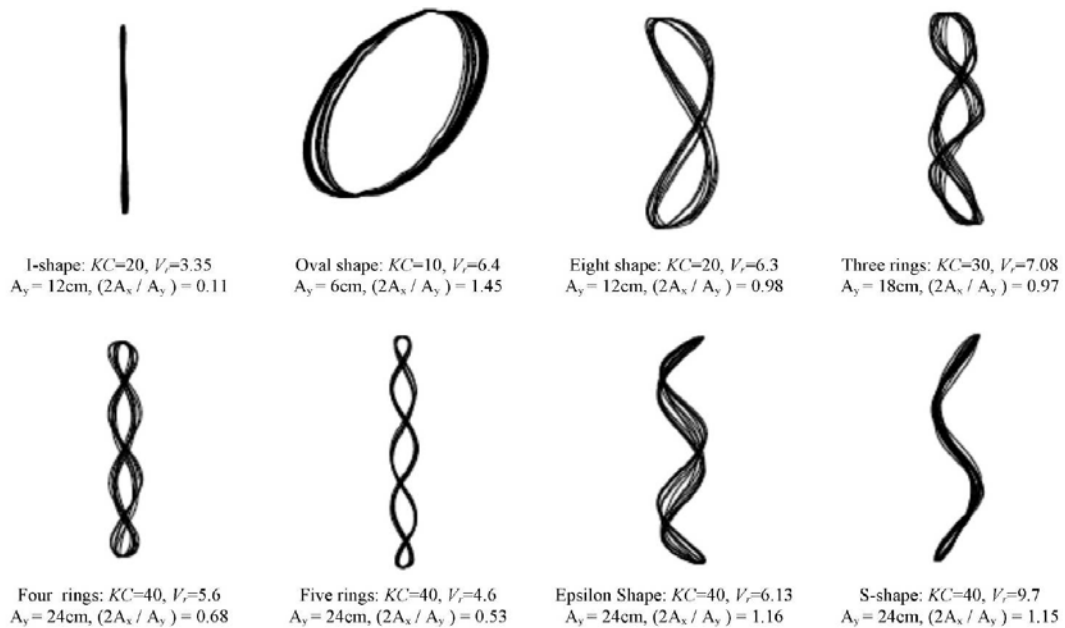
Figure 2.12: Vortex Self-Induced Vibration amplitude and frequency responses for several KC conditions. Trajectories between in-plane and out-of-plane displacements are also depict, showing the VSIV inherent synchronization.



Source: Extracted from [Fernandes et al. \(2012\)](#).

Fernandes et al. (2008) carried out experiments using two horizontal cylinders ($\mathcal{O}(L/D) \sim 10$ and $\mathcal{O}(L/D) \sim 20$), imposing a series of harmonic vertical motion and measuring the correspondent transverse response. The experiments were conducted at the Laboratory of Waves and Current of COPPE in the Federal University of Rio de Janeiro (LOC/COPPE/UFRJ). The imposed movement consisted of a sinusoidal displacement varying its amplitude and frequency, keeping fixed Keulegan-Carpenter parameters; $KC = 10$, $KC = 20$ and $KC = 30$, respectively. The experimental results also displayed good agreement to what was reported regarding an elastic mounted cylinder subjected to oscillatory flow (SUMER; FREDSSØE, 1989; KOZAKIEWICZ; SUMER; FREDSSØE, 1994).

Figure 2.13: Trajectories found in the VSIV in-plane and out-of-plane response synchronization for several experimental conditions.



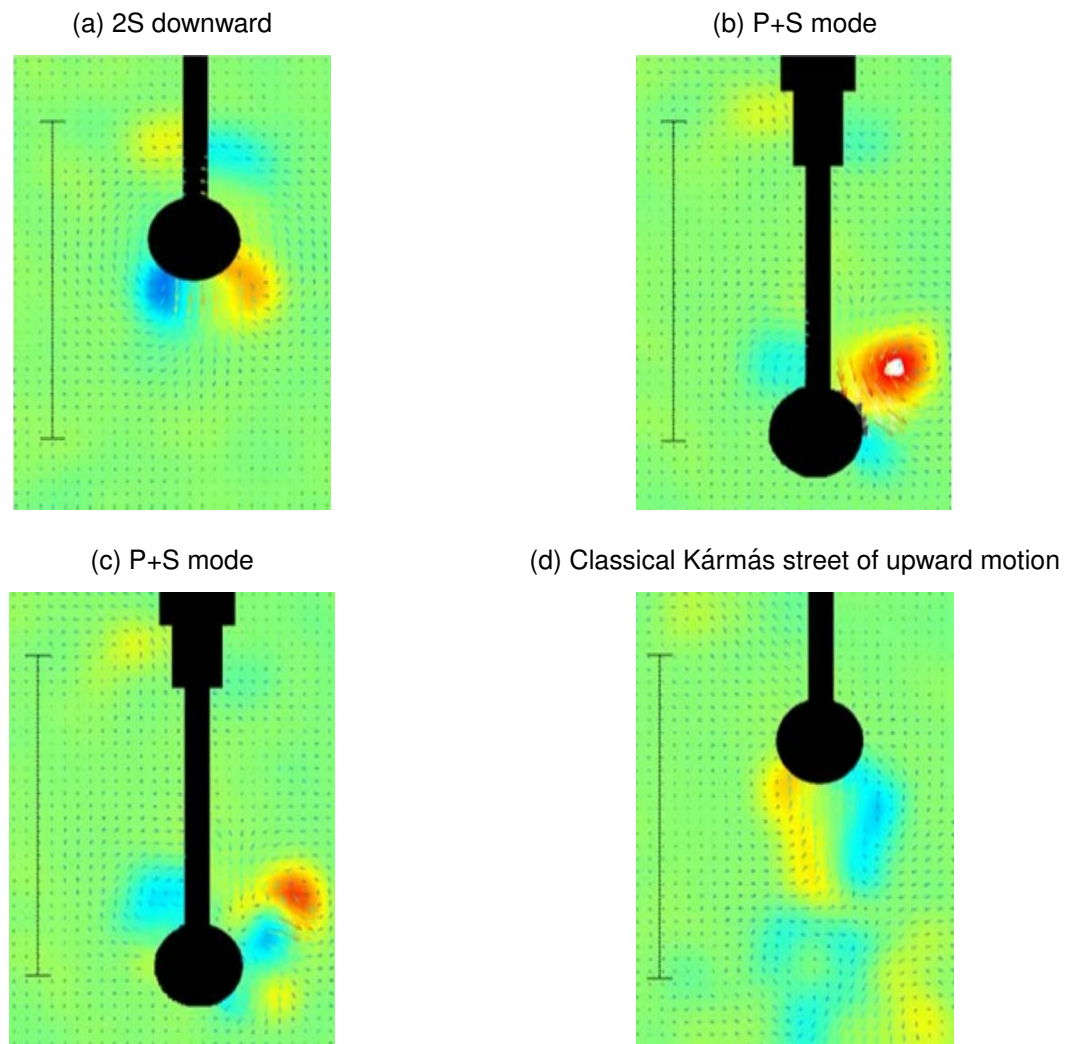
Source: Extracted from Fernandes, Mirzaei Sefat, and Cascão (2014).

Some improvements were done in the scotch-yoke apparatus presented in (FERNANDES et al., 2008), aiming at a better VSIV response characterization and kinematics understanding. Such improvements include the minimization of the motion damping due to friction on the lateral VSIV response, and the measurement of the fluid field and vortex shedding (FERNANDES et al., 2011; FERNANDES et al., 2012; FERNANDES; MIRZAEI SEFAT; CASCÃO, 2014).

The experimental tests in Fernandes et al. (2011) aimed to measure amplitude and frequency response due to VSIV for $KC = 10$ and $KC = 20$; see Figures 2.12a-2.12b.

The main motivation was to analyze how the VSIV could affect the fatigue life of a SCR structure using the experimental tests as a paradigm in order to understand typical amplitude and frequency response for several excitation values.

Figure 2.14: Vortex patterns measurements (PIV) in VSIV motion for $KC = 10$ and $V_R = 4.65$.



Source: Extracted from [Fernandes et al. \(2012\)](#).

The characteristic persistent response with large amplitude values occurred for both $KC = 10$ and $KD = 20$ and the frequency synchronization varied, reaching $N = 2$ for large imposed frequency values ([SUMER; FREDSE, 1988](#); [KOZAKIEWICZ; SUMER; FREDSE, 1994](#)); see Figures 2.12a-2.12b. Hence, the VSIV could displayed an important role in the fatigue life of SCR, in agreement with previous works ([GRANT et al., 2000](#); [MARK CHANG; ISHERWOOD, 2003](#)).

The vortex shedding pattern measured showed to be a function of the Keulegan-

Carpenter parameter (KC), occurring more complex patterns as high values of KC are observed (FERNANDES *et al.*, 2012; FERNANDES; MIRZAEI SEFAT; CASCÃO, 2014); see Figures 2.12c-2.12d and Figure 2.13. Several shedding patterns were observed by Fernandes *et al.* in different stages of the imposed movement cycle, such as: 2S, P+S, classical von Kármán street, mixing modes, amid others; (SARPKAYA, 2004; WILLIAMSON; GOVARDHAN, 2004); see Figure 2.14.

Fernandes, Mirzaei Sefat, and Cascão (2014) conclude that the maximum fatigue damage due to the VSIV occurs when high modes are excited, which is the case of real scale SCR in typical Brazilian sea conditions. Consequently, high frequencies combined with large curvature values due to the VSIV at the SCR bottom span seems to decrease the overall structural integrity.

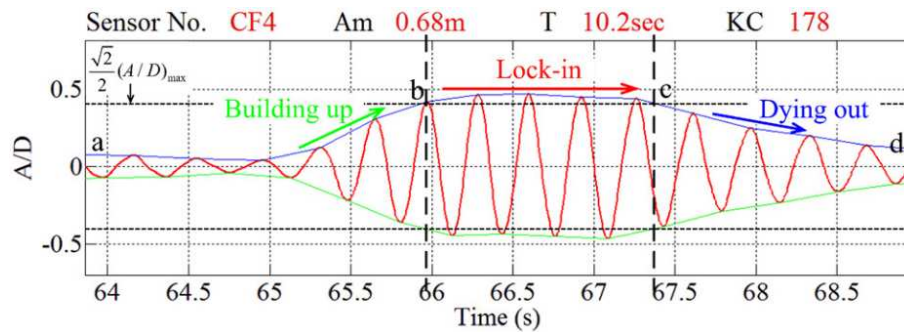
From 2012 onward, new experimental data were reported using small-scale flexible riser models in two different geometrical configuration: highly taut horizontal cylinder (FU *et al.*, 2013a); and two distinguished catenary-like models (RATEIRO *et al.*, 2013; WANG *et al.*, 2014).

Fu *et al.* (2013a,b) carried out tests with a taut cylinder at the Shanghai Jiao Tong University, using a highly tensioned horizontal cylinder of aspect ratio $\mathcal{O}(L/D) \sim 160$. The model was mounted under a towing car which was able to impose movement in the horizontal plane. Within this configuration, the VSIV response was observed in the vertical plane. The phenomenon was measured using a set of strain gauges placed over the cylinder surface, creating a lattice distribution of gauges on the vertical and horizontal model section extremities.

The in-plane displacement evaluation (also velocity and acceleration) was executed under the linear rheology and small deformation assumptions. Carrying out Galerkin's decomposition using a set of trigonometric modes, the displacement series can be reconstructed for any cylinder section as a linear sum of modal amplitudes.

In order to obtain the modal amplitude series, the assumption of small deformation is used to express the cable model curvature as proportional to the modal shape functions second derivative. Thus, the obtained deflection deformation could indirectly measure the cylinder displacement series in a given direction knowing that the strain is proportional to the curvature and the cylinder radius. Besides, wavelet techniques were employed to enrich the analysis with measurements of the shedding frequency instantaneous values, assuming $St = 0.2$.

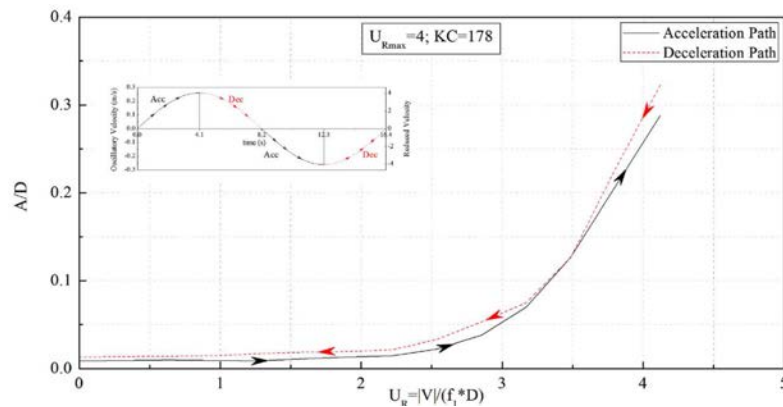
Figure 2.15: Typical VSIV response in high KC regime with its proposed division into: building-up region; lock-in region; and dying out region. The asymmetry between building-up and dying out regions characterizes a hysteresis loop.



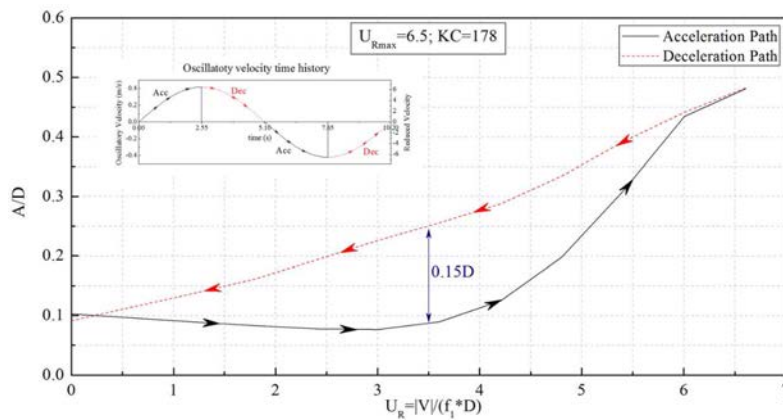
Source: Extracted from Fu et al. (2013a).

Figure 2.16: Hysteresis showed in the VSIV amplitude response during an imposed movement cycle.

(a) $KC = 178, V_{R,max} = 4$



(b) $KC = 178, V_{R,max} = 6.5$



Source: Extracted from Fu et al. (2013a).

Note: Dependence of the hysteresis loop on the reduced velocity.

Using the normal displacement series, Fu et al. (2013a) showed that the typical VSIV beating response depends on the Keulegan-Carpenter number. Although that parameter must be locally evaluated, $KC(s)$, the maximum value was chosen as representative of the whole system behavior, which admitted values between 31 and 178. This experimental set-up shows similar features to the classic rigid cylinder subjected by oscillatory flow (SUMER; FREDSE, 1988; KOZAKIEWICZ; SUMER; FREDSE, 1994), as it bears partial similarity due to the cylinder geometrical configuration.

Considering high KC value regime, Fu et al. (2013a) could identify a typical beating out-of-plane response that could be segmented into three distinguished regions: building-up, when the response amplitude increases from quasi-null values as the cylinder re-enters in its own vertical semi-cycle accelerating; lock-in, when the response reaches a quasi-steady state regime as in a typical VIV case; and dying-out, when the amplitude decreases as the cylinder decelerates until reaching again quasi-null values; see Figure 2.15.

Figure 2.17 shows typical VSIV responses on two distinct KC regimes. The high $KC = 178$ test displays clearer spectra in which the frequency is more concentrated in instants when the shedding frequency assumes maximum value. There is also mode transition when the input frequency is sufficiently high, but the second mode amplitude is never higher enough to exhibit dominance.

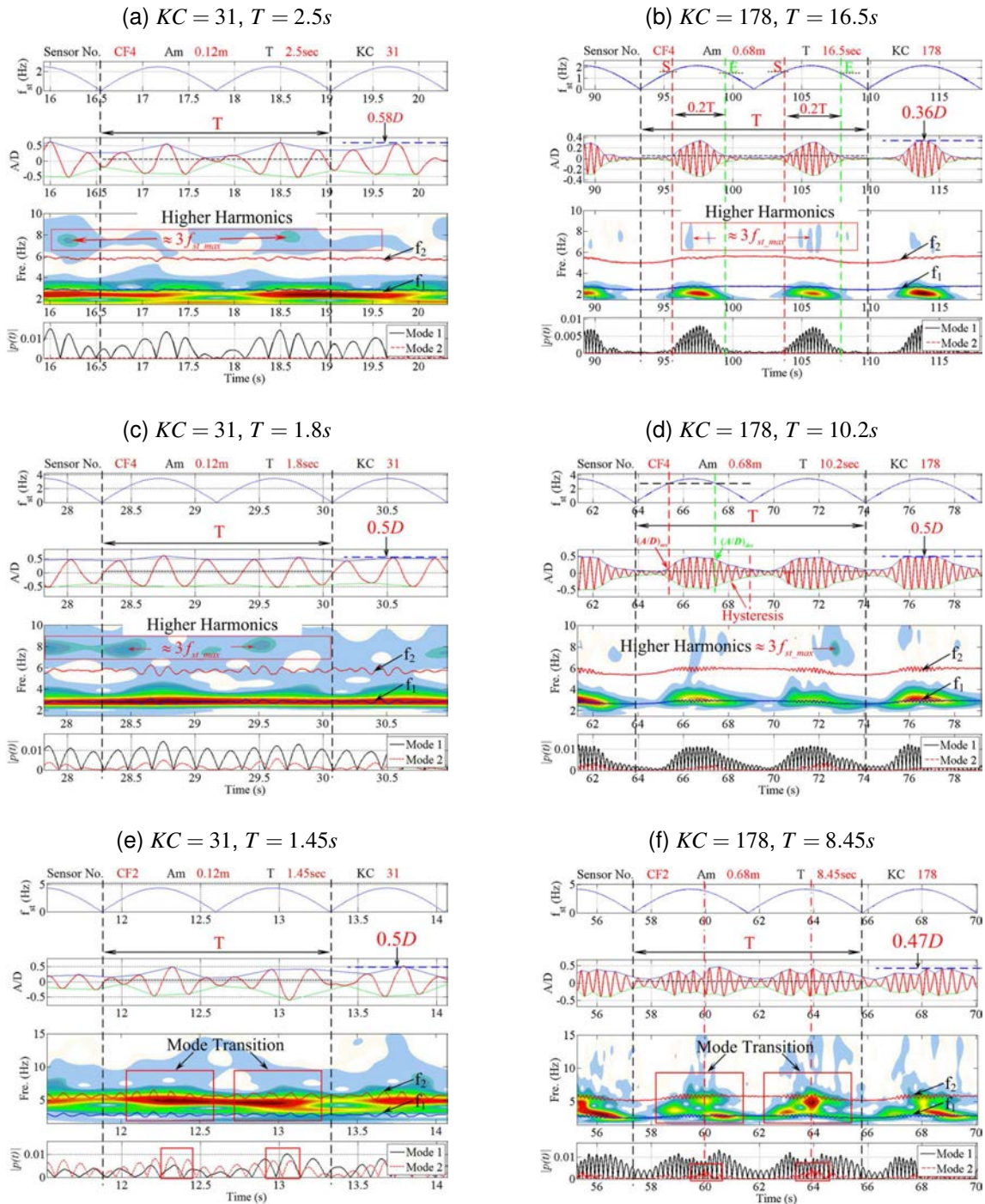
On the other hand, the spectrogram exhibits higher harmonics when $KC = 31$, specially in the high input frequency scenario due to the mode transition, in which the second mode turns dominant.

Using OpenFOAM¹¹, Fu, Wan, and Hu (2017) proposed a numerical representation for the aforementioned taut cylinder. The CFD model was based in the direct solution of the Navier-Stokes equation, averaging turbulence terms.

The numerical and experimental results showed good agreement, being able to capture nonlinear features observed in the experimental analysis, such as the presence of a hysteresis loop on the lateral amplitude with respect to the in-plane motion; see Figure 2.16. The hysteresis displays a direct dependency on the KC regime and V_R considered, exhibiting itself more prominently as the V_R increased.

¹¹Open source C++ toolbox for the development of customized numerical solvers, and pre-/post-processing utilities for the solution of continuum mechanics problems, most prominently including Computational Fluid Dynamics (adapted from Wikipedia – OpenFOAM. Last Accessed: 02/15/2022).

Figure 2.17: VSIV experimental response in two different KC . The first column corresponds to $KC = 31$ and the second, $KC = 178$; top-to-down indicate a decrease on the period (or increase on frequency) of imposed movement. For each chart: (i) shedding frequency; (ii) lateral relative amplitude response; (iii) lateral response spectrogram; and (iv) modal amplitudes measured and used in order to reconstruct the displacement signal.



Source: Extracted from Fu et al. (2013a).

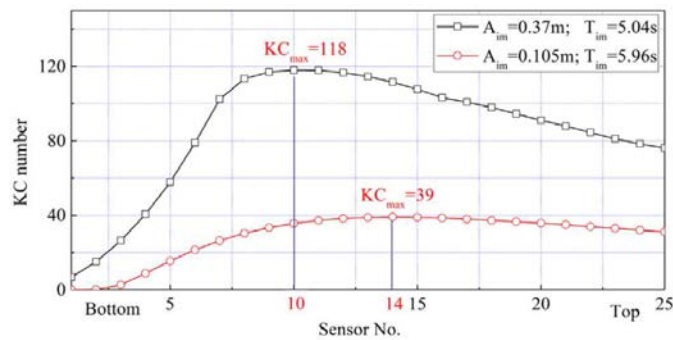
In addition, vortex shedding development and patterns illustrated the complexity of

the field flow, specially when the cylinder re-enters its own non dissipated vortex street in high KC regime, which produces the typical beating response already discussed.

Focusing now on the catenary-like configuration subjected to imposed motion at the hang-off point, [Rateiro et al. \(2013\)](#) and [Wang et al. \(2014\)](#) disclosed two different sets of experimental observations on the nonlinear nature of the VSIV response.

[Wang et al. \(2014\)](#) carried out experiments with a catenary-like cylinder at Shanghai Jiao Tong University which keeps Cauchy similitude with a deep-water DNV riser. The instrumentation was conceived similarly to what were used in [Fu et al. \(2013a\)](#), embedding local strain sensors at selected points as to directly measure deformation. Wavelet analysis is also employed to check the time-frequency behavior of the VSIV.

Figure 2.18: Distribution of $KC(s)$ throughout the model span for two different tested conditions.



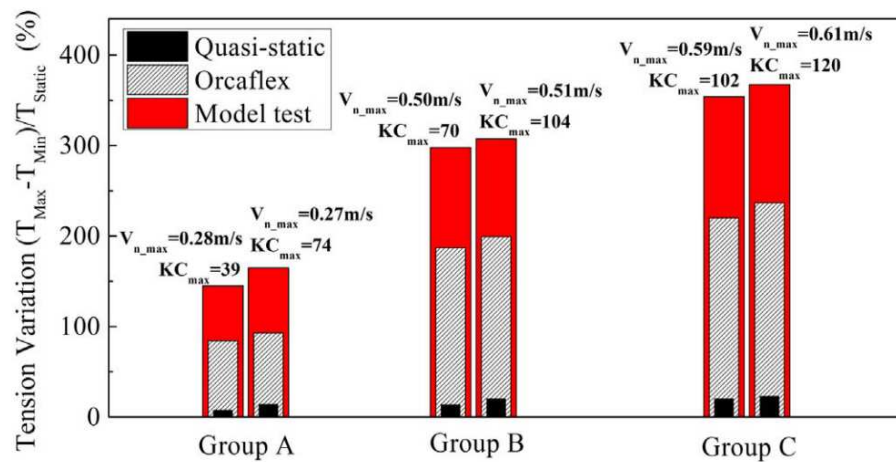
Source: Extracted from [Wang et al. \(2015\)](#).

The main purpose was to evaluate the fatigue damage due to the VSIV response, considering normal deformation around the static configuration. In light of a linear material assumption to represent the cylinder rheology, tension is directly obtained using the deformation and the material elastic modulus¹², E , so as to assess the cycling tension to fatigue evaluation through Miner's law and S-N curve methods.

The VSIV modulated response once again was observed in all tested cases with imposed amplitude ranging from $A_{i,min}^* \sim 4.4$ to $KC_{i,max}^* \sim 15.5$. The Keulegan-Carpenter number is a local value, varying through the cylinder span ($KC(s)$); the maximum KC value found within the cylinder span was chosen as a characteristic KC value, spanning from $KC_{max} = 40$ to $KC_{max} = 130$; see Figure 2.18. Typical Strouhal value ($St = 0.2$) was used to compute the time dependent shedding frequency, $f_s(t)$, which is assumed to be near the normal displacement motion frequency.

¹²Equivalently, using the Hooke's law: $\sigma = 2\mu\varepsilon + \lambda tr(\varepsilon)$, in which μ and λ are Lamé's constants.

Figure 2.19: Traction variation evaluated in the VSIV presence (model test) and in the VSIV absence (quasi-static and Orcaflex[®]).



Source: Extracted from Wang et al. (2017).

Interestingly, Wang et al. (2014) unveiled a hysteresis behavior on the in-plane movement due to variation on the geometric rigidity. Considering the cylinder motion represented in the local intrinsic basis, it was argued that the normal displacement could be segmented into lift-up and push-down (with respect to gravity) phases and the pushing-down stage would affect more the traction variation at the cylinder due to the positive apparent weight; see Figure 2.19. Ergo, the hysteresis was more pronounced at larger values of imposed amplitude tests.

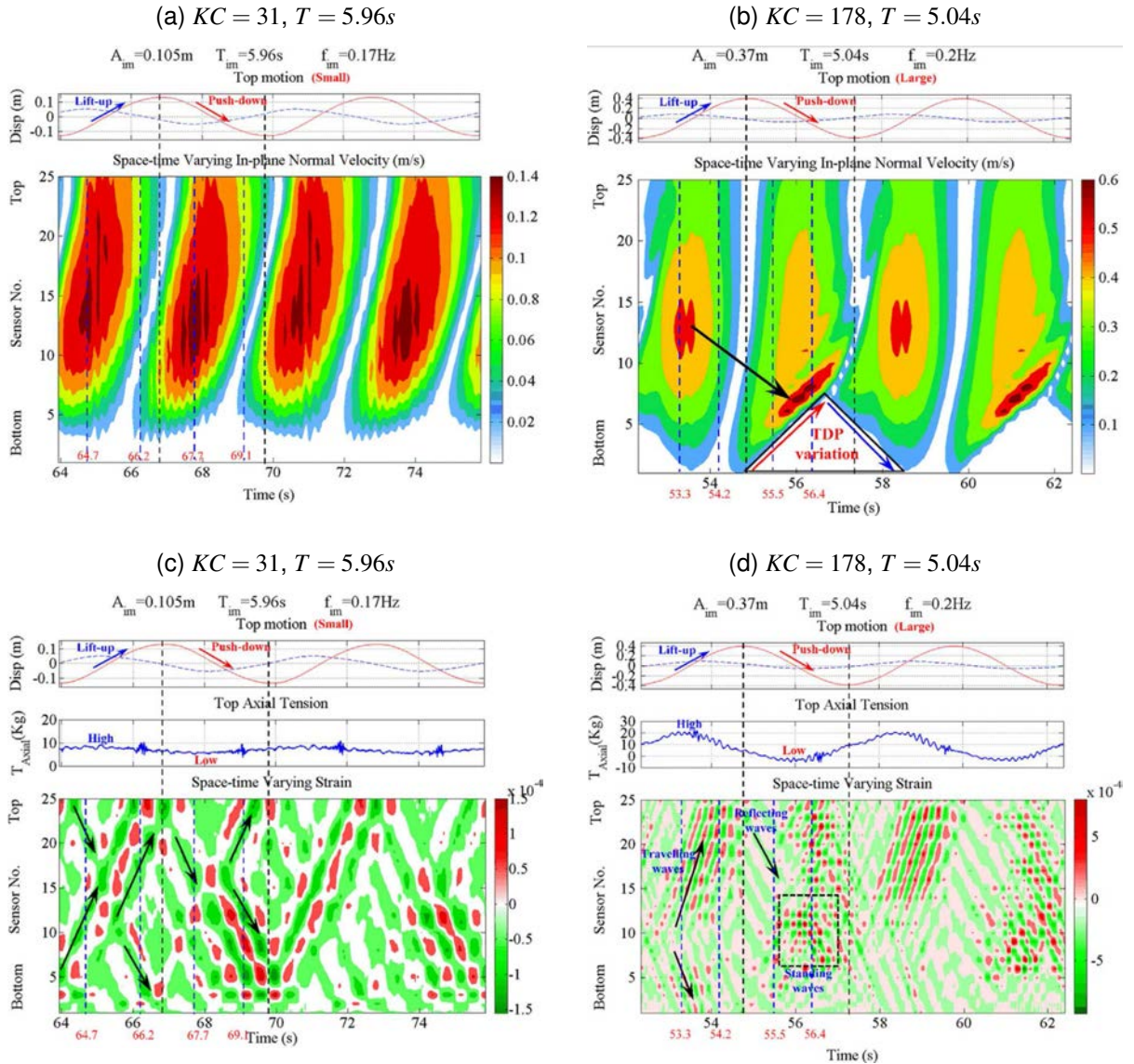
At high A_i^* tests, the variation on the cylinder traction at pushing-down phase showed to cause TDP motion, which duly exhibited a major part in the shift of shedding frequency maximum values through the cylinder span. During the lift-up phase, the shedding frequency peak occurred at the model mid-span, displaying larger normal amplitudes around half diameter.

On the other hand, throughout the pushing-down phase, the peak occurrence on the shedding frequency is right above the TDP, in the cylinder bottom sag bend, a sensitive region due to larger curvature values. Finally, Wang et al. (2014) concluded that the fatigue damage was more sensitive to changes to the imposed amplitudes than frequencies.

Sequentially, Wang et al. (2015) further analyzed the same experimental data, now focusing on the general behavior of the cylinder. Once more, it was employed the technique of indirectly measuring the model normal displacement series using the observed strain and modal reconstruction (FU et al., 2013a). Nevertheless, the mode

functions were evaluated by means of a numerical FE model.

Figure 2.20: Experimental responses in two different conditions. The first row corresponds to the in-plane motion and the second refers to the out-of-plane response.



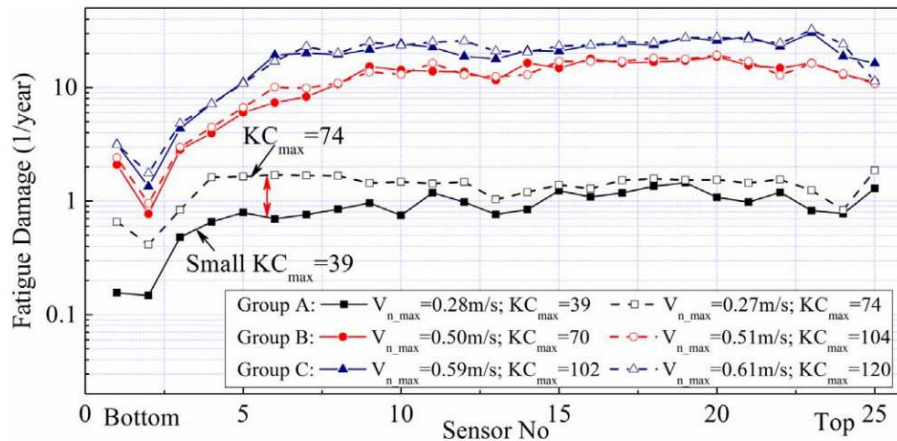
Source: Extracted from Wang et al. (2015).

Besides, Wang et al. (2015) argued on truncating the model in a reduced segment in favor of numerical analysis, stating that the area of interest was comprised of the TDZ and the bottom sag-bend region, and also simplifying the TDP boundary condition as pinned. This procedure was validated using Orcaflex and it was also provided wavelet analysis to compute the in-plane response frequency with respect to time.

When compared to low KC regime, greater KC values carried within higher modal components due to the pushing-down phase causing a more expressively traction de-

crease, which causes the variation on the structure natural frequencies to lesser values. The lift-up and push-down phases brought out the placement variation of the TDP anew, particularly in high KC regimes, having a greater impact over the estimated instantaneous reduced velocity throughout the cylinder span; see Figures 2.20a-2.20b.

Figure 2.21: Fatigue damage estimated in several conditions.



Source: Extracted from Wang et al. (2017).

Thus, it was possible to detect a multitude of phenomena occurring in the space-time varying strain measurements, such as: traveling in the lift-up phase, accompanied with reflecting waves when the pushing-down begun; additionally, standing waves could be seen when the pushing-down phase was crossing the inflection point, *i.e.* change of acceleration signal; see Figures 2.20c-2.20c. The discussion on tension variation went further, stating that:

The tension variation is sensitive to both the heave amplitude and the period. This is because the static tension is dependent on the configuration of an SCR. Meanwhile, the inertial force and hydrodynamic loads would also contribute a lot to the tension variation. Tension variation should be definitely taken into account in the future vessel motion-induced VIV prediction. (WANG et al., 2015, p. 398)

More significantly, Wang et al. (2017) carried a dominant parameters investigation through as to unravel more of the VSIV idiosyncratic features that affect the riser general dynamics, which, in the end, is intimately related to the structural fatigue life; see Figure 2.21. Unquestionably, one of the greatest difficulties found hitherto in the catenary-like model analyses is to determine a representative KC value to characterize the VSIV phenomenon, due to each cylinder section be subjected to different velocity values.

Formerly, the maximum KC measured within the cylinder span was being considered as a proper choice (WANG et al., 2014, 2015), suggesting that all the structure would be subjected to an equivalent load depending on KC_{max} , independently whether $KC(s)$ could admit values of the same order at different sections.

That previous avowal showed to be true if the maximum Keulegan-Carpenter parameter is sufficiently high, $KC_{max} > 39$ (WANG et al., 2017). Hence, the general VSIV out-of-plane response exhibited a strong dependence on the cylinder model maximum reduced velocity value, $V_{R,max}$, which is proportional to KC_{max} . Whereas, the low KC regime¹³ presented a dual dependency on KC_{max} and the local distribution of $KC(s)$ along the catenary-like span.

Moreover, considering some key results presented in Wang et al. (2014), Wang et al. (2017) assessed the VSIV out-of-plane fatigue damage taking into consideration the lateral motion behavior. Most importantly, the VSIV in-plane response is more sensitive to imposed amplitudes than frequencies, which leads to high KC_{max} regime. The VSIV synchronization exhibits lateral movement dominant frequency, $f_{b,dom}$, proportional to the in-plane dominant frequency, $f_{n,dom}$,

$$N = \frac{f_{b,dom}}{f_{n,dom}},$$

assuming larger values as the KC_{max} increases (SUMER; FREDSSØE, 1988; FERNANDES et al., 2011). As higher out-of-plane modes are excited, the local curvature variation at the TDZ causes significantly accumulated damage.

In reality, typical sea conditions induces low KC values and it is not straightforward to have a clear overview on how the VSIV promoted fatigue damage in a SCR. Mainly, this occurs due to the dual dependency of both KC_{max} and local distribution along the SCR length, $KC(s)$.

Consequently, Wang et al. (2017) also suggests that further investigation should be carried out in low KC regime for SCR and other compliant risers typical geometric configurations used *in-situ*, such as: lazy-wave risers, free-hanging risers, amid others.

In conclusion to this discussion on Wang et al. (2017), it is noteworthy that the VSIV dominant parameters discussion will be an essential and necessary subject matter to the present thesis, which shall return to this point in order to carry out the VSIV response analysis from a modal decomposition perspective, proposing modal dominant

¹³In which the VSIV amplitude response varies less in time, not displaying typical beating behavior.

parameters to study the VSIV behavior in catenary-like structures.

Last but not least, Wang et al. (2019) presented a generalized in-plane global motion reconstruction method for SCR or other slender marine structures that assumes large displacements, but small deformation. Their proposed methodology was validated both numerically and experimentally, displaying significantly accuracy (less than 1%).

Comparing measured and numerical results, there was a substantial amplification on drag coefficient in the VSIV occurrence, which could suggest that typical hydrodynamic parameters used in current offshore risers project designs need to be evaluated *in-situ* sea conditions, aiming to develop better dynamic prediction tools.

There are some important differences between the experimental set-ups carried out in Wang et al. (2014) and Rateiro et al. (2013) that should be addressed. Firstly, the small-scaled models were conceptualized using different similarity scales. For instance, Rateiro et al. (2012) presented a methodology considering Froude similitude, as also carried out in Le Cunff, Biolley, and Damy (2005), which differs from the Cauchy similarity used in Wang et al. (2014).

Besides, the conceptual design and material selection for both models are significantly distinct, inasmuch as Rateiro et al. (2012) proposed a silicon hose filled with stainless steel micro spheres and Wang et al. (2014) used a steel hose with plastic coating and inner copper core.

The material selected alters strongly which sort of sensing system ought to be used. As a steel hose presents rheology close to a linear material, the strain gauge measurements are adequate, since the Hooke's law relates both deformation and stress measurements.

Nonetheless, a silicon hose has a more complex viscoelastic rheology, in which deformation and stress cycles depends on the movement amplitude and frequency, displaying hysteresis features as well. Consequently, optical tracking cameras are more suitable due to direct displacement measurement with high accuracy and precision (SALLES; PESCE, 2019).

In addition, Wang et al. (2014) tests in air evidenced no lateral movement, contrarily to what was duly observed in the other catenary-like cylinder model (LIFE&MO, 2011c,e). This may be attributed to internal resonances within the cable model (SRINIL; REGA; CHUCHEEPSAKUL, 2006; SRINIL; REGA, 2006, 2008) due to the significant

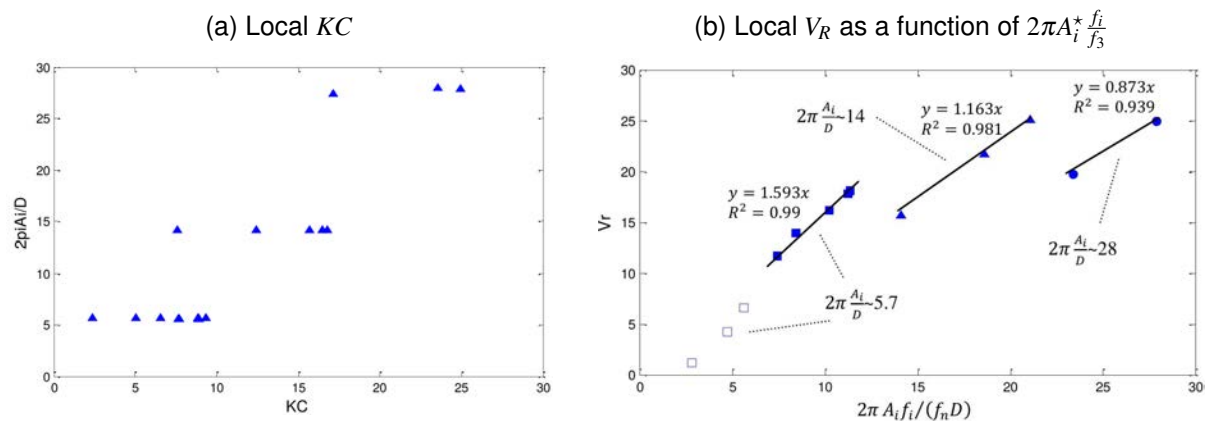
difference between both models flexural stiffness, which differs in $\mathcal{O}[EI_{Wang}/EI_{Rateiro}] \sim 100$ due to the material selected in each model.

Moving on to [Rateiro et al. \(2013\)](#), the catenary-like model was conceptualized as to maintain Froude similarity with a real riser used by Petrobras ([LIFE&MO, 2011a,b](#); [RATEIRO et al., 2012](#)). The experimental tests pertained in a much more comprehensible investigations on SCR nonlinear dynamics due to several phenomena, such as: structural, hydrodynamic and contact with marine soil ([LIFE&MO, 2011a,b,c,d,e, 2012a,b,c,d](#)).

These experimental tests ensued from a project known as “Nonlinear Dynamics of Risers” sponsored by Petrobras, which had a broad scope of theoretical, numeric and experimental approaches on the dynamic of risers subjected to nonlinear exciting loads due to current, imposed motion at the upper extremity and concomitant effect of both.

The cylinder in catenary-like configuration subjected to imposed motion at the upper end is a snippet derived from a colossal experimental database. The tests were carried out with small-scale cylinder models in vertical and catenary-like conditions, in different media (air and water) and at several facilities ([LIFE&MO, NDF, TPN, IPT](#)).

Figure 2.22: Local analysis of the target 29, including: local KC distribution with respect to the imposed displacement at the top; and local V_R as a function of an equivalent global reduced velocity.

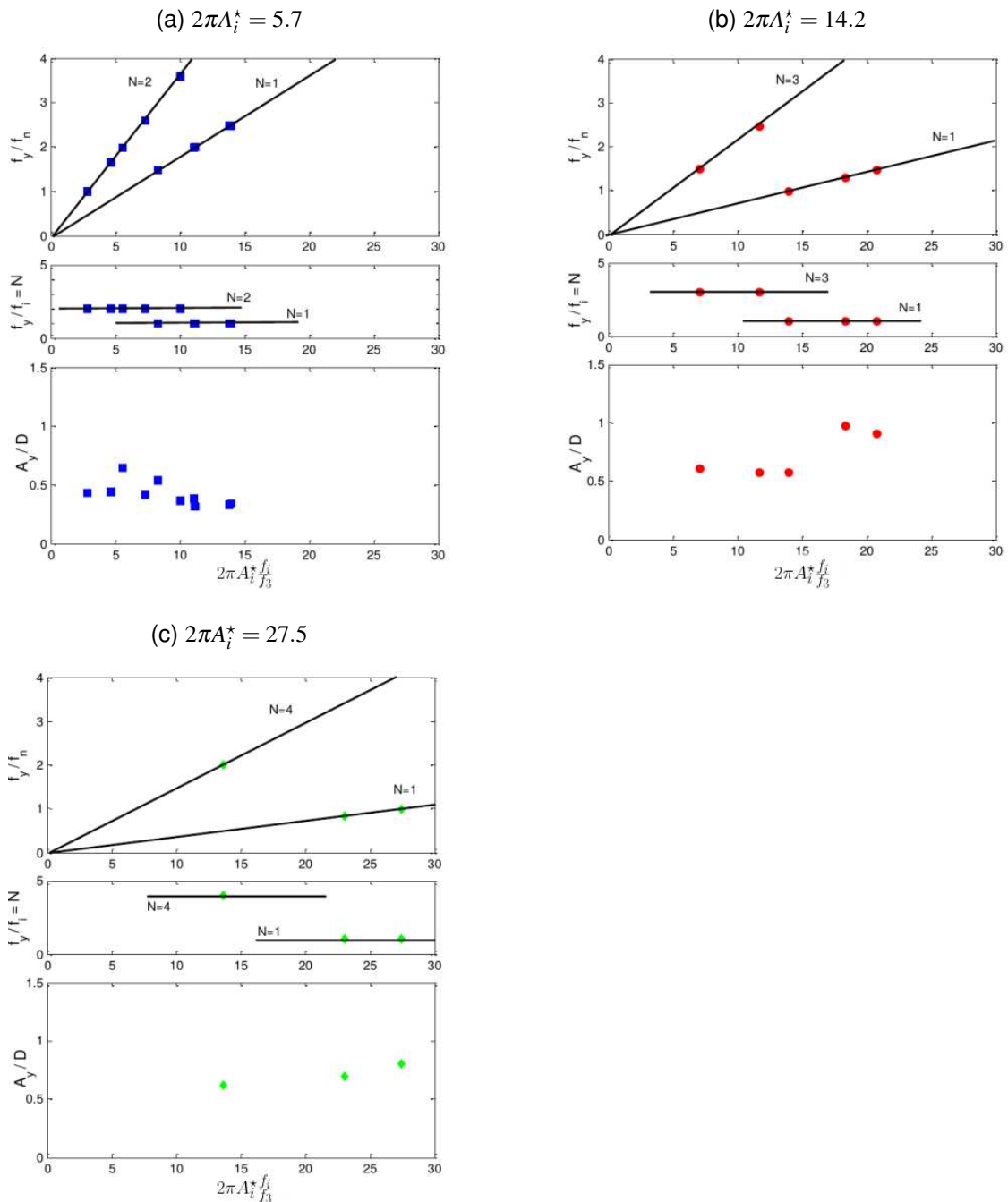


Source: Extracted from [Rateiro et al. \(2013\)](#).

Apropos of the small-scale model used in the VSIV tests, the aspect ratio was $\mathcal{O}(L/D) \sim 180$ built of a silicone hose filled with stainless steel micro spheres, maintaining similarity with a real deep water riser. The experimental set-up was rather elegant with the small-scale model launched from a fixed structure and spanning a planar

catenary-like configuration. The imposed movement occurred within the vertical plane, originating an in-plane oscillation that shed vortex responsible to induce out-of-plane dynamics.

Figure 2.23: Frequency ratio, relative frequency and amplitude responses with respect to $2\pi A_i^* \frac{f_i}{f_3}$ for different input amplitude conditions at the top.



Source: Adapted from [Rateiro et al. \(2013\)](#).

The cylinder movement was measured using a system of synchronized optical tar-

get tracking cameras, capturing the spacial displacement of each monitored section directly. This sort of assessing experimental data presents minimal interference and high accuracy ($A_{min}^* \sim 0.05$) (SALLES; PESCE, 2019), which is required in order to monitor displacement on cables or other high aspect ration structure.

The preliminary analysis of the catenary-like cylinder subjected to VSIV (RATEIRO et al., 2013) was executed in the configuration space, *i.e.* selecting specific targets, *e.g.* the 29th, as to observe local KC and reduced velocity; see Figure 2.22. Although preliminary, this analysis showed some agreement with previous results, such as the elastic mounted rigid cylinder in oscillatory flow response (SUMER; FREDSSØE, 1988; KOZAKIEWICZ; SUMER; FREDSSØE, 1994).

The synchronization observed by Rateiro et al. (2013) displayed integer values, N , between in-plane and out-of-plane responses, also depending on the local KC . Furthermore, the Keulegan-Carpenter parameter depends on how the in-plane structural response behaves, admitting different values through the cylinder span, $KC(s)$.

Ergo, the catenary-like response in space of configuration did not turn to be a straightforward task, given that the only controlled input is the imposed movement at the hang-off point and the in-plane response is duly caused by it and depends heavily in the own structural dynamics.

Rateiro et al. (2013) found that the out-of-plane experimental response, albeit complex and highly nonlinear, showed to be well gathered with respect to a global reduced value parameter,

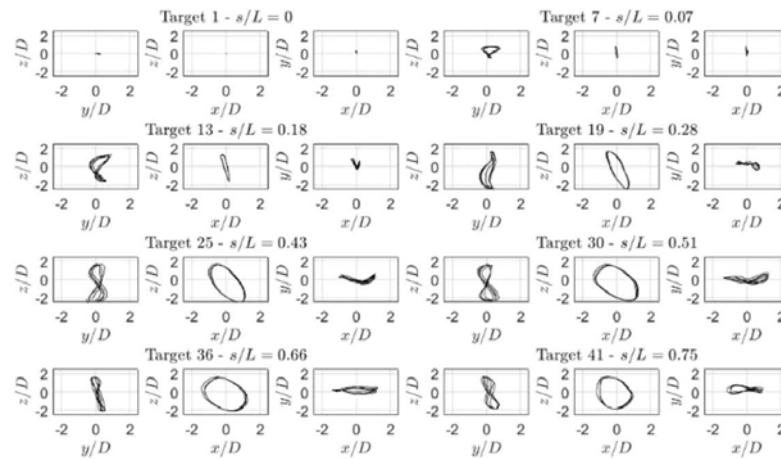
$$2\pi \frac{A_i f_i}{D f_3},$$

in which A_i and f_i correspond to the imposed movement amplitude and frequency, respectively, and f_3 is the structural third natural frequency (coinciding with the second out-of-plane mode); see Figure 2.23. Similarly, this parameter resembles the reduced velocity used in Sumer and Fredsøe (1988) and Kozakiewicz, Sumer, and Fredsøe (1994), inasmuch as the rigid cylinder local and global reduced velocity are equivalent to each other.

Although the equivalent global reduced velocity could unveil some features of the structural dynamics, the attempt of using a local reduced velocity parameter did not succeed due to the concomitant presence of different values of $KC(s)$ across the model span wise; see Figure 2.23.

In contrast with [Rateiro et al. \(2013\)](#) preliminary analyses on the VSIV response, [Pesce et al. \(2017\)](#) carried out a complementary and deeper analysis of the cylinder dynamics, including scalograms so as to display the synchronization between in-plane and out-of-plane movements through time, and also orbits of selected points to identify Lissajous loops as previously evinced in VSIV results ([GRANT; LITTON; MAMIDIPUDI, 1999](#); [LE CUNFF; BIOLLEY; DAMY, 2005](#); [FERNANDES et al., 2008](#); [FERNANDES et al., 2011](#); [FERNANDES et al., 2012](#); [FERNANDES; MIRZAEI SEFAT; CASCÃO, 2014](#)); see Figures 2.24-2.25.

Figure 2.24: Cartesian displacement trajectories for input test $2\pi A_i^* = 10$ and $f_i = 0.72Hz$; $f_i/f_3 = 1$.



Source: Extracted from [Pesce et al. \(2017\)](#).

Analyses presented in [Pesce et al. \(2017\)](#) were realized considering the cylinder movement around its static configuration¹⁴ in the global Cartesian reference frame. Coincidentally, the out-of-plane direction is placed in the y -axis, which is aligned with the binormal direction, \vec{b} ; see Figures 2.25c-2.25d.

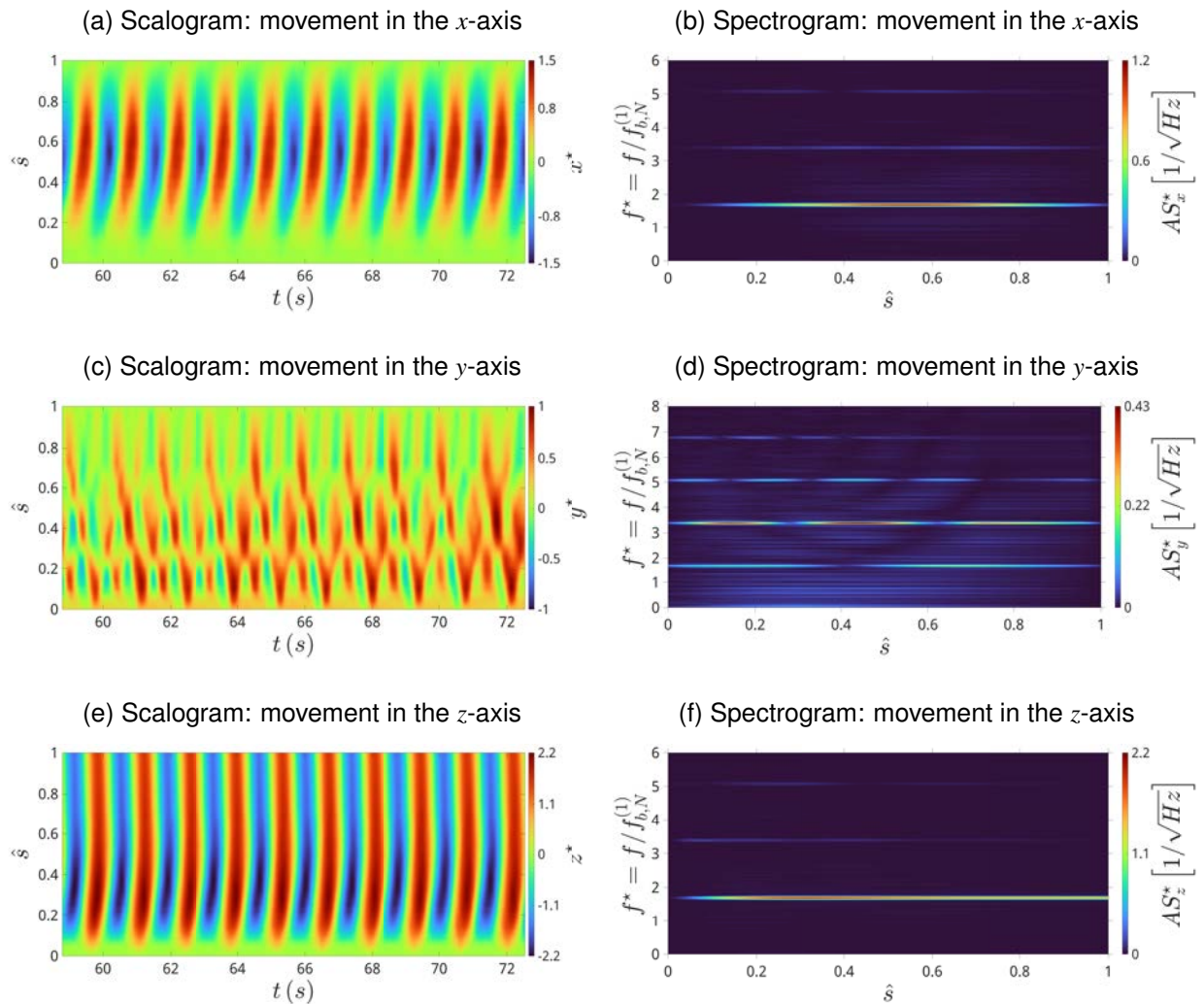
The local reference frame is composed of the tangent, $\vec{t}(s)$ ¹⁵, normal, $\vec{n}(s)$, and binormal, $\vec{b}(s)$, unit vectors, defining a positive orthonormal basis¹⁶ that spans the Euclidean space, \mathbb{R}^3 . Even so the set of intrinsic coordinates is a more suitable choice to analyze the cylinder dynamics ([WANG et al., 2019](#)), [Pesce et al. \(2017\)](#) were able to unveil lots of behaviors present in the VSIV dynamics.

¹⁴Under the assumption of small displacements.

¹⁵The coordinate s is used as the arc-length parametrization of a given differential curve in space, $\{\vec{\gamma}(s) : \mathbb{R} \rightarrow \mathbb{R}^3\}$.

¹⁶Also known as the TNB reference frame.

Figure 2.25: Analyses of the Cartesian displacements for input test $2\pi A_i^* = 10$ and $f_i = 0.72Hz$; $f_i/f_3 = 1$.

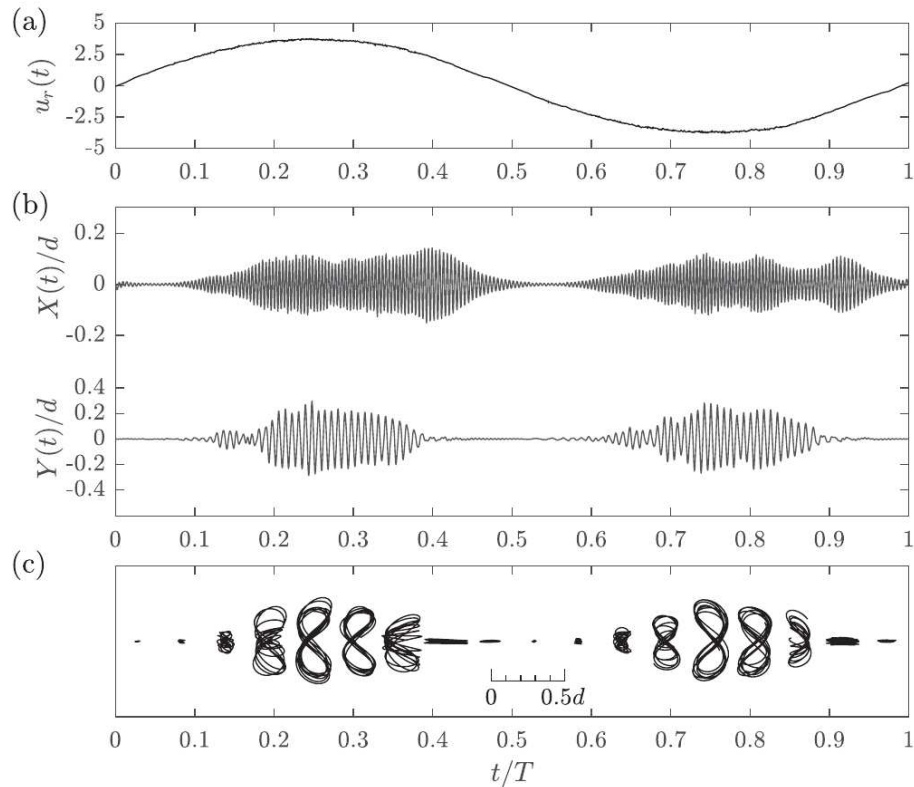


Source: Developed by the author after [Pesce et al. \(2017\)](#).

Thus, spectral analyses of in-plane motions showed to be quasi-monochromatic, except when the imposed frequency matches higher in-plane modes; see Figures 2.25b and 2.25f. In turn, the VSIV out-of-plane response exhibited multi-frequency or even scattered frequency spectrograms, and several other phenomena, such as: multi-modal behavior, parametric and internal resonance, Mathieu-like instability and traveling waves; just to mention a few.

The present work is, as a matter of fact, a set of further experimental analyses of the aforementioned results ([PESCE et al., 2017](#)), in which Galerkin's decomposition is carried out in order to obtain a reduced order system, unveiling some characteristic featured of the VSIV in catenary-like riser models.

Figure 2.26: VSIV response in the top point of a cantilever subjected to oscillatory flow: (a) the instantaneous reduced velocity imposed in the circulation water channel; (b) in-plane and out-of-plane responses, respectively; orbits between in-plane and out-of-plane responses.

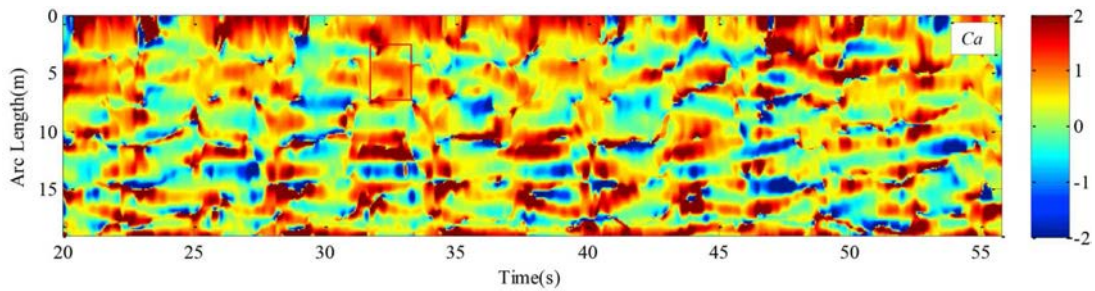


Source: Extracted from [Neshamar, van der A, and O'Donoghue \(2022\)](#).

Currently, [Neshamar, van der A, and O'Donoghue \(2022\)](#) shed light into the VSIV of cantilever structures and array of cantilevers. The experimental set-up imposed an oscillatory flow around the cantilever and the VSIV response is exhibited in both in-plane and out-of-plane movements; see Figure 2.26. Interestingly, the full synchronization between in-plane and out-of-plane responses occurred always at half period of the semi-cycle. [Neshamar, van der A, and O'Donoghue \(2022\)](#) further argues on this behavior and other characteristic features on the response phase.

Most significantly, the paper presents a discussion on the role of hydrodynamic coefficients in the VSIV, specially the author declared that the added mass must be separated into two different parcels: one that comes from flow-frequency itself; and other that is due to the own structural vibration.

Figure 2.27: Added mass coefficient evaluated using FF-LS methodology for a SCR model ($m^* = 1.53$) subjected to oscillatory flow ($A_i = 0.105m$ and $T_i = 5.96s$).



Source: Extracted from Zhang et al. (2021).

So as to evaluate the added mass and drag force coefficients, Neshamar, van der A, and O'Donoghue (2022) used the Forgetting-Factor Least Square (FF-LS) methodology presented in Liu et al. (2018, 2020) and Zhang et al. (2021). Although promising, this methodology focuses on the evaluation of optimal coefficients, which can lead to values that does not have a physical meaning.

For instance, the total inertia of an oscillating cylinder in a quiescent fluid can be written as

$$m_{tot} = m_s + m_a = m_s(1 + a), \quad (2.17)$$

in which $a = m_a/m_s$ is the added mass coefficient normalized by the structural mass. The fundamental condition for a dynamic system is that the total mass never achieves zero, $m_{tot} = 0$. Given such physical restriction, the added mass must have an asymptotic behavior, such as

$$m_{tot} \rightarrow 0^+ \iff a \rightarrow -1^+. \quad (2.18)$$

Considering that both added mass coefficients, a and C_a , are related with each other through the reduced mass,

$$C_a = \frac{m_a}{m_d} = \frac{m_a}{m_s} \frac{m_s}{m_d} = am^*, \quad (2.19)$$

then,

$$C_a \rightarrow -m^{*+}. \quad (2.20)$$

Closely inspecting Figure 2.27, it is possible to verify that the minimum added mass value estimated using FF-LS is $C_{a,min} \approx -2$ (dark blue). Ergo, the physical constrain obtained in Equation 2.20 is clearly not satisfied, $C_{a,min} \approx -2 < -m^* = -1.53$.

This divergence may be attributed to the lack of constrains in the FF-LS formulation, which searches for an optimal solution and not necessarily to one that is subjected to physical constrains, namely that the kinetic energy should be strictly positive.

The physical constrains can be considered as Lagrange's multipliers that should be introduced into the FF-LS objective function, using typical non-linear estimation methods, such as: Tikhonov's regularization; filtering algorithms; Bayesian statistical prior functions; amid others (CAMARGO, 2013; PELLEGRINI, 2019).

2.2.3 Other numerical models

Several numerical models were developed over the last decade to predict VIV and VSIV response. Generally, the VSIV models are adaptations on VIV ones, focusing on calibrating coefficients in order to capture the VSIV characteristic features (GRANT et al., 2000; LE CUNFF et al., 2009).

Wu et al. (2015) proposed an empirical model based on RIFLEX and VIVANA approach that was able to assess the fatigue damage on a catenary-like riser model. Although the assessment gave an overshoot value, given several simplification assumptions considered, the empirical model was capable of predicting the out-of-plane response frequencies and mode fairly well.

A time-domain model was introduced in Lu et al. (2019) so as to predict VSIV response on flexible risers, using a FE approach. The hydrodynamic forces were evaluated using rigid cylinders forced vibration experimental responses in which a period identification criterion was established in order to divide the entire vibration process into segments characterized by exciting and damping behavior.

Based on this criterion, a non iterative solving model evaluates modal space responses, assuming the VIV entered an ideal lock-in stage for each reduced velocity range. The time-domain model is tested and validated, comparing response predictions for steady and unsteady flows with experimental data.

Firstly considering the VIV, Thorsen, Sævik, and Larsen (2014) proposed a simplified method for time-domain simulations that takes into account a semi-empirical approach. The relative fluid velocity vector is used to decompose the external force ex-

erted by the fluid into in-plane and out-of-plane components. The out-of-plane forces are written with respect to equivalent lift, damping and added mass coefficients, considering a typical Morison approach.

The synchronization was considered to be the adjustment between frequencies and phases in a coupled oscillator system. Based on a Kuramoto synchronization model (IZHIKEVICH; KURAMOTO, 2006), the lift force instantaneous frequency is written as a sum of the shedding frequency and another function that acts as a tuning element, varying the lift force frequency around the shedding one. The lift force frequency increase or decrease depends on the relative phase between the out-of-plane movement and the correspondent lift force phases.

Experimental force coefficient data obtained by Gopalkrishnan (1993) was used in order to evaluate the proposed synchronization model. Further developments on this model were presented in Thorsen, Sævik, and Larsen (2015a,b), taking into consideration the in-plane movement as well and also simplifying the synchronization lift phase model. Thorsen, Sævik, and Larsen (2016, 2017) presented time-domain simulation regarding oscillatory flow using the same calibrated model, achieving a good agreement with experimental data previously obtained (WANG et al., 2014).

Contemporary works on the FIV phenomena have been focused in new inroads, such as Deep Neural Networks (DNN) and other Artificial Intelligence (AI) based algorithms as to predict complex dynamic behavior and assess fatigue damage (CANN, 2022; ZHANG et al., 2022). This sort of model works together with numerical analyses obtained with FE models in order to calibrate neural network to identify patterns and tune hidden layers.

The future of FIV phenomena analyses seems to go in the direction of new paths, regarding AI and physical based machine learning models in order to simplify the prediction of nonlinear systems. The computational capacity at the moment is not able to deal with CFD analyses on high aspect ratio structures subjected to a multitude of physical phenomena¹⁷ at once. This limitation is particularly due to the huge mesh size needed to fully represent a deep water riser.

Table 2.2.3 collects key references discussed in the present memoir, serving as a chronological guide that gathers some information on the VSIV. It is also given further

¹⁷Such as: 3D current profiles, internal waves, seismic phenomena on seabed, interaction with other structures, internal multiphase flow, internal material composition and surface phenomena, just to cite a few.

details on which riser model type and imposed amplitudes¹⁸ are presented.

Table 2.3: VSIV references chronological guide. Nomenclature: Steel Catenary Riser (SCR); Scaled Catenary Riser (ScCR); Rigid Right Cylinder (RRC); and Scaled Flexible Horizontal Cylinder (SFHC).

Reference	Year	Model	A_i^*
Grant <i>et al.</i>	(1999)	SCR	4, 24, 32
Grant <i>et al.</i>	(2000)	SCR	4, 24, 32
Chang and Isherwood	(2003)	SCR	4.3-43
Le Cunff <i>et al.</i>	(2005)	ScCR	352 (horizontal), 141 (vertical)
Fernandes <i>et al.</i>	(2008)	RSC	1.59, 3.19, 4.78
Le Cunff <i>et al.</i>	(2009)	ScCR	352 (horizontal), 141 (vertical)
Fernandes <i>et al.</i>	(2011)	RSC	1.59, 3.19
Fernandes <i>et al.</i>	(2012)	RSC	1.59, 3.19, 4.78, 6.37
Rateiro <i>et al.</i>	(2013)	ScCR	0.8, 1.6, 3.2, 4.8
Fu <i>et al.</i>	(2013)	SFHC	4.14-28.33
Fernandes <i>et al.</i>	(2014)	RSC	1.59, 3.19, 4.78, 6.37
Wang <i>et al.</i>	(2014)	ScCR	4.4, 8.8, 13.2, 15.4
Wu <i>et al.</i>	(2015)	ScCR	4.4, 8.8, 13.2, 15.4
Wang <i>et al.</i>	(2017)	ScCR	4.4, 8.8, 13.2, 15.4
Fu <i>et al.</i>	(2017)	SFHC	4.14-28.33

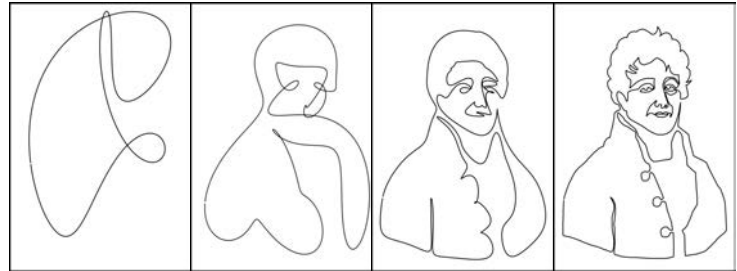
¹⁸Normalized with respect to the cylinder diameter, A_i^*

Table 2.3: VSIV references chronological guide. Nomenclature: Steel Catenary Riser (SCR); Scaled Catenary Riser (ScCR); Rigid Right Cylinder (RRC); and Scaled Flexible Horizontal Cylinder (SFHC).

Reference	Year	Model	A_i^*
Liu <i>et al.</i>	(2017)	SFHC	4.14-28.33
Pesce <i>et al.</i>	(2017)	ScCR	0.8, 1.6, 3.2, 4.8
Thorsen <i>et al.</i>	(2017)	Numerical	4.4
Yuan <i>et al.</i>	(2018)	SFHC	4.14-28.33
Lu <i>et al.</i>	(2019)	Numerical	4.14-28.33

Source: Developed by the author.

3 EXPERIMENTAL ARRANGEMENT AND ANALYSIS METHODOLOGY



Modal reconstruction on Fourier, 2022
Digital print

This chapter is devoted to the methodology which serves as a basis for the present work. It starts by presenting the testing model and the experimental arrangement used in order to observe the VSIV in a small-scale model and to record the fluid-structure interaction dynamics data.

Besides, a summary on the test matrix is going to be detailed, properly presenting the input parameters used in the experimental campaigns and how the tests were systematically conducted and registered. It is also presented a brief discussion on the real riser paradigm, including some challenges associated with technological limitations to represent a real structure dynamics in laboratory.

Finally, regarding the basis provided by the previous discussion, the last section of the following chapter serves the purpose of presenting the experimental analysis methodology, providing a necessary set of techniques employed in the present work.

3.1 Experimental description

As mentioned, this first section is a concise, albeit suffice, presentation of the materials used in order to obtain experimental data on the VSIV acting upon a catenary-like riser model.

3.1.1 Small-scale riser model: concept, design and characterization

As formerly stated, the testing model was conceptualized to maintain similarity with a real riser, which is a challenging task due to practical limitations on materials selection and experimental feasibilities. The model is built of a silicon hose filled-up with stainless steel micro-spheres and this choice of materials and design is addressed in the following paragraphs; see Figure 3.1.

The small-scale prototype main goal was to observe in laboratory some fluid-structure interaction phenomena present in risers dynamics due to incident current and imposed motion at the upper portion which is attached to a floating unit.

Figure 3.1: Prototype used to measure in air the model equivalent linear structural damping. In detail: the compact heavy filling and the optical targets attached to the model.



Source: Developed by the author.

Table 3.1 unveils some of the governing parameters on the hydroelastic dynamics of a catenary-like structure subjected to the action of Vortex Self-Induced Vibration. The set contains parameters typically found in fluid dynamics, such as the Reynolds', Strouhal's and Froude's numbers.

Others, like the Keulegan-Carpenter's number, appears in the hydrodynamics of floating structures, or the reduced mass and reduced velocity, which are commonly

associated to the VIV phenomenon.

Table 3.1: Main nondimensional parameters related to the hydroelastic dynamics of a catenary-like riser model subjected to the imposed motion at the top due to the action of gravitational waves on a floating unit.

Parameter	Symbol and definition
Froude's number	$Fr = \frac{U_i}{\sqrt{gL}} \sim \frac{2\pi\omega A}{\sqrt{gL}}$
Reynolds' number	$Re = \frac{U_n D}{\nu}$
Strouhal's number	$St = \frac{f_s D}{U_n}$
Keulegan-Carpenter's number	$KC = \frac{U_i}{f_i D} \sim 2\pi A_i^*$
Structural damping	ζ
Reduced velocity	$V_R = \frac{U_i}{f_{b,N} D}$
Reduced shedding frequency	$f_s^* = \frac{f_s}{f_{b,N}}$
Reduced mass	$m^* = \frac{m_s}{m_d} = \frac{4m_s}{\rho\pi D^2}$
Added mass	$a = \frac{m_a}{m_s}$
Added mass	$C_a = \frac{m_a}{m_d}$
Bending stiffness	$K_f = \frac{\lambda_f}{L} = \frac{1}{L} \sqrt{\frac{EI}{T}}$
Axial stiffness	$K_a = \frac{EA}{T}$
Soil stiffness	$K_s = \frac{k_s EI}{T^2}$

Source: Developed by the author.

Interestingly, the catenary-like geometry configuration is represented by the axial and bending stiffness parameters that take into consideration the cable traction at the TDZ, an important structural parameter in this case. The contact between riser with the seabed appears on the soil stiffness parameter; see Table 3.1.

Table 3.2: Mechanical properties of the chosen operational riser, the small-scale and the “as-built” models.

Data	“As-built”
Internal diameter (mm)	15.80
External diameter (mm)	22.20
Angle (°)	71.5
Water line (m)	2.50
Depth (m)	3.50
Anchor distance (m)	2.50
Total length (m)	6.65
Mass per length, m_s (kg/m)	1.14
Linear structural damping, ζ	0.53%
Weight in air (N/m)	11.18
Weight in water (N/m)	7.39
Axial rigidity, EA (kN)	1.0-1.6
Bending stiffness, EI (Nm ²)	5.60E-02
Flexural length, λ_f (mm)	49
Reduced mass, $m^* = m_s/m_d$	2.95

Source: Developed by the author.

The choice of a set of representative parameters is a difficult task. Nonetheless, it was possible to maintain similarity between real riser and scaled model considering a few physical parameters, as seen in Table 3.2.

The axial and bending rigidities obtained were typical of polymeric materials, whereas the diameter achieved was unfeasible to be monitored using conventional techniques. In the end, the model diameter was augmented, whilst maintaining the

axial and bending stiffness (LIFE&MO, 2011c,e; RATEIRO et al., 2012).

Consequently, the prototype was constructed using a polymeric circular hose filled-up with a heavy material to reach the scaled distributed mass, m_s . The filling was limited to safe, non-toxic, durable in water environment materials that should not modify the axial and bending rigidities, EA and EI , respectively.

The solution was to insert stainless steel micro-spheres into the hose, which has a second order effect on the aforementioned structural quantities variation.

Choosing a polymeric material adds to the model a hysteric behavior due to the material viscoelasticity, which was considered during the experimental axial rigidity evaluation. The viscoelastic behavior turns the model EA dependent on the deformation time rate, which, in turn, depends on the structural movement frequency.

Although the VSIV in catenary-like risers is characterized by large amplitude responses, the structural deformation is small, 1% to 2%. The deformation cycle also presents low frequencies. Such an effect is presented in the prototype mechanical characterization, in which the axial stiffness value is given as an interval; see Table 3.2.

The viscoelasticity seems to be an extra complication on the structural dynamics analysis, which can be a source of delay into the structure response given a varying load.

Nonetheless, the presence of hysteresis also occurs in real flexible-pipes risers, as there are several polymeric layers and other coating substance around metallic components in order to reduce friction.

The discussion on the testing model concept and design is extensive and full of details. The reader is invited to check the Appendix A in order to obtain further information on these topics, including the process of similarity through Froude's scale and the prototype mechanical properties experimental characterization.

3.1.2 Experimental arrangements

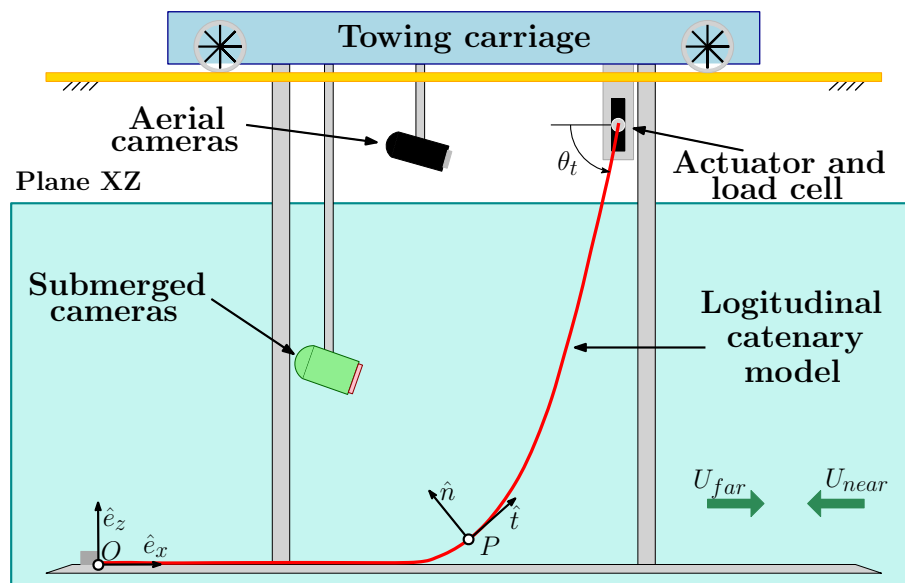
The experimental set-up constructed to study vertical and catenary-like prototypes subjected to hydroelastic phenomena, such as VIV and VSIV. The testing arrangements exploited thoroughly the towing carriage and channel in the Institute for Technological Research (IPT), which provided a plethora of experimental data on structural

non-linear dynamics due to incident flow, oscillatory imposed movement at the top in quiescent fluid and also the concomitant effect of them.

Three different small-scale models were used in the experimental campaigns and each one was tested in a different static configuration. The first model was a vertical cylinder (FRANZINI et al., 2016a; FRANZINI et al., 2016c), whilst the others were launched in the planar catenary-like shape and these models differ from each other with respect to the reference plane used to place their static configuration.

The reference planes are aligned with the towing channel in such way that one model is longitudinal to the relative flow generated by the carriage movement and the other transversal to the same flow. Ergo, they are referred as the longitudinal and transversal catenary-like models.

Figure 3.2: Sketch of the experimental arrangement used in the longitudinal catenary model.



Source: Developed by the author.

Due to its configuration, the longitudinal model presents a different dynamic response depending on whether the incident current is placed on the structure intrados or extrados regions, U_{far} and U_{near} , respectively; see Figure 3.2. In turn, the current is always perpendicular to the transversal model.

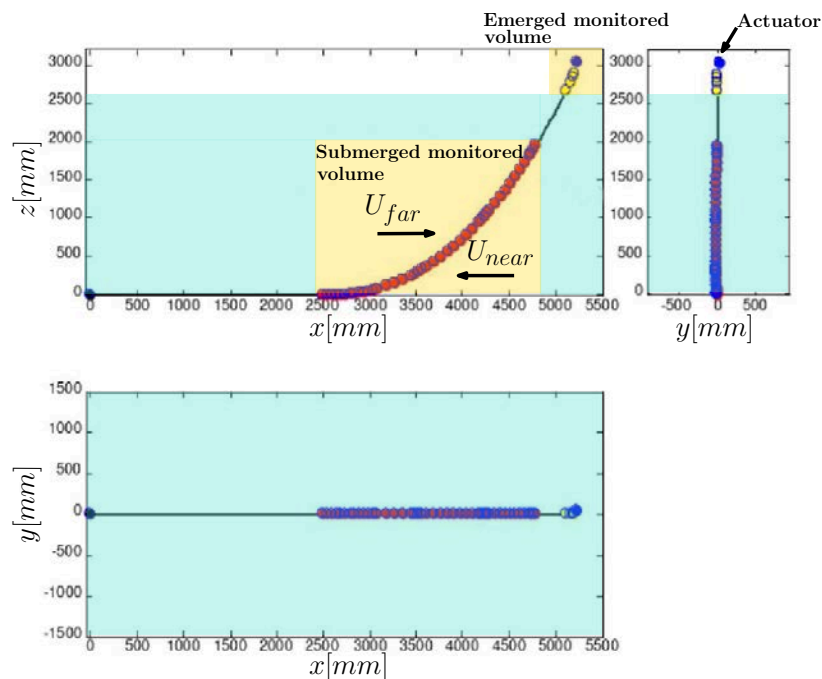
In reference to the imposed motion at the top tests, only the longitudinal model was tested due to the absence of incident current. The imposed oscillations acted as the floating unit where the riser model is attached, this movement being caused by incident gravitational waves acting on the vessel. The tests were executed with harmonic mono-

chromatic imposed motion (regular waves) and a multi chromatic one (irregular waves), evaluated using a typical JONSWAP spectrum.

Moreover, the tests were executed using two different soil contact conditions: one rigid and other over a foam layer, mimicking a softer seabed. As previously mentioned, the subsequent work is a snippet on a major experimental campaign, focusing only on tests with the longitudinal catenary-like model placed in a rigid soil and subjected to imposed mono-chromatic motion at its hang-off point.

The acquisition apparatus was composed of a LYNX[®] ADS2000 system, which has 64 channels with 16bits each (14 bits of precision). Each analog channel has its own dedicated signal conditioner circuit, LYNX[®] model AI2164, that has a second order anti-aliasing analog filter with fixed cut frequency, $f_{cut} = 3000Hz$. Besides, the acquisition system had sampling frequency of $F_s = 60Hz$, which is suffice in this particular arrangement; see Appendix B.3.

Figure 3.3: Testing model monitored span both under and out of water. The sketch also shows the planar catenary-like 3D geometric configuration in all Cartesian planes.



Source: Adapted from LIFE&MO (2012d).

Figure 3.2 also illustrates the measuring system used to record the structural dynamics, composed of an optical target tracking Qualisys[®] cameras set placed both under and above water, and a load cell that measures the traction at the hang-off point.

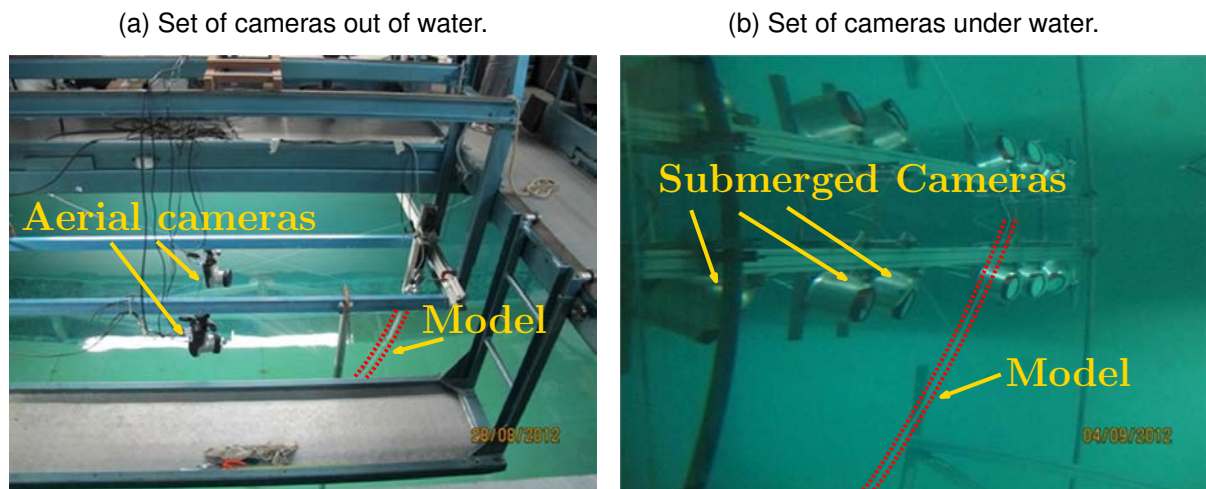
As to complete the experimental arrangement, the testing model upper extremity was connected to a servo driver attached to the towing carriage. The actuator was capable to input harmonic oscillations with controlled amplitude and frequency, and irregular oscillations based on a JONSWAP spectrum.

The connection between the model hang-off and the actuator was a cantilever with fixed angle, called the top angle or angle at the top that was measured with respect to the horizontal. Such angle was determined by the own full scale riser model that inspired the small-scale prototype design; see Table 3.2 and Appendix A.

Although the load cell calibration is fairly simple, the tracking cameras need a sophisticated method that determine a monitored volume around where the model should exist. This requires an initial educated estimation on the vibration amplitude response in order to identify the largest possible volume under and above water.

Consequently, this process can lead to an iterative reassembling of the cameras until the calibration converges. Figure 3.3 displays partially the monitored volume under and above water line where the cameras could measure the longitudinal catenary-like shape model instantaneous displacement.

Figure 3.4: Group of optical target tracking cameras used to capture 3D displacement of the model at each sampled instant.



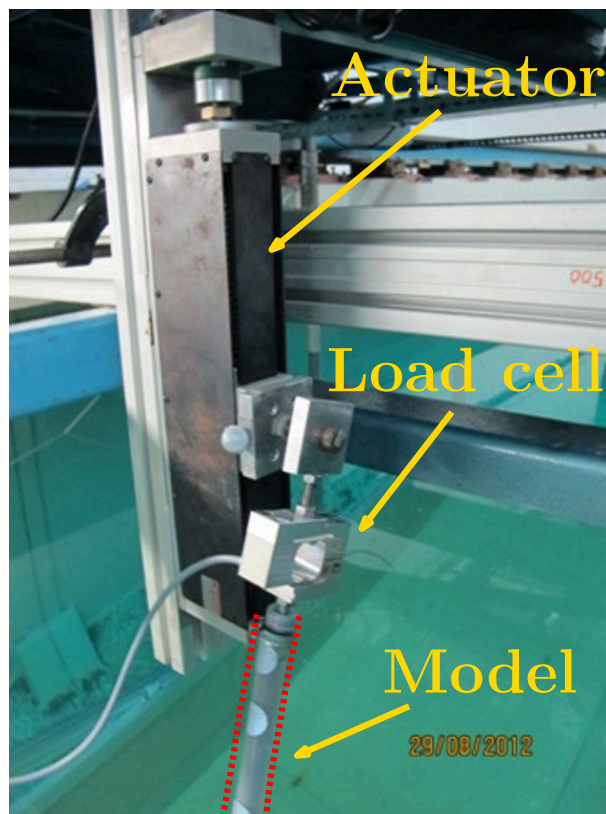
Source: Adapted from LIFE&MO (2012d).

The synchronization amid acquisition system, sensors and the tests start was possible due to a common trigger that could be activated by starting the camera recording software in each testing case. The array of tracking cameras is exhibited in Figure 3.4, in which is possible to have a clear idea on the cameras placement above and under

the water free surface; see Figures 3.4a-3.4b, respectively.

It is necessary at least 2 cameras, albeit ideally 3 or more, to determine each optical target position in space. For that reason, the set of submerged cameras worked in different depth and spatial angle ranges, observing the same target in at least 2 of them. Still, some targets could not be totally observable in the final data base, specially the ones placed near the water line region.

Figure 3.5: Aerial portion of the longitudinal catenary-like model showing in detail the imposing heave motion actuator and the load cell installed at the hang-off point.



Source: Adapted from LIFE&MO (2012d).

In turn, Figure 3.5 focus on the model hang-off point, which is attached to a load cell and a cantilever connection with the actuator. The servo driver is composed of a step motor that acts on a endless screw that provides a controlled vertical displacement. The actuator is connected to a control system that is set by an user to execute a particular motion.

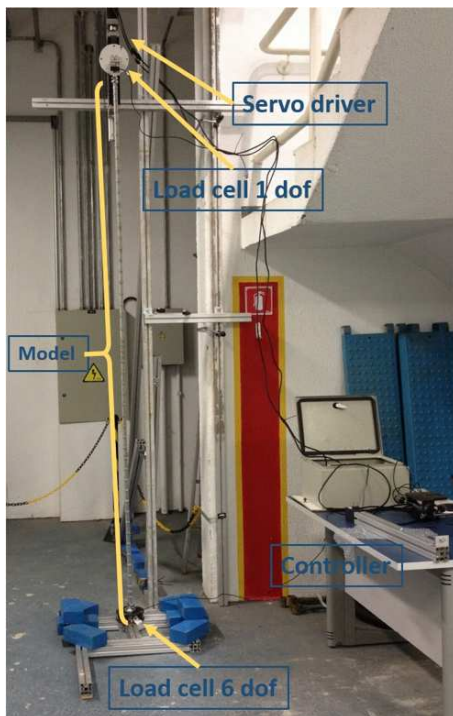
The load cell is a typical 1D S-type that is capable of measuring directly the traction at the hang-off point. The top traction, T_t , is a valuable experimental data due to the riser dynamic behavior be highly dependable on the geometric stiffness in region where

the curvature rate of change is negligible, *i.e.* away from the extremities where the bending effect is important.

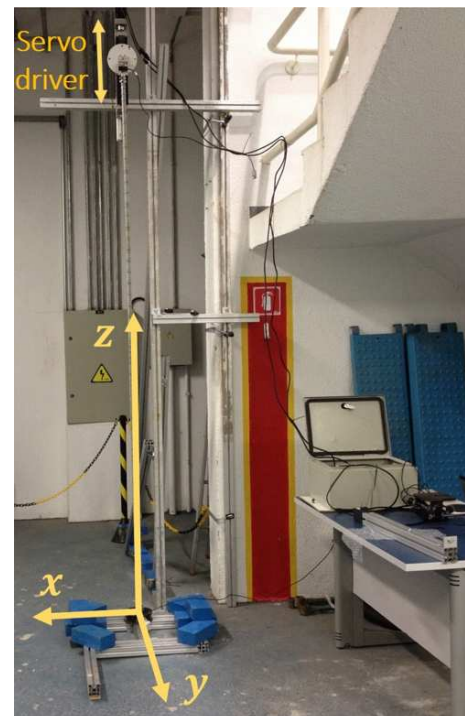
The top traction variation over time is also important, because it is responsible for a modulation on the structure natural frequencies. This variation showed to produce a substantial difference on the structural behavior, as mentioned previously (SILVEIRA et al., 2007; WANG et al., 2015).

Figure 3.6: Vertical model testing set-up carried out in TPN facility.

(a) Experimental arrangement description



(b) Cartesian axes



Source: Extracted from Salles (2016).

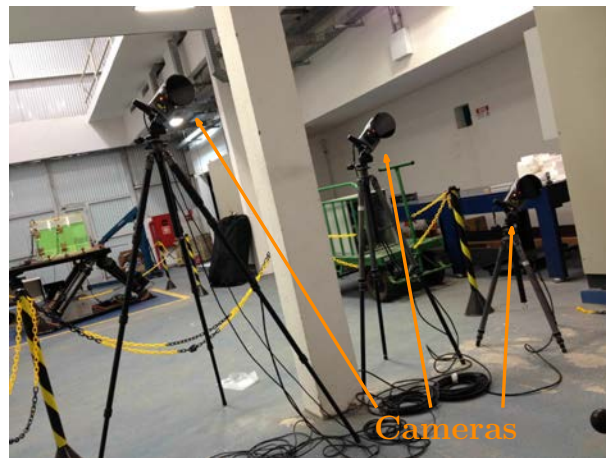
Finally, Salles (2016) conducted another experimental campaign with a vertical model in air at the TPN facility. These tests focused on assessing further results obtained with the vertical riser tests in water. Nonetheless, Salles (2016) also measured an equivalent viscous linear structural damping coefficient which is also adopted to all other prototypes based on the same model, among them the longitudinal catenary-like; see Table 3.2.

The experimental arrangement was fairly simple, composed of a prototype obtained as described in Appendix A, placed in a vertical configuration; see Figure 3.6. The same actuator described previously was used at the top and the model was attached to it through a S-type load cell that measured the top traction.

In addition, a robust load cell capable of measuring load in all direction and rotation, 6 dof, was placed at the bottom extremity; see Figure 3.6a. This was done for the model weight in air caused some variation on the bottom traction due to relaxation of the model viscoelastic hose material.

Hence, every test was preceded by a check on the bottom load in order to avoid compression and, if necessary, another calibration on the top. Figure 3.6b shows the testing arrangement.

Figure 3.7: Optical target tracking cameras used in the vertical riser model tests in air.



Source: Extracted from Salles (2016).

These extra tests conducted with a vertical model in air were monitored using a similar set of optical tracking Qualisys[®] cameras and, inasmuch as the experimental set-up in air is simple, only 3 cameras were needed; see Figure 3.7. The acquisition system was the same used in the tests in water at IPT facility.

3.2 Longitudinal catenary-like model: modal characterization

Following the experimental arrangement assemblage, a series of free decay tests were executed to evaluate the structural system natural frequencies and their respective modal functions. The small-scale model is a catenary-like circular tube and its vibration modes occur in two different planes, namely in the catenary plane (in-plane) and perpendicular to the catenary plane (out-of-plane).

The in-plane and out-of-plane are uncoupled due to a negligible torsional load in the

experimental arrangement. In the TDP region, some torsional loads can occur caused by of some assemblage misalignment, loss of the tube circular symmetry, contact with a non-rigid seabed or even rolling movements at the TDZ. However, such torsional effects are minimal and, consequently, the in-plane and out-of-plane modes are duly uncoupled from each other.

Table 3.3: Experimental natural frequencies obtained from free decay tests in water and their correspondent mode occurrence plane.

Global mode	Natural frequency, f_N (Hz) (CI 95%)	Occurrence plane
I	0.4265 (0.4185 to 0.4346)	Out-of-plane
II	0.7205 (0.7105 to 0.7306)	In-plane
III	0.8582 (0.8382 to 0.8782)	Out-of-plane
IV	1.1258 (1.1140 to 1.1377)	In-plane
V	1.2865 (1.2633 to 1.3097)	Out-of-plane
VI	1.6207 (1.5944 to 1.6470)	In-plane
VII	1.7378 (1.6427 to 1.8328)	In-plane
VIII	1.7494 (1.6756 to 1.8232)	Out-of-plane
IX	2.0960 (2.0250 to 2.1669)	In-plane
X	2.1824 (2.1386 to 2.2263)	Out-of-plane
XI	2.3900 (2.2847 to 2.4952)	In-plane
XII	2.6479 (2.5199 to 2.7759)	Out-of-plane
XIII	2.9940 (2.9551 to 3.0328)	In-plane
XIV	3.0207 (2.9788 to 3.0626)	Out-of-plane
XV	3.6495 (3.4944 to 3.8047)	In-plane
XVI	3.7547 (3.6970 to 3.8123)	Out-of-plane

Source: Developed by the author.

Table 3.3 shows the experimental characterization obtained executing 6 different free decay tests. The natural frequencies were computed in the frequency domain by analyzing all optical targets temporal series after an impulsive input.

The methodology was fairly simple, taking advantage of the frequency response of all targets displacement series evaluated using a typical Fast Fourier Transform (FFT), necessary windowing and zero-padding procedures.

Each mode is evinced as a peak in the frequency response and the correspondent

eigenvalue is determined as the mean of all peaks around a fixed frequency value. The confidence interval (CI) is computed as a typical statistical hypothesis test, using two tailed Student's T-distribution with fixed confidence, $p = 0.05$ (95%).

The occurrence plane could be identified due to both in-plane and out-of-plane modes be uncoupled and the plane catenary-like geometric configuration be contained in the XZ plane, whilst the y -axis points to the out-of-plane direction; see Figure 3.2-3.3. Thus, the former were observed in the x, z -axes Cartesian displacements series, whilst the latter in the y -axis Cartesian displacements ones.

Accordingly, analytic or numerical approaches should be considered as to characterize the structural modes. Whilst the latter are generally Finite Element (FE) models composed of 3D beam or cable elements that are commonly computed by means of commercial solvers, *e.g.* Orcaflex[®], the former are only possible to be obtained by using perturbation methods along with curved beam models, such as the WKB(J)¹ approximation (PESCE et al., 1998; PESCE; MARTINS, 2005; CHATJIGEORGIOU, 2008).

For instance, Pesce and Martins (2005) present a closed form solution for the Sturm-Liouville's problem of a linearized catenary-shaped riser, considering its dynamics to occur only in the structure plane (2D). The elastica is supposed to be inextensible and hinged-hinged at the bottom and upper points. Bending effect and TDP movement are not considered as well.

Both eigenvalues and normal eigenvectors, Ω_n and $\varphi_n(\theta(\xi), \theta_L)$, respectively, can be obtained with respect to the hang-off angle, θ_L , and the unstretched Lagrangian nondimensional arc-length, $\xi = s/L$,

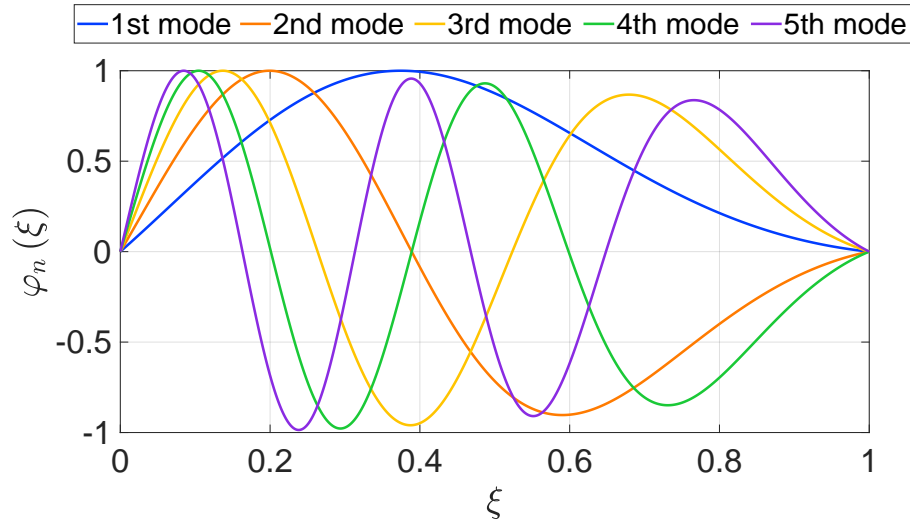
$$\begin{aligned} \varphi_n(\theta(\xi), \theta_L) &\sim \cos^{1/4}(\theta(\xi)) \sin \left[\Lambda_n \int_0^{\theta(\xi)} \cos^{-3/2}(\theta') d\theta' \right], \\ \Omega_n &= \Lambda_n \tan(\theta_L) \sqrt{\frac{T_0}{(m + m_a)L}}, \\ \Lambda_n &= \frac{n\pi}{\int_0^{\theta_L} \cos^{-3/2}(\theta') d\theta'}, \end{aligned} \quad (3.1)$$

in which n is the mode number; T_0 , the traction at the TDP; m and m_a , structural and

¹The perturbation technique is usually known as the acronym WKB(J), which stands for Wentzel–Kramers–Brillouin(-Jeffreys), or even as the Liouville–Green (LG) method.

added masses, respectively; and L , the structural length; see Figure 3.8.

Figure 3.8: Some normal normalized eigenvectors for catenary-shaped riser obtained by Pesce and Martins using the WKB approximation.



Source: Developed by the author.

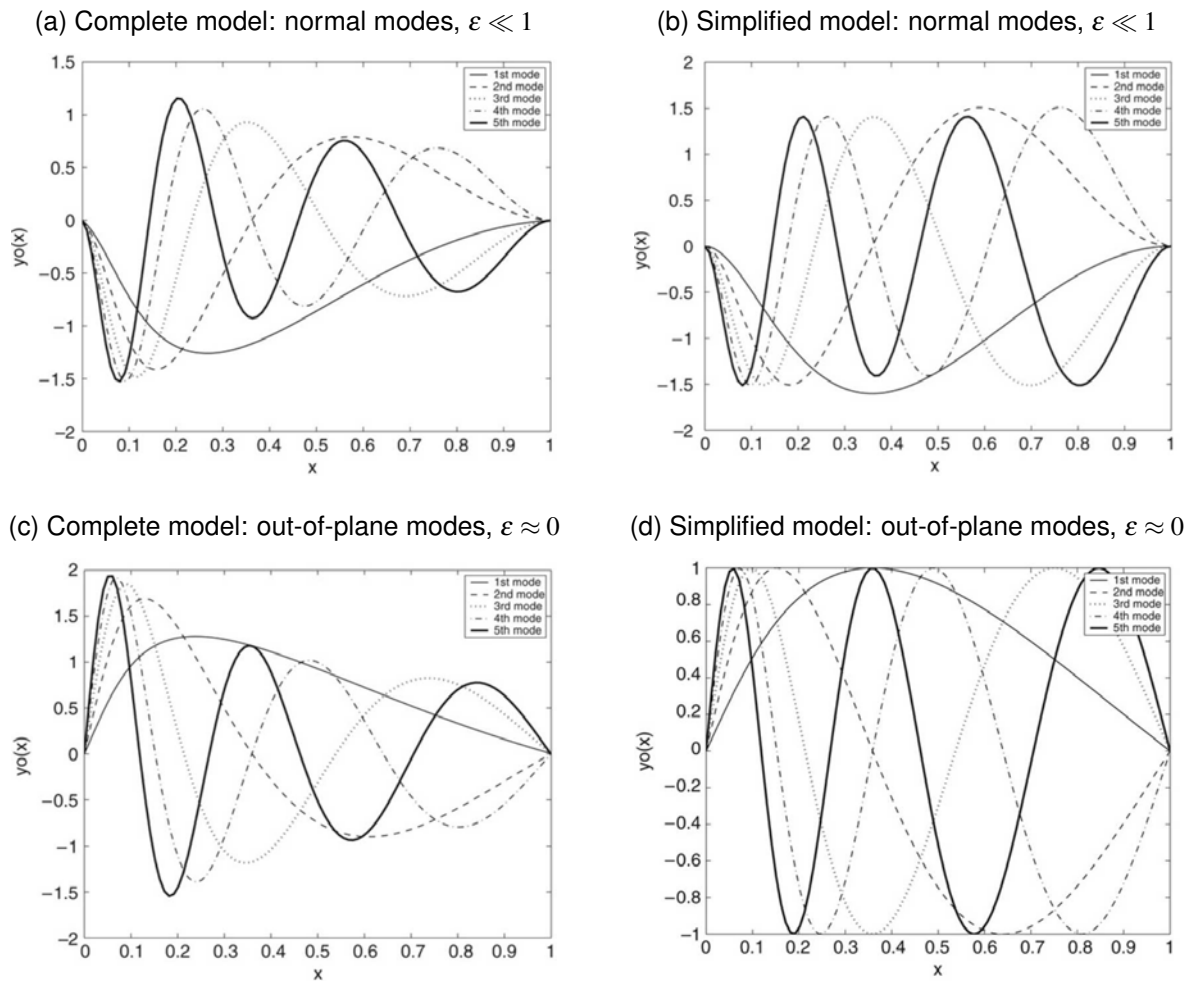
Chatjigeorgiou (2008) presents another application of the WKB method to the linearized catenary-like risers, assuming nonzero bending stiffness at the bottom sag region where the curvature varies considerably. In addition to bending effect, the model takes into account variations on the geometric stiffness and static configuration along the structure span, and the TDP is supposed fixed.

Figures 3.9a-3.9b and 3.9c-3.9d illustrate the in-plane normal and out-of-plane modal shapes for a catenary-shaped structure, respectively. Chatjigeorgiou argues that the complete model can be simplified if the static configuration effect is considered to be one order of magnitude smaller than the one due to geometric stiffness.

The variation on static configuration plays a major role only in the in-plane dynamics, where the structural effective weight breaks symmetry imposing static curvature along the span. Consequently, both complete and simplified models should retain terms of the order $\mathcal{O}(\varepsilon)$ if the in-plane modes are considered, $\varepsilon \ll 1$.

Chatjigeorgiou identifies that omitting terms of the order $\mathcal{O}(\varepsilon)$, alternatively $\varepsilon \approx 0$, would diminish the static configuration variation influence on the structural response, pointing out that this would be a defensible assumption for the out-of-plane modes attainment.

Figure 3.9: Structural modal shapes obtained by Chatjigeorgiou's complete and simplified models using the WKB approximation.



Source: Extracted from Chatjigeorgiou (2008).

Note: Following Chatjigeorgiou's nomenclature notation: x is the nondimensional arc-length; $y_0(x)$, the modal shape; and the perturbation scale parameter, ε .

Pesce and Martins (2005) presented a closed form solution for both in-plane modes normal and tangent parcels, $\varphi_n(\xi)$ and $\psi_n(\xi)$, respectively, attained from the 2D catenary-shaped structural formulation. In turn, Chatjigeorgiou (2008) started its WKB approximation from a linear Euler-Bernoulli curved beam formulation and, thus, only the normal parcel was obtained.

The precise nomenclature should be in-plane and out-of-plane modes, however, it is acceptable to reason that the latter always occurs in the binormal direction in a planar catenary-like structure. Ergo, the normal and binormal nomenclatures are borrowed from the differential geometry context and they are used in order to call the in-plane normal parcel and out-of-plane modes, respectively.

Considering the complete model, the differences between normal and binormal modes are subtle for lower modes. Nonetheless, it is possible to note a little variation on the modal shape maximum displacement position in which the out-of-plane modes seem to be more shifted towards the TDP, presenting these maximum at lower points nearer to the fixed TDP when compared to the normal modes. Besides, the bending rigidity effect is more pronounced in the normal modes due to the asymmetry caused by the static configuration on the structural elastica; see Figures 3.9a-3.9b.

More significantly, even though Chatjigeorgiou (2008) takes into account nonzero bending, Figures 3.9b and 3.9d resemble closely the normal modes obtained in Pesce and Martins (2005), in which the bending effect is absent; see Figure 3.8.

Nevertheless, from the Galerkin's decomposition perspective, all modes presented so far are equivalent, as they do not violate the boundary conditions of the catenary-shaped structural configuration².

The resemblance on the normal and binormal modes topology, equivalently their general shape, is accounted for the linearization on the plane catenary-shaped structural model. Full 3D catenary-like structural models, such as in Triantafyllou (1994) and Chatjigeorgiou and Mavrakos (2010), sheds light on how the normal and binormal linearized oscillators present similar terms in their equations, which can indicate why both modal shapes are similar when it is assumed that the structure is inextensible and in the small out-of-plane displacement and angle regime.

The numerical approach is based on a small-scale model³ that was implemented in Orcaflex[®] so as to compute the structural eigenfunctions. The FE model assumes that the structural material is linear, as it is currently impossible to define a material of different rheology on the numeric solver.

²It is noteworthy that the modes obtained by Pesce and Martins (2005) are indeed for a classical catenary structural configuration and, in turn, the ones by Chatjigeorgiou (2008) represents a catenary-like structure due to the presence of bending stiffness. Thus, *s.str.*, the terminology "catenary-shaped" is only applicable in the context of Pesce and Martins (2005).

³Orcaflex[®] cannot simulate the experimental prototype in its as-built scale due to the geometric and mechanical properties values are too small. So, the small-scale model was scaled using the Froude scale methodology with $\lambda' = 100 : 1$; see Appendix A.

Table 3.4: Natural frequencies and modal shapes obtained from Orcaflex[®] numerical model.

(continued on next page)




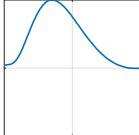
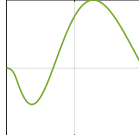
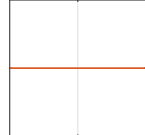

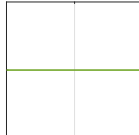
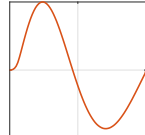
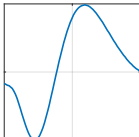
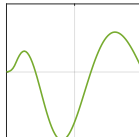


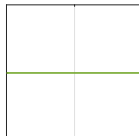
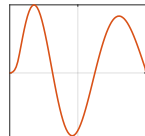
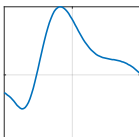
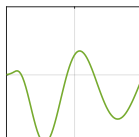


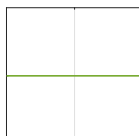
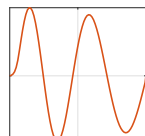
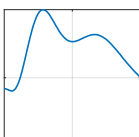
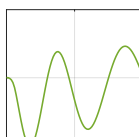
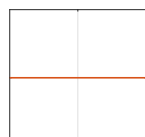
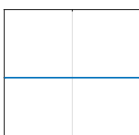
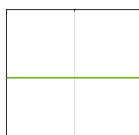
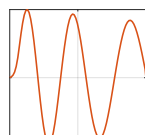
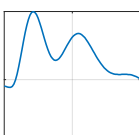
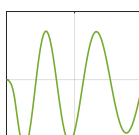
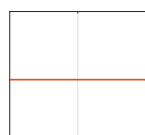


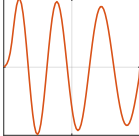
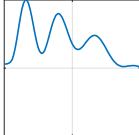
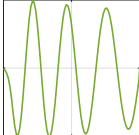


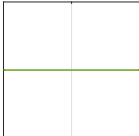
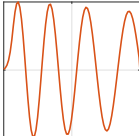
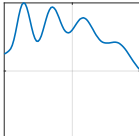
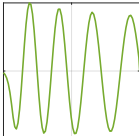


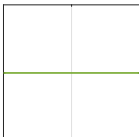
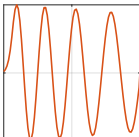
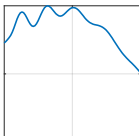
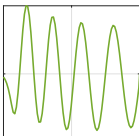


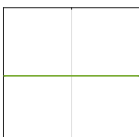
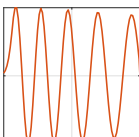
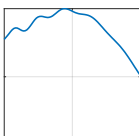
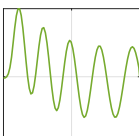
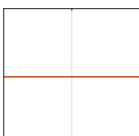
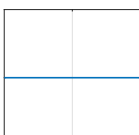
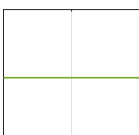
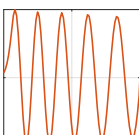
Global mode	f_N (Hz)	Occurrence plane	Modal shape		
			$T(\hat{s})$	$N(\hat{s})$	$B(\hat{s})$
I	0.4235	Out-of-plane			
II	0.7113	In-plane			
III	0.8420	Out-of-plane			
IV	1.1159	In-plane			
V	1.2663	Out-of-plane			
VI	1.5367	In-plane			
VII	1.6983	Out-of-plane			
VIII	1.7329	In-plane			
IX	2.1397	Out-of-plane			
X	2.1466	In-plane			

Table 3.4: Natural frequencies and modal shapes obtained from Orcaflex[®] numerical model.

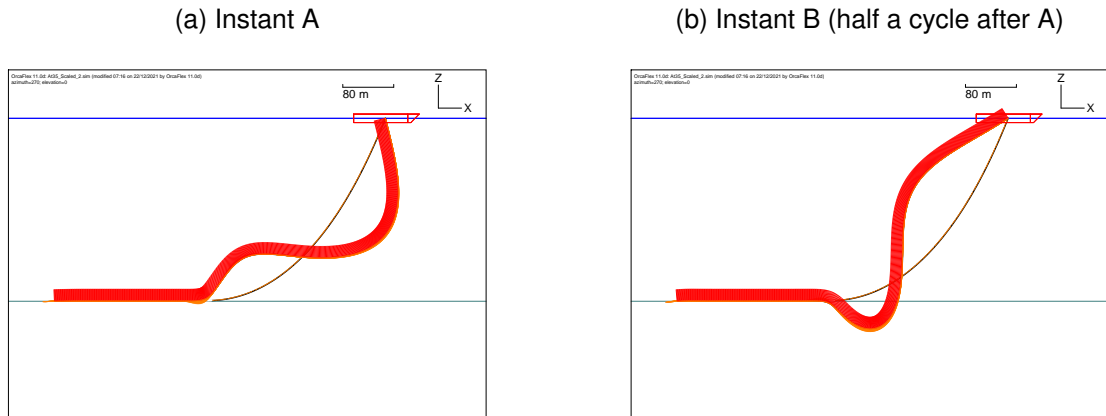
(final page)

Global mode	f_N (Hz)	Occurrence plane	Modal shape		
			$T(\hat{s})$	$N(\hat{s})$	$B(\hat{s})$
XII	2.5922	Out-of-plane			
XIII	3.0401	In-plane			
XIV	3.0568	Out-of-plane			
XV	3.5003	In-plane			
XVI	3.5346	Out-of-plane			
XVII	3.9719	In-plane			
XVIII	4.0261	Out-of-plane			
XIX	4.1484	In-plane			
XX	4.5313	Out-of-plane			

Source: Developed by the author.

Note: The anchor non-monitored span is not represented.

Figure 3.10: Structural II mode (1st in-plane mode), $f_{N,n}^{(1)} = 0.7113\text{Hz}$, obtained with the numerical model on Orcaflex[®]. Normal and binormal vectors are displayed in red and orange, respectively.



Source: Developed by the author.

The numerical model is constructed from a steel catenary riser hinged at the floating unit and it is launched forming a half catenary-like shape, in which the bottom part is in touch with the seabed and the anchor is located far away from the TDZ; see Figure 3.10. The TDP is also supposed fixed for each mode.

The modal shapes obtained by the Orcaflex[®] numerical model are thoroughly presented in Table 3.4. The numerical solver considers a nonrigid soil which affects the in-plane normal mode, as it can be seen detailed in Figure 3.10, where the riser penetrates slightly the soil, creating an extra small lobe in the first normal mode (II mode); see Figure 3.10b⁴.

Table 3.4 depicts the secondary lobe presence up to the third normal mode (II, IV and VI modes). The absence of this secondary lobe in higher modes could be accounted for the bending effect at the bottom sag region limiting the curvature locally, which mitigates steadily the soil penetration.

More importantly, the Orcaflex[®] modes show the static configuration effect on higher modes. The static curvature breaks the symmetry and it appears an oblique tendency on the vibration shape.

⁴The scale factor used in Orcaflex[®] exaggerates the amount of penetration that would occur in a real case.

Table 3.5: Out-of-plane modes natural frequencies, $f_{N,b}$ (Hz), obtained in free-decay tests and numerically using Orcaflex[®].

Mode	$f_{N,b}$ (Hz)	
	Experimental (95% CI)	Orcaflex
1 st	0.4265 (0.4185 to 0.4346)	0.4235
2 nd	0.8582 (0.8382 to 0.8782)	0.8420
3 rd	1.2865 (1.2633 to 1.3097)	1.2663
4 th	1.7494 (1.6756 to 1.8232)	1.6983
5 th	2.1824 (2.1386 to 2.2263)	2.1397
6 th	2.6479 (2.5199 to 2.7759)	2.5922
7 th	3.0207 (2.9788 to 3.0626)	3.0568
8 th	3.7547 (3.6970 to 3.8123)	3.5346
9 th	-	4.0261
10 th	-	4.5313

Source: Developed by the author.

The rising question is what set of modal shapes should be considered as to use in the Galerkin's decomposition. The analytic modes are easier to be used, inasmuch as their closed form is straightforward to compute (PESCE; MARTINS, 2005; CHATJIGE-ORGIOU, 2008). In turn, the Orcaflex[®] modes are closer to the experimental prototype modal shape, since it takes into consideration the extensibility and bending effects at the bottom sag region.

On top of this, the structural "as-built" eigenvectors are farther complicated than those presented due to the variation on TDP position with respect to time, causing modulation on the structural eigenfrequencies.

Tables 3.5-3.6 shows the natural frequencies computed by Orcaflex[®]. The out-of-plane natural frequencies, in the binormal direction, Table 3.5, show excellent agreement with all experimental eigenvalues within their confidence interval. It is defensible that such agreement points to a conclusion that the Orcaflex[®] binormal modes are excellent estimations of the true modal shapes.

Table 3.6: In-plane modes natural frequencies, $f_{N,n} = f_{N,in-plane} (Hz)$, obtained in free-decay tests and numerically using Orcaflex[®].

Mode	$f_{N,n} (Hz)$	
	Experimental (95% CI)	Orcaflex
1 st	0.7205 (0.7105 to 0.7306)	0.7113
2 nd	1.1258 (1.1140 to 1.1377)	1.1159
3 rd	1.6207 (1.5944 to 1.6470)	1.5367
4 th	1.7378 (1.6427 to 1.8328)	1.7329
5 th	2.0960 (2.0250 to 2.1669)	2.1466
6 th	2.3900 (2.2847 to 2.4952)	2.5673
7 th	2.9940 (2.9551 to 3.0328)	3.0401
8 th	3.6495 (3.4944 to 3.8047)	3.5003
9 th	-	3.9719
10 th	-	4.1484

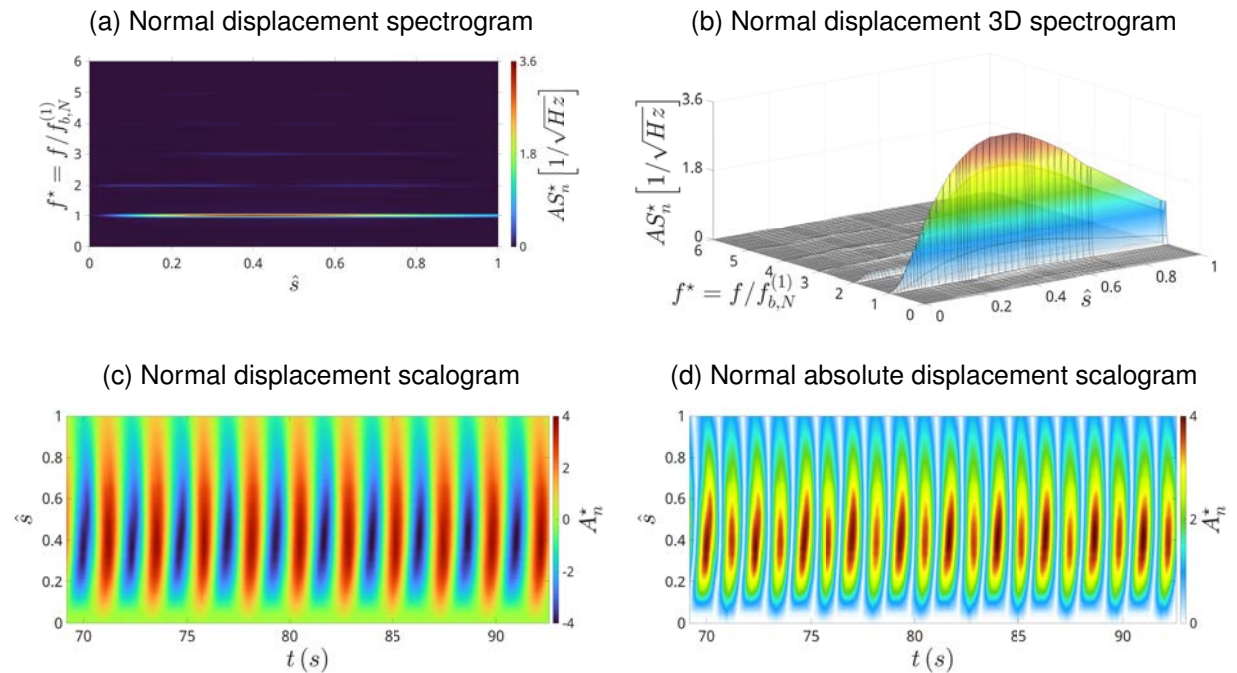
Source: Developed by the author.

In contrast, the in-plane natural frequencies obtained in the experimental free decay tests are a bit off the ones computed by Orcaflex[®]; see Table 3.6. This could be explained by the lesser quality on free decay tests in in-plane coordinates compared to the out-of-plane tests. Furthermore, the experimental arrangement has a rigid soil, differing slightly from the Orcaflex[®] model.

Figure 3.11 displays a typical normal amplitude response found in the present experimental data. Figure 3.11b shows in detail that the first normal mode does not present the small lobe as the one presented in the Orcaflex[®] first in-plane modal shape; see Figure 3.10.

This difference may be attributable to the discrete model used in the Orcaflex[®] modal analysis, since the developed model did not take into consideration a rigid soil contact condition at the bottom.

Figure 3.11: Typical experimental normal displacement spectrogram and scalogram found in the present work. Case: $A_i = 70\text{mm}$ and $f_i = 0.42\text{Hz}$, alternatively At70-ID16.



Source: Developed by the author.

The VSIV is characterized by the out-of-plane movement and the Orcaflex[®] modal analysis show excellent agreement with the experimental results obtained. Contrastingly, the numerical in-plane normal modes were not very representative of what could be observed in the experimental data, as the discrete model did not have the rigid soil contact condition at the bottom.

Considering the results presented in [Pesce and Martins \(2005\)](#) and [Chatjigeorgiou \(2008\)](#), the normal modes show great similarity with the out-of-plane modes and, for this reason, the Galerkin's decomposition of the in-plane normal motion will be also carried out using the binormal eigenfunctions in lieu of the ones obtained previously.

3.2.1 Test matrix and selected cases

The experimental tests were carried out considering variations on the displacement amplitude and its imposed frequency at the structure hang-off point. Each experimental group was composed of a fixed imposed amplitude value at the top, seriatim varying the input frequency.

The imposed amplitudes, A_i , were chosen as to resemble typical low KC values

measured in offshore floating units. Table 3.7 brings the amplitude values used in its first row, which varied from 17.5mm up to 105mm.

Thereon, the correspondent floating unit reduced amplitude,

$$2\pi \frac{A_i}{D} = 2\pi A_i^*,$$

assumed values in the range of 5 up to 30, turning possible to define a nondimensional velocity number,

$$v_i = 2\pi A_i^* \frac{f_i}{f_{N,b}^{(1)}} = 2\pi A_i^* f_i^*, \quad (3.2)$$

that resembles closely the reduced velocity number, V_R , as if it was computed considering the floating unit vertical movement; see Table 3.7.

Such velocity number, v_i , takes into consideration the structural I mode natural frequency, alternatively the 1st out-of-plane, as it is commonly employed in the rigid cylinder subjected to oscillatory flow reduced velocity characterization (SARPKAYA; RAJABI, 1979; SUMER; FREDSSØE, 1988; KOZAKIEWICZ; SUMER; FREDSSØE, 1994; FERNANDES et al., 2008).

The correspondent velocity is then varied steadily, assuming values comprehended in a typical VIV test range⁵. Consequently, the input vertical motion frequency can be evaluated by means of the input reduced frequency, f_i^* , considering the out-of-plane eigenfrequency thereof; see Equation 3.2.

A close inspection in Table 3.7 reveals the power limitation on the mechanism that imposes motion at the hang-off point. For that reason, the input frequency, f_i , alternatively the reduced input frequency, f_i^* , can only vary up to a maximum figure, which differs depending on the experimental test imposed amplitude.

⁵Even though the limelight is upon the VSIV, the VIV enlightens much of the experimental praxis on the VSIV.

Table 3.7: Test matrix for the longitudinal catenary-like model subjected to imposed movement at the top, in which $v_i = 2\pi A_i^* f_i^*$, $f_i^* = f_i/f_{N,b}^{(1)}$ and $f_{N,b}^{(1)} = 0.4265Hz$.

A_i (mm)	17.5		35		70		105	
$2\pi A_i^*$	5		10		20		30	
Test ID	v_i	f_i^*	v_i	f_i^*	v_i	f_i^*	v_i	f_i^*
00	0	0.00	0	0.00	0	0.00	0	0.00
01	2	0.40	2.3	0.23	5	0.26	7	0.23
02	3	0.60	3	0.30	6	0.30	8	0.26
03	4	0.79	4	0.40	7	0.35	9	0.30
04	5	1.00	5	0.51	8	0.40	10	0.33
05	6	1.21	6	0.60	9	0.44	11	0.37
06	7	1.40	7	0.70	10	0.51	12	0.40
07	8	1.60	8	0.79	11	0.56	13	0.44
08	9	1.79	9	0.91	12	0.60	14	0.47
09	10	2.00	10	1.00	13	0.65	15	0.51
10	11	2.21	11	1.09	14	0.70	16	0.53
11	12	2.40	12	1.21	15	0.74	17	0.56
12	13	2.60	13	1.30	16	0.79	18	0.60
13	14	2.79	14	1.40	17	0.86	19	0.63
14	15	3.00	15	1.51	18	0.91	20	0.67
15	16	3.21	16	1.60	19	0.95	21	0.70
16	17	3.40	17	1.70	20	1.00	22	0.74
17	18	3.60	18	1.79	21	1.05	23	0.77
18	19	3.79	19	1.91	22	1.09	24	0.79
19	20	4.00	20	2.00	23	1.14	25	0.84
20	21	4.21	21	2.09	24	1.21	26	0.86
21	-	-	-	-	-	-	27	0.91
22	-	-	-	-	-	-	28	0.93
23	-	-	-	-	-	-	29	0.98
24	-	-	-	-	-	-	30	1.00
25	-	-	-	-	-	-	31	1.02

Source: Developed by the author.

In addition to the VSIV, other nonlinear structural phenomena can occur in in-plane, out-of-plane, or both dynamics. In particular, Mathieu-type instability depends on the possible input frequency range, since higher frequencies would be needed to create a scenario in which typical frequency ratios such as 2 : 1 can be obtained.

In turn, still considering parametric instability, the excessive damping due to drag in water acts as a stabilizer and larger amplitude values are necessary in order to achieve the instability bifurcation.

Ergo, the test matrix, albeit large, faces limitations on the hydroelastic response observability, which reduces occasionally the occurrence of multiple phenomena on the experimental response. Conversely, this limitation is also beneficial and desirable in terms of studying the VSIV and isolating it from other nonlinear phenomena.

In the current analyses, emphasis will be placed on tests whose amplitude conditions are larger, namely, $A_i = 35\text{mm}$, 70mm and 105mm . The case $A_i = 17.5\text{mm}$ will also be addressed as the input frequency assumes larger values in this particular group and other interesting structural phenomena may be seen.

Notwithstanding, as to study the VSIV under the modal perspective, the other tested groups, whose amplitudes are larger, seem to provide better results due to the $KC(s)$ can assume larger values along the riser span, which turns possible to find richer synchronization relations amid the model dynamics.

More significantly, the Appendix C is comprised of experimental supplementary results whose importance might be secondary, or due to the quantity of results to be presented seriatim.

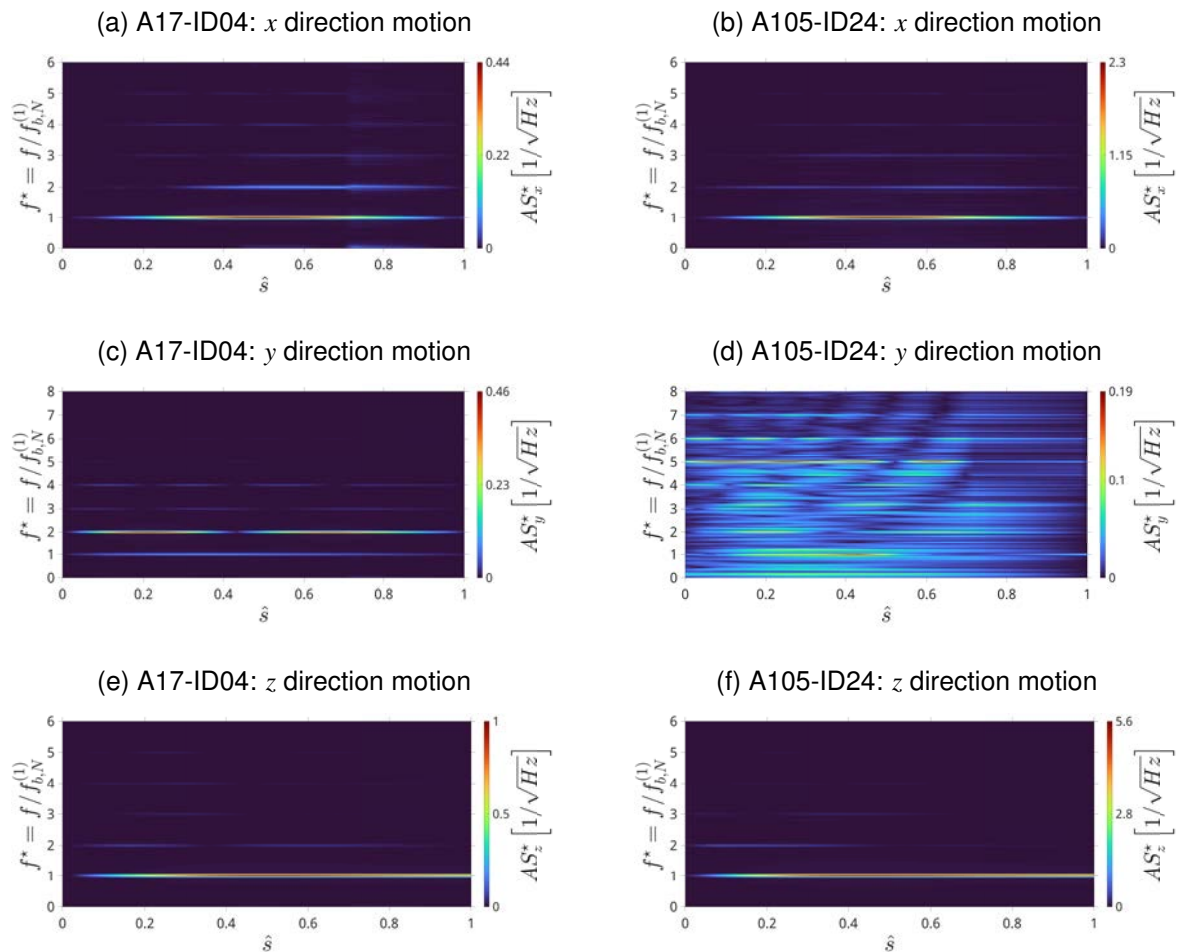
3.2.2 Real riser paradigm and the experimental methodology motivation

Taking advantage of the previous discussion on concomitance of several phenomena in the small-scale model dynamics, one could wonder whether it would be possible to have a model that could encompass the real case paradigm, including all loads that are applicable to a certain riser.

Clearly, no experimental small-scale model would fit such requirements, not only a real sea state is impossible to achieve at laboratory conditions, including all hydrodynamic and geophysical phenomena, but also the small-scale methodology cannot match the Reynolds number between *in situ* and laboratory models; see Appendix A.

As a general rule, analytic formulations are limited to a few fairly simple conditions and even perturbation techniques cannot deal with this much of complexity. Hence, numerical models could be an alternative, insofar as the domain and structural discretizations can commonly handle variations on loads and other parameters.

Figure 3.12: Motion spectra in the global reference coordinates of two cases whose the input frequency is kept constant, $f_i^* = 1$, whereas the imposed amplitude varies from 17.5mm to 105mm, corresponding to the cases A17-ID04 and A105-ID24, respectively.



Source: Developed by the author.

Note: The input $f_i^* = 1$ corresponds to the 1st out-of-plane natural frequency (mode I). Additionally, the spectrum intensity was normalized by its own maximum value.

The main issue is that the full representation of a riser is nearly impossible on a numeric solver. The high aspect ratio, L/D , would be responsible for a rapid exponential increase on the system Degrees-of-Freedom (DOF) and the calculations alone would take an almost infinite amount of time, considering the current technology.

Although discouraging at a first glance, these challenges and limitations reinforce

the crucial role of experimental results on understanding the phenomenology behind complex phenomena, such as the VSIV, which serves as paradigm to other Reduced Order Models (ROM).

For this reason, the current work sought to develop an useful analysis methodology, aiming to create an experimental phenomenological paradigm from the Galerkin's decomposition perspective.

It is certainly true that the number of generalized coordinates in a continuum structure is infinite and any sort of discretization is so good and suitable as the amount of considered measuring points.

Modal analysis acts as a spatial filter that redistributes the system dynamical information within a finite number of modes, allowing the usage of any discretization points quantity as necessary so to obtain a good structural representation.

Ergo, it is possible to reintroduce the concept of generalized coordinates as the own modes used within the modal decomposition methodology, insofar as the analysis can be executed using only a set containing the most relevant and energized modes.

For instance, Figure 3.12 displays spectra results for two different testing conditions whose reduced input frequency is kept constant, $f_i^* = 1$, corresponding to an input of the same value as the first out-of-plane mode natural frequency, alternatively mode I, whereas the imposed amplitude varies from 17.5mm to 105mm.

The synchronization observed as a result of the VSIV depends closely on the imposed amplitude and frequency. Moreover, the synchronization complexity increases as the imposed amplitudes and frequency assume higher values. Figure 3.12 shows the effect of increasing the exciting amplitude, whereas maintaining the same frequency, and, as it can be seen, the structural response assumes a more complex and rich synchronization.

Whilst the in-plane motions, directions x and z , do not show significant variation on its modal response which is mainly characterized as a quasi-monochromatic movement, Figures 3.12a, 3.12b, 3.12e and 3.12f, the same behavior cannot be seen in the out-of-plane motion as the synchronization is far more complex, Figures 3.12c-3.12d, displaying multimodal responses.

The filtering process is characterized by means of the reduced number of necessary coordinates used to represent the structure dynamics, which can also be regarded as a modal ROM. Considering again the behavior depicted in Figure 3.12, the modal

decomposition can assist the analysis by selecting only the most relevant modes to be considered.

Notwithstanding, as any other ROM, the price to be paid is loss of local information on the structural behavior, as the emphasis was placed on the global dynamics. Furthermore, as to achieve a minimum number of generalized coordinates for the proposed ROM, the choice of modal functions must be such that a few modes are capable of represent the general structural behavior. Generally, such modal shapes are obtained closely as possible to the structural eigenvectors, which resumes the former subject on selecting a proper modal basis.

3.3 Experimental analysis methodology: modal approach to the VSIV

This final section contains the mathematical methodology devised in order to analyze the structural modal response due to the VSIV. Firstly, it will be presented some modeling assumptions used in the experimental data processing, specially regarding the signal treatment necessary to develop further outcomes.

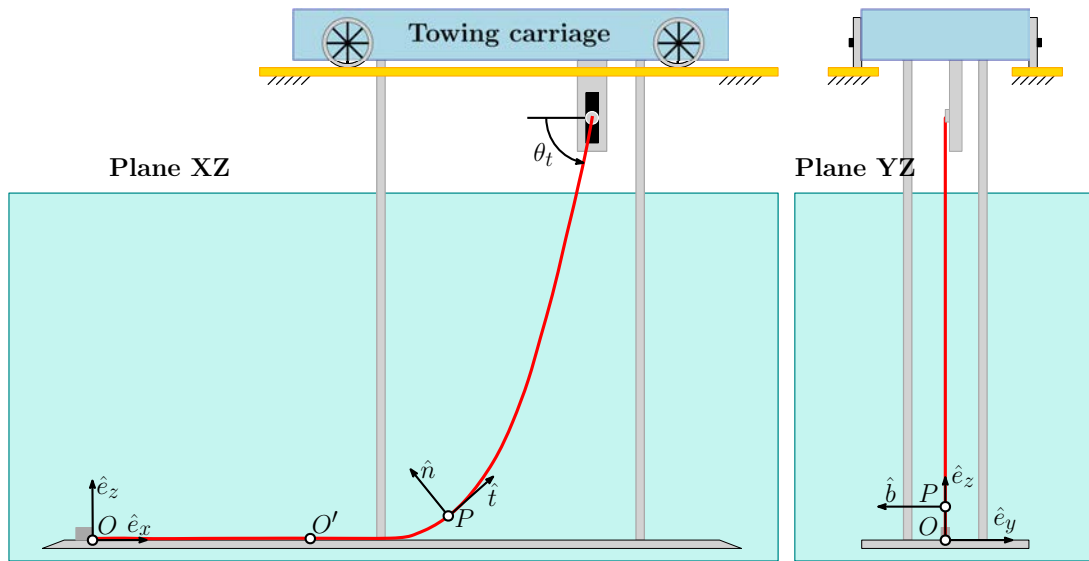
Accordingly, the methodology will be divided into three stages, which refers to the data pre-processing so to obtain the displacement series decomposed into local reference frames, namely TNB, then the modal decomposition and, finally, the post-processing responsible to compute and refine the experimental analysis, leading to the final results.

Algorithms and other specific numerical methods used within the analysis are presented in the Appendix B, aiming to improve the text readability. Always when necessary, the reader will be invited to check a specific method or content there.

For the most part, the data measured by the optical tracking cameras is the targets spatial positions varying in time. The displacement series are obtained with respect to a global Cartesian reference frame, $\Sigma_O = (\hat{e}_x, \hat{e}_y, \hat{e}_z)$, fixed at the anchor point, O ; see Figure 3.13.

Figure 3.13 also depicts the first monitored optical target, point O' , which is placed far away from the anchor point. The former, O' , position was chosen by virtue of numeric estimations on the general model dynamics, aiming to capture the TDZ region kinematics without losing the TDP during any experimental run.

Figure 3.13: Schematic experimental arrangement depicting the adopted reference frames. In detail: Global Cartesian, $\Sigma_O = (\hat{e}_x, \hat{e}_y, \hat{e}_z)$; first monitored optical target, O' ; and local TNB at a generic point, $\Sigma_P = (\hat{t}(s), \hat{n}(s), \hat{b}(s))$.



Source: Developed by the author.

Although the local reference frame will be addressed properly in the following subsection, the reader can already see the TNB at the point P , arbitrarily chosen over the model span. The local frame depends on the point where it is placed on, therefore, it is depicted as $\Sigma_P = (\hat{t}(s), \hat{n}(s), \hat{b}(s))$ with respect to the natural arclength coordinate, s .

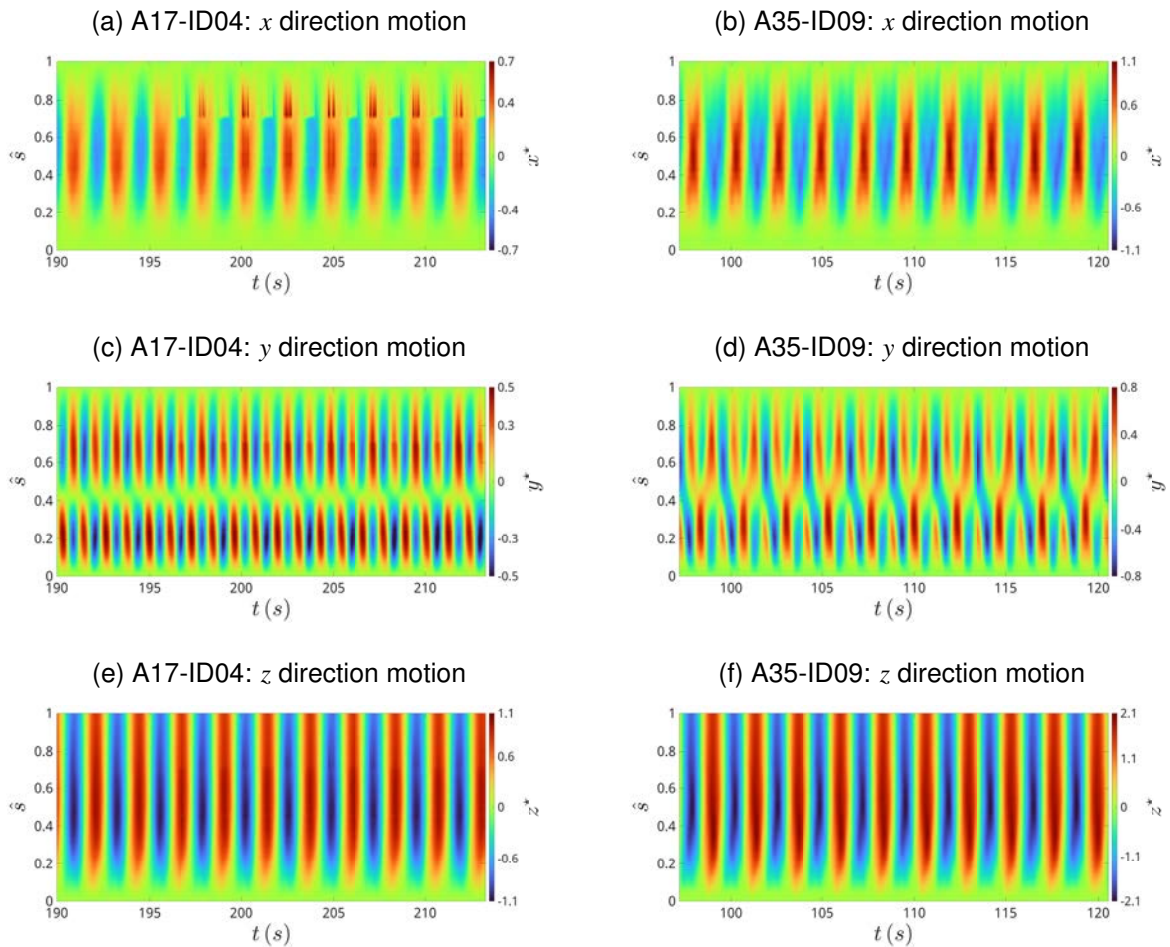
As to illustrate the measured data, Figures 3.14-3.15 display four different experimental tests whose input frequency is kept constant, $f_i^* = 1$, and the imposed amplitude corresponds to the cases 17.5mm, 35mm, 70mm and 105mm.

Interestingly, there is a major difference on the out-of-plane responses presented in Figures 3.14-3.15. The former depicts two different amplitude values of 17.5mm and 35mm, Figures 3.14c-3.14d, respectively, responding more significantly in the first and second out-of-plane modes, modes I and III.

The first mode acts more subtly in the first case, Figure 3.14c, as the second out-of-plane node region is better characterized, whilst in the second case, Figure 3.14d, considerable displacement in the same region can be observed.

This may be attributable to the VSIV synchronization that typically presents a cycle number $N = 2$ for low KC regime. The concomitant existence of $N = 1$ and $N = 2$ in the out-of-plane response could be a result of the fact that multimodal response is expected.

Figure 3.14: Motion spectra in the global reference coordinates of two cases whose the input frequency is kept constant, $f_i^* = 1$, whereas the imposed amplitude varies from 17.5mm to 35mm, corresponding to the cases A17-ID04 and A35-ID09, respectively.

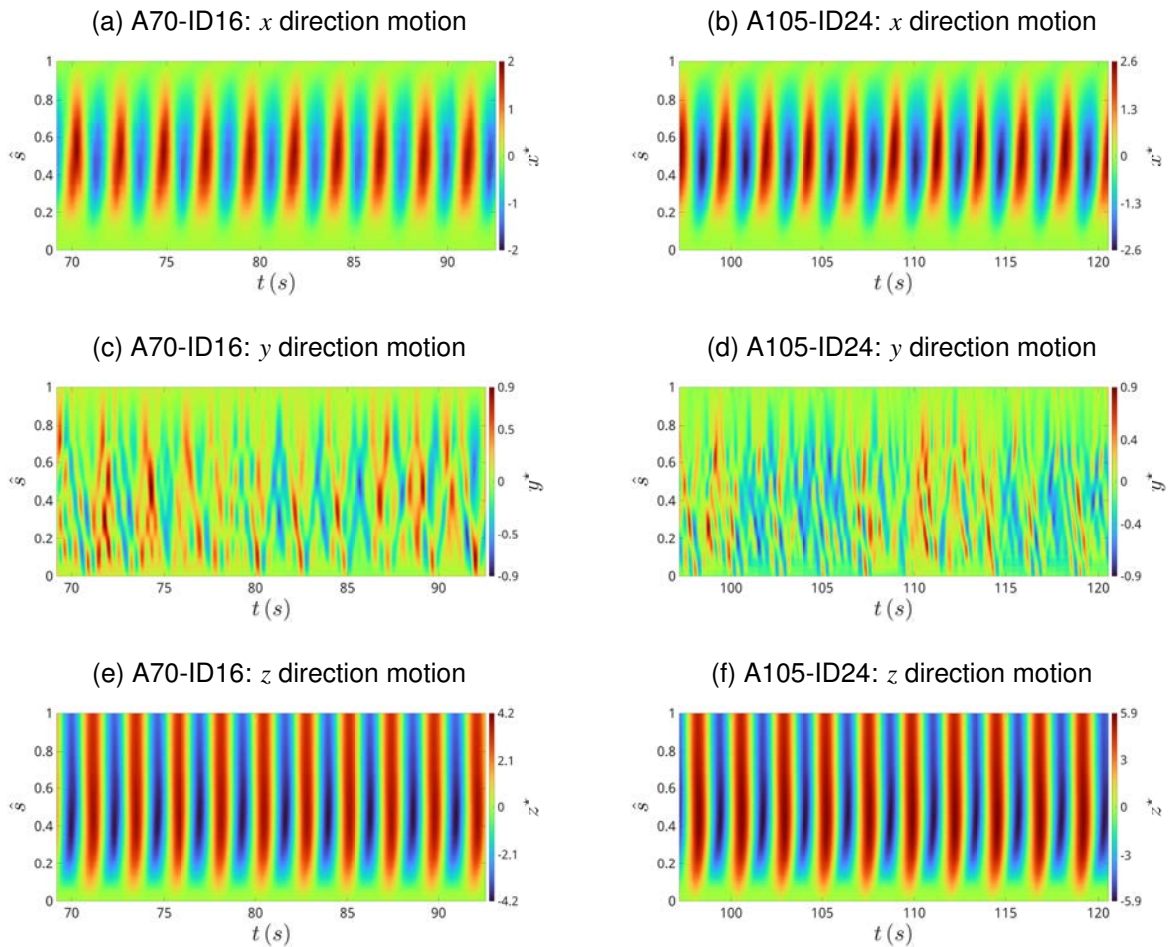


Source: Developed by the author.

Note: The input $f_i^* = 1$ corresponds to the 1st out-of-plane natural frequency (mode I). Additionally, the spectrum intensity was normalized by its own maximum value.

Conversely, the other cases whose the imposed amplitude is larger, 70mm and 105mm, respectively, display a more complex synchronization due to the VSIV; see Figure 3.15. The in-plane motion in both conditions, Figures 3.15a-3.15b and 3.15e-3.15f, shows the same quasi monochromatic behavior as before, Figures 3.14a-3.14b and 3.14e-3.14f, whilst the out-of-plane motion, Figures 3.15c-3.15d, is far more erratic, presenting multimodal response behavior in lieu.

Figure 3.15: Motion spectra in the global reference coordinates of two cases whose the input frequency is kept constant, $f_i^* = 1$, whereas the imposed amplitude varies from 70mm to 105mm, corresponding to the cases A70-ID16 and A105-ID24, respectively.



Source: Developed by the author.

Note: The input $f_i^* = 1$ corresponds to the 1st out-of-plane natural frequency (mode I). Additionally, the spectrum intensity was normalized by its own maximum value.

The out-of-plane response behaviors depicted in Figures 3.14c and 3.15d is also evinced in the spectra presented in Figures 3.12c-3.12d. The amplitude effect on the VSIV response results in a rich synchronization behavior, agreeing with previous works, such as [Fernandes, Mirzaei Sefat, and Cascão \(2014\)](#) and [Wang et al. \(2017\)](#).

The local KC effect on the VSIV dynamics presented in [Wang et al. \(2017\)](#) can be also observable in the present experimental data. Large amplitude regime, as the A105-ID24, displays a slightly different displacement response in the vertical movement at the bottom sag region when the imposed motion is the lift-up or push-down semi cycle, which is an evidence of the TDP variation; see Figures 3.11d and 3.15f in which the lift-up motion (red) is stretched downwards if compared to the push-down

one (blue).

More importantly, there are two main assumptions inherent in the analyses carried out in the present work and they are:

- the out-of-plane motion is considerably smaller than the in-plane one;
- thus, the hydroelastic system is linearized around the its own structural static configuration.

The first assumption can be verified checking the out-of-plane displacements (motion in the y -axis) for they are generally one order smaller than the maximum in-plane amplitude response (motion in the z -axes); see Figures 3.14-3.15.

The second assumption is a consequence of the first one for, albeit highly nonlinear, the out-of-plane motion due to the VSIV can be considered as small amplitudes and angles, hence, its nonlinear behavior is of second order. Moreover, Chatjigeorgiou (2008) had already argued favorably about this assumption, insofar as the static configuration curvature is less relevant in the out-of-plane motion.

Figures 3.14-3.15 also act as an illustration on the measured experimental data, which are 3D displacements at each sampled instant by the optical target tracking cameras. This last discussion also serves as a starting point to the experimental methodology developed in the following texts, as the reader can comprehend two relevant points: firstly, the chosen rational used in order to carry out the experimental analyses; and, lastly, the present work relevance in the state-of-the-art of flexible risers subjected to VSIV.

3.3.1 Raw data pre-processing

The raw data pre-processing methodology focus on the local reference frame attainment, namely the TNB basis, that will be used in order to obtain the correspondent displacement data series in the structural natural coordinates.

As previously discussed, the measured experimental data is given with respect to the global reference frame that differs from the natural coordinates of a spatial curve, which are composed by the tangent, \hat{t} , normal, \hat{n} , and binormal, \hat{b} , unit vectors.

The TNB bases are generally non unique over a spatial curve span and a formal definition could be expressed with respect to the natural coordinate arclength, s , such

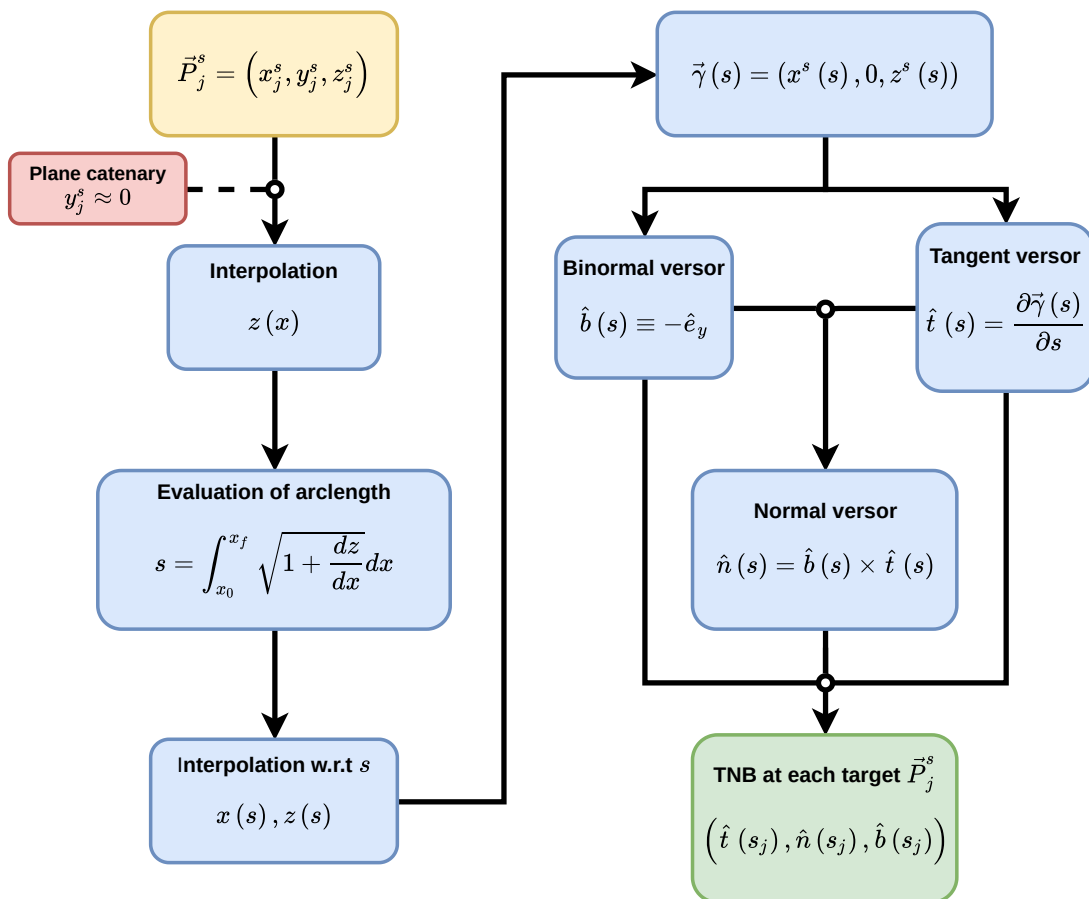
that a local reference frame, Σ_P placed at a material point, P , on the curve is given by

$$\{\Sigma : \mathbb{R} \rightarrow \mathcal{M}_3(\mathbb{R}) \mid s \in [0, L], \Sigma_P = \Sigma(s) = (\hat{t}(s), \hat{n}(s), \hat{b}(s))\}, \quad (3.3)$$

in which $\mathcal{M}_3(\mathbb{R})$ is the matrix vector space of rank 3 over the real numbers body; and L , the curve total length.

Clearly, the spatial curve will be considered as the mean static position measured in the experimental tests with no movement imposed, ID00 in any testing group. Using the natural coordinate, s , the relations so as to obtain each versor can be obtained as function of the curve parametrization and through differential geometry of curves.

Figure 3.16: Flowchart on the evaluation of the local reference frame, TNB, at each monitored target.



Source: Developed by the author.

The main problem is that the experimental static configuration is measured as points in the space and some interpolation should be carried out as to find the curve parametrization.

Consequently, the problem could be divided in two parts: find the curve parametrization algebraic equation with respect to the natural coordinate, $\vec{\gamma}(s)$; obtain the local reference frame, Σ_P , using the curve parametrization.

Figure 3.16 shows the developed strategy in order to evaluate the local basis in any point of the static configuration spatial curve. The flowchart shows that the algorithm is fairly simple, taking advantage of the fact that the curve is planar, $y_j^s \approx 0$ for any point P_j considered in the domain $s \in [0, L]$.

Table 3.8: Fitting curves coefficients used in each experimental group in order to evaluate model arclength and local reference frames.

Curve	Coefficient	$A_i (mm)$			
		17.5	35	70	105
$z(x)$	a_1	15.43	0.40	0.43	0.97
	a_2	-4.14E-02	3.92E-02	3.83E-02	5.90E-03
	a_3	1.86	2.39	2.39	2.33
	a_4	0.20	1.17	1.15	0.78
$x(s)$	b_1	5.90	4.48	4.15	1.31
	b_2	-3.97E-02	-1.62E-02	-7.96E-03	-1.26E-01
	b_3	-5.92	-4.50	-4.16	0.00
	b_4	-0.22	-0.26	-0.27	-
$z(s)$	c_1	5.84	10.42	4.74	2.36
	c_2	5.40E-02	4.14E-02	5.97E-02	4.73E-02
	c_3	1.74	1.82	1.70	1.96
	c_4	0.31	0.23	0.34	0.47

Source: Developed by the author.

Firstly, the natural coordinate should be evaluated for each experimental sampled point, P_j , and the arclength is computed using the classical approach using the curve slope,

$$s_j = \int_0^{x_j} \sqrt{1 + \frac{dz}{dx}} dx,$$

in which the vertical position is interpolated as a function of the horizontal one, $z(x)$. The interpolation function is chosen as a combination of the classical catenary equation flattened by an exponential term,

$$z(x, \mathbf{a}) = a_1 e^{-a_2 x^{a_3}} [\cosh(a_4 x) - 1], \quad (3.4)$$

and the experimental static configuration points are used as to find the coefficients, \mathbf{a} , using a typical nonlinear minimization algorithm available in Matlab[®]. The interpolation function coefficients are presented in Table 3.8.

Table 3.9 brings the model evaluated total length obtained by virtue of Equation 3.4. The numeric total length value, L , is given within a confidence interval (CI 95%) as 4.160m (4.135 to 4.189), which agrees with the measured model total length, 4.150m.

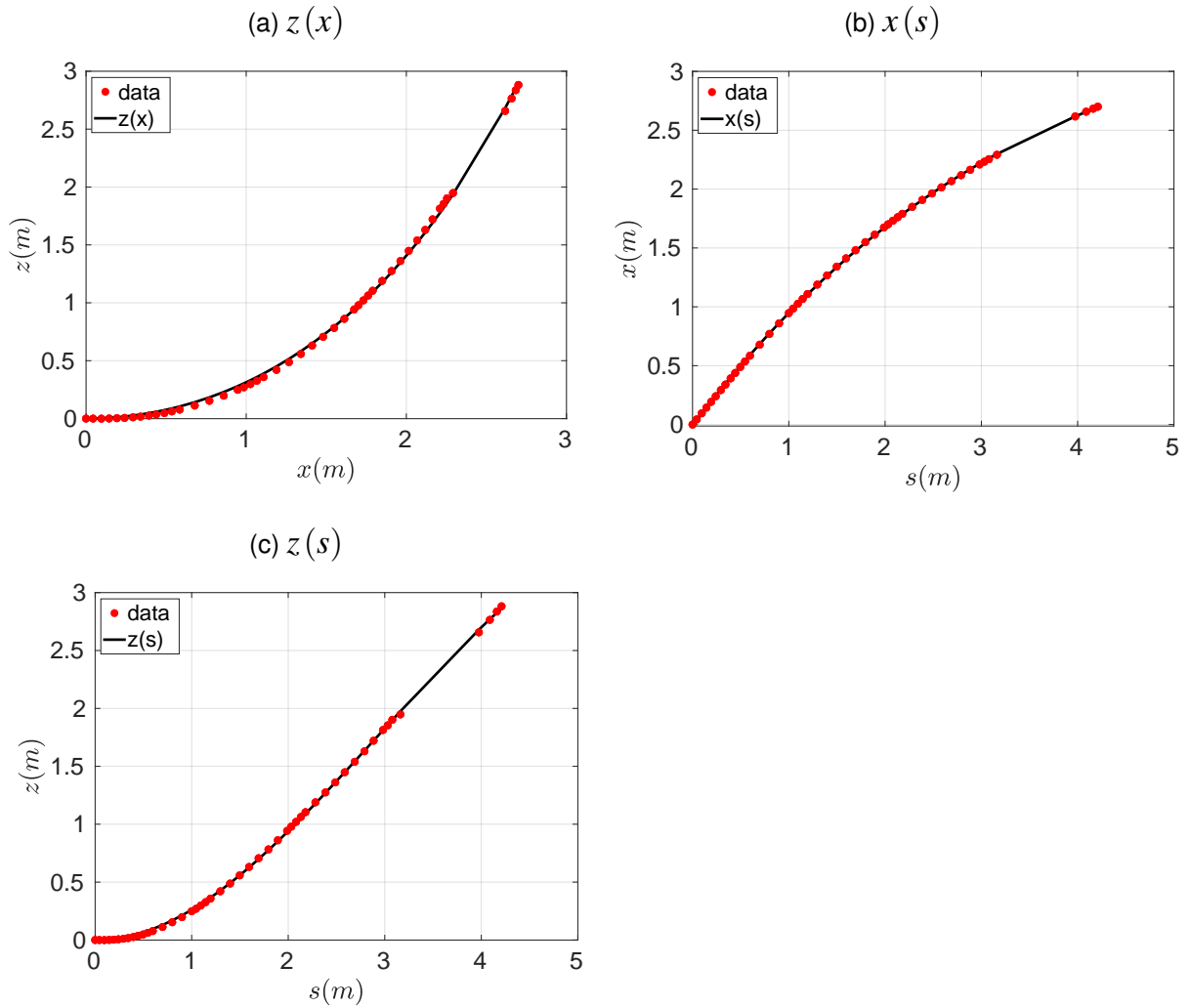
Table 3.9: Targets with poorly measured temporal displacement series and evaluated total length, L , for each testing group using the correspondent interpolation coefficients.

$A_i (mm)$	Bad targets	$L (m)$
17.5	6,12,44	4.1662
35	6,43,44	4.1710
70	29,43,44,45	4.1548
105	31,42,43,44,45	4.1497

Source: Developed by the author.

A quality check on the displacement series was executed for each tracked target and the amount of bad targets for each testing groups is also presented in Table 3.9. The variation on interpolation coefficients shown in Table 3.8 may be attributable to the considered sampled data in each testing group, which varies in number depending on the bad targets amount.

Figure 3.17: Interpolations on the catenary-like model static configuration obtained as to evaluate the arclength, s , and the local reference frame (TNB), $(\hat{t}(s), \hat{n}(s), \hat{b}(s))$.



Source: Developed by the author.

Following, a second fitting curve step with respect to the previous obtained arclength is carried out, $x(s)$ and $z(s)$. The $x(s)$ interpolation used are chosen as a bi exponential function with coefficients \mathbf{b} , whilst the $z(s)$ is the same function used for $z(x)$ with respect to the coefficients \mathbf{c} ; see Equations 3.5-3.6. Figure 3.17 illustrates the fitting curves found for the testing group A70.

$$x(s, \mathbf{b}) = b_1 e^{b_2 s} + b_3 e^{b_4 s} \quad (3.5)$$

$$z(s, \mathbf{c}) = c_1 e^{-c_2 s^{c_3}} [\cosh(c_4 s) - 1] \quad (3.6)$$

Accordingly, the curve parametrization is obtained with respect to the arclength coordinate, as

$$\vec{\gamma}(s) = (x^s(s), 0, z^s(s)), \quad (3.7)$$

and the local reference frame unit vectors can be determined in three steps: firstly, the tangent unit vector is evaluated using $\vec{\gamma}(s)$,

$$\hat{t} = \frac{\partial \vec{\gamma}}{\partial s} = (x^{s'}(s), 0, z^{s'}(s)); \quad (3.8)$$

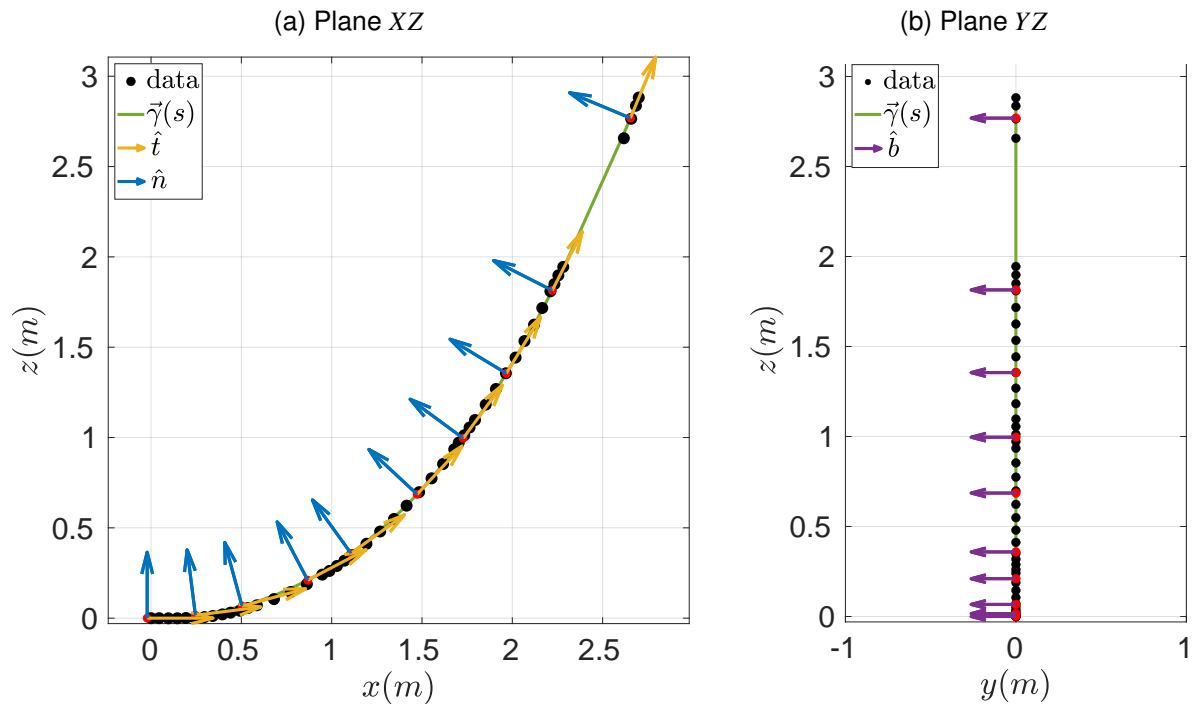
then, taking advantage that in this planar configuration the binormal unit vector is constant, Figure 3.18b,

$$\hat{b} = (0, -1, 0); \quad (3.9)$$

and, finally, the normal unit vector can be found using the previous ones, as the basis is orthonormal,

$$\hat{n} = \hat{b} \times \hat{t}. \quad (3.10)$$

Figure 3.18: Plane catenary-like model static configuration depicting the TNB frame evaluated at some sampled points. Data retrieved from the experimental test A70-ID00.

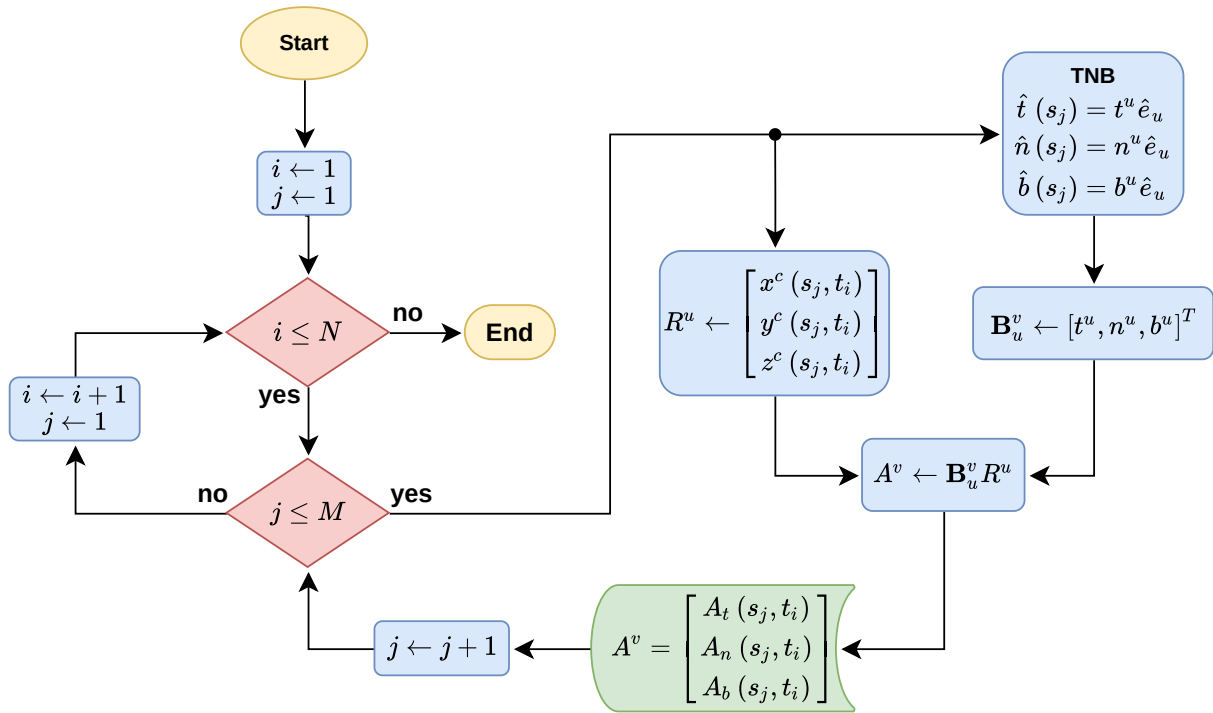


Source: Developed by the author.

Finally, the TNB basis can be computed at each sampled static configuration point by substituting the correspondent arclength value, s_j ; see Figure 3.18. The basis obtained by the previous algorithm, Figure 3.16, is already orthonormal due to the evaluation was done using the curve natural coordinate, s , and no additional normalization step is necessary.

The next step is projecting the 3D displacements series onto the local reference frames obtained previously. Figure 3.19 brings a flowchart on the pseudo-algorithm used as to compute the structural motion with respect to the TNB frames.

Figure 3.19: Flowchart on the algorithm used in the measured data projection into the TNB reference frame.



Source: Developed by the author.

The general algorithm requires two nested recursions containing heavy calculations, one within the other, in order to evaluate the projected position of each monitored target in each time instant. This solution is very time consuming and, thus, an alternative that uses only one recursion is used.

In turn, the inefficient algorithm is best suitable for explaining purposes. The algorithm assumes that the experimental data contains N time instants, t_1, t_2, \dots, t_N , and M monitored targets characterized by their arclength values, s_1, s_2, \dots, s_M .

So as to project the movement onto the local reference frames, the backwards change of basis matrix, $\mathbf{B} = B_u^v$ with $u, v = 1, 2, 3$, is constructed using the TNB unit vectors obtained previously. Such transformation matrix is time independent due to the movement be considered around the structural configuration, which depends solely on the arclength coordinate. The nested recursion algorithm inefficiency arises from the construction of B_u^v for each target at each time instant.

Parallel to the evaluation of B_u^v , the global displacement vector, henceforth called centered displacement vector, $R^u \hat{e}_u$, is computed for each target by subtracting the correspondent static configuration from its displacement series,

$$R(s_j, t_i) = \begin{bmatrix} x^c(s_j, t_i) \\ y^c(s_j, t_i) \\ z^c(s_j, t_i) \end{bmatrix} = \begin{bmatrix} x(s_j, t_i) - x^s(s_j) \\ y(s_j, t_i) - y^s(s_j) \\ z(s_j, t_i) - z^s(s_j) \end{bmatrix}. \quad (3.11)$$

As depicted in Figure 3.19, the local position is simply computed using the centered displacement vector and the transformation matrix, as

$$A^v = B_u^v R^u, \quad (3.12)$$

in which the TNB displacement, $A^v \hat{e}_v$, is composed of the tangent, normal and binormal amplitude responses, A_t , A_n and A_b ⁶, respectively, as

$$A^v = \begin{bmatrix} A_t(s_j, t_i) \\ A_n(s_j, t_i) \\ A_b(s_j, t_i) \end{bmatrix}, \quad (3.13)$$

resuming the recursion algorithm until the end, when every target at all time instants were computed.

Figure 3.20 displays the scalograms and spectra evaluated in the TNB reference frames considering the same case presented in Figures 3.15, 3.15b, 3.15d and 3.15f. As expected the movements registered in the y and binormal directions are equivalently, only differing in sign due to the relation between unit vectors, $\hat{b} = -\hat{e}_y$; see Figures 3.15d and 3.20e.

⁶Alternatively, the normal and binormal displacement may appear as \hat{p} and \hat{q} , respectively.

Figure 3.20: Motion scalograms and spectra in the local reference coordinates considering imposed amplitude of 105mm and input frequency $f_i^* = 1$; alternatively, the case A105-ID24.

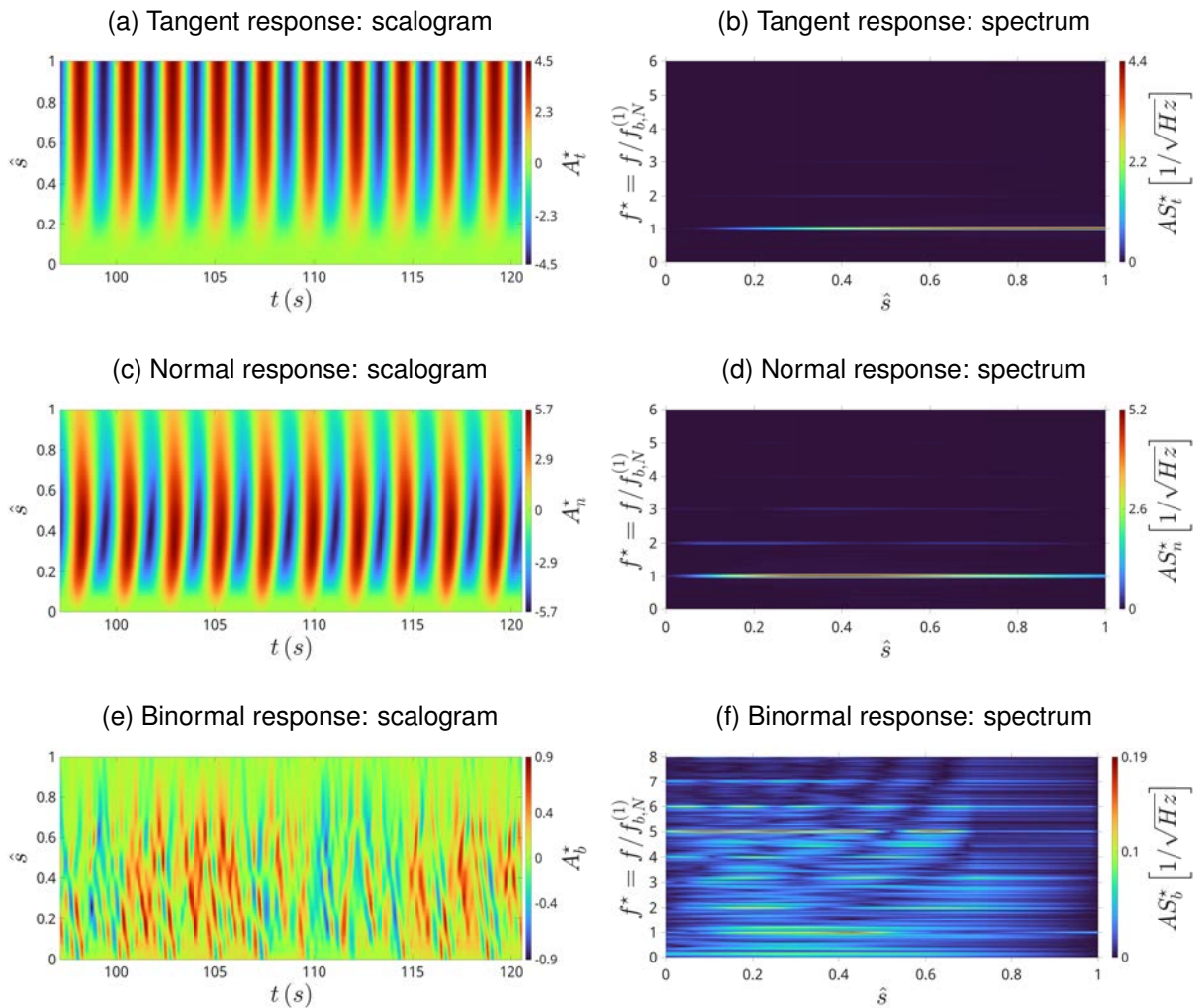
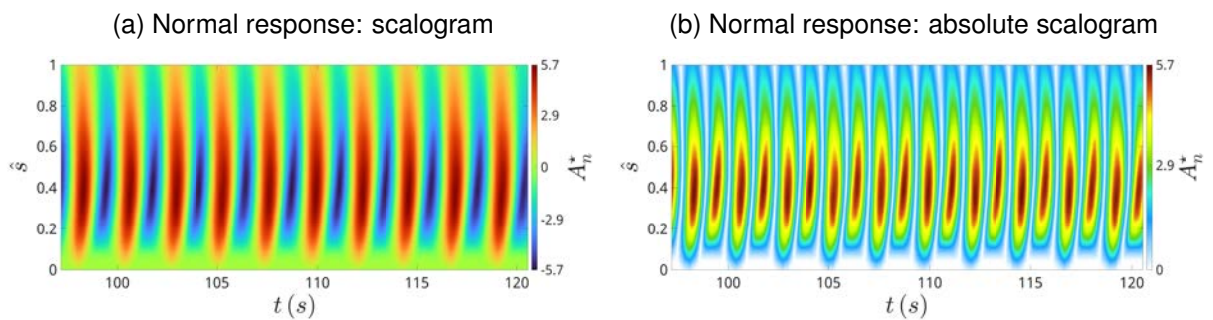


Figure 3.21: Normal displacement and absolute scalograms regarding the previous case, A105-ID24, depicting in detail the TDP variation within a vibration cycle.



Source: Developed by the author.

Note: By virtue of the static configuration curvature due to the apparent weight, the push-down semi-cycle displacement assumes larger absolute values (darker reddish hue).

On the other hand, the in-plane motion evaluated in the local frames presents a more meaningful behavior on the testing dynamics. Particularly, the normal amplitude response shows precisely the TDP variation if compared the push-down (blue) and lift-up intervals at the TDZ (WANG et al., 2017); see Figure fig:Motivation-A105ID24-Normal-Scalogram+Abs.

3.3.2 Modal space and Galerkin's decomposition

The Galerkin's decomposition takes into account a finite number of modes and projects the amplitude responses onto the same modes, obtaining a series of modal amplitude responses. The method is based on the separation of variables technique with generally used in Partial Differential Equations (PDE) problems.

A generic amplitude response, $\mathbf{A}(s, t)$, that varies with respect to position and time is decomposed into two different functions that solely depends on one variable each,

$$\mathbf{A}(s, t) = A(t) \varphi(s), \quad (3.14)$$

therefore, it is possible to consider the original response as a composition of an amplitude temporal series, $A(t)$, and a shape function, $\varphi(s)$.

As a general rule, vibration problems arise from EDPs that assume an infinite number of shape functions, called modal shapes. Each mode is associate with a natural frequency and the modal shapes are ascending sorted, in which the mode associated to the minimum natural frequency is known as the fundamental mode.

Supposing the obtained modes are linear, the exact representation of the amplitude response $\mathbf{A}(s, t)$ should be evaluated as an infinite sum of each modal amplitude associated with its modal shape,

$$\mathbf{A}(s, t) = A^1(t) \varphi_1(s) + A^2(t) \varphi_2(s) + \dots \quad (3.15)$$

This process is equivalently to a typical vector representation in an Euclidean space spanned by unit vectors, \hat{e}_k with $k = 1, 2, \dots$, however, using functions as directions.

This particular subsection deals with the actual modal decomposition procedure and its idiosyncrasies. The modal basis chosen in the previous section is composed of numerical modes obtained by means of an Orcaflex[®] scaled model.

Moreover, it was reasoned about the usage of binormal modes also in the normal decomposition due to the fact that the obtained modes were not representative for the rigid soil used in the experimental arrangement. The justification on the adoption of the binormal modes as to construct the modal basis relied on the results obtained in [Pesce and Martins \(2005\)](#) and [Chatjigeorgiou \(2008\)](#).

Consider that the k -th out-of-plane mode, φ_k with $k \in \mathbb{N}^*$, is a function defined in a real Hilbert vector subspace, V , so

$$\{\varphi_k(s) : \mathbb{R} \mapsto V \subset \mathcal{H}(\mathbb{R}) \mid k \in \mathbb{N}^*, s \in [0, L] \text{ and } \varphi_k(0) = \varphi_k(L) = 0\}, \quad (3.16)$$

thus, the modal basis, \mathcal{B}_∞ , is constructed so that

$$\mathcal{B}_\infty = \{\varphi_1(s), \varphi_2(s), \dots, \varphi_k(s), \dots\}. \quad (3.17)$$

Although the modal basis, \mathcal{B}_∞ , has infinite dimension, the testing model discretization, *i.e.* the amount of monitored targets, limits the number of modes that can be observable in the experimental analysis. Thus, contrarily of the exact value obtained in Equation 3.15, the modal decomposition will evaluate an approximation,

$$\mathbf{A}(s, t) \approx A^k(t) \varphi_k(s), \quad (3.18)$$

considering only a finite basis with $k = 1, \dots, L$,

$$\mathcal{B} = \{\varphi_1(s), \varphi_2(s), \dots, \varphi_k(s), \dots, \varphi_L(s)\}. \quad (3.19)$$

As the modal functions are elements of a Hilbert subspace, $V \subset \mathcal{H}(\mathbb{R})$, it is possible to define their norm, $\|\varphi_k(s)\|$, by means of an inner product, as

$$\|\varphi_k(s)\| = \sqrt{\langle \varphi_k(s), \varphi_k(s) \rangle} \quad (3.20)$$

in which the inner product is evaluated as

$$\langle u, v \rangle = \int_0^L u(s) v(s) ds = \int_0^1 u(\hat{s}) v(\hat{s}) L d\hat{s}. \quad (3.21)$$

Most significantly, the technical literature on modal analysis recommends that the modal basis should be orthonormal in order to uncouple the structural system mass matrix (MEIROVITCH, 1980).

Table 3.10: Orthogonality index evaluated using the Orcaflex[®] binormal modes, $\varphi_n(s)$. Each mode norm is in the diagonal.

Modes	Out-of-plane modes				
	1 st	2 nd	3 rd	4 th	5 th
1 st	1.9035	1.71E-05	-2.29E-05	1.91E-05	-5.04E-05
2 nd	1.71E-05	1.6682	3.62E-05	-3.34E-05	6.22E-05
3 rd	-2.29E-05	3.62E-05	1.6386	8.88E-05	-1.13E-04
4 th	1.91E-05	-3.34E-05	8.88E-05	1.6626	1.58E-04
5 th	-5.04E-05	6.22E-05	-1.13E-04	1.58E-04	1.6895
6 th	6.00E-05	-9.40E-05	1.38E-04	-1.71E-04	2.26E-04
7 th	-6.81E-05	8.92E-05	-1.48E-04	2.21E-04	-2.82E-04
8 th	6.50E-05	-1.33E-04	1.92E-04	-2.70E-04	3.14E-04
9 th	-8.82E-05	1.37E-04	-2.05E-04	3.15E-04	-3.84E-04
10 th	7.22E-05	-1.77E-04	2.25E-04	-3.25E-04	4.00E-04

Modes	Out-of-plane modes				
	6 th	7 th	8 th	9 th	10 th
1 st	6.00E-05	-6.81E-05	6.50E-05	-8.82E-05	7.22E-05
2 nd	-9.40E-05	8.92E-05	-1.33E-04	1.37E-04	-1.77E-04
3 rd	1.38E-04	-1.48E-04	1.92E-04	-2.05E-04	2.25E-04
4 th	-1.71E-04	2.21E-04	-2.70E-04	3.15E-04	-3.25E-04
5 th	2.26E-04	-2.82E-04	3.14E-04	-3.84E-04	4.00E-04
6 th	1.7360	3.42E-04	-3.83E-04	4.62E-04	-4.82E-04
7 th	3.42E-04	1.7542	4.44E-04	-5.45E-04	6.06E-04
8 th	-3.83E-04	4.44E-04	1.7679	6.04E-04	-7.23E-04
9 th	4.62E-04	-5.45E-04	6.04E-04	1.8518	7.65E-04
10 th	-4.82E-04	6.06E-04	-7.23E-04	7.65E-04	1.7874

Source: Developed by the author.

Albeit an additional step, the attainment of an orthonormal basis aids in the modal decomposition algorithm, and, by virtue of uncoupling the mass matrix, there is no

cross-modal added mass coefficients, which is desirable if one wants to deal with the modal added mass coefficients values.

Accordingly, a rising concern comes from the fact that it is not guaranteed that the chosen modal functions computed in Orcaflex[®] are in fact orthonormal. As a general rule, numeric modes are not necessarily orthogonal⁷, whereas in some cases they may be quasi-orthogonal insofar as the lower modes, for instance the ones presented in Figure 3.9d and Table 3.4, which are quasi-sinusoidal.

Table 3.10 shows the orthogonality index calculated for all out-of-plane modes pair, including their norm depicted in the diagonal. As expected, the binormal modes are quasi-orthogonal to one another two-by-two and this may be attributable to the aforementioned reasons, even so they are not normalized.

For that reason, the Modified Gram-Schmidt (MGS) orthonormalization algorithm is employed as to obtain orthonormal out-of-plane modes based on the Orcaflex[®] ones. Inasmuch as the modes were already quasi-orthogonal, there are little differences on the orthonormal mode functions shape with respect to the original ones.

Table 3.11: Orthogonality index evaluated using the Orcaflex[®] binormal modes after orthonormalization process, $\hat{\phi}_n(s)$. Each mode norm is in the diagonal. Any cross coefficient is of order $\mathcal{O} \sim 10^{-17}$ and, practically, considered null.

Modes	Out-of-plane modes									
	1 st	2 nd	3 rd	4 th	5 th	6 th	7 th	8 th	9 th	10 th
1 st	1.00	0	0	0	0	0	0	0	0	0
2 nd	0	1.00	0	0	0	0	0	0	0	0
3 rd	0	0	1.00	0	0	0	0	0	0	0
4 th	0	0	0	1.00	0	0	0	0	0	0
5 th	0	0	0	0	1.00	0	0	0	0	0
6 th	0	0	0	0	0	1.00	0	0	0	0
7 th	0	0	0	0	0	0	1.00	0	0	0
8 th	0	0	0	0	0	0	0	1.00	0	0
9 th	0	0	0	0	0	0	0	0	1.00	0
10 th	0	0	0	0	0	0	0	0	0	1.00

Source: Developed by the author.

⁷Depending on the numeric method used as to evaluate the FE modal analysis, the obtained eigenvectors can display some degree of orthogonality, specially if algorithms as QR-decomposition are used.

Consequently, the main difference is their amplitude values, which are normalized by the correspondent mode norm; see the diagonal coefficients in Table 3.10. Accordingly, Table 3.11 displays the orthogonality index of the binormal modes set and their norm in the diagonal. The cross coefficients are considered null, in lieu of their approximate values ($\mathcal{O} \sim 10^{-17}$), and the norms are unitary.

Resuming the modal decomposition, the procedure is executed projecting the instantaneous amplitude value onto each mode function in $\hat{\mathcal{B}} = \{\hat{\phi}_1(s), \dots, \hat{\phi}_{10}(s)\}$. Whereas the modal basis is now orthonormal, the k -th modal amplitude may be evaluated as

$$A^k(t) = \frac{\langle \mathbf{A}(s,t), \hat{\phi}_k(s) \rangle}{\|\hat{\phi}_k(s)\|} \frac{\hat{\phi}_k(s)}{\|\hat{\phi}_k(s)\|} = \langle \mathbf{A}(s,t), \hat{\phi}_k(s) \rangle \hat{\phi}_k(s), \quad (3.22)$$

for each one of the ten out-of-plane modes considered, $k = 1, \dots, 10$. Accordingly, the amplitude response may be reconstructed using the approximation described in Equation 3.18, as

$$A(s,t) \approx A^k(t) \hat{\phi}_k(s) = \sum_{k=1}^{10} A^k(t) \hat{\phi}_k(s), \quad (3.23)$$

in which the modal ROM is characterized by the one variable functions $A^k(t)$ and $\hat{\phi}_k(s)$.

3.3.3 Results post-processing

As to follow the experimental analysis, it is necessary to define the nomenclature that is going to be used in the present work. There are several sub- and superscripts related to the modal response executed in the normal or binormal direction and they can be easily mistaken.

The nomenclature, albeit a little cumbersome at first, is straightforward to use for superscripts in parentheses always represents which mode is being considered, whereas subscripts display orientation planes, such as \square_n and \square_b , in which \square is a generic variable representation in the normal and binormal directions, respectively. Moreover, the superscripts $\square^{(d)}$ and $\square^{(s)}$ relate to the ‘‘Dominant’’ and ‘‘Sub-dominant’’ modes, respectively.

The dominant (sub-dominant) mode presents the largest amplitude peak value (second largest) and the subscript \square_N is reserved to ‘‘Natural’’ as in natural frequency.

The former will be presented as superscripts between parenthesis, whilst the latter, as subscript placed after the correspondent direction, n or b .

Particularly, the in-plane normal and out-of-plane binormal modes will be addressed using $j = 1, \dots, 10$ and $k = 1, \dots, 10$ indexes, respectively, when necessary to differentiate both in-plane and out-of-plane modes. Otherwise, the same superscript k will be used.

The dominant frequency of any given response is evaluated using its spectrum, finding the frequency slot that corresponds to the maximum peak value, so that

$$f_{n,dom}^{(j)} \Leftrightarrow \max_f \left\{ |AS_n^j(f)| \right\},$$

$$f_{b,dom}^{(k)} \Leftrightarrow \max_f \left\{ |AS_b^k(f)| \right\}.$$
(3.24)

Accordingly, the sub-dominant frequency is found by means of the second largest peak value.

Even though the in-plane normal amplitude series presents a polichromatic spectrum, the response is usually characterized by a dominant peak at a certain frequency value, which is defined as a dominant frequency. For instance, the j -th dominant frequency of a given normal response will be denoted as $f_{n,dom}^{(j)}$, whose notation carries a subscript indicating it.

It is noteworthy that the word dominant is being used in two different context: as a superscript to indicate the dominant mode, *i.e.* the one assuming the largest displacement; and also as a subscript to denote the dominant frequency of a given response.

Both usages ought not to be mistaken, since they can be used concomitantly, denoting the dominant frequency of the dominant (sub-dominant) modal response, $f_{n,dom}^{(d)}$ ($f_{n,dom}^{(s)}$).

It is also the case that normalized quantities are displayed with the superscript \square^* , which, if necessary, is going to be placed after the modal number in parentheses, $\square^{(k)*}$.

Table 3.12 brings an illustration on the devised nomenclature, considering as example the nominal and normalized amplitude responses, and natural frequency for the j, k -th, dominant and sub-dominant modes.

The only input in the hydroelastic system is the imposed movement at the hang-off point and the normal and binormal dynamical behaviors are a response of the system input. The general 3D flow around the cylinder couples both normal and binormal movements for one is affected by the other.

Table 3.12: Illustration on the modal nomenclature used in the present work.

Quantity	Mode	Symbol	
		Normal	Binormal
Amplitude response	j, k -th	$A_n^{(j)}$	$A_b^{(k)}$
	Dominant	$A_n^{(d)}$	$A_b^{(d)}$
	Sub-dominant	$A_n^{(s)}$	$A_b^{(s)}$
Normalized amplitude response	j, k -th	$A_n^{(j)*}$	$A_b^{(k)*}$
	Dominant	$A_n^{(d)*}$	$A_b^{(d)*}$
	Sub-dominant	$A_n^{(s)*}$	$A_b^{(s)*}$
Natural frequency	j, k -th	$f_{n,N}^{(j)}$	$f_{b,N}^{(k)}$
	Dominant	$f_{n,N}^{(d)}$	$f_{b,N}^{(d)}$
	Sub-dominant	$f_{n,N}^{(s)}$	$f_{b,N}^{(s)}$
Dominant frequency	j, k -th	$f_{n,dom}^{(j)}$	$f_{b,dom}^{(k)}$
	Dominant	$f_{n,dom}^{(d)}$	$f_{b,dom}^{(d)}$
	Sub-dominant	$f_{n,dom}^{(s)}$	$f_{b,dom}^{(s)}$

Source: Developed by the author.

In turn, the in-plane measurements unveil that the out-of-plane dynamics has a second order effect on it which may be attributable to the latter amplitude values be of lesser order than the former. Thus, it is possible to make an ansatz in which the binormal motion should be a consequence of the normal hydrodynamic loads due to the VSIV, the normal motion should not be affected by the binormal dynamics.

This assumption is a strong constrain that sets a causality relation on the hydroelastic system for the normal motion is regarded as an equivalent input that causes the out-of-plane movement and, at the same time, removes any flow effect that would let the former dynamics depends on the latter.

Although being a strong assumption, the causality relation, which may be summarized as

$$A_n(s, t_{i+1}) = f(t_i, A_n(s, t_i), \dot{A}_n(s, t_i)) \quad (3.25)$$

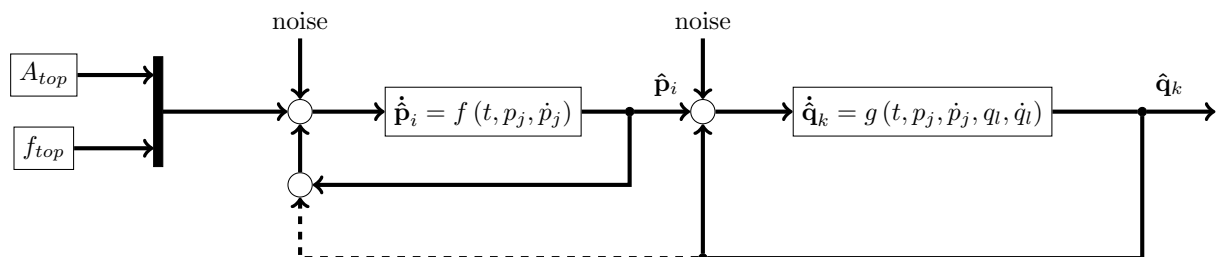
$$A_b(s, t_{i+1}) = g(t_i, A_n(s, t_i), \dot{A}_n(s, t_i), A_b(s, t_i), \dot{A}_b(s, t_i)),$$

is defensible by virtue of the out-of-plane motion always being lesser in value than the one measured in-plane. Note that the true input, characterized by A_i and f_i^* (imposed motion), is the responses through their explicit dependence on time.

In particular, considering the most critical case whose input amplitude and frequency are $A=105\text{mm}$ and $f^* = 1$, in which the in-plane motion presents the largest amplitude values, the measured out-of-plane displacement is still about a order less in value; see Figure 3.20.

Alternatively, Figure 3.22 also depicts the causality assumption adopted, displaying as a dashed line the weak effect of the binormal response in the normal one. Here, the notation used differs slightly from the previous one and the normal and binormal response states are presented as \hat{p}_i and \hat{q}_k , respectively, in which the indexes refer to monitored targets.

Figure 3.22: Causality between normal and binormal responses depicted as a block diagram.



Source: Developed by the author.

Note: In the block diagram, the normal and binormal amplitude responses are presented as \hat{p} and \hat{q} , respectively.

Another fact that may support the causality ansatz is that the in-plane normal motion is generally quasi-monochromatic, presenting a dominant frequency equal or close to the imposed movement one (or an integer multiple of it).

Furthermore, upon checking Figure 3.20d, it is possible to verify that there is no frequency registry of a typical VSIV response, which is characterized by the cycle number, N (SUMER; FREDSE, 1988; FERNANDES; MIRZAEI SEFAT; CASCÃO, 2014); e.g. the dominant $N = 5$ found in the out-of-plane motion (Figure 3.20f).

Complementary to the temporal modal amplitude registry from which spectra and synchronization features can be analyzed, the evaluation of a mean modal amplitude value is important in order to characterize the VSIV response.

The signals are supposed zero-average ones and their mean amplitude response will be evaluated by means of its Root Mean Square (RMS) value multiplied by a factor of $\sqrt{2}$,

$$A^{(k)} = \sqrt{2} \left\langle A^{(k)}(t) \right\rangle_{rms}, \quad (3.26)$$

in which the temporal interval is fixed in size, being a total of 4096 samples taken from the instant $T = 2T_f/5$ onward with T_f representing the experiment total time. The factor $2/5$ was chosen upon inspection of all experimental data in order to remove their transitory response stage.

It is noteworthy that, as to avoid turning the adopted nomenclature more inconvenient and cumbersome, the k -th peak amplitude response will be represented by $A^{(k)}$ (alternatively the peak-to-peak amplitude, $2A^{(k)}$) and, when necessary to discuss its temporal registry, it will be explicitly shown its time dependence, $A^{(k)}(t)$.

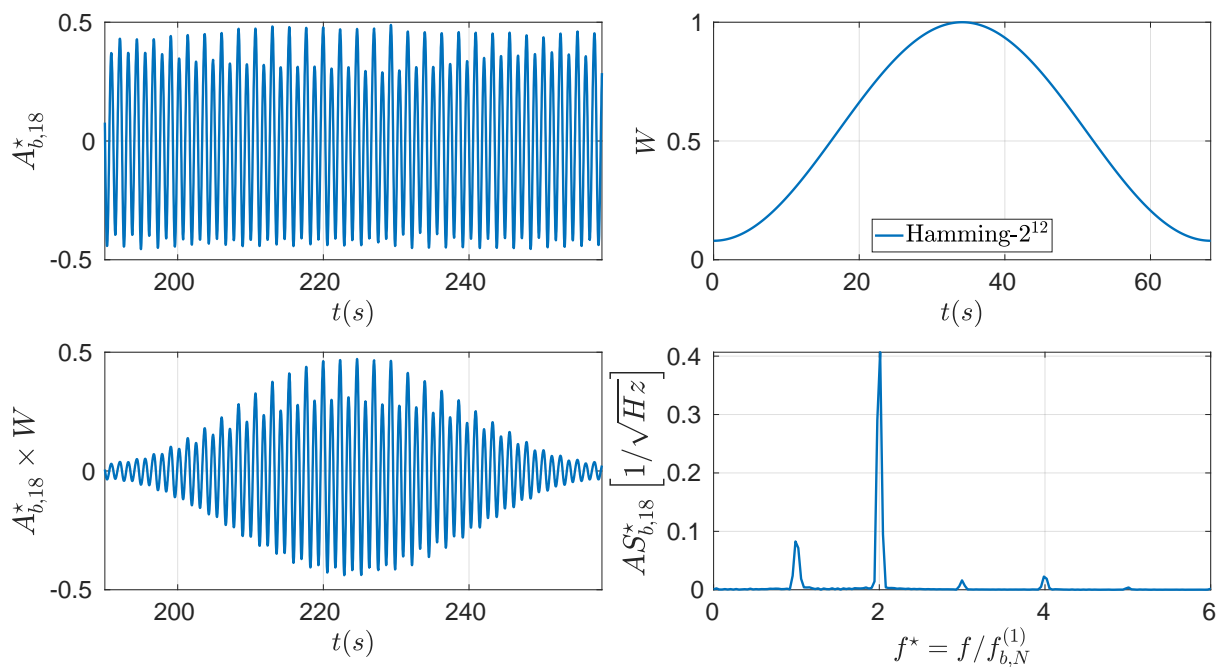
The measured and computed experimental data will be always filtered using a typical FIR digital filter in order to attenuate high frequency noise that could cause aliasing. More information on the filtering algorithm employed can be found in Appendix B.3.

Although the hydroelastic system is highly nonlinear, the frequency domain analyses are carried out using Fast Fourier Transform (FFT). The choice of employing the FFT comes from the sampling frequency value, F_s , being large enough with respect to the VSIV response frequency range, avoiding significant discrepancies between the results obtained employing FFT or other frequency analysis method, such as the Hilbert-Huang Transform (HHT).

Inasmuch as the Hamming window presents nonzero values at its end points, little leakage effect may occur during the frequency response evaluation. In turn, it can be argued that the Hamming window is employed due its high accuracy in isolating frequency peaks that may occur in the neighborhood of other peak.

This feature can be easily verified as the Hamming window frequency response shows a large gain at zero that is rapidly attenuated reaching up to $-300dB$. Hence, any additional frequency peak in the vicinity of other is attenuated by virtue of the windowing procedure in time domain equivalently to a convolution in the frequency domain.

Figure 3.23: Out-of-plane spectrum response attainment of a mid-span target (18) considering the testing case whose amplitude is $A_i = 17.5mm$ and $f^* = 1$ (A17-ID04). In detail: the temporal response ($A_{b,18}^*$); the Hamming window employed (W); the computed windowed response ($A_{b,18}^* \times W$); and the correspondent amplitude spectrum ($AS_{b,18}^*$).



Source: Developed by the author.

An illustration on the procedures carried out in order to attain any of the responses spectra is displayed in the Figure 3.23. As it can be verified, the resonating frequency peaks present good resolution, which is characterized by their thin shape and small width.

Furthermore, the amplitude spectrum is evaluated single-banded, showing the

peak amplitude response of the analyzed signal. Thus, each peak magnitude represents the actual amplitude associated to that frequency term in their Fourier series.

3.3.4 Governing parameters and their modal counterparts

It is known that the VSIV shows a characteristic behavior with respect to some hydrodynamic parameters, such as the reduced velocity, V_R , synchronization cycle, Keulegan-Carpenter and Reynolds numbers, N , KC and Re , respectively.

In fact, previous studies carried out in [Le Cunff, Biolley, and Damy \(2005\)](#) and [Fernandes, Mirzaei Sefat, and Cascão \(2014\)](#) have unveiled the similarity on the VSIV and the dynamics behavior found with cylinders subjected to oscillatory flow, thoroughly studied in [Sarpkaya \(1976\)](#), [Sumer and Fredsøe \(1988\)](#), and [Kozakiewicz, Sumer, and Fredsøe \(1994\)](#).

Although their analysis focused mainly on the space of configuration, [Le Cunff, Biolley, and Damy \(2005\)](#) had already executed a proto modal analysis, using wavelets, as to determine locally which would be the dominant modal response due to the necessity of finding a characteristic natural frequency on the V_R evaluation.

The following works on VSIV also employed the same analysis methodology, based on reduced velocity, showing its strong effect on the hydroelastic response. Most importantly, whereas the natural frequency was evaluated with respect to modal analysis, the definition of a characteristic KC was carried out by means of the maximum value measured withing the structural span.

Thus, this hybrid analysis methodology, using both modal and space of configuration characterization, shows some limitations on the $KC(s)$ distribution along the riser span for it is considered as fixed parameter, disregarding if the local values occurs in a narrow or broad range.

[Wang et al. \(2017\)](#), for instance, argued that the local $KC(s)$ regime has a strong and direct impact over the structural dynamics, presenting evidences that, below the critical $KC = 39$ value, the local $KC(s)$ distribution may contribute to the vortex diffusion along the span and 3D flow effects turn out to be important, meaning that a typical strip assumption is not valid.

In other words, as the $KC(s)$ distribution shows similar values all over the structure, it is not possible to characterize the dominant mode natural frequency very well, and thus the reduced velocity. This may be attributable to the amplitude response along the

span being of the same order and, as a consequence, the multimodal response would lead to distinct modes being quasi-dominant in different regions, specially the bottom sag in which the fatigue response is critical.

Hence, it would be beneficial to the experimental analysis to avoid using the space of configuration due to the huge amount of DOF in the structural model, or, equivalently, mixing global (modal methodology) and local dynamics characteristics on the hydroelastic response.

Within this context, the present experimental methodology adopts a global dynamics characterization, using the modal decomposition as spacial filter that evaluates mean amplitude values as to find similarity on the VSIV response. Consequently, when considering the modal representation, there is no longer the use of local and global values as in the aforementioned hybrid analysis.

Moreover, the modal decomposition produces ROMs taking into consideration only the most representative modes within it. The local dynamics may be also easily retrieved using modal reconstruction, summing each mode contribution at any point on the riser span.

Therefore, it is of utmost importance to characterize the hydroelastic governing parameters in the modal domain, *i.e.* V_R , N , KC and Re , amid others. This task is not trivial by virtue of, as already discussed, the only true system input is the external forced movement at the hang-off point, which causes the in-plane and out-of-plane dynamics.

In turn, the VSIV is a consequence of the driving motion and there is a complex causality relation between the observed in-plane and out-of-plane responses. Therefore, the VSIV presented in a catenary-like structure differs tremendously from that measured using a rigid straight cylinder, as it is not possible to identify in-plane motion as solely responsible for the out-of-plane oscillations.

Although the normal motion in the plane is a direct response of the imposed excitation, the ansatz that it acts as the driving mechanism for the binormal oscillation is necessary as a starting point of the analysis. Extending the govern parameters to their modal counterparts is not trivial due to the abstract leap necessary to link the space of configuration and the modal domain.

Notwithstanding, in the multimodal response context, the reduced velocity may present a more tangible meaning in the modal domain, since the natural frequency

evaluation in flexible structure requires modal analysis in some degree (LE CUNFF; BIOLLEY; DAMY, 2005).

It is certainly true that each mode is characterized by an unique natural frequency value and, hence, the modal reduced velocity parameter can be evaluated as

$$V_R^{(j,k)} = \frac{U_n^{(j)}}{Df_{N,b}^{(k)}} \sim \frac{2\pi A_n^{(j)} f_{n,dom}^{(j)}}{Df_{b,N}^{(k)}}, \quad (3.27)$$

in which the modal in-plane normal velocity, $U_n^{(j)}$, can be approximated as $2\pi A_n^{(j)} f_{n,dom}^{(j)}$, since the normal amplitude response is generally quasi-monochromatic with dominant frequency given by $f_{n,dom}^{(j)}$.

The term $2\pi A_n^{(j)}/D$ in Equation 3.27 resembles closely a modal Keulegan-Carpenter number considering that the in-plane normal movement is monochromatic. It is certainly the case that the normal modal amplitude is quasi monochromatic, thus, the j -th equivalent modal $KC^{(j)}$ could be defined as

$$KC^{(j)} = \frac{U_n^{(j)}}{Df_{n,dom}^{(j)}} \sim \frac{2\pi A_n^{(j)}}{D} = 2\pi A_n^{(j)*}, \quad (3.28)$$

which can be used in Equation 3.27 as to obtain the modal reduced velocity with respect to the modal Keulegan-Carpenter number, $KC^{(j)}$, and a frequency ratio between the in-plane motion dominant frequency, $f_{n,dom}^{(j)}$ and an out-of-plane eigenvalue, $f_{b,N}^{(k)}$, so that

$$V_R^{(j,k)} = KC^{(j)} \frac{f_{n,dom}^{(j)}}{f_{b,N}^{(k)}}. \quad (3.29)$$

The modal Reynolds' number can be also obtained with respect to the modal Keulegan-Carpenter parameter,

$$Re^{(j)} = \frac{U_n^{(j)} D}{\nu} = \frac{KC^{(j)} f_{n,dom}^{(j)} D^2}{\nu}, \quad (3.30)$$

in which ν is the fluid kinematic viscosity.

Another important nondimensional parameter is the cycle number, N , that is the

number of vibrations in one cycle of the oscillating flow (SUMER; FREDSE, 1988). Using the proposed causality ansatz, the cycle number should be the ratio between the amount of out-of-plane vibrations in one in-plane cycle.

In this context, it is chosen the dominant k -th in-plane mode frequency and the bi-normal k -th amplitude series frequency response in order to evaluate the cycle number as

$$N^{(k)} = \frac{f_b^{(k)}}{f_{n,dom}^{(k)}}. \quad (3.31)$$

Other governing parameters, such as Strouhal's and Roshko's numbers, and added mass, just to cite a few, can be obtained likewise, using the concepts of dominant mode, dominant frequency and modal peak amplitude.

However, it is not possible to guarantee that the currently known experimental relations and regimes for each one of these parameters hold true in the modal domain.

Following the VSIV analysis devised in Sumer and Fredsøe (1988), the modal reduced velocity, $V_R^{(j,k)}$, modal Keulegan-Carpenter, $KC^{(j)}$, and modal cycle number, $N^{(k)}$, could be suffice to characterize the experimental responses available in the present analysis.

Consequently, the VSIV modal domain Buckingham's Π analysis leads to the dimensionless governing parameters,

$$\begin{aligned} A_b^{(k)\star} &= F\left(KC^{(j)}, Re^{(j)}, V_R^{(j,k)}, \dots\right), \\ N^{(k)} &= G\left(KC^{(j)}, Re^{(j)}, V_R^{(j,k)}, \dots\right), \end{aligned} \quad (3.32)$$

in which it is being chosen a combination of governing parameters that encompasses at least three of the most important quantities in the hydroelastic system so as to characterize the fluid-structure interaction: the structural out-of-plane eigenvalue, $f_{b,N}^{(k)}$; the fluid kinematic viscosity, ν ; the imposed motion frequency, $f_{n,dom}^{(j)}$.

It is noteworthy that the hydroelastic phenomenon depends on other parameters along the model span, such as: shedding frequency; cylinder surface roughness, geometry and specific weight; structural damping; flow turbulence; added mass, drag and

lift coefficients; soil stiffness, to cite a few; see Table 3.1 and (SARPKAYA; RAJABI, 1979).

Furthermore, the present database, albeit extensive, has its own limitations and the fundamental group of nondimensional parameters available in the current analysis must be obtained by grouping the aforementioned parameters in a physical and rational way using the Buckingham's II theorem.

For instance, the modal reduced velocity resembles a second order tensor that has direct components ($j = k$) and other cross terms that take into consideration the effect of j -th in-plane mode to all other binormal modal responses ($j \neq k$). Additionally, the modal KC depends on both the imposed motion at the hang-off point, frequency and amplitude, and the mode chosen to be studied.

Particularly, the variation due to choosing an in-plane normal mode is more pronounced than the one caused by the imposed motion, insofar as each mode generally has a very characteristic amplitude parcel in the response modal reconstruction of a considered test. Thus, the modal reduced velocity "tensor" components vary considerably with respect to the plane mode due to the $KC^{(j)}$ values for each mode in a given test.

Contrarily to fundamental results obtained with rigid straight cylinders (SUMER; FREDSSØE, 1988; FERNANDES; MIRZAEI SEFAT; CASCÃO, 2014), the modal KC is not fixed due to the in-plane response dependence on the driving frequency. This behavior may be attributable to the exciting frequency being able occur in the sub-resonant, resonant or super-resonant regime, depending on the plane natural frequencies values.

More importantly, the modal KC is not a fixed input parameter, but a response of the nonlinear hydroelastic dynamics. Consequently, choosing the modal reduced velocity as a governing parameter is not ideal due to its direct dependence on the modal KC.

Rearranging the parameters using Buckingham's II theorem in Equation 3.29 unveils the nondimensional parameter $f^{(j,k)\star}$, such that

$$f^{(j,k)\star} = \frac{V_R^{(j,k)}}{KC^{(j)}} = \frac{f_{n,dom}^{(j)}}{f_{b,N}^{(k)}}, \quad (3.33)$$

in which the modal KC variation is removed from the analysis nondimensional group. A closer inspection on the new governing parameter reveals that the term is a reinter-

pretation on the nondimensional driving frequency parameter commonly used in forced linear system dynamics.

Interestingly, the reduced velocity was firstly used in the VSIV context due to the VIV heavy influence on it. As argued in the previous chapter, even though the VIV plays an important role in the VSIV analysis since both phenomena share some similarities, the VSIV is unique and presents a great deal of idiosyncrasies that cannot be found in the VIV.

The other way around, the VSIV is caused by a driving motion in a complex non-linear hydroelastic system and the relation obtained in Equation 3.33 is nothing but a reinterpretation on frequency ratio found in the most fundamental case of a forced dynamical system.

It is important to point out that, although the in-plane motion is being used as a driving mechanism to the out-of-plane movement (causality assumption), it is still a response obtained from the hydroelastic system. Consequently, not only the modal KC varies, as already discussed, but also the dominant plane response frequency, $f_{n,dom}^{(j)}$, evaluated to a particular in-plane response may vary for each test.

For the most part, the dominant normal response frequency assumes values near the driving one at the hang-off point. Notwithstanding, in some cases, it was observed that another harmonic of the driving frequency showed to be dominant.

Frequency domain analysis will be thoroughly presented in the next chapter, but, in general, this variation occurred in few cases whose in-plane motion showed a typical bi-harmonic response, and the fundamental and second harmonics had similar peak frequency values.

Then, it could be argued that, even so the nondimensional parameter were recombined, the governing terms still present some variation on them and similarity in the modal context may not be easily achieved. On the whole, the effect due to the dominant plane response frequency variation is more subtle than the one caused by the modal KC variation.

As a result, modal similarity could be achieved in the present work analysis, but these cases in which there is variation on the dominant plane frequency should be analyzed carefully.

More significantly, the out-of-plane response dependence on the modal governing parameters presented in Equation 3.32 can be rewritten as:

$$A_b^{(k)\star} = F \left(KC^{(j)}, Re^{(j)}, \frac{f_{n,dom}^{(j)}}{f_{b,N}^{(k)}}, \dots \right), \quad (3.34)$$

$$N^{(k)} = G \left(KC^{(j)}, Re^{(j)}, \frac{f_{n,dom}^{(j)}}{f_{b,N}^{(k)}}, \dots \right),$$

which will be used later in the experimental analysis, considering the modal frequency ratio in lieu of the modal reduced velocity.

The modal analysis allowed to filter the spatial data, focusing only in a few number of modes in which the majority of energy was concentrated. The modal reconstruction, as argued, will never be achieved completely due to the continuum structure discretization in a finite number of DOFs.

A closer inspection in Equation 3.34 reveals that, although the Galerkin's decomposition reduced the number of DOF in the hydroelastic system, the VSIV response, characterized by the out-of-plane (binormal) dynamics, is a function of all in-plane modes, $j = 1, \dots, 10$.

This is also explicit when it was defined the modal frequency ratio (modal reduced velocity) “tensor”, Equation 3.33 (3.29), which represents the effect of a certain j -th plane mode in the k -th binormal mode, *i.e.* the VSIV response.

Notwithstanding, it would be advantage if, in a first approximation, all the binormal dynamics were a response of the dominant in-plane movement, which is the most energetic mode oscillating in a given test (or modes, since the in-plane response can be multi-modal).

Figure 3.24: Block diagram showing the simplified modal hydroelastic ROMs.

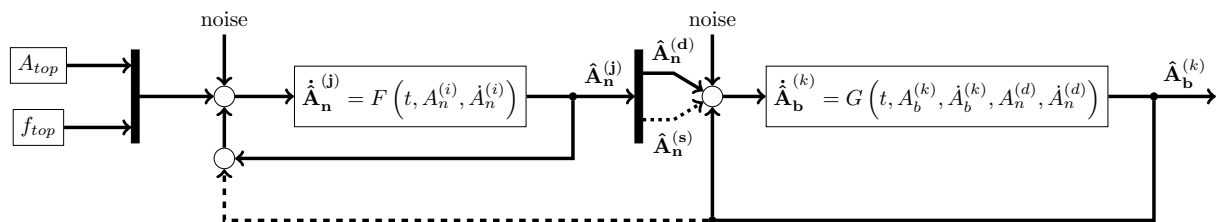


Figure 3.24 displays this proposed hydroelastic ROMs as a block diagram, con-

sidering that the modal VSIV response is a reaction of the dominant in-plane normal movement. Moreover, it is also considered that the binormal modes are uncoupled between each other due to the eigenfunctions be orthonormal with respect to the mass matrix.

The dashed lines in Figure 3.24 refer to second order effects, mainly the role of the sub-dominant plane mode in the VSIV response, specially when there is multi-modal in-plane dynamics. It is also considered that the out-of-plane movement action in the normal dynamics is of second order.

In these ROMs, the plane dynamics is important for it is the driving mechanism for the VSIV response. However, Figure 3.24 shows that the in-plane modes are coupled to each other, $i, j = 1, \dots, 10$. This assumption is not far-fetched, since the plane movement carries non-linear geometric effects due to the curvature and presents large displacements, albeit small strain.

Moreover, the Galerkin's in-plane motion decomposition was executed using the binormal mode functions. Although the eigenfunctions set used is valid under the perspective of modal decomposition, it is not guaranteed that the resultant plane modal system is uncoupled.

The relations obtained in Equation 3.34 can be rewritten, considering that each out-of-plane modal response depends only on the dominant in-plane movement, such that

$$A_b^{(k)\star} = F \left(KC^{(d)}, Re^{(d)}, \frac{f_{n,dom}^{(d)}}{f_{b,N}^{(k)}}, \dots \right) \quad (3.35)$$

$$N^{(k)} = G \left(KC^{(d)}, Re^{(d)}, \frac{f_{n,dom}^{(d)}}{f_{b,N}^{(k)}}, \dots \right),$$

in which the super-script $\square^{(d)}$ is the indication for the dominant mode; see Table 3.12.

Thus, the VSIV response for each binormal mode, $k = 1, \dots, 10$, could be written as a function of the following parameters: the dominant Keulegan-Carpenter, $KC^{(d)}$; the dominant modal Reynolds, $Re^{(d)}$; the modal frequency ratio evaluated using the dominant frequency found in the dominant in-plane modal spectral response, $f^{(d,k)\star} = f_{n,dom}^{(d)} / f_{b,N}^{(k)}$; amid other parameters.

3.3.5 Structural and hydrodynamic oscillators

The assumption that the hydroelastic response should be, in a first approximation, caused by the dominant in-plane mode is based on the modal KC range obtained for each plane mode. Such assumption is defensible when the dominant modal KC is much larger than the other modal KC, $KC^{(d)} \gg KC^{(j)}$ with $j \neq d$, referring to the other modes.

Moreover, this condition is equivalently to the out-of-plane response maximum KC dependence reported in Wang et al. (2017) and both assumes regimes in which the global dynamics is suffice to understand the hydroelastic response.

In turn, when the measured $KC^{(d)}$ is similar in order with the one from other mode, the local dynamics turns out to be relevant in the hydroelastic response. Nonetheless, the present methodology exhibits a *quasi*-uncoupled modal system⁸ and it should works sufficiently well if the system structural part governs the hydroelastic response.

The *quasi* uncoupled is a rather complicated discussion subject due to the existence of a structural model coupled to a hydrodynamic oscillator. Little is known about the latter and even its terms and coefficients should also depend on the hydroelastic response state instantaneously.

Whereas it is acceptable to consider a linear Euler-Bernoulli curved beam model as representative for the present structural system and even use its orthogonal eigenfunctions in the Galerkin's decomposition in order to obtain an uncouple structural modal system, the hydrodynamic oscillator eigenfunctions are not necessarily equivalent to the structural ones.

Thus, it is little defensible to argue that the hydrodynamic oscillator is indeed uncoupled. For this reason, a set of fundamental questions arise from this fact: is there an oscillator, structural or hydrodynamic, that is the most important one in the VSIV, assuming a governing behavior upon the other? Then, which one?

These fundamental and concerning questions are difficult to be answered generally. However, the present results and analyses will try to address them in the present experimental range and conditions.

Accordingly, should the structural oscillator be the governing one in the VSIV analysis, the devised modal methodology will be suffice to predict when some modal am-

⁸Due to the mass matrix be diagonal as a result of the orthogonal set of eigenfunctions.

plitude peak responses should occur, since the hydrodynamic oscillator could be decomposed in modal parcels that are *quasi*-orthogonal to one another two by two.

Consequently, the case in which the dominant and sub-dominant modal KCs assume same order values should not be a major problem in the present analysis due to the hydroelastic modal responses are nearly uncoupled and the causality assumption is still a good ansatz, *i.e.* the plane dynamics causes the binormal one, but the latter does not contribute in the former.

4 VSIV MODAL RESPONSE ANALYSIS

*Para onde vou, de onde vim?
 Não sei se me acho ou me extravio.
 Ariadne não fia seu fio
 à frente, mas sim atrás de mim.
 Não será a saída um desvio
 E o caminho o verdadeiro fim?*

CICERO, A., *In: O Livro de Sombras
 de Luciano.*

This chapter deals with the attained experimental results using the proposed methodology previously presented. The main goal is to obtain some sort of similarity amid previous experimental results and those from the multi-modal catenary-like response arrangement (SUMER; FREDSE, 1988; FERNANDES; MIRZAEI SEFAT; CASCÃO, 2014; PESCE et al., 2017).

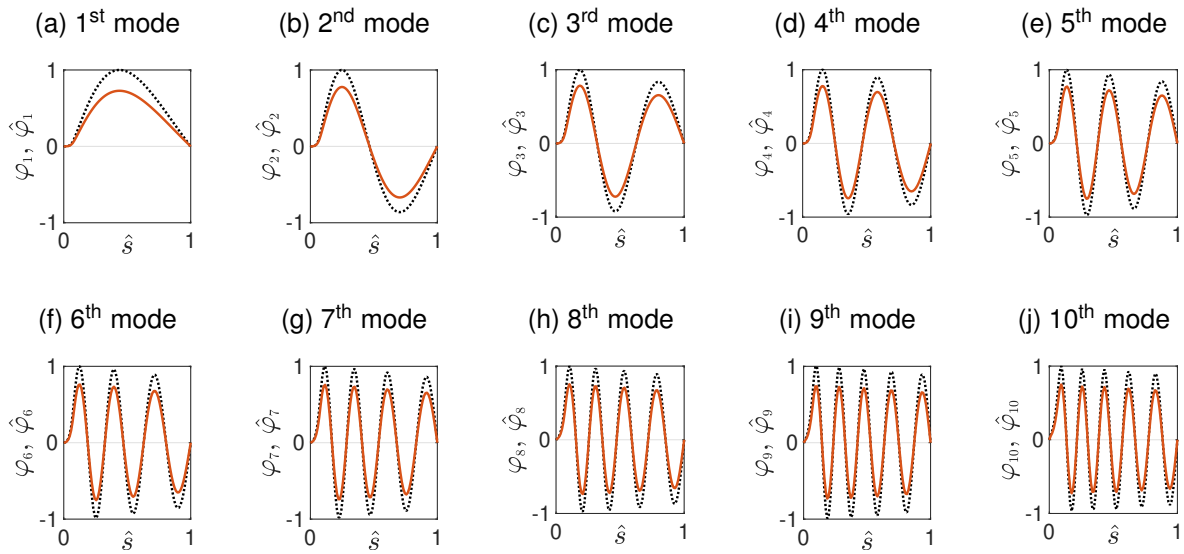
As a brief recapitulation, Figure 4.1 depicts the orthonormal eigenfunctions, $\hat{\varphi}_n$, used in the Galerkin's decomposition, comparing them with the quasi-orthogonal modes, φ_n , obtained numerically in Orcaflex[®]. The major visible difference between them is the amplitude value due to the normalization using the inner product used in the Hilbert vector subspace.

Additionally, the orthonormal set, $\hat{\mathcal{B}}$, is used in both the in-plane normal and out-of-plane binormal modal projection processing, inasmuch as the plane modes obtained using the discrete model did not reproduce the rigid soil contact accordingly with the experimental set-up condition.

The tests differ with respect to the imposed harmonic motion at the top, and, due to the actuator power limitations, higher exciting frequencies were possible only in small imposed amplitudes cases. Hence, the dominant modal KC assumes larger values mainly due to the imposed amplitude value at the hang-off point.

Moreover, the dominant KC value varies within each testing group due to the imposed motion frequency. The movement frequency at the upper end do not reach the first in-plane natural frequency, $f_{n,N}^{(1)}/f_{b,N}^{(1)} = 1.69$, in the testing groups $A_i = 70\text{mm}$ and $A_i = 105\text{mm}$, whose maximum input is of $f_{i,A70}^* = 1.21$ and $f_{i,A105}^* = 0.86$, respectively; see Table 3.7.

Figure 4.1: Modal functions, $\varphi_n(\hat{s})$ (dotted black), and their orthonormal counterparts used in Galerkin's decomposition, $\hat{\varphi}_n(\hat{s})$ (solid orange).



Source: Developed by the author.

As a result, the experimental in-plane amplitude response ought to be considered as sub-resonant with respect to the first in-plane eigenmode and, thus, the dominant modal Keulegan-Carpenter parameter, $KC^{(d)}$, increases proportionally to the input frequency; see Table 4.1. On the other hand, the other testing groups, $A_i = 17.5\text{mm}$ and $A_i = 35\text{mm}$, present exciting frequencies at the upper extremity that assume values around in-plane modes eigenfrequencies.

The latter case, $A_i = 35\text{mm}$, whose maximum driven frequency is $f_{i,A35}^* = 2.09$, achieves the first in-plane natural frequency, which can be directly observed in the $KC^{(d)}$ values presented in Table 4.1, as the parameter firstly increases in value, reaching a maximum value slightly above the in-plane resonance and then decreasing.

The former case, $A_i = 17.5\text{mm}$, shows a more complex response, as multi-modal in-plane resonance occurs due to the higher imposed frequencies (maximum $f_{i,A17.5}^* = 4.21$). Consequently, the dominant modal KC in such case occurs in several in-plane normal modal amplitude series, particularly in the first, second and third in-plane modes: $f_{n,N}^{(1)}/f_{b,N}^{(1)} = 1.69$, $f_{n,N}^{(2)}/f_{b,N}^{(1)} = 2.64$ and $f_{n,N}^{(3)}/f_{b,N}^{(1)} = 3.80$, respectively.

Table 4.1: Dominant modal Keulegan-Carpenter ($KC^{(d)}$) evaluated for all testing groups and the correspondent dominant in-plane normal mode occurrence.

ID	A_i (mm)							
	17.5		35		70		105	
	$KC^{(d)}$	Mode	$KC^{(d)}$	Mode	$KC^{(d)}$	Mode	$KC^{(d)}$	Mode
01	7.82	1 st	15.28	1 st	30.12	1 st	45.33	1 st
02	8.07	1 st	15.45	1 st	30.41	1 st	45.22	1 st
03	8.42	1 st	15.46	1 st	30.40	1 st	45.26	1 st
04	8.90	1 st	15.68	1 st	30.66	1 st	45.30	1 st
05	9.76	1 st	15.80	1 st	30.70	1 st	45.60	1 st
06	10.56	1 st	16.12	1 st	30.93	1 st	45.77	1 st
07	10.45	1 st	16.34	1 st	31.28	1 st	45.96	1 st
08	9.17	1 st	16.67	1 st	31.65	1 st	46.05	1 st
09	7.55	2 nd	17.16	1 st	31.63	1 st	46.11	1 st
10	8.13	2 nd	17.07	1 st	31.79	1 st	46.07	1 st
11	7.09	1 st	17.86	1 st	31.95	1 st	46.61	1 st
12	7.58	1 st	17.68	1 st	32.13	1 st	46.48	1 st
13	7.62	1 st	17.97	1 st	32.54	1 st	46.96	1 st
14	8.08	3 rd	16.87	1 st	32.63	1 st	47.20	1 st
15	8.14	3 rd	16.34	1 st	32.99	1 st	47.37	1 st
16	8.24	3 rd	16.32	1 st	33.11	1 st	47.49	1 st
17	7.32	1 st	16.09	1 st	33.18	1 st	47.65	1 st
18	7.39	1 st	14.09	1 st	33.24	1 st	47.58	1 st
19	7.32	1 st	14.13	1 st	33.70	1 st	47.97	1 st
20	7.25	1 st	12.96	1 st	33.91	1 st	47.88	1 st
21	-	-	-	-	-	-	47.95	1 st
22	-	-	-	-	-	-	47.65	1 st
23	-	-	-	-	-	-	47.59	1 st
24	-	-	-	-	-	-	47.76	1 st
25	-	-	-	-	-	-	47.94	1 st

Source: Developed by the author.

Accordingly, the ensuing experimental analysis will follow an order determined with respect to the in-plane resonance occurrence due to the forced motion at the hang-off point. Thus, the analysis will be executed considering firstly the largest imposed

amplitude, $A_i = 105\text{mm}$, and then considering the other cases in inverse order, 70mm, 35mm and 17.5mm, respectively.

More significantly, the modal analysis could unveil some intrinsic behaviors that cannot be perceived in a plain space of configuration analysis. For instance, the attainment of each mode VSIV response individually may assist in the search for modal intrasimilarities, comparing the modal response one to another.

Moreover, should it be possible to observe an modal intrasimilarity in each testing group, it will be possible to compare these idiosyncratic synchronization and peak responses in order to check the evidence of inter-modal similarities amid the different experimental conditions available.

Although large plane amplitude response can be observed, the structure is subjected to small strains. Hence, the majority of nonlinear phenomena are related to the hydroelastic interactions and the multi-modal response behavior, including internal and parametric resonances.

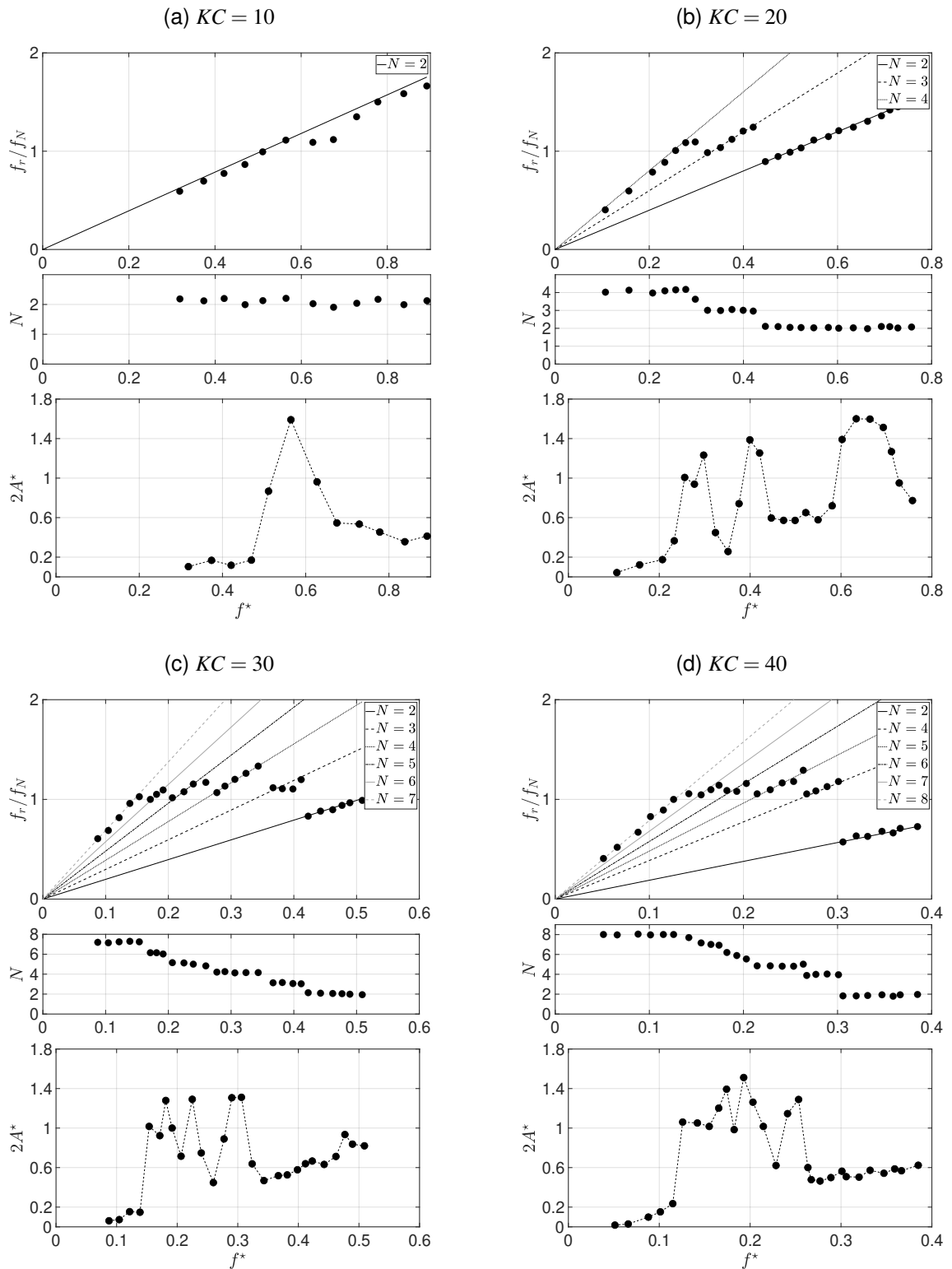
In addition, flow measurements were impossible to be carried out in the experimental arrangement. It is certainly true that such measurements would enrich the present analyses. Nonetheless, the results to be depicted show great similarity with previous analysis using rigid straight cylinders subjected to oscillatory flow and VSIV (SUMER; FREDSSØE, 1988; FERNANDES; MIRZAEI SEFAT; CASCÃO, 2014).

4.1 Rigid straight cylinders

Previously, it was presented experimental results using rigid straight cylinders obtained in Sumer and Fredsøe (1988) and Fernandes, Mirzaei Sefat, and Cascão (2014); see Figures 2.6 and 2.12, respectively. These analyses were carried out using the reduced velocity, V_R , parameter, which is indeed very suitable for both cases, having fixed KC values in each executed test.

Figure 4.2 displays the experimental data reported in Sumer and Fredsøe (1988), re-scaling the abscissa using the frequency ratio parameter, f^* . Interestingly, the amplitude peak responses occur in rational values of f^* . For instance, the $KC = 20$ presents amplitude peaks in $f^* = 0.25, 0.4$ and 0.7 ; see Figure 4.2b.

Figure 4.2: Frequency and amplitude response with respect to f^* . Exp. I.



Source: Adapted from Sumer and Fredsøe (1988).

The case in which $KC = 10$, Figure 4.2a, shows peak response between $f^* = 0.5$ and 0.6, whilst the larger KC cases present a more complex behavior and amplitude

peaks happen near $f^* = 0.2, 0.25$ and 0.3 , and $f^* = 0.18$ and 0.25 for $KC = 30$ and $KC = 40$, respectively; see Figures 4.2c-4.2d.

The experimental data shows that the occurrence of $f^* = 0.25$ happens in most cases, except in the $KC = 10$ case. Nevertheless, the former case, $KC = 10$, presents a peak amplitude response near $f^* = 0.5$.

It is also possible to observe that high KC value cases, Figures 4.2c-4.2d, present peak response in lower frequency ratio values. This may be attributable to the synchronization and high N values found in large KC tests due to the hydroelastic response responding in higher frequencies.

In turn, Figure 4.3 shows the experimental results reported in Fernandes, Mirzaei Sefat, and Cascão (2014) using the frequency ratio parameter, f^* .

Once more, it is possible to observe peak amplitude responses around rational frequency ratio values. Moreover, the occurrence of peak amplitude responses at $f^* = 0.25$ is more evident in these tests.

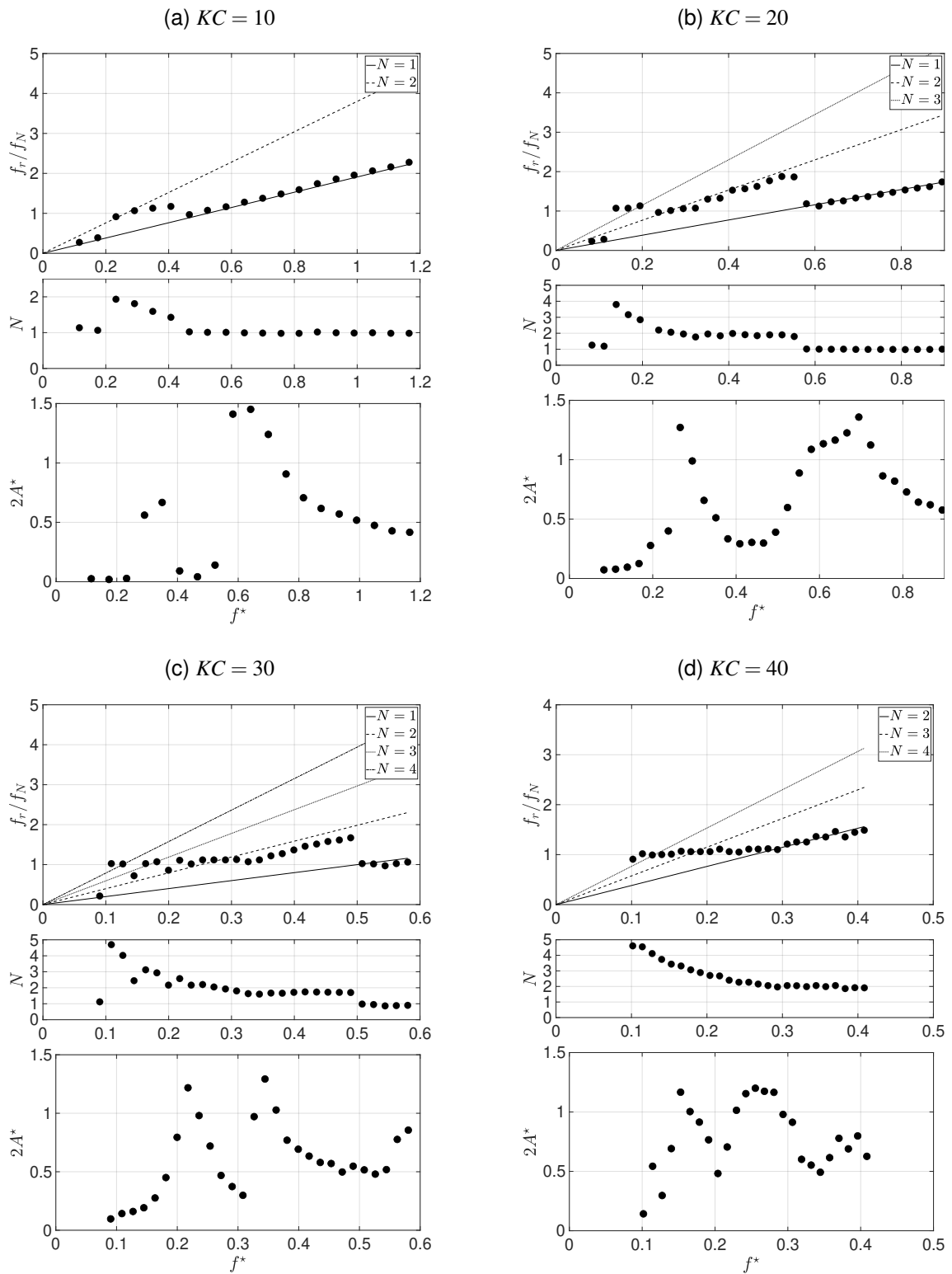
Contrastingly to what was reported in Figure 4.2, the $KC = 10$ test shows more than one peak response, happening close to $f^* = 0.25$ and 0.6 ; see Figure 4.3a. The case $KC = 20$, Figure 4.3b, presents peaks in $f^* = 0.25$ and 0.75 .

Similarly to the $KC = 30$ results in Figure 4.2c, the $KC = 30$ case, Figure 4.3c, also shows peak response in a frequency ratio value near $f^* = 0.3$. The same can be observed in the case $KC = 40$ which has a peak response near $f^* = 0.18$; see Figure 4.3d. The latter also shows a peak amplitude response in $f^* = 0.40$.

Furthermore, conversely to the amplitude response reported in Figure 4.2, the experimental results obtained by Fernandes, Mirzaei Sefat, and Cascão (2014) shows a response whose amplitude peaks occur in a more comprehensible fashion with distinguishable peaks; see Figure 4.3.

The frequency ratio could shed light in the results reported in Sumer and Fredsøe (1988) and Fernandes, Mirzaei Sefat, and Cascão (2014), unveiling an interesting pattern on the distribution of amplitude peaks with respect to values of f^* . Particularly, Sumer and Fredsøe (1988) argued that the transition which occurs in the synchronization parameter, N , happens when there is a resonance in the system, *i.e.* the response frequency is approximately equal to the natural one, $f_r/f_N \sim 1$.

Figure 4.3: Vortex Self-Induced Vibration amplitude and frequency responses for several KC conditions with respect to f^* .



Source: Adapted from [Fernandes et al. \(2012\)](#).

Considering the synchronization parameter, $N = f_r/f_i$, and the frequency ratio, $f^* =$

f_i/f_N , it is possible to obtain the following relation,

$$f^* = \frac{f_i}{f_N} = \frac{f_r}{N f_N} = \frac{1}{N} \frac{f_r}{f_N}, \quad (4.1)$$

in which the synchronization number, N , shows up in the frequency ratio. If a resonance occurs, *i.e.* $f_r/f_N \sim 1$, then the frequency ratio can be written in the following form:

$$f^* \sim \frac{1}{N}. \quad (4.2)$$

The previous results show that the occurrence of amplitude peak response in the vicinity of a rational f^* value is not a coincidence, but a necessary condition. Unquestionably, when high KC values are used in the experimental test, the measured response will assume higher N values and, consequently, resonance amplitude peaks will occur in the vicinity of smaller f^* values.

For instance, Figure 4.2d displays that the cylinder response assumes $N = 2, \dots, 8$ and, considering the result obtained in Equation 4.2, it is possible to verify that the response amplitude peaks are occurring in the range $0.125 \leq f^* \leq 0.5$, as predicted.

Although Equation 4.2 is a reasonably prediction of a amplitude peak, the VSIV is a nonlinear phenomenum and presents peaks that are not necessarily located in $f^* \sim N^{-1}$.

This can be evidenced in Figure 4.2b in which there is a resonance peak in $f^* \sim 2/3$, whilst $N = 2$ is observed. The same behavior can be observed in Figures 4.3a-4.3c, in which all cases present a peak response around $f^* \sim 0.6$, whilst measuring $N = 1$.

4.2 VSIV response in a catenary-like cylinder

After this brief reinterpretation of results, the present chapter will follow the analysis order presented previously, beginning with the $A_i = 105\text{mm}$ test group, followed by the other cases in inverse order of imposed amplitude values, $A_i = 70\text{mm}$, 35mm and 17.5mm , respectively.

The present experimental results will be presented following a color scheme, assigning an unique color and its hues to each mode. For instance, the first mode is assigned to the color **blue**; the second, to **orange**; the third, to **yellow**; the fourth, to

green; and the fifth, to purple.

As a general rule, if two hues of a same color appear at the same time, the darker hue will be assigned to the dominant mode, while the lighter one to a subdominant mode. The same applies to when there is the intention of evidencing which measurements are obtained from a dominant or subdominant mode.

The other modes, seventh up to tenth, are also assigned to an unique color. Nonetheless, these higher modes are less important than the ones specified previously and their color code might be checked in the results to be presented afterwards.

Otherwise indicated, henceforth, these colors will be used only in the context of their correspondent mode, except in the following cases: the green used for citing references; the blue, for cross-reference of textual elements; and the red, for hyperlinks.

4.2.1 Testing group $A_i = 105mm$

The first part of this section will present the modal plane and binormal movement synchronization using modal orbits and results in a similar fashion to what was reported in Figures 4.2-4.3, followed by the analysis of these results in the modal context. Complementary results can be found in the Appendix C.

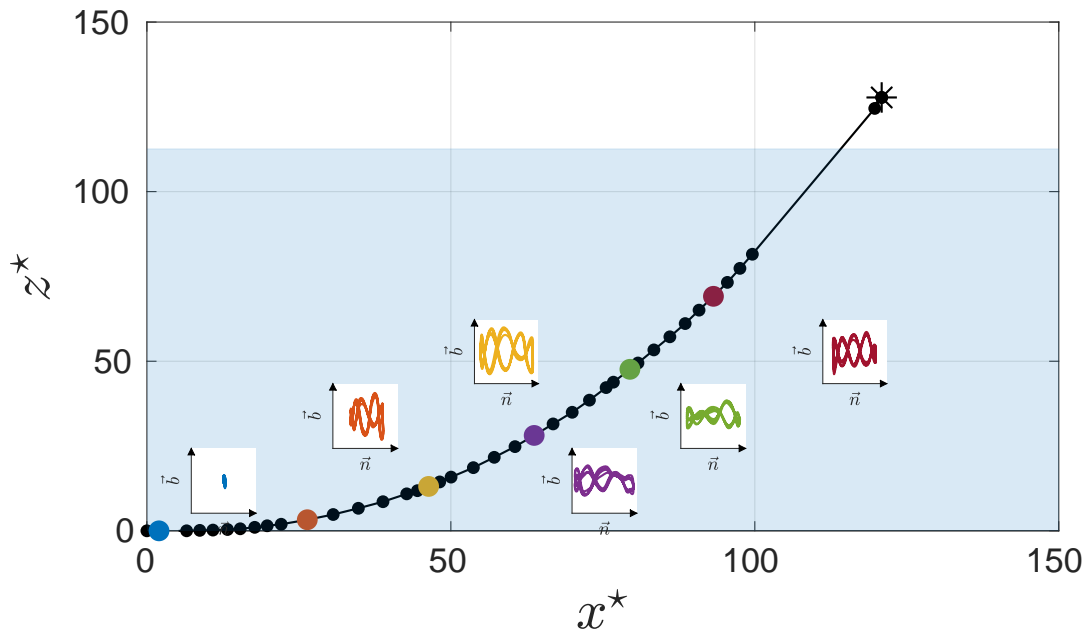
The second part will focus on the similarity obtained using the modal responses with respect to the dominant frequency measured in the dominant in-plane modal dynamics, $f_{n,dom}^{(d)}$. This analysis will check the robustness of the proposed methodology to variations in the plane response, considered to act as an input to the binormal oscillations.

Figure 4.4 exhibits some of the synchronization in the space of configuration reported in the present testing group. Particularly, the synchronization was obtained in the experimental run ID 06 whose used driving frequency is $f_i^* = f_i/f_{b,N}^{(1)} = 0.42$.

The experimental results showed in Figures 4.2-4.3 also exhibited some interesting synchronization results when the frequency ratio was in the range $0.35 \leq f_i^* \leq 0.45$, namely in Figures 4.2b and 4.3d.

Additionally, the modal analysis reveals that the ratio of the exciting frequency with respect to other modes, e.g. the second one $f_i/f_{b,N}^{(2)} = 0.21$, can suggest that the existence of a resonant peak response in the second mode, i.e. the modal synchronization would assume a whole number value.

Figure 4.4: Exemplifying the synchronization displayed using orbits in the space of configuration between normal and binormal displacements measured at specific points selected in the model span considering the testing group $A_i = 105\text{mm}$.



Source: Developed by the author.

Note: The modal color scheme is not applied in this case and the colors merely represent the selected points at the cylinder span.

An early analysis of the possible resonant peak using Equation 4.2 suggest that the synchronization number should evaluate to $N = 5$ in the aforementioned case. A thorough discussion regarding this sort of apparent modal resonant response will be addressed accordingly in the following section. Such discussion will also serve as a basis to the following cases analysis.

4.2.1.1 Modal orbits, synchronization and amplitude results

Firstly, Table 4.2 shows the modal KC for the five first plane modes, $j = 1, \dots, 5$, in the $A_i = 105\text{mm}$ case. It is possible to observe that the dominant KC is indeed occurring in the first mode, as previously presented in Table 4.1, and that the modal KC increased as the exciting frequency enlarged as well.

The subdominant KC occurs both in the second and third modes, IDs 01-12 and 15-25, respectively, and the IDs 13-14 show co-subdominance of both modes. The dominant KC is larger than the subdominant one, being approximately an order higher in magnitude.

Table 4.2: Modal Keulegan-Carpenter, $KC^{(j)}$, evaluated for all relevant modes in the $A_i = 105\text{mm}$ testing group along with the correspondent nondimensional frequency parameter, $f^{(j,k)*} = f_{n,dom}^{(j)} / f_{b,N}^{(k)}$.

ID	Modes							
	1st		2nd		3rd		4th	
	$KC^{(1)}$	$f^{(1,1)*}$	$KC^{(2)}$	$f^{(2,2)*}$	$KC^{(3)}$	$f^{(3,3)*}$	$KC^{(4)}$	$f^{(4,4)*}$
01	45.3	0.24	4.4	0.12	4.7	0.08	0.7	0.06
02	45.2	0.28	4.3	0.14	4.7	0.09	0.7	0.07
03	45.3	0.31	4.3	0.16	4.7	0.10	0.7	0.08
04	45.3	0.35	4.3	0.17	4.7	0.12	0.8	0.09
05	45.6	0.38	4.3	0.19	4.6	0.13	0.8	0.10
06	45.8	0.42	4.3	0.21	4.7	0.14	0.9	0.10
07	46.0	0.45	4.3	0.23	4.6	0.15	0.8	0.11
08	46.1	0.48	4.3	0.24	4.6	0.16	0.8	0.12
09	46.1	0.52	4.5	0.26	4.6	0.17	0.9	0.13
10	46.1	0.55	4.4	0.28	4.6	0.19	0.9	0.14
11	46.6	0.55	4.4	0.28	4.6	0.19	0.9	0.14
12	46.5	0.62	4.6	0.31	4.8	0.21	1.1	0.16
13	47.0	0.62	4.6	0.31	4.6	0.21	1.0	0.16
14	47.2	0.69	4.7	0.35	4.7	0.23	1.1	0.17
15	47.4	0.69	4.8	0.35	4.6	0.23	1.2	0.17
16	47.5	0.76	5.1	0.38	4.8	0.26	1.2	0.19
17	47.7	0.80	5.7	0.40	4.9	0.27	1.4	0.20
18	47.6	0.80	5.7	0.40	5.0	0.27	1.4	0.20
19	48.0	0.87	6.2	0.44	5.3	0.29	1.5	0.22
20	47.9	0.87	6.4	0.44	5.5	0.29	1.6	0.22
21	48.0	0.93	7.5	0.47	5.7	0.31	1.8	0.23
22	47.7	0.93	7.9	0.47	6.0	0.31	1.9	0.23
23	47.6	1.00	8.7	0.51	6.5	0.34	2.1	0.25
24	47.8	1.00	8.7	0.51	6.5	0.34	2.1	0.25
25	47.9	1.04	9.0	0.52	6.7	0.35	2.2	0.26

Source: Developed by the author.

This large distance in range of the dominant and subdominant KCs are favorably to

the assumption that, in a first approximation, the VSIV dynamics is a response of only the dominant normal movement. The reader is encouraged to check the Appendix C.1 in order to see modal amplitude series and their spectral content for each analyzed mode.

Figures 4.5-4.6 depicts the synchronization between plane and out-of-plane movements using Lissajous' curves. The modal orbits are scaled with respect to the highest out-of-plane ones observed in the whole testing group.

The modal orbits are plotted considering each binormal modal amplitude series with respect to the in-plane normal dominant mode displacement, *i.e.* the plane movement whose amplitude is the largest observed.

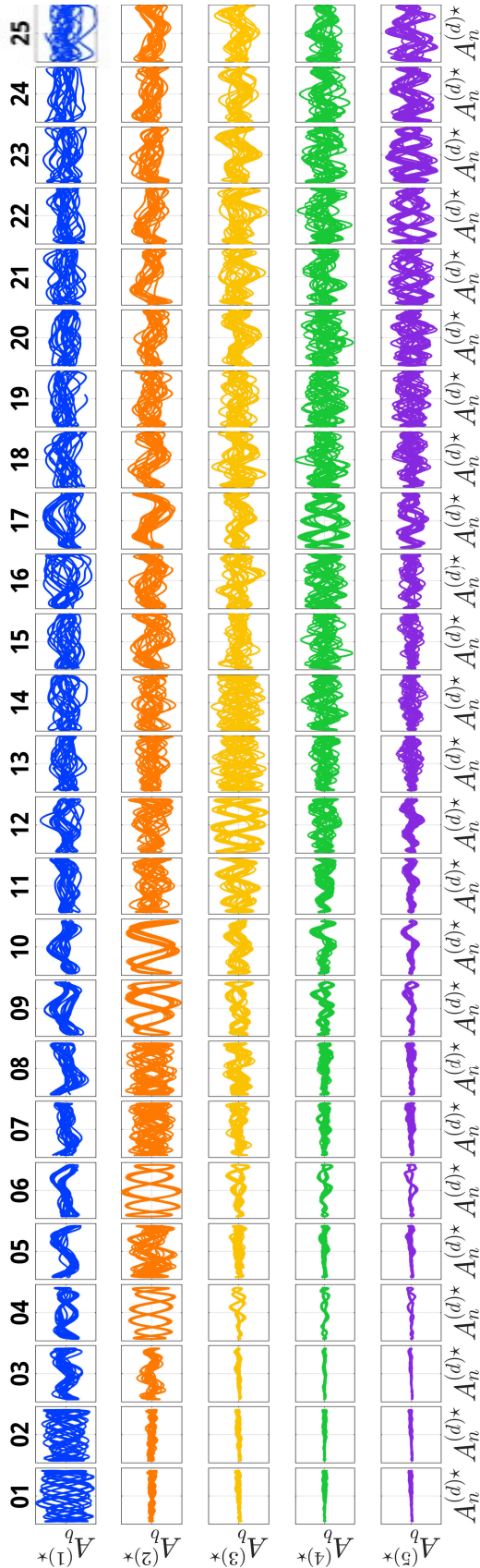
Visual inspection in Figure 4.5 reveals that there are some synchronization patterns in each mode, which indicates that the modal synchronization parameter, $N^{(k)}$, can assume approximately whole values in some situations.

This behavior is easily seen in the second mode in the runs ID04, ID06, ID09 and ID10. For instance, the second mode in the run ID06 clearly shows a synchronization with 5 lobes, in other words $N^{(2)} = 5$, as previously estimated. The first mode mode also presents a distinct synchronization with higher $N^{(1)}$. Additionally, the other modes, namely third, fourth and fifth, show synchronization patterns in some cases.

Higher exciting frequency values in the imposed motion causes distinct synchronization pattern in higher modes, leading to larger out-of-plane modal displacements.

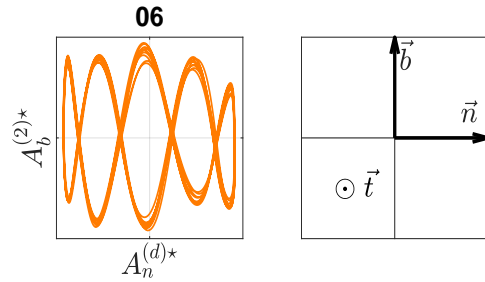
It is noteworthy that frequency ratio, $f^{(d,k)*} = f_{n,dom}^{(d)} / f_{b,N}^{(k)}$, *i.e.* the ratio between the dominant frequency obtained in the plane dominant mode with respect to the k -th out-of-plane mode, presented in Table 4.3 shows that some distinct synchronization observed in Figure 4.5 seems to occur near $f^{(d,k)*}$ values that are similar to the ones found in Figures 4.2-4.3.

Figure 4.5: Modal orbits for out-of-plane modes against dominant in-plane mode; out-of-plane modes: 1st to 5th.



Source: Developed by the author.

Figure 4.6: Modal orbits and their local reference frame orientation.



Source: Developed by the author.

Table 4.3: Ratio $f^{(j,k)*} = f_{n,dom}^{(j)}/f_{b,N}^{(k)}$ ($j = k$) for all test with imposed movement at the top $A_i = 105\text{mm}$, regarding dominant in-plane mode; out-of-plane modes: 1st to 5th.

Out-of-plane modes					
ID	1st	2nd	3rd	4th	5th
01	0.24	0.12	0.08	0.06	0.05
02	0.28	0.14	0.09	0.07	0.06
03	0.31	0.16	0.10	0.08	0.06
04	0.35	0.17	0.12	0.09	0.07
05	0.38	0.19	0.13	0.10	0.08
06	0.42	0.21	0.14	0.10	0.08
07	0.45	0.23	0.15	0.11	0.09
08	0.48	0.24	0.16	0.12	0.10
09	0.52	0.26	0.17	0.13	0.10
10	0.55	0.28	0.19	0.14	0.11
11	0.55	0.28	0.19	0.14	0.11
12	0.62	0.31	0.21	0.16	0.12
13	0.62	0.31	0.21	0.16	0.12
14	0.69	0.35	0.23	0.17	0.14
15	0.69	0.35	0.23	0.17	0.14
16	0.76	0.38	0.26	0.19	0.15
17	0.80	0.40	0.27	0.20	0.16
18	0.80	0.40	0.27	0.20	0.16
19	0.87	0.44	0.29	0.22	0.17
20	0.87	0.44	0.29	0.22	0.17
21	0.93	0.47	0.31	0.23	0.19
22	0.93	0.47	0.31	0.23	0.19
23	1.00	0.51	0.34	0.25	0.20
24	1.00	0.51	0.34	0.25	0.20
25	1.04	0.52	0.35	0.26	0.21

Source: Developed by the author.

Thus, Equations 4.1-4.2 could be extended in the modal context using the same arguments, such that

$$f^{(d,k)\star} = \frac{f_{n,dom}^{(d)}}{f_{b,N}^{(k)}} = \frac{f_b^{(k)}}{N^{(k)} f_{b,N}^{(k)}} = \frac{1}{N^{(k)}} \frac{f_b^{(k)}}{f_{b,N}^{(k)}}, \quad (4.3)$$

$$f^{(d,k)\star} \sim \frac{1}{N^{(k)}},$$

as $f_b^{(k)}/f_{b,N}^{(k)} \sim 1$ and in which $f_b^{(k)}$ is the binormal frequency response associated to the k -th mode. Again, this prediction of a peak response is an approximation, assuming a typical resonance condition observed in a linear system, which, by no means, is the presented hydroelastic case.

Figures 4.7-4.8 display, in the modal context, the same analysis carried out in Figures 4.2-4.3. Here, observations show that the modal response of the first, second, third and fourth modes are characterized by some resonance peaks.

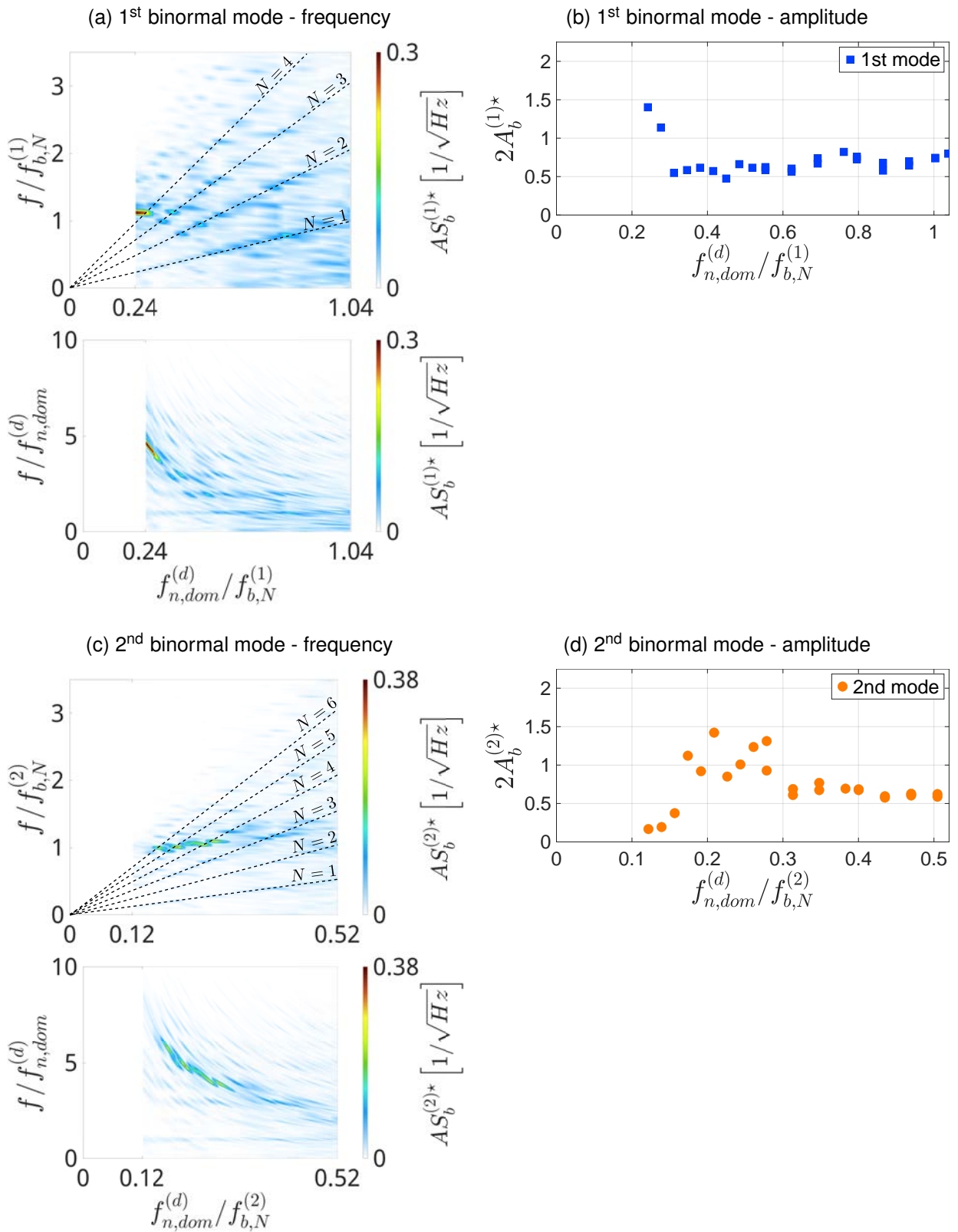
Even though the other higher modes must also be considered in the global context, only these modes are presented in order to focus on general aspects of the hydroelastic system response. Later, all modal peak amplitude responses will be addressed together.

Figures 4.7b, 4.7d, 4.8b and 4.8d present the modal amplitude peak response with respect to the modal frequency ratio. Due to the imposed exciting frequency values, the modal results are bounded in a fixed range whose value decreases as the natural frequency increases.

Consequently, the first mode response, Figures 4.7a-4.7b, presents a maximum amplitude around $f^{(d,1)\star} = 0.25$ (1.5D), which is coherent to the prediction obtained in Equation 4.3 for it is observed $N^{(1)} \sim 4$ at that spot. Some peak responses are also observable nearby $f^{(d,1)\star} = 0.33$ (0.5D) and 0.5 (0.6D), corresponding to $N^{(1)} = 3$ and 5, respectively.

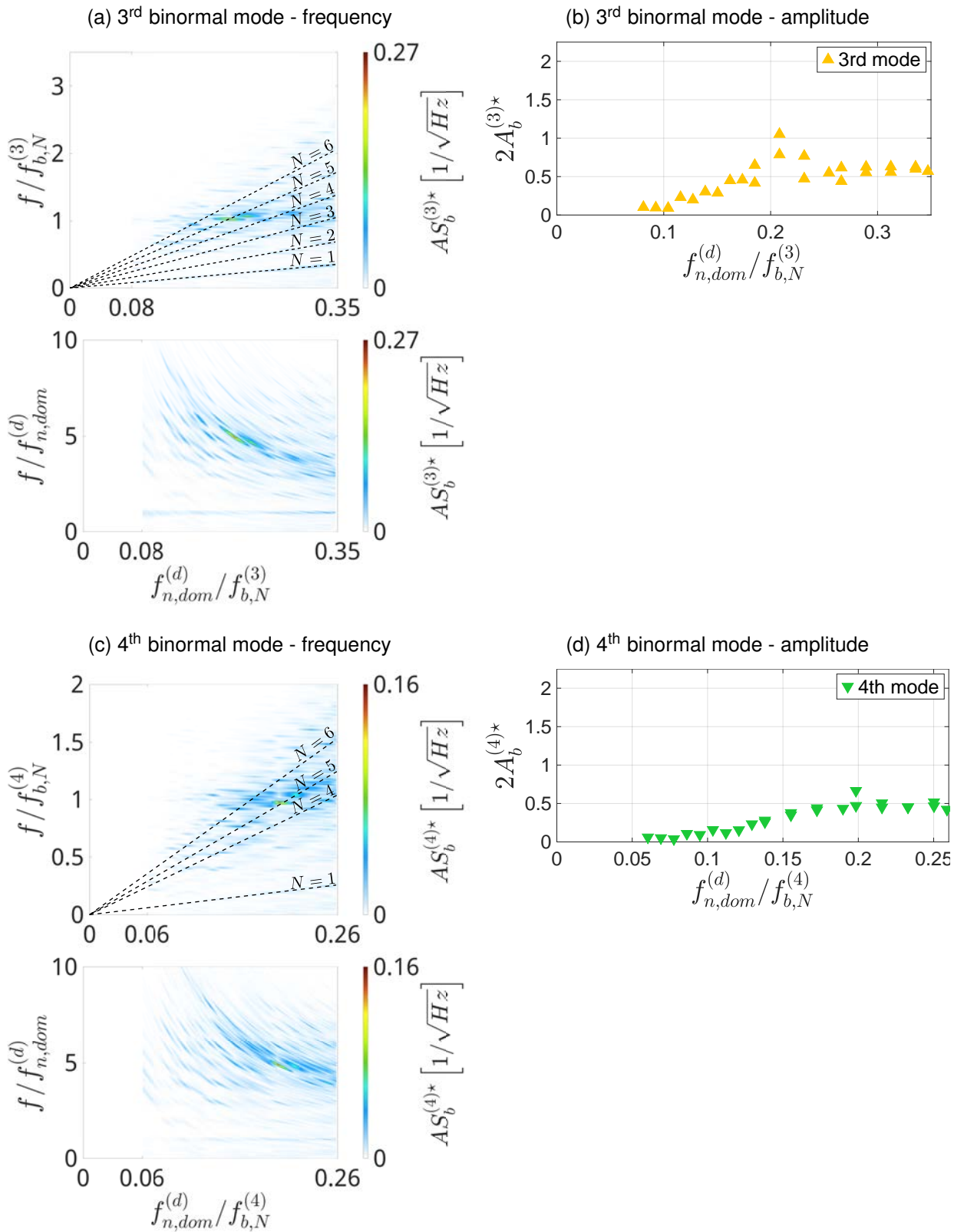
As reported in Sumer and Fredsøe (1988), the synchronization number, $N^{(1)}$, transition is occurring when $f_b^{(1)}/f_{b,N}^{(1)} \sim 1$. Additionally, a small peak response is also obtained in the range $0.7 \leq f^{(d,1)\star} \leq 0.8$ (0.8D), which was also observed in some experimental cases using rigid straight cylinders; see Figures 4.2-4.3.

Figure 4.7: Modal response of the first and second out-of-plane modes with respect to the modal frequency ratio parameter: $45.2 \leq KC^{(d)} \leq 48$.



Source: Developed by the author.

Figure 4.8: Modal response of the third and fourth out-of-plane modes with respect to the modal frequency ratio parameter: $45.2 \leq KC^{(d)} \leq 48$.



Source: Developed by the author.

The second mode, Figures 4.7c-4.7d, presents maximum peak amplitude of the same order observed in the first mode (0.5D-1.5D) and some interesting synchronization patterns were measured, specially in the tests IDs 04, 06 and 09; see Figure 4.5. Figure 4.7c evidences that there are considerable amplitudes in the spectral response placed on the synchronization $N^{(2)} = 6, 5$ and 4.

A closer inspection on Table 4.3 shows that in these cases the frequency ratio is approximately $f^{(d,2)*} = 0.17, 0.21$ and 0.26 , respectively. These frequency ratio values fit the prediction given in Equation 4.3.

Likewise, the third mode present a peak spectral response on the synchronization $N^{(3)} = 5$ and an amplitude peak around the predicted $f^{(d,3)*} = 0.2$ (1D); see Figures 4.8a-4.8b. The fourth mode shows a smaller amplitude response; nevertheless, its peak occurs in the vicinity $f^{(d,4)*} = 0.2$ (0.7D), corresponding to $N^{(4)} = 5$; see Figures 4.8c-4.8d.

The reader is asked to check Figure 4.5 and Table 4.3 whenever possible as to seek more information, *e.g.* in which IDs cases the peak resonance occurs, and to visualize the modal orbit characterizing the synchronization.

4.2.1.2 Modal similarity

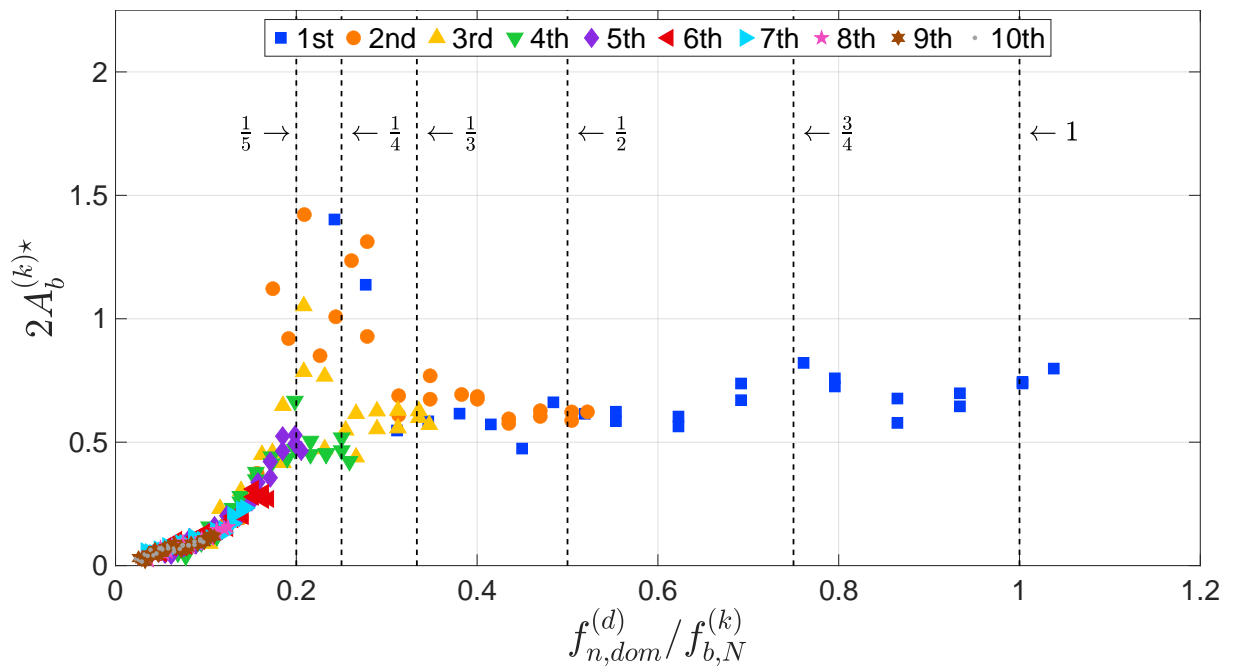
Previously, it was presented and analyzed the out-of-plane modal responses using both their amplitude and spectral contents. The analyses showed great similarity to the results obtained using a rigid straight cylinder Sumer and Fredsøe (1988) and Fernandes, Mirzaei Sefat, and Cascão (2014), which was possible due to the recombination of governing parameters and adoption of the modal frequency ratio, $f^{(d,k)*}$.

In the following analysis, it will be considered only the modal amplitude response, seeking to obtain an modal intrasimilarity. Figure 4.9 shows the peak-to-peak amplitude evaluated for each mode in all testing cases with respect to the modal frequency ratio.

In this case, the modal frequency ratio is evaluated for each mode consistently. Thus, the abscissa is written with respect to $k = 1, \dots, 10$. The reader is also asked to regard the color and marker schemes used to distinguish each mode data.

Until now, the modal responses were presented separately with respect to the frequency ratio, $f^{(d,k)*}$. It would be interesting if all modal amplitude peaks could be displayed at once in order to check how the modal responses are related to each other.

Figure 4.9: Modal peak-to-peak amplitude response, considering all out-of-plane modes with respect to the dominant plane modal displacement $45.2 \leq KC^{(d)} \leq 48$.



Source: Developed by the author.

Surprisingly, the data evidenced an modal intrasimilarity, unveiling much information on the structural response. For instance, a direct comparison on the amplitude magnitude reveals that the first and second mode present the largest responses.

Nonetheless, the third mode shows considerable high displacement of the diameter order and the fourth presents peak amplitude slightly above half diameter. The other modes exhibit modal displacement less than half diameter, which may seem small, but their frequency response and local curvature at the TDP are larger in value, which may trigger more fatigue cycles (WANG et al., 2014).

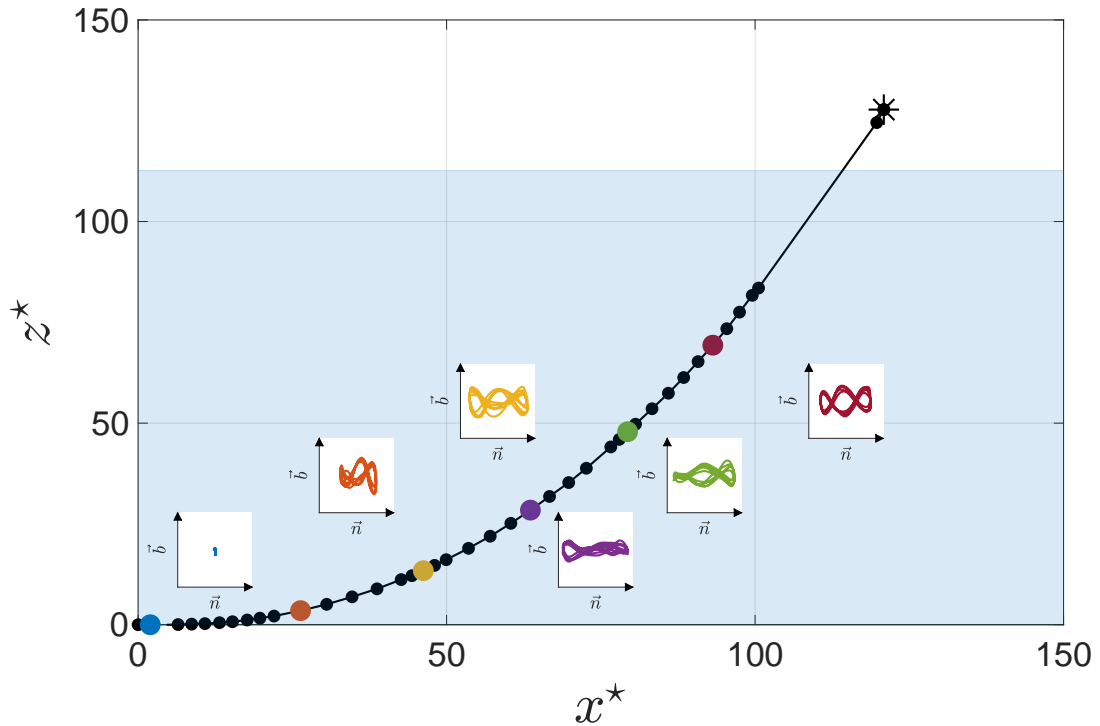
4.2.2 Testing group $A_i = 70mm$

The previous section set some foundation that will be used in the following testing cases analysis. Thus, these analyses will be carried out in similar fashion, however, the results will be exhibited in a more concise way in order to avoid redundancy.

Figure 4.10 exhibits some of the synchronization in the space of configuration reported in the present testing group. Particularly, the synchronization was obtained in the experimental run ID 09 whose used driving frequency is $f_i^* = f_i/f_{b,N}^{(1)} = 0.65$.

The experimental results showed in Figures 4.2-4.3 also exhibited some interesting synchronization results when the frequency ratio was in the range $0.60 \leq f_i^* \leq 0.75$, namely in Figures 4.2b and 4.3b.

Figure 4.10: Exemplifying the synchronization displayed using orbits in the space of configuration between normal and binormal displacements measured at specific points selected in the model span considering the testing group $A_i = 70\text{mm}$.



Source: Developed by the author.

Note: The modal color scheme is not applied in this case and the colors merely represent the selected points at the cylinder span.

4.2.2.1 Modal orbits, synchronization and amplitude results

Table 4.4 shows the evaluated modal KC in each testing case for the first up to the fifth mode. The dominant KC occurs in the first in-plane mode in all experimental runs and the sub-dominant in-plane modes are the third (IDs 01-10) and the second (IDs 13-20); the cases IDs 11-12 exhibit a dual modal sub-dominance and both second and third modes displayed the same modal KC values.

More significantly, the dominant KC is an order larger than the sub-dominant one, which is favorably to the assumption that the out-of-plane depends solely on the dominant plane motion as a first approximation. More details on the modal series can be found in the Appendix C.2.

Equation 4.3 set a prediction to when a peak amplitude response may occur, displaying a clear synchronization pattern. Considering the modes exhibited in Table 4.4, it is possible to select some cases based on their resonant modal frequency ratio, $f^{(d,k)*}$.

The first, second, third and fourth modes candidates and their correspondent frequency ratio ($f^{(d,k)*}$) are:

1st IDs IDs 02 (0.31), 16 (1.00);

2nd IDs IDs 02/03 (0.16/0.17), 04 (0.21), 09 (0.33), 15/16 (0.49/0.51);

3rd IDs 06 (0.17), 07/08 (0.19/0.21), 11 (0.26), 15/16 (0.32/0.34);

4th IDs 08/09/10 (0.16/0.16/0.17), 11/12 (0.19/0.20), 15/16 (0.24/0.25).

Inspecting the modal orbits displayed in Figure 4.11 confirms that some of these candidates duly present a characteristic Lissajous' curves. Particularly, these synchronization patterns are better depicted in the following cases: ID 02 (1st mode) ; ID 09 (2nd mode); IDs 07 and 11 (3rd mode); IDs 09, 11 and 15 (4th mode).

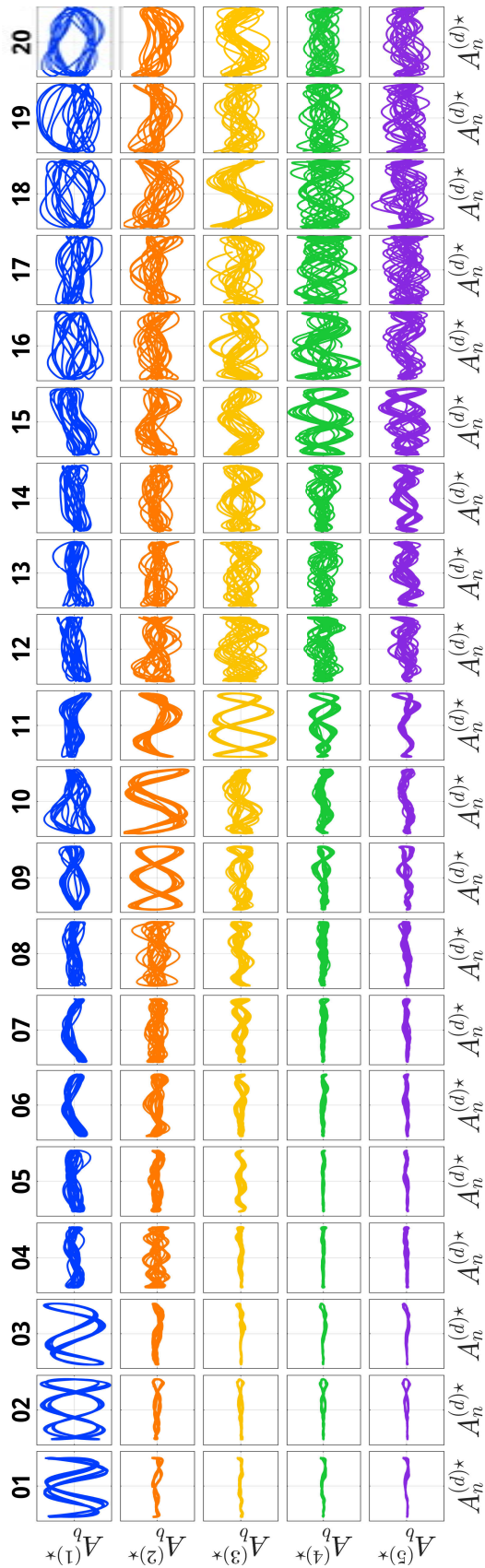
Some of the other candidates also depicted a comprehensible modal orbit. Nevertheless, they appeared with lesser visual quality due to noise or phase change during the resonance, or both. Surprisingly, the case ID 20 in the first mode, $f^{(d,1)*} = 1.21$, showed a distinguished pattern typically found in 1 : 1 internal resonance.

Table 4.4: Modal Keulegan-Carpenter, $KC^{(j)}$, evaluated for all relevant modes in the $A_i = 70\text{mm}$ testing group along with the correspondent nondimensional frequency parameter, $f^{(j,k)*} = f_{n,dom}^{(j)} / f_{b,N}^{(k)}$.

ID	Modes							
	1st		2nd		3rd		4th	
	$KC^{(1)}$	$f^{(1,1)*}$	$KC^{(2)}$	$f^{(2,2)*}$	$KC^{(3)}$	$f^{(3,3)*}$	$KC^{(4)}$	$f^{(4,4)*}$
01	30.1	0.28	3.0	0.14	3.4	0.09	0.3	0.07
02	30.4	0.31	2.9	0.16	3.3	0.10	0.3	0.08
03	30.4	0.35	2.9	0.17	3.3	0.12	0.3	0.09
04	30.7	0.42	2.8	0.21	3.3	0.14	0.3	0.10
05	30.7	0.45	2.8	0.23	3.2	0.15	0.3	0.11
06	30.9	0.52	2.8	0.26	3.2	0.17	0.4	0.13
07	31.3	0.55	2.7	0.28	3.2	0.19	0.4	0.14
08	31.7	0.62	2.6	0.31	3.1	0.21	0.4	0.16
09	31.6	0.66	2.6	0.33	3.1	0.22	0.5	0.16
10	31.8	0.69	2.7	0.35	3.1	0.23	0.6	0.17
11	32.0	0.76	3.2	0.38	3.2	0.26	0.7	0.19 5
12	32.1	0.80	3.2	0.40	3.2	0.27	0.7	0.20
13	32.5	0.87	3.6	0.44	3.2	0.29	0.8	0.22
14	32.6	0.93	3.9	0.47	3.3	0.31	0.8	0.23
15	33.0	0.97	4.8	0.49	3.6	0.32	1.1	0.24
16	33.1	1.00	4.9	0.51	3.6	0.34	1.1	0.25
17	33.2	1.07	5.6	0.54	3.9	0.36	1.2	0.27
18	33.2	1.11	6.0	0.56	4.1	0.37	1.3	0.28
19	33.7	1.18	6.4	0.59	4.2	0.39	1.4	0.29
20	33.9	1.21	7.6	0.61	4.7	0.41	1.6	0.30

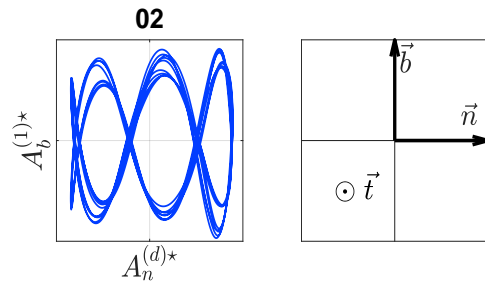
Source: Developed by the author.

Figure 4.11: Modal orbits for out-of-plane modes against dominant in-plane mode; out-of-plane modes: 1st to 5th.



Source: Developed by the author.

Figure 4.12: Modal orbits and their local reference frame orientation.



Source: Developed by the author.

Table 4.5: Ratio $f^{(j,k)*} = f_{n,dom}^{(j)} / f_{b,N}^{(k)}$ ($j = k$) for all test with imposed movement at the top $A_i = 70\text{mm}$, regarding dominant in-plane mode; out-of-plane modes: 1st to 5th.

ID	Out-of-plane modes				
	1st	2nd	3rd	4th	5th
01	0.28	0.14	0.09	0.07	0.06
02	0.31	0.16	0.10	0.08	0.06
03	0.35	0.17	0.12	0.09	0.07
04	0.42	0.21	0.14	0.10	0.08
05	0.45	0.23	0.15	0.11	0.09
06	0.52	0.26	0.17	0.13	0.10
07	0.55	0.28	0.19	0.14	0.11
08	0.62	0.31	0.21	0.16	0.12
09	0.66	0.33	0.22	0.16	0.13
10	0.69	0.35	0.23	0.17	0.14
11	0.76	0.38	0.26	0.19	0.15
12	0.80	0.40	0.27	0.20	0.16
13	0.87	0.44	0.29	0.22	0.17
14	0.93	0.47	0.31	0.23	0.19
15	0.97	0.49	0.32	0.24	0.19
16	1.00	0.51	0.34	0.25	0.20
17	1.07	0.54	0.36	0.27	0.21
18	1.11	0.56	0.37	0.28	0.22
19	1.18	0.59	0.39	0.29	0.23
20	1.21	0.61	0.41	0.30	0.24

Source: Developed by the author.

The modal response can be further analyzed with aid of Figures 4.13-4.14. The first mode exhibit amplitude peaks occurring in the vicinity of $f^{(d,1)*} = 0.31, 0.66$ and 1.00 whose magnitude varies from approximately half up to one and half diameter (0.5D-1.5D).

The testing run ID 02 present the maximum peak response (1.5D), $f^{(d,1)*} = 0.31$, and the last testing case presents a large amplitude of the diameter order (1D); however it is not possible to classify it as a peak; see Figure 4.13b.

The spectral response reveals that the maximum amplitude peak occurs in $N^{(1)} = 3$, which was previously predicted as a candidate point; see Figure 4.13a. In turn, the synchronization characterized by $N^{(1)} = 1$ exhibits two spectral peaks, corresponding to the IDs 16 and 20, $f^{(d,1)*} = 1.00$ and 1.21 , respectively.

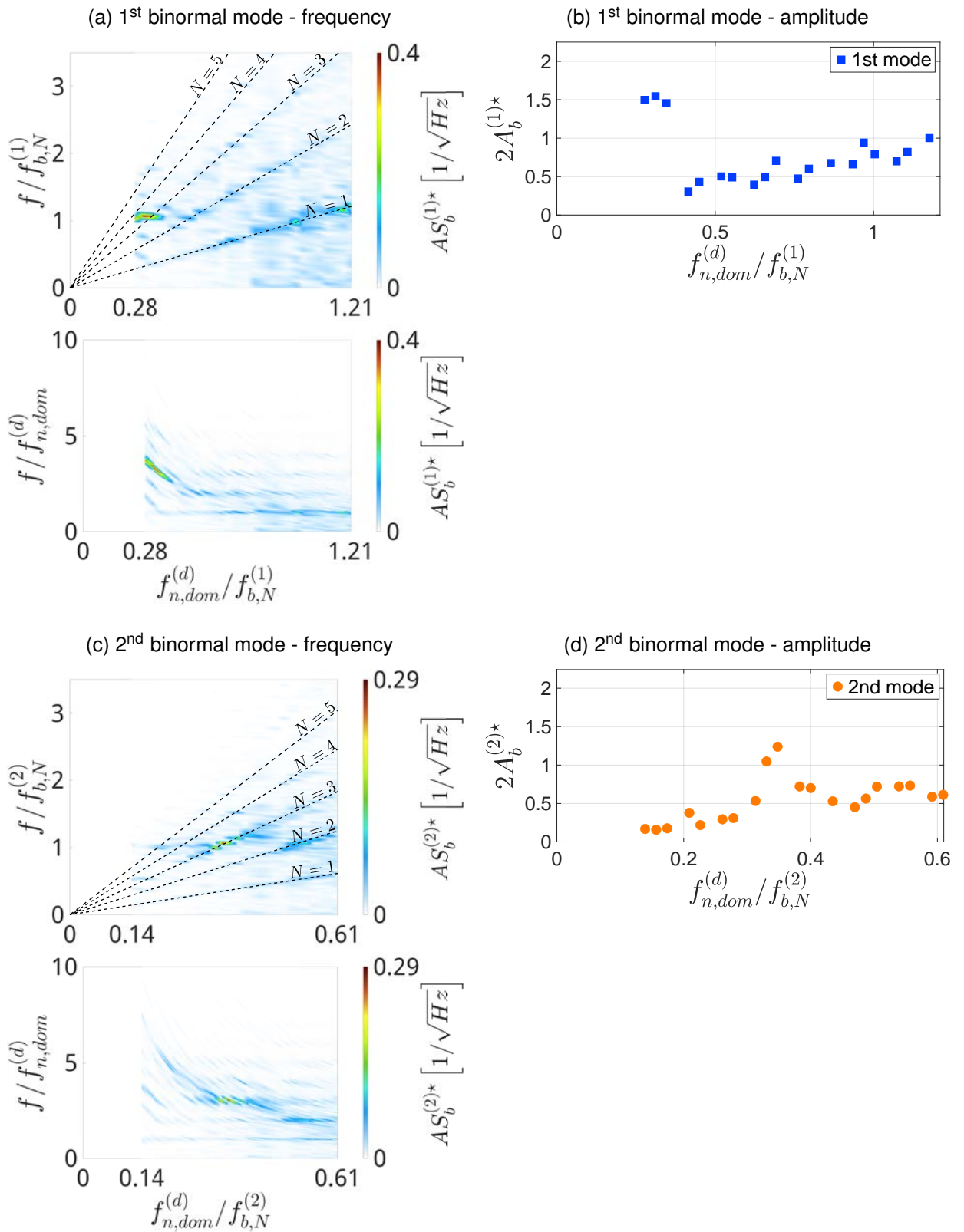
Considering the second mode, three different peaks could be identified in the amplitude response, Figure 4.13d, varying in magnitude from half to one and a half diameter (0.5D-1.5D). Once more, the first and second modes present modal amplitudes similar to one another, as reported in the $A_i = 105\text{mm}$ testing group.

The first amplitude peak occur around $f^{(d,2)*} = 0.20$ (0.5D), the second peak approximately in $f^{(d,2)*} = 0.35$ (1.3D) and the last one somewhere in the range $0.5 \leq f^{(d,2)*} \leq 0.55$ (0.75D). These peaks correspond to the cases IDs 04, 10 and 16-18. The largest peak responds with $N^{(2)} = 3$ and it is a resonant case, *i.e.* $f_b^{(2)}/f_{b,N}^{(2)} \sim 1$; see Figure 4.13c.

Figure 4.14b shows that the third mode has a resonant peak response in the vicinity of $f^{(d,3)*} = 0.25$ (1D), which corresponds to the case ID 11 and is characterized by $f_b^{(3)}/f_{b,N}^{(3)} \sim 1$. This peak occurs in $N^{(3)} = 4$ and it is possible to observe an augmented spectral amplitude towards $f^{(d,3)*} = 0.33$ (0.75D), which is the ID 18 and $N^{(3)} = 3$; see figure 4.14a. The first were predicted using Equation 4.3, whilst the second is in near the predicted case ID 16.

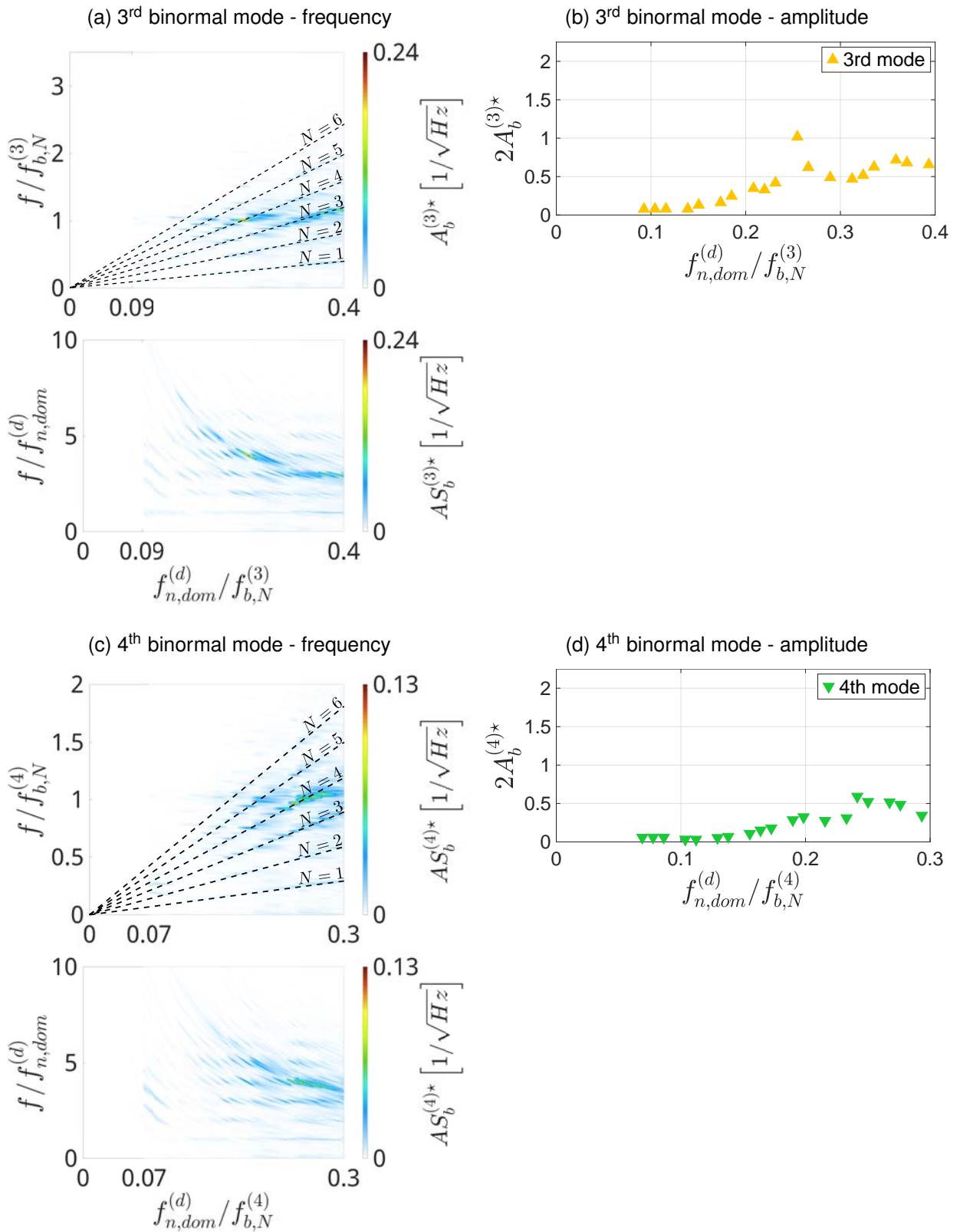
Lastly, the fourth mode is the smallest in amplitude magnitude, achieving a maximum displacement of about half diameter (0.5D); see Figure 4.14d. It is possible to clearly identify on peak in the vicinity of $f^{(d,4)*} = 0.25$, in turn, a more subtle peak could be seen around $f^{(d,4)*} = 0.20$ as well.

Figure 4.13: Modal response of the first and second out-of-plane modes with respect to the modal frequency ratio parameter: $30.1 \leq KC^{(d)} \leq 33.9$.



Source: Developed by the author.

Figure 4.14: Modal response of the third and fourth out-of-plane modes with respect to the modal frequency ratio parameter: $30.1 \leq KC^{(d)} \leq 33.9$.



Source: Developed by the author.

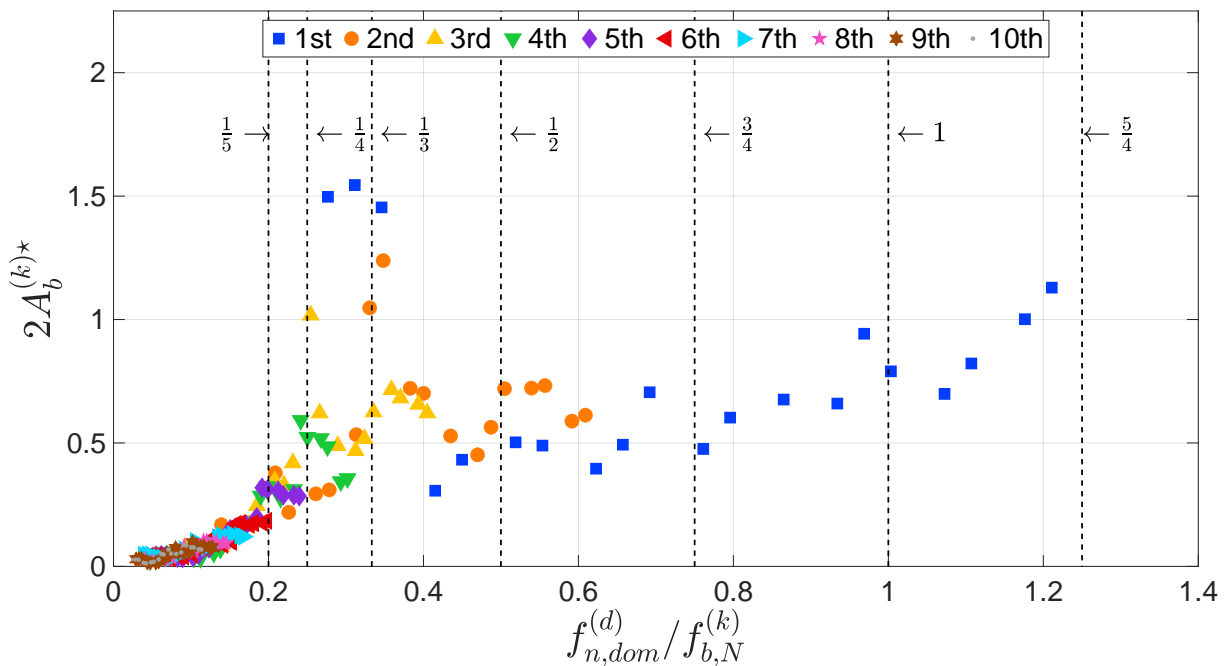
The spectral amplitude response confirms the previous observations, exhibiting a resonant peak lying on $N^{(4)} = 5$ line and another, on $N^{(4)} = 4$; see Figure 4.14c. Both peaks occur when $f_b^{(4)}/f_{b,N}^{(4)} \sim 1$, characterizing them as resonant and being predicted by Equation 4.3.

4.2.2.2 Modal similarity

Figure 4.15 exhibits the modal intrasimilarity obtained in the $A_i = 70\text{mm}$ testing group. The result is similar to the one presented in Figure 4.9, when considering the previous testing group, $A_i = 105\text{mm}$.

The actual testing group present a slightly smaller amplitude, allowing to impose higher exciting frequencies under the actuator power limit. It is possible to observe that there could be amplitude peaks in the region $f^{(d,k)} > 1$, which is not predictable by Equation 4.3 whose limit is the unit, as the synchronization parameter is reported to achieve a plateau value $N = 2$ or $N = 1$ Sumer and Fredsøe (1988) and Fernandes, Mirzaei Sefat, and Cascão (2014).

Figure 4.15: Modal peak-to-peak amplitude response, considering all out-of-plane modes with respect to the dominant plane modal displacement and $30.1 \leq KC^{(d)} \leq 33.9$.



Source: Developed by the author.

It is certainly true that the peaks not predictable by Equation 4.3 should be a result of the nonlinearities present in the hydroelastic system. It is noteworthy that this behavior also occurred in fundamental experiments with rigid straight cylinders (SUMER; FREDSE, 1988; FERNANDES; MIRZAEI SEFAT; CASCÃO, 2014), thus, it is currently not possible to discern if these peaks are due to the fluid excitation or structural internal and parametric resonances.

The modal intrasimilarity exhibited common peaks around $0.25 \leq f^{(d,k)} \leq 0.33$, presenting a slightly shifted towards $f^{(d,k)} = 0.33$ in lieu of $f^{(d,k)} = 0.25$ observed in Figure 4.9.

4.2.3 Testing group $A_i = 35mm$

The remaining testing groups, $A_i = 17.5mm$ and $35mm$, present in-plane resonance and the analysis must be carried out more carefully, expecting that the dominant and subdominant KC can assume values of similar order in some cases.

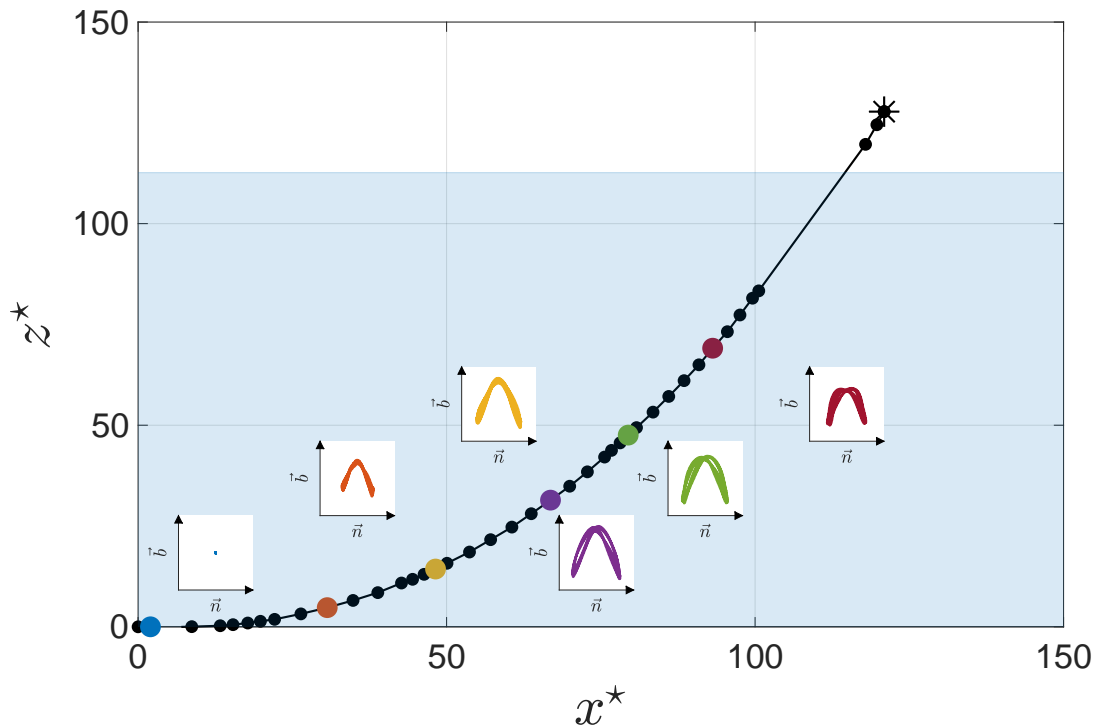
Figure 4.16 exhibits some of the synchronization in the space of configuration reported in the present testing group. Particularly, the synchronization was obtained in the experimental run ID 04 whose used driving frequency is $f_i^* = f_i/f_{b,N}^{(1)} = 0.51$.

The experimental results showed in Figure 4.2 also exhibited some interesting synchronization results when the frequency ratio was in the range $0.45 \leq f_i^* \leq 0.48$, namely in Figures 4.2c.

4.2.3.1 Modal orbits, synchronization and amplitude results

Table 4.6 shows the evaluated modal KC in each testing case for the first up to the fifth mode. The dominant KC occurs in the first in-plane mode in all experimental runs and the sub-dominant in-plane modes are the third (IDs 01-08) and the second (IDs 09-20).

Figure 4.16: Exemplifying the synchronization displayed using orbits in the space of configuration between normal and binormal displacements measured at specific points selected in the model span considering the testing group $A_i = 35\text{mm}$.



Source: Developed by the author.

Note: The modal color scheme is not applied in this case and the colors merely represent the selected points at the cylinder span.

The first and second modes present modal KC of similar order in the cases IDs 14-20 and the assumption that, in a first approximation, the dominant plane mode is the main cause of the VSIV response should be revisited, considering the previous discussion on governing modal oscillator within the hydroelastic response. More details on the modal series can be found in the Appendix C.3.

Equation 4.3 set a prediction to when a peak amplitude response may occur, displaying a clear synchronization pattern. Considering the modes exhibited in Table 4.6, it is possible to select some cases based on their resonant modal frequency ratio, $f^{(d,k)*}$.

Table 4.6: Modal Keulegan-Carpenter, $KC^{(j)}$, evaluated for all relevant modes in the $A_i = 35\text{mm}$ testing group along with the correspondent nondimensional frequency parameter, $f^{(j,k)*} = f_{n,dom}^{(j)}/f_{b,N}^{(k)}$.

ID	Modes									
	1st		2nd		3rd		4th		5th	
	$KC^{(1)}$	$f^{(1,1)*}$	$KC^{(2)}$	$f^{(2,2)*}$	$KC^{(3)}$	$f^{(3,3)*}$	$KC^{(4)}$	$f^{(4,4)*}$	$KC^{(5)}$	$f^{(5,5)*}$
01	15.3	0.24	1.3	0.12	1.8	0.08	0.4	0.06	1.5	0.05
02	15.5	0.31	1.3	0.16	1.8	0.10	0.4	0.08	1.5	0.06
03	15.5	0.42	1.2	0.21	1.8	0.14	0.4	0.10	1.5	0.08
04	15.7	0.52	1.3	0.26	1.8	0.17	0.5	0.13	1.5	0.10
05	15.8	0.62	1.4	0.31	1.7	0.21	0.5	0.16	1.5	0.12
06	16.1	0.69	1.1	0.35	1.7	0.23	0.5	0.17	1.5	0.14
07	16.3	0.80	1.0	0.40	1.6	0.27	0.6	0.20	1.5	0.16
08	16.7	0.93	1.5	0.47	1.7	0.31	0.6	0.23	1.4	0.19
09	17.2	1.00	2.2	0.51	1.7	0.34	1.0	0.25	1.5	0.20
10	17.1	1.11	2.4	0.56	1.7	0.37	0.9	0.28	1.5	0.22
11	17.9	1.21	2.8	0.61	1.7	0.41	0.9	0.30	1.4	0.24
12	17.7	1.32	3.4	0.66	2.1	0.44	1.0	0.33	1.5	0.26
13	18.0	1.42	4.5	0.71	2.7	0.47	1.2	0.35	1.4	0.28
14	16.9	1.52	7.1	0.77	3.7	0.51	1.4	0.38	1.5	0.30
15	16.3	1.63	7.3	0.82	3.5	0.54	1.3	0.41	1.5	0.32
16	16.3	1.73	8.2	0.87	3.9	0.58	1.4	0.43	1.6	0.34
17	16.1	1.83	8.9	0.92	4.2	0.61	1.5	0.46	1.6	0.36
18	14.1	1.94	9.8	0.97	4.9	0.65	1.7	0.48	2.0	0.38
19	14.1	2.04	11.0	1.03	5.0	0.68	2.0	0.51	2.0	0.40
20	13.0	2.15	11.4	1.08	5.4	0.72	2.2	0.54	2.2	0.43

Source: Developed by the author.

Respecting the actuator power limitations, the experimental group $A_i = 35\text{mm}$ could be tested using higher driving frequencies inputs and more modes could achieve significant resonant response. The first, second, third, fourth and fifth modes candidates and their correspondent frequency ratio ($f^{(d,k)*}$) are:

1st IDs 01 (0.24), 09 (1.00);

2nd IDs 09/10 (0.51/0.56);

3rd IDs 14/15 (0.51/0.54);

4th IDs 09 (0.25), 12 (0.33) and 18/19 (0.48/0.51);

5th IDs 11/12 (0.24/0.26) and 15/16 (0.32/0.34).

Inspecting the modal orbits displayed in Figure 4.17 confirms that some of these candidates duly present a characteristic Lissajous' curves. Particularly, these synchronization patterns are better depicted in the following cases: IDs 01 and 09 (1st mode) ; IDs 09 and 10 (2nd mode); ID 15 (3rd mode); IDs 09 and 12 (4th mode); IDs 12 and 16 (5th mode).

As in the previous cases, some of the other candidates also depicted a comprehensible modal orbit, nevertheless, they appeared with lesser visual quality due to noise or phase change during the resonance, or both. Besides the resonant candidates, the modal response also exhibited peaks around other characteristic frequency ratio values.

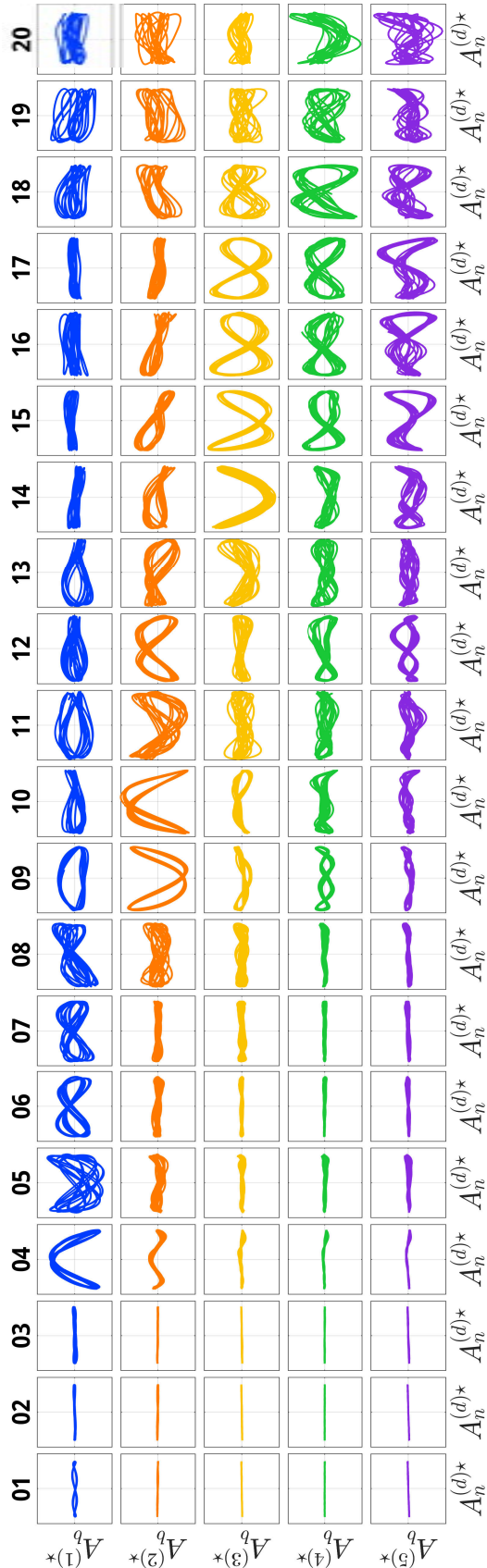
For instance, the first mode exhibits amplitude peaks occurring in the vicinity of $f^{(d,1)*} = 0.50, 1.00, 1.25, 1.50$ and 2.00 , whose magnitude varies from approximately half up to one and half diameter (0.5D-1.5D); see Figures 4.19-4.20.

The testing run ID 04 present the maximum peak response (1.5D), $f^{(d,1)*} = 0.52$, followed by amplitude peaks around half diameter (0.5D) in IDs 08, 11 and 13, corresponding to $f^{(d,1)*} = 0.93, 1.21$ and 1.42 , respectively. It seems to occur a peak of half diameter (0.5D) in ID 16, $f^{(d,1)*} = 1.73$, and the last one of about one diameter (1D) in ID 19, $f^{(d,1)*} = 2.04$; see Figure 4.19b.

The spectral response reveals that the maximum amplitude peak occurs in $N^{(1)} = 2$, which was previously predicted as a candidate point; see Figure 4.19a. In turn, the synchronization transition characterized by $N^{(1)} = 2 \rightarrow 1$ occurs when $f_b^{(1)}/f_{b,N}^{(1)} \sim 2$.

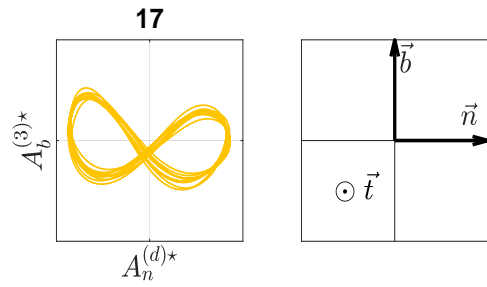
Interestingly, if the frequency ratio used in the first mode analysis were renormalized using the second out-of-plane mode natural frequency, $\tilde{f}^{(d,1)*} = f_{n,dom}^{(d)}/f_{b,N}^{(2)}$, which is approximately $f_{b,N}^{(2)} \approx 2f_{b,N}^{(1)}$, the points in which response peaks occurred would exhibit the following frequency ratio values: $\tilde{f}^{(d,1)*} = 0.26, 0.47, 0.61, 0.71$ and 1.02 ; moreover, the aforementioned synchronization transition would occur around 1.

Figure 4.17: Modal orbits for out-of-plane modes against dominant in-plane mode; out-of-plane modes: 1st until 5th.



Source: Developed by the author.

Figure 4.18: Modal orbits and their local reference frame orientation.



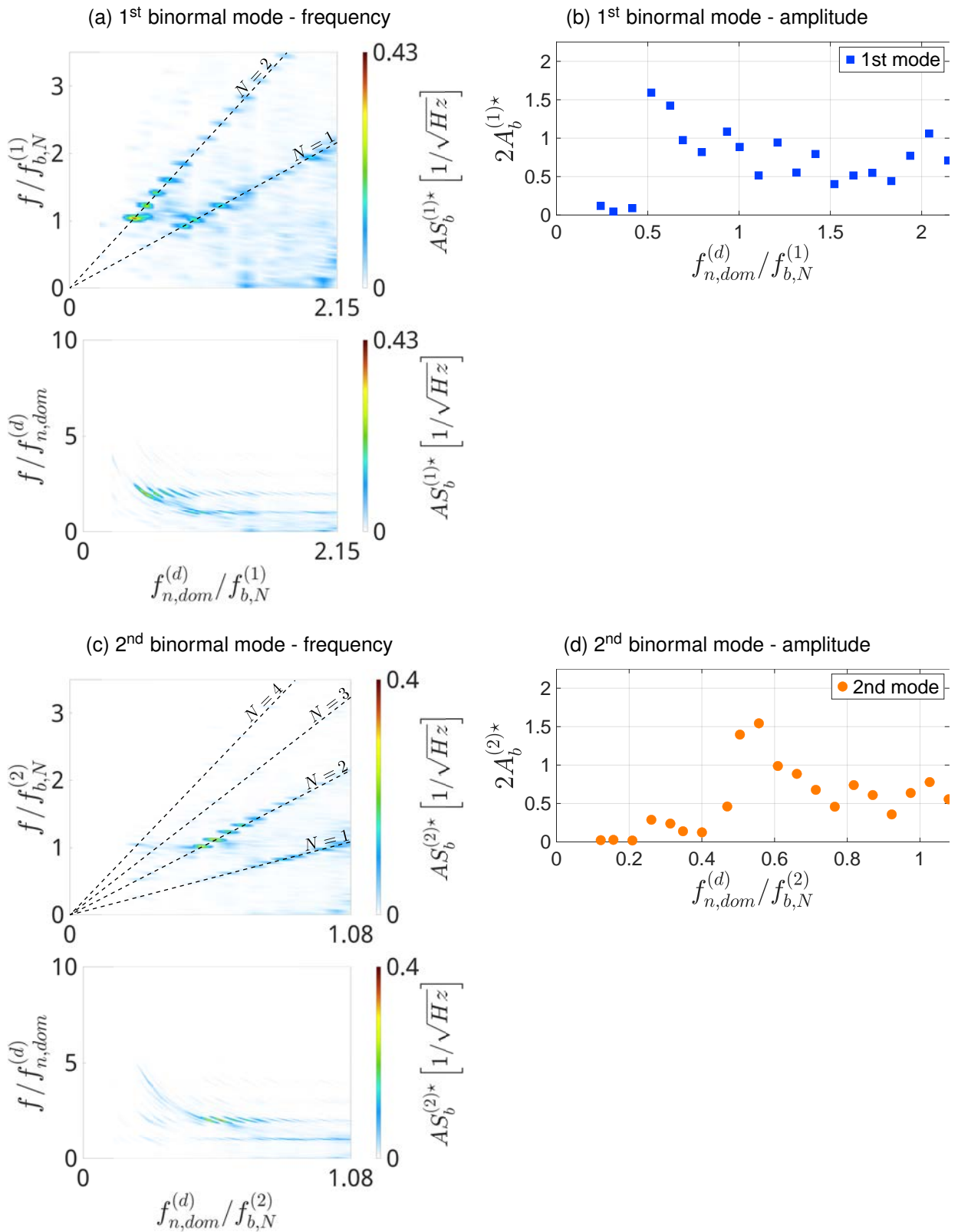
Source: Developed by the author.

Table 4.7: Ratio $f^{(j,k)*} = f_{n,dom}^{(j)} / f_{b,N}^{(k)}$ ($j = k$) for all test with imposed movement at the top $A_i = 35\text{mm}$, regarding dominant in-plane mode; out-of-plane modes: 1st until 5th.

Out-of-plane modes					
ID	1st	2nd	3rd	4th	5th
01	0.24	0.12	0.08	0.06	0.05
02	0.31	0.16	0.10	0.08	0.06
03	0.42	0.21	0.14	0.10	0.08
04	0.52	0.26	0.17	0.13	0.10
05	0.62	0.31	0.21	0.16	0.12
06	0.69	0.35	0.23	0.17	0.14
07	0.80	0.40	0.27	0.20	0.16
08	0.93	0.47	0.31	0.23	0.19
09	1.00	0.51	0.34	0.25	0.20
10	1.11	0.56	0.37	0.28	0.22
11	1.21	0.61	0.41	0.30	0.24
12	1.32	0.66	0.44	0.33	0.26
13	1.42	0.71	0.47	0.35	0.28
14	1.52	0.77	0.51	0.38	0.30
15	1.63	0.82	0.54	0.41	0.32
16	1.73	0.87	0.58	0.43	0.34
17	1.83	0.92	0.61	0.46	0.36
18	1.94	0.97	0.65	0.48	0.38
19	2.04	1.03	0.68	0.51	0.40
20	2.15	1.08	0.72	0.54	0.43

Source: Developed by the author.

Figure 4.19: Modal response of the first and second out-of-plane modes with respect to the modal frequency ratio parameter: $13 \leq KC^{(d)} \leq 18$.



Source: Developed by the author.

Some of these normalized points would be placed in the vicinity of resonant peaks frequency ratios, namely $\tilde{f}^{(d,1)*} = 0.25, 0.5$ and 1 . The remaining points, $\tilde{f}^{(d,1)*} = 0.61$ and 0.71 , appear in the neighborhood of values that were already reported previously, 0.66 and 0.75 , respectively.

Considering the second mode, four different peaks could be identified in the amplitude response, Figure 4.19d, varying in magnitude from half to one and a half diameter ($0.5D-1.5D$). Once more, the first and second modes present modal amplitudes similar to one another, as reported in the $A_i = 70\text{mm}$ and 105mm testing groups.

The first amplitude peak occur around $f^{(d,2)*} = 0.26$ ($0.3D$), the second peak approximately in $f^{(d,2)*} = 0.56$ ($1.5D$), the third peak in $f^{(d,2)*} = 0.82$ ($0.75D$) and the last one in $f^{(d,2)*} \leq 1.03$ ($0.75D$). These peaks correspond to the cases IDs 04, 10, 15 and 19. The largest peak responds with $N^{(2)} = 2$ and it is a resonant case, *i.e.* $f_b^{(2)}/f_{b,N}^{(2)} \sim 1$; see Figure 4.19c.

Figure 4.20b shows that the third mode has a small resonant peak response in the vicinity of $f^{(d,3)*} = 0.20$ ($0.1D$), which corresponds to the case ID 05; however spectral results were to faded as to determine its response synchronization parameter $N^{(3)}$.

A large amplitude peak is found in $f^{(d,3)*} = 0.54$ ($1.25D$), corresponding to the run ID 15. Spectral results show that this point is a resonant peak and $N^{(3)} = 2$; see Figure 4.20a.

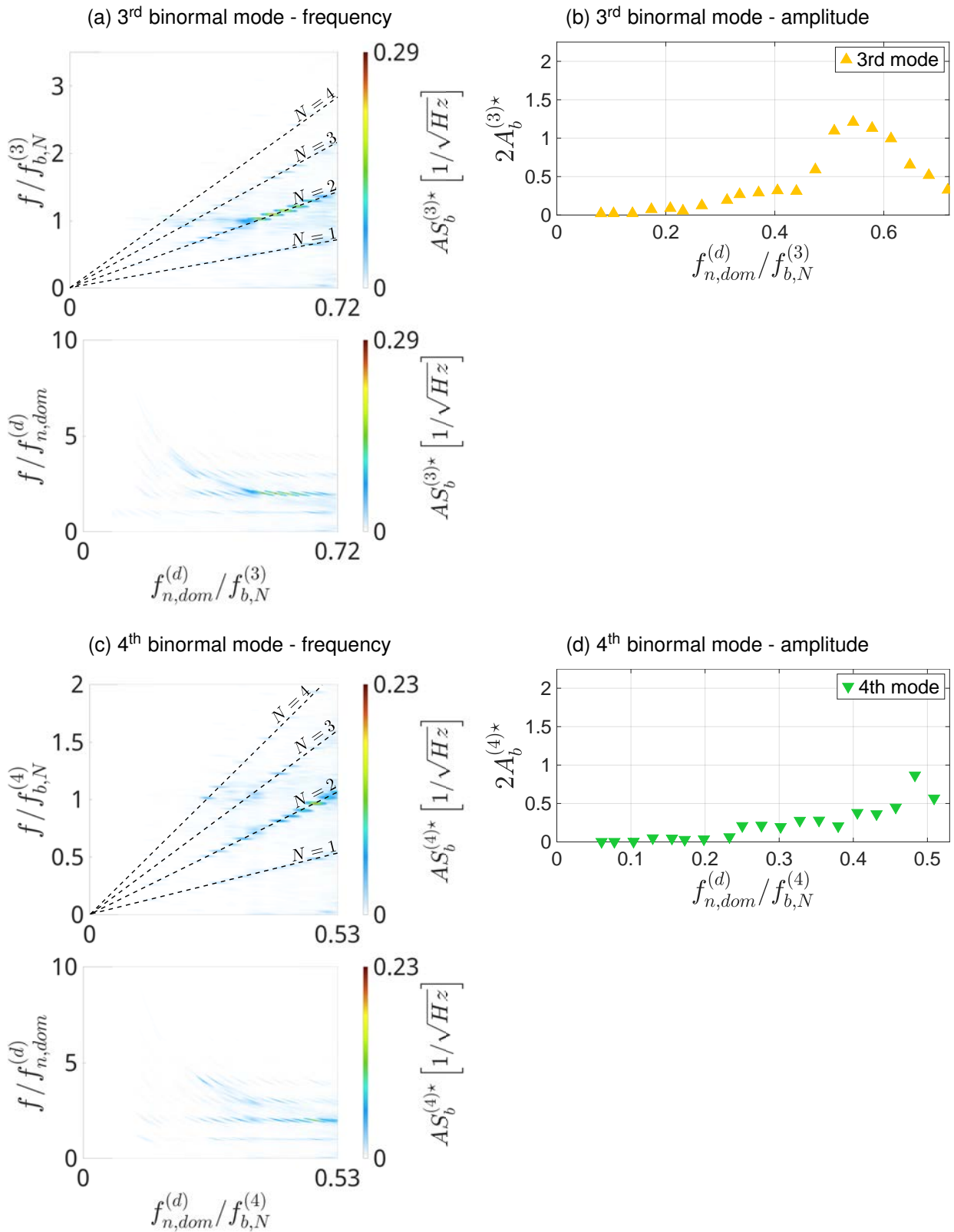
The fourth mode presents three amplitude peaks, occurring in $f^{(d,4)*} = 0.25$ ($0.3D$), 0.33 ($0.45D$) and 0.51 ($1.0D$); see Figure 4.20d. These points correspond to the cases IDs 09, 12 and 19, which were predicted using Equation 4.3.

The spectral response shows that all these peaks are resonant ones, exhibiting $N^{(4)} = 4$ (ID 09), 3 (ID 12) and 2 (ID 19); see Figure 4.20c. The largest spectral amplitude reported occurs in $f^{(d,4)*} = 0.51$ ($N^{(4)} = 2$).

Lastly, the fifth mode exhibits maximum amplitude of about half diameter ($0.5D$) and it is difficult to identify its peaks visually, using Figure 4.21b. Nonetheless, the spectral response reveals that the synchronization transitions, $N^{(5)} = 4 \rightarrow 3$, occur in $f_b^{(5)}/f_{b,N}^{(5)} \sim 1$, classifying any amplitude peak as resonant and predictable using Equation 4.3.

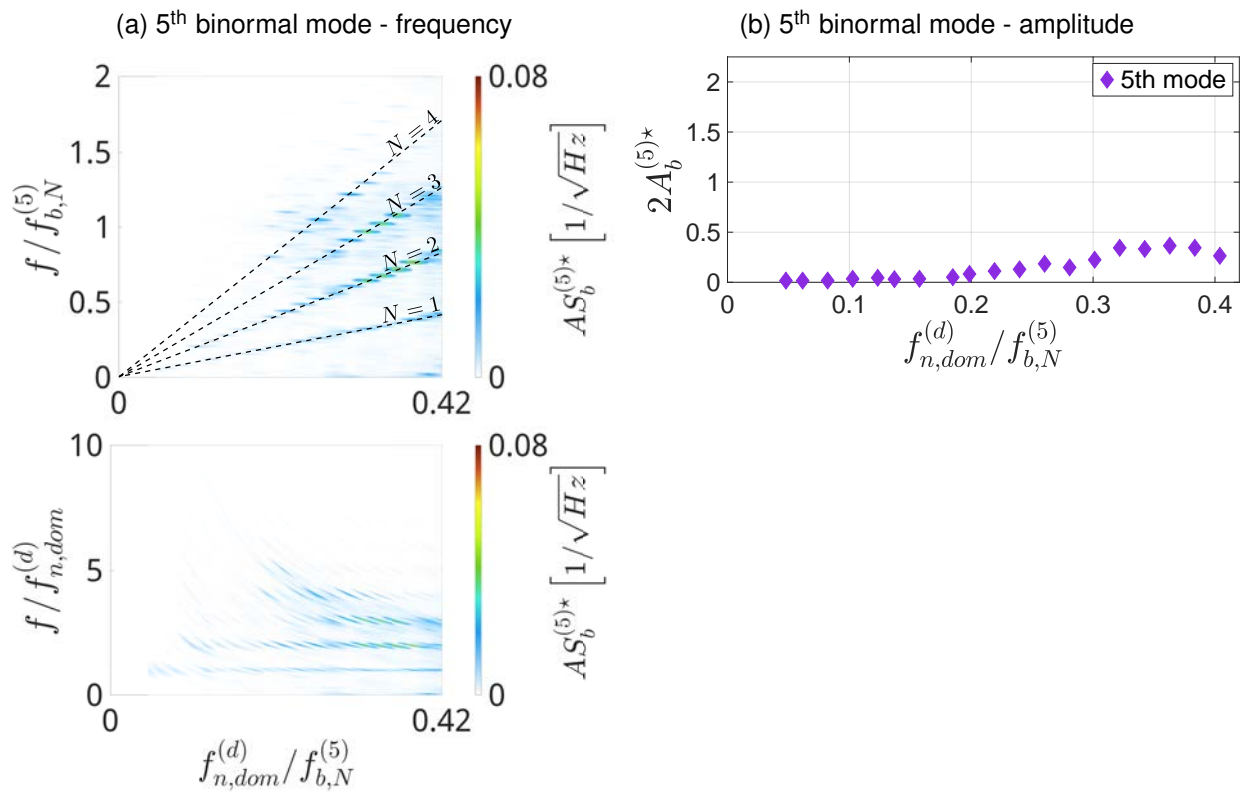
A closer inspection on the fifth mode frequency ratio in Table 4.6 and in Figures 4.21a-4.21b unveils the existence of some small peaks in $f^{(d,5)*} = 0.20$ ($0.05D$), 0.26 ($0.25D$), around 0.33 ($0.5D$), corresponding to IDs 09, 12 and 15/17.

Figure 4.20: Modal response of the third and fourth out-of-plane modes with respect to the modal frequency ratio parameter: $13 \leq KC^{(d)} \leq 18$.



Source: Developed by the author.

Figure 4.21: Modal response of the fifth out-of-plane mode with respect to the modal frequency ratio parameter: $13 \leq KC^{(d)} \leq 18$.



Source: Developed by the author.

4.2.3.2 Modal similarity

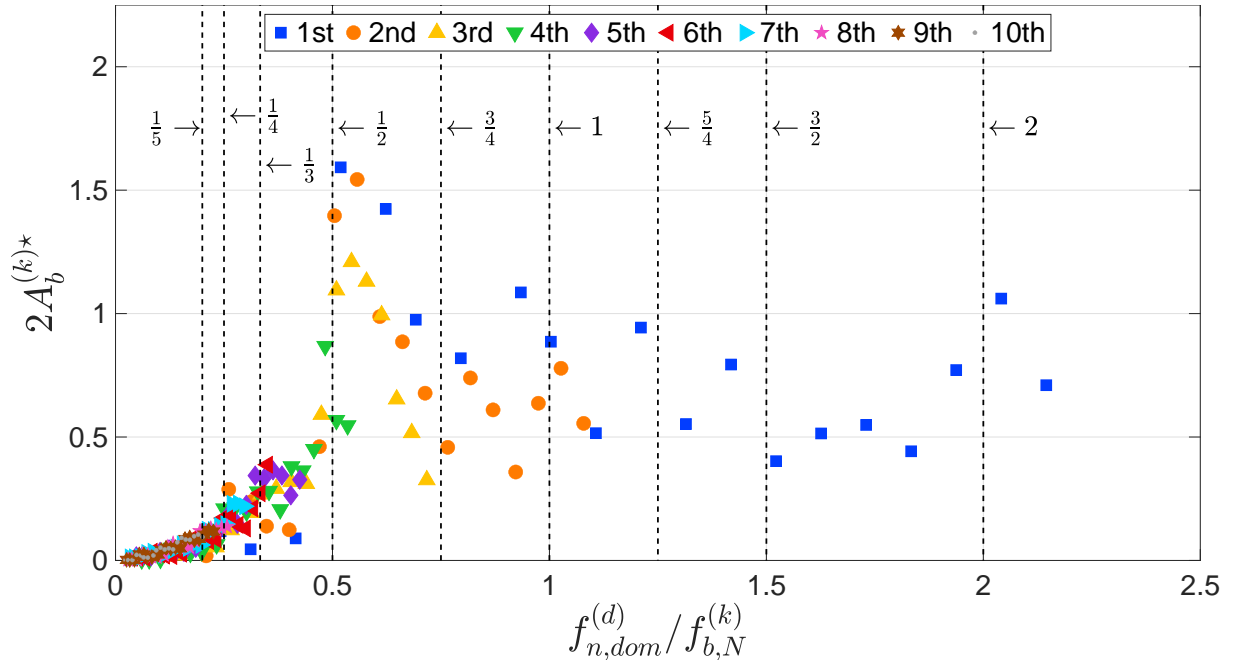
Figure 4.22 exhibits the modal intrasimilarity obtained in the $A_i = 35\text{mm}$ testing group. The present results is rather unique, when compared to the other cases presented in Figures 4.9 and 4.15, corresponding to the $A_i = 105\text{mm}$ and 70mm imposed amplitude cases, respectively.

The main difference is that the common peak response is located in the range $0.50 \leq f^{(d,k)} \leq 0.60$, farther from $f^{(d,k)} = 0.25$ that was observed in Figures 4.9 and 4.15. Nevertheless, this particular testing group also presented some peculiarities in its modal dynamics.

For instance, the first mode presents an odd behavior characterized by the synchronization transition occurring in $f_b^{(1)}/f_{b,N}^{(1)} \sim 2$. Although the renormalization using $\tilde{f}^{(d,1)*} = f_{n,dom}^{(d)}/f_{b,N}^{(2)}$ appeared to be natural, the amplitude response reported in Figure 4.22 suggests otherwise, as the second and third modes exhibit common peak response in the same range in which the first mode has a local maximum amplitude

value.

Figure 4.22: Modal peak-to-peak amplitude response, considering all out-of-plane modes with respect to the dominant plane modal displacement and $13 \leq KC^{(d)} \leq 18$.



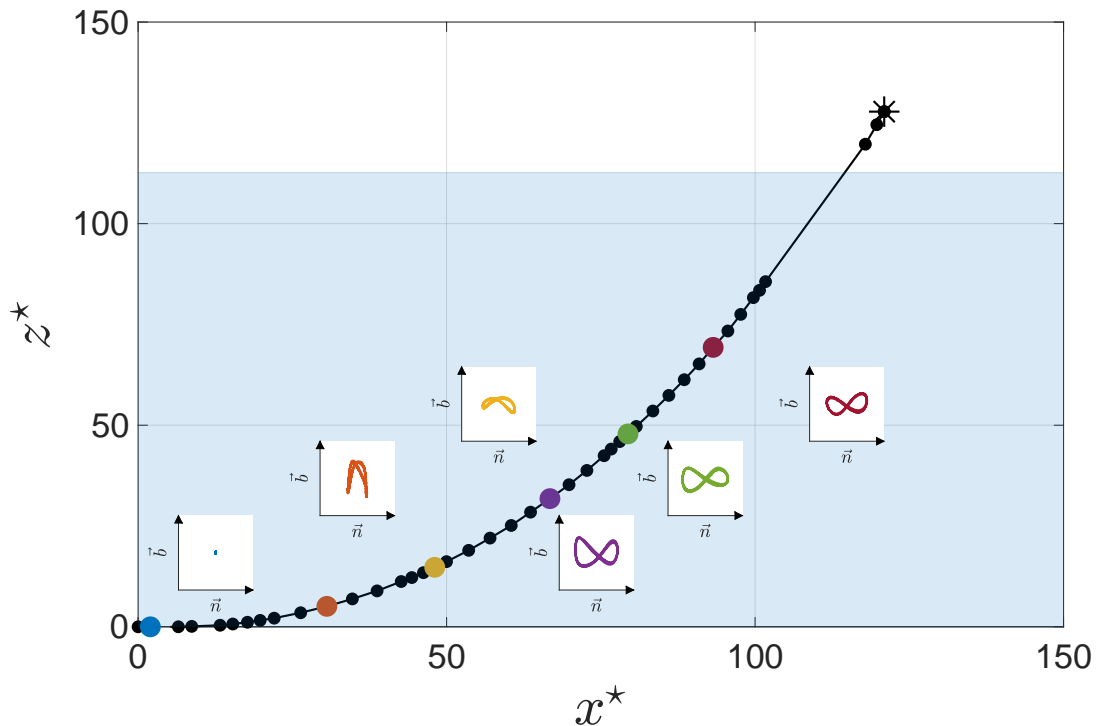
Source: Developed by the author.

The modal intrasimilarity depicted in Figure 4.22 also presents a common modal amplitude peak response around $f^{(d,k)*} = 0.50$ with respect to the first, second, third and fourth modes; the other modes growth tendency appears to agree with it.

4.2.4 Testing group $A_i = 17.5mm$

The present case exhibits several in-plane resonances due to the driving frequency achieving the highest values of all experiments described in the current work. Thus, the number of solicited modes to be analyzed is larger and a more complex and varied spectral response is reported.

Figure 4.23: Exemplifying the synchronization displayed using orbits in the space of configuration between normal and binormal displacements measured at specific points selected in the model span considering the testing group $A_i = 17.5\text{mm}$.



Source: Developed by the author.

Note: The modal color scheme is not applied in this case and the colors merely represent the selected points at the cylinder span.

Figure 4.23 exhibits some of the synchronization in the space of configuration reported in the present testing group. Particularly, the synchronization was obtained in the experimental run ID 06 whose used driving frequency is $f_i^* = f_i/f_{b,N}^{(1)} = 1.40$.

The selected case driving frequency range is not reported in Figures 4.2-4.3 and it is not possible to access much information on the space of configuration. In contrast, the modal approach reveals that $f_i/f_{b,N}^{(3)} = 0.47$, $f_i/f_{b,N}^{(4)} = 0.35$ and $f_i/f_{b,N}^{(5)} = 0.24$, presenting the possibility of resonant peak response in these modes.

Thus, the synchronization evidenced in the space of configuration could be attributable to multi-modal response, which cannot be explained by a plain analysis regarding only the exciting frequency and the first out-of-plane natural frequency.

4.2.4.1 Modal orbits, synchronization and amplitude results

Table 4.8 shows the evaluated modal KC in each testing case for the first up to the eighth mode. The dominant KC is measured in the first, second and third modes, corresponding to the cases: IDs 01-08, 11-13 and 17-20 (1st mode); IDs 09-10 (2nd mode); and IDs 14-16 (3rd mode).

Thus, the subdominant KC also occurs in different in-plane modes, such as in the cases: IDs 09-10 and 14-16 (1st mode); IDs 04-08 (2nd mode); and IDs 01-03, 12-13 and 17-20 (3rd mode).

The present testing group exhibits the dominant and subdominant KCs achieving similar values in several cases, Table 4.8, differently from what was observed in the previous group, $A_i = 35\text{mm}$, in which they only assumed similar values in the last runs.

The first mode is dominant, whilst the other present lower values, only in the cases IDs 01-06. From there, the first mode presents similar values to the second and third ones in the cases IDs 07-11 and 14-20, respectively. All three modes (1st, 2nd and 3rd) exhibit similar modal KC values in the cases IDs 12-13.

Consequently, the present testing group, $A_i = 17.5\text{mm}$, is the most intrinsically complex one, presenting up to three plane modes with similar modal KCs concomitantly. More details on the modal series can be found in the Appendix C.4.

Equation 4.3 set a prediction to when a peak amplitude response may occur, displaying a clear synchronization pattern. Considering the modes exhibited in Table 4.8, it is possible to select some cases based on their resonant modal frequency ratio, $f^{(d,k)*}$.

The first, second, third, fourth, fifth, sixth, seventh and eighth modes candidates and their correspondent frequency ratio ($f^{(d,k)*}$) are:

1st ID 04 (1.00);

2nd IDs 01 (0.21), 02 (0.31), 04 (0.51) and 09 (1.03);

3rd IDs 02 (0.21), 04 (0.34), 06/07 (0.47/0.54) and 13/14 (0.95/1.02);

4th IDs 02 (0.16), 03 (0.20), 04 (0.25), 05/06 (0.30/0.35), 09/10 (0.51/0.56) and 19/20 (1.01/1.06);

5th IDs 02 (0.12), 03 (0.16), 04 (0.20), 05 (0.24), 07 (0.32) and 11/12 (0.48/0.53);

6th IDs 03 (0.13), 04 (0.16), 05 (0.20), 06 (0.23), 09 (0.33) and 14/15 (0.50/0.53);

7th IDs 05 (0.17), 06 (0.20), 08/09 (0.25/0.28), 11 (0.34) and 17 (0.51);

8th IDs 04 (0.12), 06 (0.17), 07 (0.20), 09 (0.25), 12/13 (0.32/0.34) and 20 (0.51);

Inspecting the modal orbits displayed in Figures 4.24 and 4.28 confirms that some of these candidates duly present a characteristic Lissajous' curves. Particularly, these synchronization patterns are better depicted in the following cases: ID 04 (2nd mode); ID 07 (3rd mode); IDs 06 and 09 (4th mode); IDs 11 and 12 (5th mode); IDs 09, 14 and 15 (6th mode); IDs 06, 11 and 17 (7th mode); IDs 06, 09, 12 and 20 (8th mode).

Some of the other candidates also depicted a comprehensible modal orbit, nevertheless, they appeared with lesser visual quality due to noise, or phase change during the resonance, or both.

Besides the resonant candidates, the modal response also exhibited peaks around other characteristic frequency ratio values. Interestingly, some of the best modal orbits displayed in Figures 4.24 and 4.28 occurred in these non predictable candidates, obtained using Equation 4.3.

The first mode exhibits a rather peculiar response varying in the range of half and one diameter (0.5D-1D). The peaks occur in $f^{(d,1)*} = 1.00, 3.05$ and 3.67 , from which the first and second present synchronization $N^{(1)} = 1$, the first occurring when $f_b^{(1)}/f_{b,N}^{(1)} \sim 1$, whilst the other around $f_b^{(1)}/f_{b,N}^{(1)} \sim 2$. The latter modal synchronization parameter is not in the range of whole numbers; see Figures 4.26a-4.26b.

In turn, the second mode presents a well characterized response whose amplitude peaks occur in the vicinity of $f^{(d,1)*} = 0.5$ (1.2D), 1 (0.5D), 1.45 (0.5D) and 1.9 (0.75D); see Figure 4.26d. Only the first and second peaks were predicted using Equation 4.3.

The spectral results show that the synchronization transition $N^{(2)} = 2 \rightarrow 1$ occurs when $f_b^{(2)}/f_{b,N}^{(2)} \sim 1$, in special the first peak is resonant, presenting $N^{(2)} = 2$, whilst the others, $N^{(2)} = 1$; see Figure 4.26c.

Table 4.8: Modal Keulegan-Carpenter, $KC^{(j)}$, evaluated for all considered modes in the $A_i = 17.5\text{mm}$ testing group along with the correspondent nondimensional frequency parameter, $f^{(j,k)*} = f_{n,dom}^{(j)}/f_{b,N}^{(k)}$ and $f^* = f^{(n,n)*}$.

(continued on next page)

ID	Modes															
	1st		2nd		3rd		4th		5th		6th		7th		8th	
	$KC^{(1)}$	f^*	$KC^{(2)}$	f^*	$KC^{(3)}$	f^*	$KC^{(4)}$	f^*	$KC^{(5)}$	f^*	$KC^{(6)}$	f^*	$KC^{(7)}$	f^*	$KC^{(8)}$	f^*
01	7.8	0.42	0.6	0.21	1.0	0.14	0.2	0.10	0.7	0.08	0.4	0.07	0.6	0.06	0.1	0.05
02	8.1	0.62	0.5	0.31	0.9	0.21	0.2	0.16	0.7	0.12	0.4	0.10	0.5	0.09	0.1	0.08
03	8.4	0.80	0.3	0.40	0.8	0.27	0.2	0.20	0.7	0.16	0.4	0.13	0.5	0.11	0.1	0.10
04	8.9	1.00	0.9	0.5	0.7	0.34	0.4	0.25	0.64	0.20	0.5	0.16	0.5	0.14	0.2	0.12
05	9.8	1.21	1.1	0.6	0.5	0.41	0.4	0.30	0.57	0.24	0.5	0.20	0.5	0.17	0.2	0.15
06	10.6	1.42	3.1	0.7	1.3	0.47	0.6	0.35	0.58	0.28	0.6	0.23	0.4	0.20	0.3	0.17
07	10.5	1.63	5.1	0.8	1.9	0.54	0.8	0.41	0.65	0.32	0.6	0.27	0.5	0.23	0.3	0.20
08	9.2	1.83	8.3	0.9	2.6	0.61	0.9	0.46	0.93	0.36	0.5	0.30	0.6	0.25	0.4	0.22
09	6.3	2.04	7.6	1.1	2.6	0.68	0.9	0.51	1.10	0.40	0.5	0.33	0.6	0.28	0.3	0.25
10	6.2	2.25	8.2	1.5	2.4	0.75	1.3	0.56	1.09	0.45	0.4	0.37	0.6	0.31	0.2	0.27
11	7.1	2.42	6.9	1.2	3.8	0.81	1.4	0.60	1.26	0.48	0.5	0.40	0.7	0.34	0.3	0.29
12	7.6	2.66	5.39	1.4	5.6	0.89	1.5	0.66	1.5	0.53	0.6	0.44	0.9	0.37	0.4	0.32
13	7.6	2.84	5.07	1.5	7.2	0.95	1.8	0.71	1.9	0.56	0.7	0.46	1.0	0.39	0.5	0.34
14	7.0	3.05	3.74	1.6	8.1	1.02	1.7	0.76	1.6	0.60	0.9	0.50	1.1	0.42	0.6	0.37
15	6.8	3.25	3.14	1.7	8.2	1.09	1.5	0.81	1.6	0.64	1.2	0.53	1.2	0.45	0.5	0.39
16	7.6	3.46	3.12	1.8	8.3	1.16	1.5	0.86	1.7	0.69	1.3	0.57	1.2	0.48	0.6	0.42

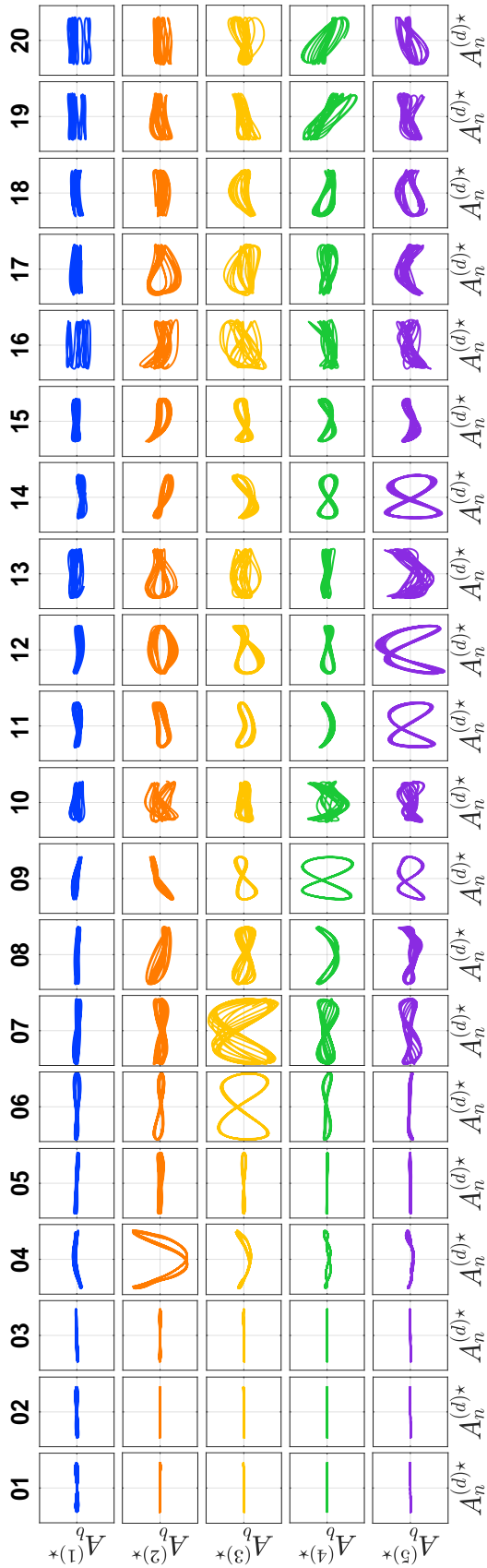
Table 4.8: Modal Keulegan-Carpenter, $KC^{(j)}$, evaluated for all considered modes in the $A_i = 17.5\text{mm}$ testing group along with the correspondent nondimensional frequency parameter, $f^{(j,k)*} = f_{n,dom}^{(j)} / f_{b,N}^{(k)}$ and $f^* = f^{(n,n)*}$.

(final page)

Modes																
ID	1st		2nd		3rd		4th		5th		6th		7th		8th	
	$KC^{(1)}$	f^*	$KC^{(2)}$	f^*	$KC^{(3)}$	f^*	$KC^{(4)}$	f^*	$KC^{(5)}$	f^*	$KC^{(6)}$	f^*	$KC^{(7)}$	f^*	$KC^{(8)}$	f^*
18	7.4	3.88	3.37	2.0	6.3	1.30	2.6	0.97	2.03	0.77	0.7	0.63	1.7	0.54	0.8	0.46
19	7.3	4.05	3.31	2.1	5.7	1.35	3.7	1.01	2.14	0.80	0.8	0.66	1.8	0.56	0.7	0.49
20	7.3	4.26	3.07	2.2	5.4	1.42	3.2	1.06	2.14	0.84	0.8	0.70	1.2	0.59	1.1	0.51

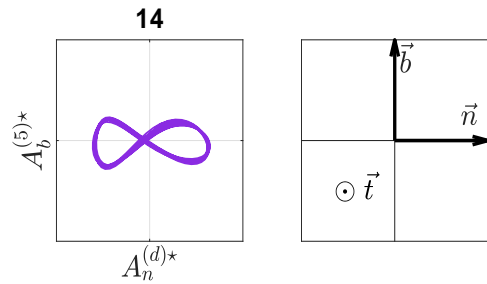
Source: Developed by the author.

Figure 4.24: Modal orbits for out-of-plane modes against dominant in-plane mode; out-of-plane modes: 1st until 5th.



Source: Developed by the author.

Figure 4.25: Modal orbits and their local reference frame orientation.



Source: Developed by the author.

Table 4.9: Ratio $f^{(j,k)*} = f_{n,dom}^{(j)}/f_{b,N}^{(k)}$ ($j = k$) for all test with imposed movement at the top $A_i = 17.5\text{mm}$, regarding dominant in-plane mode; out-of-plane modes: 1st until 5th.

ID	Out-of-plane modes				
	1st	2nd	3rd	4th	5th
01	0.42	0.21	0.14	0.10	0.08
02	0.62	0.31	0.21	0.16	0.12
03	0.80	0.40	0.27	0.20	0.16
04	1.00	0.51	0.34	0.25	0.20
05	1.21	0.61	0.41	0.30	0.24
06	1.42	0.71	0.47	0.35	0.28
07	1.63	0.82	0.54	0.41	0.32
08	1.83	0.92	0.61	0.46	0.36
09	2.04	1.03	0.68	0.51	0.40
10	2.25	1.13	0.75	0.56	0.45
11	2.42	1.22	0.81	0.60	0.48
12	2.66	1.34	0.89	0.66	0.53
13	2.84	1.43	0.95	0.71	0.56
14	3.05	1.53	1.02	0.76	0.60
15	3.25	1.64	1.09	0.81	0.64
16	3.46	1.74	1.16	0.86	0.69
17	3.67	1.85	1.23	0.92	0.73
18	3.88	1.95	1.30	0.97	0.77
19	4.05	2.04	1.35	1.01	0.80
20	4.26	2.14	1.42	1.06	0.84

Source: Developed by the author.

Figure 4.27b displays that the third mode has at least four different amplitude peaks, occurring around $f^{(d,3)*} = 0.34$ (0.25D), 0.5 (0.9D), 0.95 (0.5D) and 1.30 (0.5D). The spectral amplitude response shows that the first, second and third ones present modal synchronization $N^{(3)} = 2$. The last peak is the only that could not be predicted, exhibit $N^{(3)} = 1$; see Figure 4.27a.

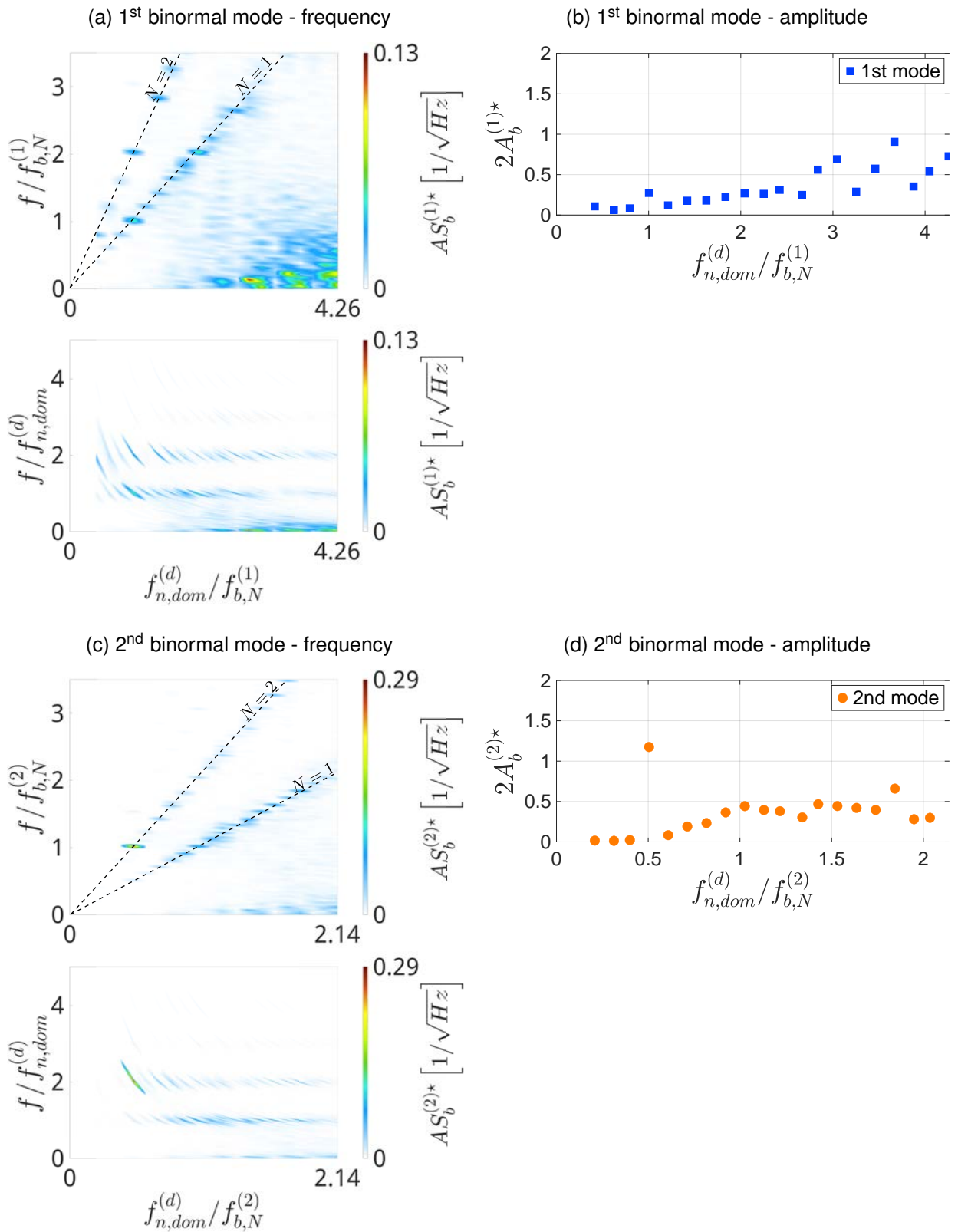
Regarding the fourth mode, its amplitude and spectral responses are bounded in the frequency range $f^{(d,4)*} < 1$, showing visually three different peaks and a last point that presents a local maximum value. These points occur in $f^{(d,4)*} = 0.25$ (0.15D), 0.51 (1D), 0.76 (0.5D) and 1.06 (0.75D); see Figure 4.27d. Considering the frequency values in which the peaks occurred, the first, second and last one were the only among predicted candidates.

The spectral graphics do not accurately present a modal synchronization parameter for the first peak, which should be heuristically placed in $N^{(4)} = 4$. On the other hand, the remaining points are either in $N^{(4)} = 2$ or 1; see Figure 4.27c. The largest peak is resonant, occurring in the synchronization transition $N^{(4)} = 2 \rightarrow 1$.

The fifth and final mode presents some of the most visually pleasing modal orbits depicted in Figure 4.24. Figures 4.30a-4.30b exhibit the spectral and amplitude responses, respectively, and it is possible to identify at least five different amplitude peaks in its response.

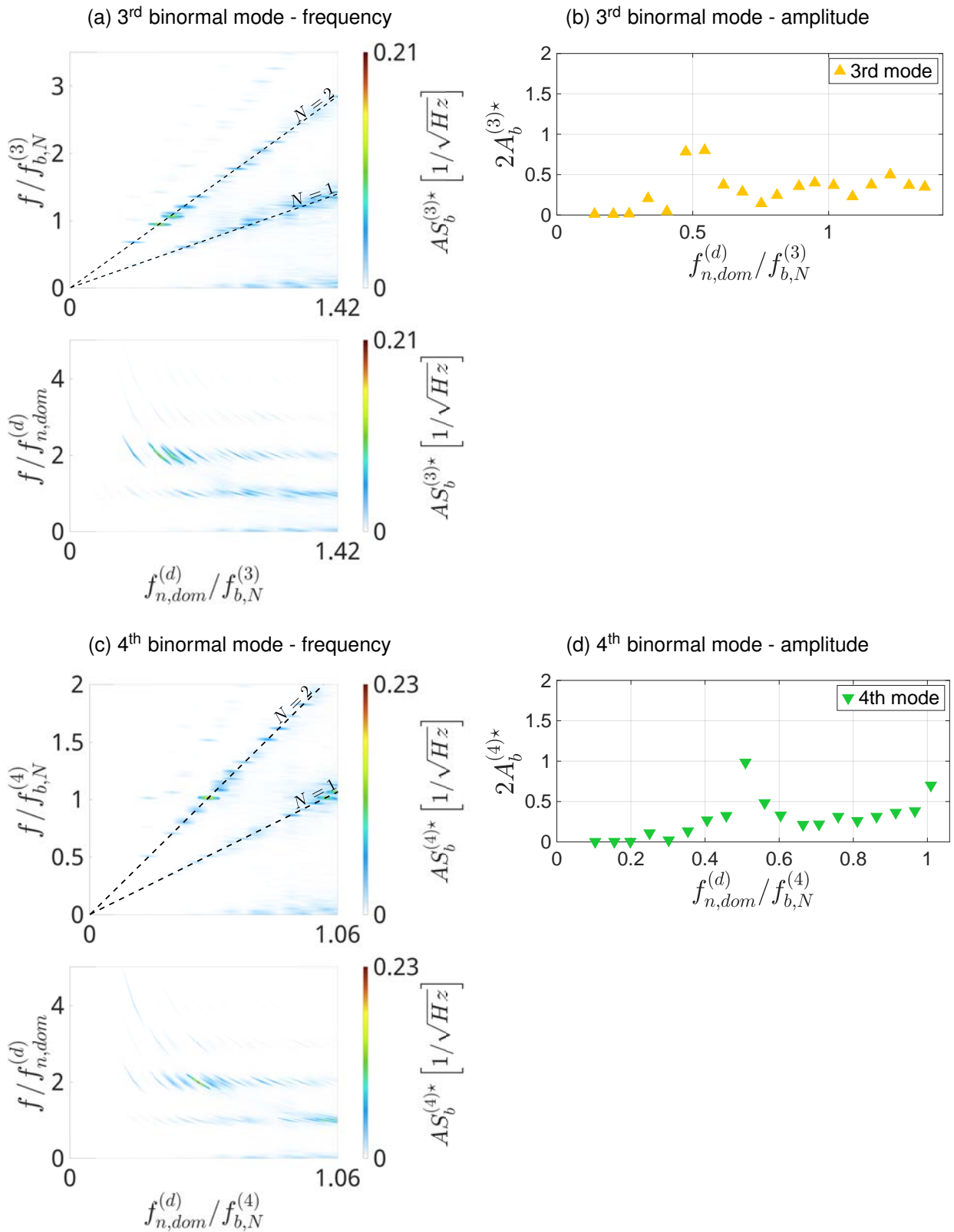
The peaks occurs in the vicinity of $f^{(d,5)*} = 0.2$ (0.1D), 0.32 (0.25D), 0.4 (0.4D), 0.52 (0.7D), 0.6 (0.5D) and lastly 0.77 (0.4D). The synchronization transition is different from the previous cases, exhibiting $N^{(5)} = 2 \rightarrow 1$ when $f_b^{(5)}/f_{b,N}^{(5)} \sim 1.5$, similarly with the first mode analyzed in Figures 4.19a-4.19b.

Figure 4.26: Modal response of the first and second out-of-plane modes with respect to the modal frequency ratio parameter: $7 \leq KC^{(d)} \leq 10.6$.



Source: Developed by the author.

Figure 4.27: Modal response of the third and fourth out-of-plane modes with respect to the modal frequency ratio parameter: $7 \leq KC^{(d)} \leq 10.6$.



Source: Developed by the author.

The sixth, seventh and eighth modal orbits are presented in Figure 4.28. The sixth mode exhibits three distinguishable peaks in its spectral and amplitude peak-to-peak responses; see Figures 4.30c-4.30d.

The first visible peak has very low amplitude, occurring in $f^{(d,6)*} = 0.16$ (0.1D), whilst the other peaks are located in $f^{(d,6)*} = 0.4$ (0.35D) and 0.53 (0.75D), being the last one, whose magnitude is the largest, a predicted candidate.

There is not enough data to identify the modal synchronization parameter associated to the first peak, which could be heuristically guessed as $N^{(6)} = 6$. The second peak lies in $N^{(6)} = 1$ and the last one is resonant, occurring in the vicinity of the modal synchronization transition, *i.e.* $N^{(6)} = 2 \rightarrow 1$.

Figures 4.31a-4.31b displays the modal response of the seventh mode. It is possible to identify at least three amplitude peaks visually, which occurs at $f^{(d,7)*} = 0.28$ (0.2D), 0.42 (0.5D) and 0.51 (0.55D). The first and last peaks are among the candidates predicted previously.

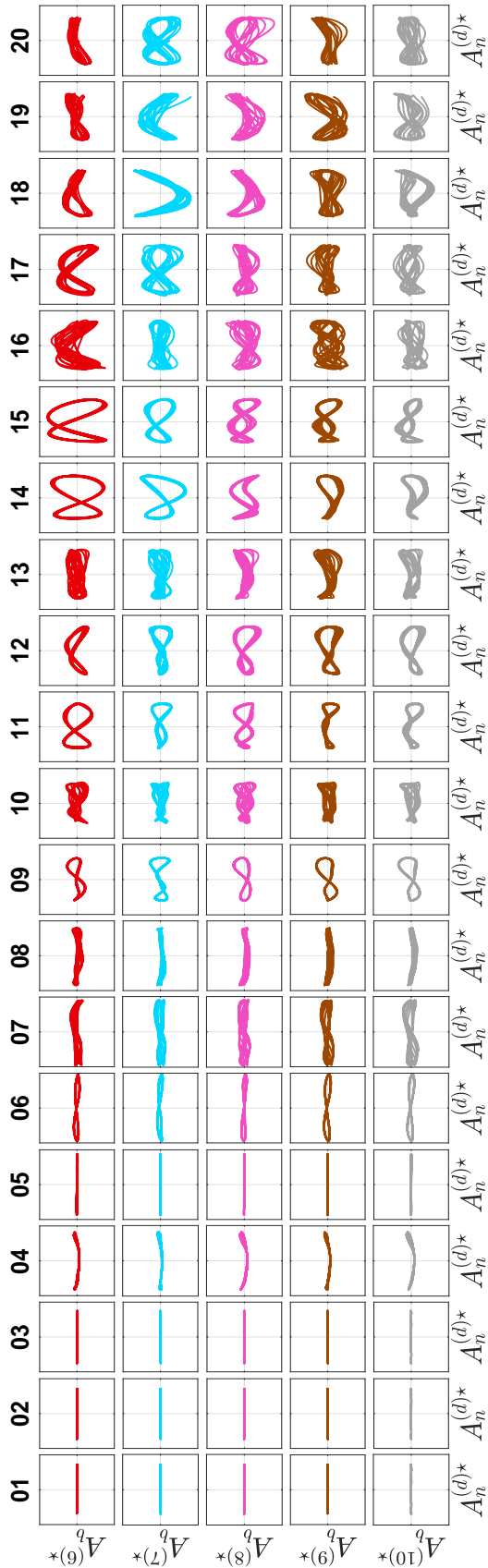
Once more, there is not enough data to characterize the modal synchronization number of the first peak, which should be heuristically expected to be $N^{(6)} = 4$. The transition between modal synchronization values occurs in $f_b^{(7)}/f_{b,N}^{(7)} \sim 1$ and the last peak is resonant, *i.e.* it lies in the region in which $N^{(6)} = 2 \rightarrow 1$.

Lastly, the eighth mode presented in Figures 4.31c-4.31d shows small amplitude response, not reaching half diameter in value. A carefully visual inspection shows that amplitude peaks occur in $f^{(d,8)*} = 0.12$ ($< 0.1D$), 0.2 ($< 0.1D$), 0.25 (0.15D), 0.32 (0.2D) and 0.44 (0.3D); an additional amplitude local maximum is displayed in $f^{(d,8)*} = 0.51$.

Among these points, all except the one in $f^{(d,8)*} = 0.44$ could be predicted using Equation 4.3, suggesting that they are probably resonant peaks. Unfortunately, there is not enough data to characterize the synchronization parameter in most of the cases.

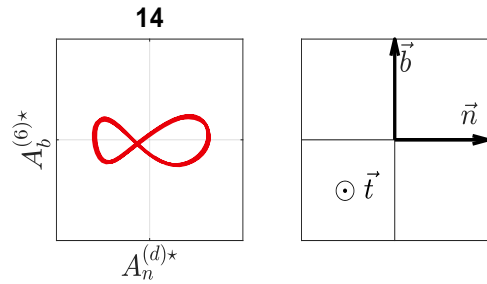
Thus, it was possible to identify synchronization transitions $N^{(6)} = 3 \rightarrow 2 \rightarrow 1$ in the vicinity of $f_b^{(8)}/f_{b,N}^{(8)} \sim 1$. The points located in $f^{(d,8)*} = 0.32$ and 0.51 are placed around the resonant region in which the transitions occur.

Figure 4.28: Modal orbits for out-of-plane modes against dominant in-plane mode; out-of-plane modes: 6th until 10th.



Source: Developed by the author.

Figure 4.29: Modal orbits and their local reference frame orientation.



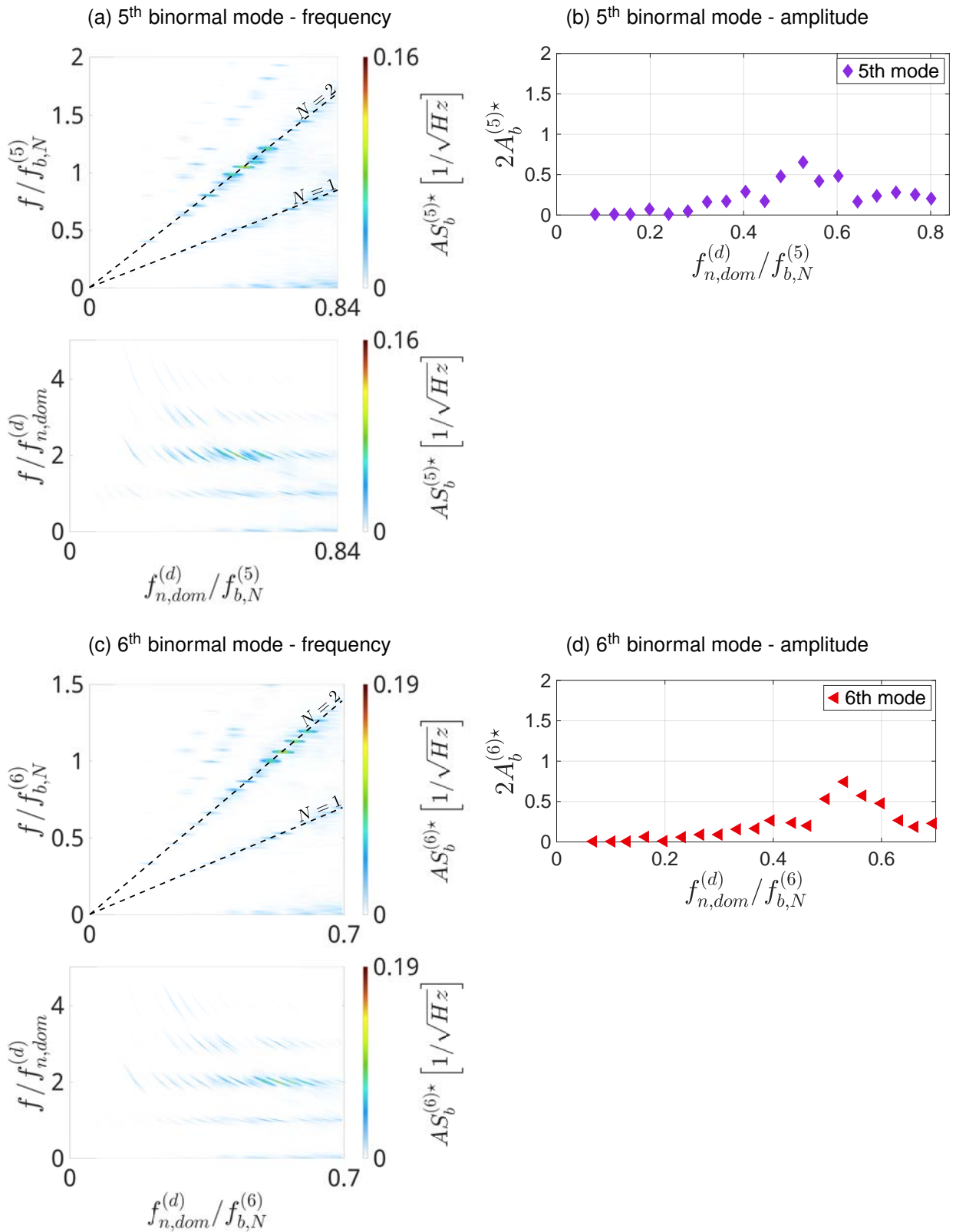
Source: Developed by the author.

Table 4.10: Ratio $f^* = f_{n,dom}^{(d)} / f_{b,N}^{(k)}$ for all test with imposed movement at the top $A_i = 17.5\text{mm}$, regarding dominant in-plane mode; out-of-plane modes: 6th until 10th.

ID	Out-of-plane modes				
	6th	7th	8th	9th	10th
01	0.07	0.06	0.05	0.04	0.04
02	0.10	0.09	0.08	0.07	0.06
03	0.13	0.11	0.10	0.08	0.07
04	0.16	0.14	0.12	0.11	0.09
05	0.20	0.17	0.15	0.13	0.11
06	0.23	0.20	0.17	0.15	0.13
07	0.27	0.23	0.20	0.17	0.15
08	0.30	0.25	0.22	0.19	0.17
09	0.33	0.28	0.25	0.22	0.19
10	0.37	0.31	0.27	0.24	0.21
11	0.40	0.34	0.29	0.26	0.23
12	0.44	0.37	0.32	0.28	0.25
13	0.46	0.39	0.34	0.30	0.27
14	0.50	0.42	0.37	0.32	0.29
15	0.53	0.45	0.39	0.34	0.30
16	0.57	0.48	0.42	0.36	0.32
17	0.60	0.51	0.44	0.39	0.34
18	0.63	0.54	0.46	0.41	0.36
19	0.66	0.56	0.49	0.43	0.38
20	0.70	0.59	0.51	0.45	0.40

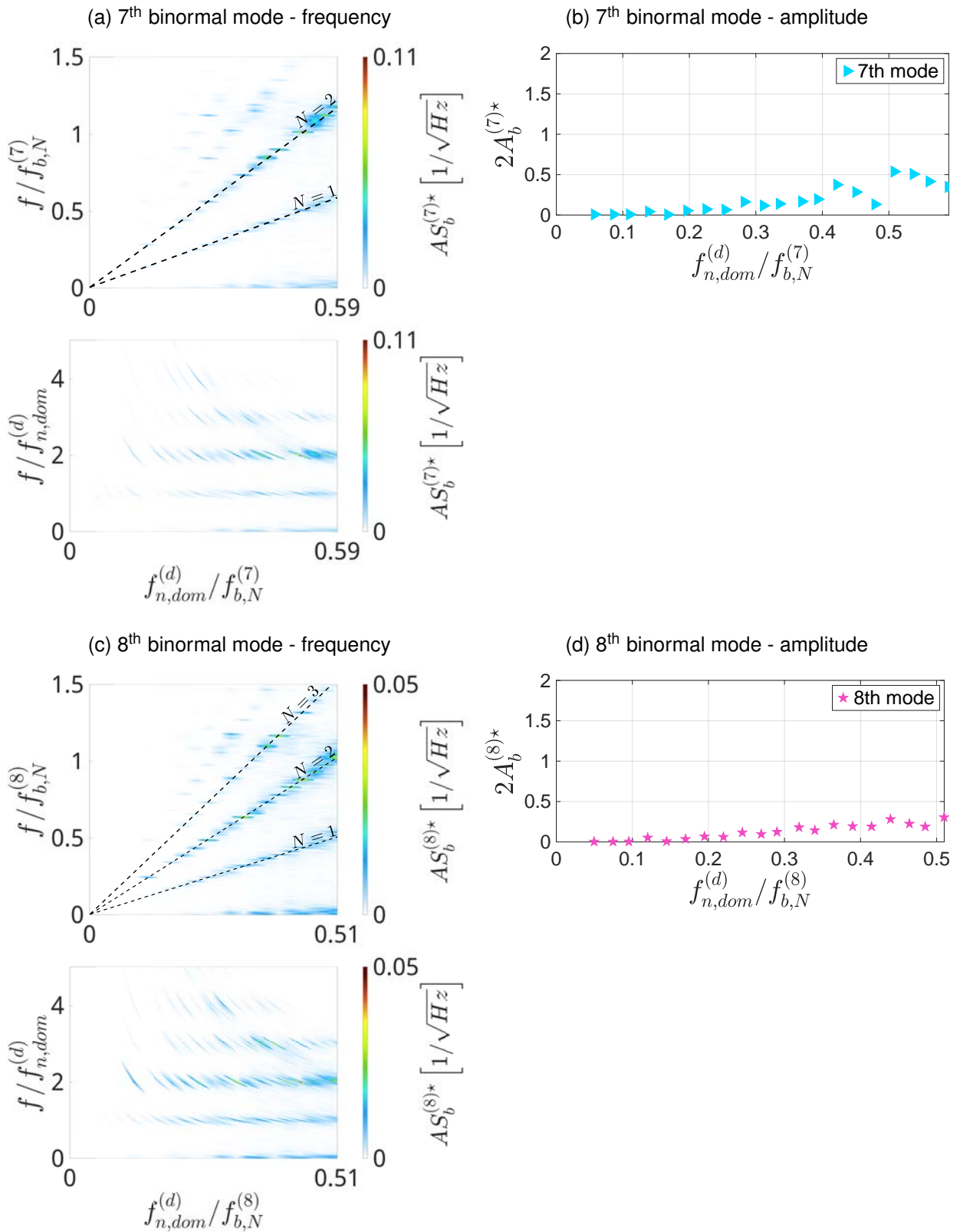
Source: Developed by the author.

Figure 4.30: Modal response of the fifth and sixth out-of-plane modes with respect to the modal frequency ratio parameter: $7 \leq KC^{(d)} \leq 10.6$.



Source: Developed by the author.

Figure 4.31: Modal response of the seventh and eighth out-of-plane modes with respect to the modal frequency ratio parameter: $7 \leq KC^{(d)} \leq 10.6$.



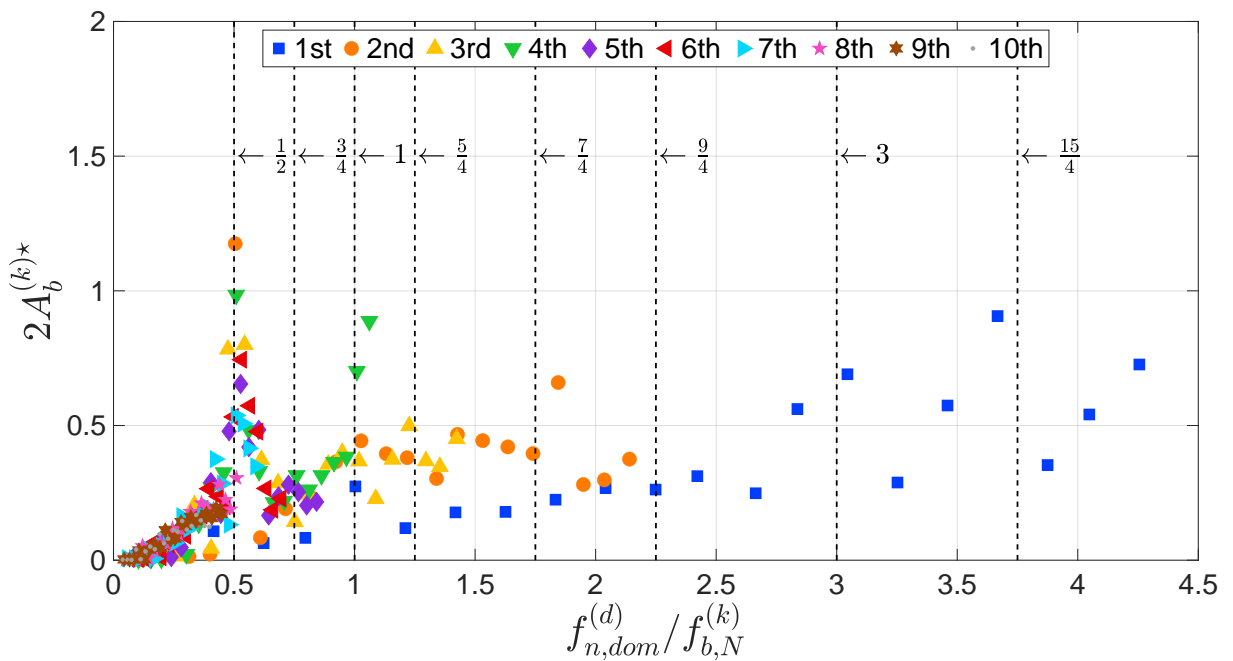
Source: Developed by the author.

4.2.4.2 Modal similarity

Figure 4.32 exhibits the modal intrasimilarity obtained in the $A_i = 17\text{mm}$ testing group. The present results is similar to the one obtained in Figure 4.22, differing from the other cases presented in Figures 4.9 and 4.15.

Similarly to Figure 4.22, the present modal intrasimilarity presents a common peak modal response in the vicinity of $f^{(d,k)\star} = 0.50$. Several modes contribute to the this common peak, namely the second, third, fourth, fifth, sixth and seventh modes.

Figure 4.32: Modal peak-to-peak amplitude response, considering all out-of-plane modes with respect to the dominant plane modal displacement and $7 \leq KC^{(d)} \leq 10.6$.



Source: Developed by the author.

The modal intrasimilarity results in Figure 4.32 also exhibit other peaks that are shared by more than one mode. For instance, there is a cluster of small peak response around $f^{(d,k)\star} = 0.75$ obtained from the fourth and fifth modes.

Although the fourth mode has a maximum value instead of a peak lying around $f^{(d,4)\star} = 1$, another shared peak resonant responses from the first, second, third and fourth modes could be observed there.

The second mode exhibits more peaks, $f^{(d,2)\star} = 1.40$ and 1.75 , and the first mode has additional peaks in $f^{(d,1)\star} = 3$ and 3.75 , and a local maximum value in the last

case.

The first mode exhibits a different behavior than the other modes, which can be attributable to the response reported in Figures 4.26a-4.26b that shows a region in which the modal synchronization parameter seems to not assume whole number value.

4.3 Intra and intersimilarities

The modal intrasimilarities obtained in Figures 4.9, 4.15, 4.22 and 4.32 evidenced that there is a set of predictable frequency ratio values in which peak amplitude responses can be observed.

The prediction takes into the account that there are descending jumps from different synchronization branches in which the measured k -th modal out-of-plane response frequency can assume a value similar to its correspondent eigenvalue, $f_b^{(k)}/f_{b,N}^{(k)} \sim 1$.

These branches are characterized by the synchronization parameter assuming an approximately whole number value, *i.e.* $N^{(k)} = 3 \rightarrow 2 \rightarrow 1$. More importantly, these frequency ratio values could be previously determined using the typical synchronization patterns observed in a given case.

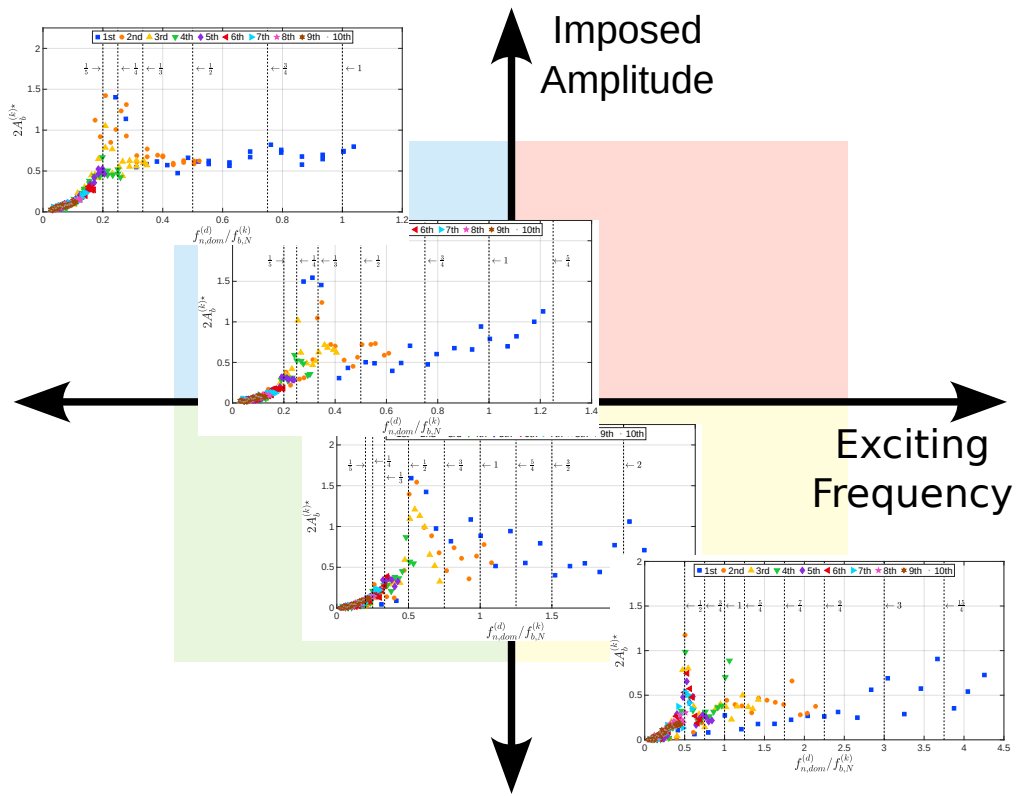
Furthermore, there are some other interesting frequency values in which a peak response can occur, assuming a non resonant nature. The same feature is also observed in the rigid cylinder cases, in which peak responses were measured around points, such as $f^* = 0.66, 0.75$, to cite a few.

These values are considered non resonant due to the synchronization observed be characterized by a value that does not correspond to the frequency ratio estimation, *i.e.* $f^* \not\sim 1/N$; alternatively, $f_r/f_N \not\sim 1$.

Since these values could be also observed in the rigid cylinder tests, it is not possible to infer, in the flexible structure context, if they are originated by the hydrodynamic oscillator, the structural one, or both.

Undoubtedly, the amount of synchronizations that can be observed in a given experimental set-up depends mostly on the imposed amplitude and exciting frequency range disposable.

Figure 4.33: Effect of imposed amplitude and exciting frequency range on the modal intrasimilarities.



Source: Developed by the author.

Note: The figure is a vector file and more details can be seen as the reader zooms-in in the digital version.

Figure 4.33 depicts that cases whose imposed amplitude may assume large values will exhibit large amplitude peaks in high synchronization branches. On the other hand, exciting the system with large frequency values will cause more relevant amplitude peaks due to higher modes responding in larger frequency ratio values.

For instance, the testing group $A_i = 105\text{mm}$ shares a common amplitude peak with the first, second and third modes at $f^{(d,k)*} \approx 0.25$, which corresponds to $N^{(k)} = 4$ in each out-of-plane response; see Figures 4.26-4.27.

The following group, $A_i = 70\text{mm}$, also shares a common peak with the first, second and third modes; however, the location is shifted towards $f^{(d,k)*} = 0.33$ due to the driving frequency range be a little broader. Some peak responses with large amplitude can be also observed at $f^{(d,k)*} \approx 1$.

In turn, the group $A_i = 35\text{mm}$ shares a common peak response at $f^{(d,k)*} \approx 0.5$, in which it is possible to observe that the fourth mode has joined the previous ones and all first, second, third and fourth modes exhibit relevant peak-to-peak amplitude response.

The effect of broadening the driven frequency range is easily seen in the next group, $A_i = 17.5\text{mm}$.

Inasmuch as the exciting frequency could achieve values up to the fourth out-of-plane mode eigenvalue, a characteristic secondary amplitude peak appears in the vicinity $f^{(d,k)*} \approx 1$ for the fourth mode and 2, for the second one. These peaks exhibit peak-to-peak displacement similar to the first response peak, located at $f_{(d,k)*} \approx 0.5$.

With exception of the group $A_i = 105\text{mm}$, the other also presented peaks above the prediction resonant range, delimited by $N^{(k)} = 1$ ($f^{(d,k)*} = 1$). Additionally, these peaks may exhibit large amplitude values.

There is evidence to suggest that experimental tests whose driven frequency range is broader will display several amplitude peaks, which can occur in higher modes, and large peak responses above the prediction range. On the other hand, cases whose imposed amplitude is large evidence that peak responses are located in higher synchronization branches.

Currently, the experimental data available cannot provide a case in which both the high imposed amplitude and broaden exciting frequency range conditions are satisfied concomitantly. This is due to the driving actuator power limitation.

Notwithstanding, the available data suggests that the hydroelastic multimodal responses share a common behavior that could be regarded as a modal intersimilarity, which is characterized by the presence of peak responses that can exhibit higher modes contributions at some frequency values, or be located in higher synchronization branches, or a combination of both.

The modal intersimilarity could also be extended to the similar behavior found in the rigid cylinder response with comparison to the multimodal ones, if modes are studied separately.

The contribution of higher modes in forming peak responses is due to the frequency range, whilst the presence of responses in higher synchronization branches as a result of larger imposed amplitude values.

Considering flexible pipes design methodology, the scenarios shown in Figure 4.33 are rather interesting due to the dichotomy presented in both the imposed amplitude and frequency range effects insofar as considering fatigue caused by the multimodal VSIV response.

For the most part, should it be possible to consider the effect of amplitude or fre-

quency one at a time, the presence of higher synchronization branches will cause some low order modes with large peak-to-peak amplitude to vibrate in high frequency values; the other way around, a broader frequency range will be responsible for higher modes oscillating in lower synchronization branches, nonetheless, higher modes can present larger local curvature variation.

On one hand, lower modes with large amplitude response, despite having small natural frequencies, can oscillate in higher synchronization branches and, thus, assuming values close to higher modes natural frequency and presenting locally small curvature variations.

On the other hand, higher modes can oscillate with large amplitude in lower synchronization branches, assuming response frequencies not much higher than their own natural one and presenting locally larger curvature variations.

Therefore, considering the available data and the modal intersimilarity, it turns out that it is necessary to evaluate fatigue damage due to the VSIV multimodal response in both conditions: large imposed amplitude with narrow frequency range (large modal amplitude in high synchronization branches); and low amplitude with broad frequency range (high modes exhibiting large modal amplitudes in low synchronization branches).

5 CONCLUSIONS AND FURTHER WORKS

(...)
*Das Ewig-Weibliche
Zieht uns hinan.*

GOETHE, J.W., *In: Faust - 2. Teil.*

5.1 Considerations on the modal methodology approach

The present work made a humbly effort to shed new light on the VSIV multimodal response of a flexible plane catenary-like circular cylinder. The current methodology applies tools of modal analysis in order to unveil some idiosyncratic features of the VSIV response, seeking for some degree of similitude with other fundamental experimental results considering rigid straight cylinders.

The catenary-like model was monitored using a high speed tracking targets cameras set that was able to detect and measure the structural displacement at each sampled instant, creating a full spacial animation of the structural response.

Even tough the tracking system measured every monitored target during the tests, the data was obtained considering a global Cartesian reference frame fixed at the anchor. Using the static configuration measured by the cameras, it was possible to compute local reference frames positioned at each monitored target. Each target displacement series was projected in the new local references frames, carrying out a linearization of the system dynamics around the static configuration.

every local reference frame was constructed using differential curves theory, obtaining at each point a tangent and normal unit vectors that spanned locally an osculating plane. The reference frame basis was completed using a third unit vector orthogonal to the osculating plane, specifying the out-of-plane (binormal) direction.

Whereas modal analysis is not a new research topic, the proposed methodology is pioneer due to the proposition of a complete modal characterization for a catenary-like structure subject to VSIV. Early analyses were carried out in the space of configura-

tion and modal analysis methods, specially wavelets, were employed just to evaluate instantaneous variations on the cylinder response within the oscillation cycle.

The amount of modes necessary to execute the modal analysis is dictated by how close the trial functions are from the system eigenfunctions. Many approaches were considered as to obtain a set of functions that could be the closest to actual model eigenfunctions.

Consequently, it was decided to use the modes obtained from a numerical model simulated in Orcaflex[®]. The numerical modes were reasoned to be the closest due to the numerical solver taking into consideration several other effects that are not represented in analytical approaches.

Orcaflex[®] also considered the effect of soil stiffness and contact at the bottom. The soft soil condition was responsible to evaluate in-plane normal modes that were little representative of the results obtained using spectral analysis. On the other hand, the binormal modes showed excellent agreement with the experimental results, including in the estimation of the structural natural frequencies.

Nonetheless, the normal modes were actually similar to the binormal ones, a results that had already been reported in previous analytic formulations. Thus, the binormal modes were used both in the in-plane and out-of-plane Galerkin's decomposition method.

Qualitative analysis showed that the firsts ten modes were sufficient to represent the structural system displacement series. This analysis was executed comparing each experimental response with its modal reconstruction one.

The modal basis was also orthonormalized with respect to the structural mass matrix and, as a result, uncoupling the modal structural inertial forces. This is an important feature on the current methodology, since it serves as basis for more fundamental considerations that arose from the hydroelastic system representation.

One of them is the causality between in-plane and out-of-plane dynamics. Contrarily to experiments carried out with rigid cylinders, the only input in the catenary-like arrangement is the imposed movement at top; thus, the in-plane and out-of-plane dynamics are both responses of the hydroelastic oscillator.

The classical VSIV is characterized by the out-of-plane movement being induced by the in-plane motion and, as both in-plane and out-of-plane are responses of the excitation at the top, it was necessary to taken into consideration an ansatz that con-

siders the in-plane motion as the driving mechanism of the out-of-plane hydroelastic response. Such ansatz made the problem physically treatable, as it was possible to establish a causality relation between the in-plane and out-of-plane oscillations.

Another innovative aspect of the devised methodology is the reinterpretation of governing parameters, determining their modal counterparts. Typical hydrodynamic parameters as the Keulegan-Carpenter's, Reynolds' and Strouhal's numbers are essential to the VSIV response characterization. This leap from the space of configuration into the modal realm was possible and based on variational methods, *i.e.* regarding the system eigenfunctions as its own generalized coordinates.

Finally, the present work also proposed a modal Reduced Order Model obtained using the modal governing parameters as to characterize the multimodal VSIV response. One key element of this modal ROM is the assumption that the dominant in-plane mode can be regarded as the main driving input of the out-of-plane hydroelastic response.

The hypothesis present in the current analysis were tested using the proposed experimental methodology, seeking a similitude paradigm between the multimodal responses with the rigid cylinder ones. Moreover, these fundamental considerations will be addressed later at the end of this chapter.

5.2 VSIV multi-modal response

Table 5.1 exhibits a summary of the VSIV experimental results reported in the rigid cylinder cases; in addition, the present multimodal results are also presented.

The results are mainly the frequency ratio values at which it was observed peak responses in the cylinders subjected to VSIV. These frequency values can be classified either resonant or not, depending on their location.

For instance, the present terminology refers as resonant to values that can be obtained considering the relations presented in Equation 4.2, *i.e.* when the frequency value is evaluated in the vicinity of a synchronization transitions.

Table 5.1: Comparison of the frequency ratio parameter values in which could be observed amplitude peak response between the rigid straight cylinder model and the present flexible catenary-like one.

Rigid straight cylinder		$f^* = f_r/f_N$
Sumer and Fredsøe (1988)		
	10	[0.5, 0.62]
	20	[0.25, 0.35], [0.38, 0.45], [0.60, 0.70]
<i>KC</i>	30	[0.15, 0.20], [0.22, 0.25], [0.28, 0.35]
	40	[0.12, 0.15], [0.15, 0.18], [0.19, 0.21], [0.23, 0.27]
Fernandes, Mirzaei Sefat, and Cascão (2014)		
	10	0.34, 0.62
	20	0.26, 0.68
<i>KC</i>	30	0.22, 0.34, 0.49
	40	0.12, 0.16, 0.25, 0.37, 0.39
Flexible catenary-like cylinder		$f^{(d,k)*} = f_{n,d}^d / f_{b,N}^{(k)}$ (approximately)
	[45.2, 48]	0.12, 0.2, 0.25, 0.3, 0.33, 0.4, 0.45, 0.5, 0.66, 0.75, 0.8, 1, 1.2, 1.45, 1.75, 2, 3, 3.67
<i>KC^(d)</i>	[30.1, 33.9]	0.2, 0.25, 0.33, 0.45, 0.5, 0.66, 0.75, 0.8, 1, 1.2, 1.45, 1.75, 2
	[13, 18]	0.2, 0.25, 0.33, 0.66, 1, 1.2
	[7, 10.6]	0.17, 0.2, 0.25, 0.33, 0.75

Source: Developed by the author.

Note: Intervals are denoted with brackets: $x \in [0, 1] \equiv 0 \leq x \leq 1$.

As reported in [Sumer and Fredsøe \(1988\)](#) and [Fernandes, Mirzaei Sefat, and Cascão \(2014\)](#), the synchronization transitions always occurs from a higher branch, characterized by a large whole number N , into a lower branch that presents the synchronization parameter $N - 1$. Considering all possible branches, the lowest synchronization allowed is characterized by $N = 1$.

Considering the multimodal approach, the same behavior is observed, presenting branches transitions around specific frequency values that can be obtained using Equation 4.3, the modal counterpart of the last one. The same applies in the modal space, the modal synchronization parameter can only admit whole number values, $N^{(k)}$, and the branch transitions are bounded to the limit $N^{(k)} = 1$.

The multimodal VSIV individual responses also showed agreement with those reported in the rigid cylinder case with respect to the imposed amplitude performed in each test. This comparison is only possible due to the pioneer use of modal governing parameters.

The rigid cylinder exhibits causality between forced oscillation and out-of-plane hydroelastic response, which is not observed in the flexible structure context due to the in-plane movement causing different values of KC distributed along structure span. In the context of VSIV, the KC dependence on the structural arc-length is also reported in [Wang et al. \(2014, 2017\)](#).

Particularly, [Wang et al. \(2017\)](#) carried out an thorough analysis on how the local values of KC acted on the general global dynamic response. The concept of a dominant KC, obtained from the maximum KC value measured along the span, was reinterpreted in the current analysis, but considering the dominant in-plane mode as main driving mechanics for the multimodal out-of-plane response.

Furthermore, the experienced KC values may differ with respect to variations in exciting frequency. Hence, it is impossible to obtain testing cases that share a fixed KC value in both plane of configuration and modal space.

Consequently, the modal reduced velocity varies considerably in different modes, as it is proportional to the KC. An alternative is also proposed in the present work, considering a reorganization in the governing parameter obtained from the Buckingham's Π theorem.

The modal frequency parameter, defined as the ratio between the dominant frequency measured in the in-plane dominant mode to each k out-of-plane eigenvalue,

$f^{(d,k)*} = f_{n,dom}^{(d,k)*} / f_{b,N}^{(k)}$, is used in lieu of the modal reduced velocity parameter, achieving better comprehension of the results.

More importantly, a thorough inspection on Table 5.1 reveals that the multimodal responses kept similarity with the rigid cylinder case, presenting resonant peaks located at frequency ratio values that can be obtained using Equations 4.2 and 4.3.

As to illustrate, resonant frequency values in the rigid cylinder case, $f^* \approx 1/N = 1, 0.5, 0.33, 0.25 \dots$, are also observable in the multimodal responses, $f^{(d,k)*} \approx 1/N^{(k)} = 1, 0.5, 0.33, 0.25 \dots$; thus, considering the lowest allowed synchronization, $N = 1$ and $N^{(k)} = 1$, the maximum frequency that can be predicted is located at 1.

Other amplitude peak responses are evidenced in other frequency values, such as $f^* \approx 0.75, 0.66, 0.4$, to mention a few. These peaks are denominated non resonant in the present work for they are not obtained using the resonance relation, $f_r / f_N \sim 1$ or $f_b^{(k)} / f_{b,N}^{(k)}$.

These non resonant peaks also displayed similarity between the rigid cylinder and catenary-like one. The non resonant peaks always occur in two cases: between two consecutive synchronization transitions, *e.g.* $0.5 < 0.66 < 1$; or above $f^* = 1$, maintaining the limit synchronization branch, $N = 1$.

Particularly, there is evidence between the rigid cylinder and the flexible catenary-like one to suggest that the resonant peaks may occur in frequency ratios that assume rational number values. Although this condition is sufficient, it is not necessary for other more complex peaks also showed in the multimodal response case.

Lastly, the concepts of modal intrasimilarity and the intersimilarity one are proposed in the present work. The former is characterized by the common response or amplitude peaks growth tendencies shares by all modes in a given testing group; in turn, the latter refers to the common general response that can be observed comparing each testing group cases.

The available data showed that the intrasimilarity is present in every analysed testing group. The imposed amplitude can responsible for the presence of lower modes vibrating in higher synchronization branches, being able to assume response frequencies much higher than its own natural frequency. The lower modes exhibit large amplitude response in these lower branches.

In turn, large exciting frequency values can cause higher modes to vibrate in lower synchronization branches, assuming large amplitude values. These higher modes ex-

hibit large natural frequency values and, due to their eigenfunctions, they also present larger curvature variations.

Regarding fatigue evaluation, the modal intersimilarity suggests it is possible that, depending on the maximum exciting frequency value in a given range, considerable damage could be accumulated at the cylinder bottom-sag due to VSIV even in cases presenting small imposed amplitudes.

Under the perspective of risers design and analysis methodologies, fatigue damage could be assessed individually for each mode using the present results in the available testing conditions as to determine in which mode and condition the accumulated damage is larger.

Currently, there is no available data for a critical case in which the imposed amplitude and maximum driving frequency are concomitantly larger in value.

5.3 Final thoughts on the VSIV modal approach

During the experimental analysis carried out in the present work, it was possible to verify that the VSIV multimodal response kept similarity with the intrinsic responses reported in the technical literature.

The evidence shows that modal responses could be studied individually in a first approximation for they behave equivalently to the classical VSIV response found in rigid straight cylinders.

Additionally, the VSIV can contribute to accumulate fatigue damage and failure in *in-situ* risers; the obtained results can be used in order to devise new methodology aspects for design and analysis of such structures. Thus, the present work also presents a relevant contribution for engineering project and the offshore industry.

The results also confirmed that the causality relation between the in-plane movement and the out-of-plane response is defensible, assuming that the out-of-plane motion is smaller than the in-plane one. In this context, the out-of-plane response displays a second order dynamic role in the in-plane movement.

Moreover, the Galerkin's decomposition of both structural and hydrodynamic oscillators using the structural eigenfunctions could be explored and, in the context of the VSIV and the available data, the assumption proved to be defensible and the structural oscillator exhibited some degree of dominance in the coupled hydroelastic system.

A key element of the present analysis is the construction of modal parameters that could govern the multimodal VSIV response in some degree. These modal governing parameters assisted in the attainment of similarity between the rigid cylinder response with the flexible catenary-like one.

The dominant modal KC, $KC^{(d)}$, displayed a protagonist role in the characterization of the VSIV multimodal response. Particularly, the assumption that the dominant in-plane mode should be regarded as main driving mechanism to the out-of-plane response showed great agreement with fundamental experimental results.

More significantly, the modal intersimilarity suggests that the devised methodology displayed robustness in cases whose sub-dominant KC assumed values similar to the dominant one.

Although the reduced velocity was inherent from the VIV context to the VSIV one, the out-of-plane multimodal responses showed lesser comprehensibility using this parameter. This may be attributable to the variation on the KC from a testing case to other in a same group, as the reduced velocity can be written as function of KC.

Using the Buckingham's Π theorem, it was possible to choose a second modal parameter, the frequency ratio, $f^{(d,k)}$ ¹, which was more suitable for the experimental analysis. Considering that the VSIV is caused by a forced oscillation in a dynamic system, this parameter could be interpreted as an extension of the frequency ratio used to study forced linear damped systems response.

Finally, if the reader wants a brief summary of some contributions found in the present work, they are:

- Experimental methodology, using linear modal analysis in order to successfully represent a complex hydroelastic system;
- Finding similarity between the fundamental rigid cylinder results with the VSIV multimodal response;
- Exploring the Galerkin's decomposition of the hydroelastic system showed that, in the context of VSIV, the hydrodynamic oscillator could be carried out using the structural eigenfunctions;
- Use of modal governing parameters;

¹In this context, characterized by the dominant in-plane mode.

- A critic review on using the reduced velocity as governing parameter, suggesting the frequency ratio as more meaningful one;
- Representation of the VSIV multimodal response using ROMs as a function of modal governing parameters;
- The present results can be used for calibration and benchmarking of predictions models.

It is noteworthy that the devised methodology using modal governing parameters is pioneer in the offshore context and such devised experimental methodology can be adapted for other phenomena.

5.4 Further works

There are many aspects that could improve the present experimental methodology, specially replicating it in other contexts, using other hydroelastic phenomena; thus, enhancing its robustness.

It would also be interesting to explore the nature of modal governing parameter in the hydrodynamic field, exploring new relations amid them, specially characterizing the Reynolds' and Strouhal's numbers in multimodal hydroelastic responses.

Although experimental campaigns are expensive and arduous, the necessity of more experimental data is extreme important as to calibrate new predictive models and serve as paradigm for other numerical methods.

Particularly, experimental tests with different models, reaching the conditions of large imposed amplitude and maximum exciting frequency values, are extremely necessary in order to have a better assessment of fatigue damage in a catenary-like cylinder.

In-situ experiments, with riser models in full-scale, by using new offshore laboratory facilities, for sure can be devised in a near future, where the present methodology could be applied, after proper adaptations to the real scenario.

REFERENCES¹

- ARANHA, J. A. P.; MARTINS, C. A.; PESCE, C. P. Analytical Approximation For the Dynamic Bending Moment At the Touchdown Point of a Catenary Riser. *International Journal of Offshore and Polar Engineering*, v. 7, n. 04, Dec. 1997. ISSN 1053-5381. eprint: <https://onepetro.org/IJOPE/article-pdf/2188947/isope-97-07-4-293.pdf>.
- CAMARGO, E. D. L. B. de. *Desenvolvimento de algoritmo de imagens absolutas de tomografia por impedância elétrica para uso clínico*. May 2013. PhD – Universidade de São Paulo, São Paulo. DOI: [10.11606/T.3.2013.TDE-26062014-205827](https://doi.org/10.11606/T.3.2013.TDE-26062014-205827).
- CANN, M. *A Data-Driven Approach for Generating Vortex Shedding Regime Maps for an Oscillating Cylinder*. 2022. PhD – University of Waterloo, Waterloo, UK. Last accessed: 01/20/2022. eprint: https://uwspace.uwaterloo.ca/bitstream/handle/10012/17930/Cann_Matthew.pdf?sequence=3.
- CHATJIGEORGIU, I. K. Application of the WKB method to catenary-shaped slender structures. *Mathematical and Computer Modelling*, v. 48, n. 1, p. 249–257, 2008. ISSN 0895-7177. DOI: [10.1016/j.mcm.2007.08.012](https://doi.org/10.1016/j.mcm.2007.08.012).
- CHATJIGEORGIU, I. K.; MAVRAKOS, S. A. The 3D Nonlinear Dynamics of Catenary Slender Structures for Marine Applications. In: EVANS, T. (Ed.). *Nonlinear Dynamics*. Vukovar, Croatia: IntechOpen, 2010. chap. 8, p. 173–198. ISBN 978-953-7619-61-9.
- ETIENNE, S.; BIOLLEY, F.; FONTAINE, E.; C., L.; HEURTIER, J. M. Numerical Simulations of Vortex-Induced Vibrations of Slender Flexible Offshore Structures. In: ISOPE International Ocean and Polar Engineering Conference. June 2001. ISOPE-I-01-295. Last accessed: 01/25/2022. eprint: <https://onepetro.org/ISOPEIOPEC/proceedings-pdf/ISOPE01/All-ISOPE01/ISOPE-I-01-295/1889839/isope-i-01-295.pdf>.
- FACCHINETTI, M. L.; DE LANGRE, E.; BIOLLEY, F. Vortex-Induced Waves Along Cables. In: ASME International Mechanical Engineering Congress and Exposition.

¹In agreement with Brazilian Association of Technical Standards (ABNT NBR 6023).

- New Orleans, Louisiana, USA: American Society of Mechanical Engineers, June 2008. p. 195–205. ISBN 0-7918-3659-2. DOI: [10.1115/IMECE2002-32161](https://doi.org/10.1115/IMECE2002-32161).
- FALTINSEN, O. *Sea Loads on Ships and Offshore Structures*. Cambridge University Press, 1993. (Cambridge Ocean Technology Series). ISBN 978-0-521-45870-2.
- FERNANDES, A. C.; MIRZAEI SEFAT, S.; CASCÃO, L. V. Fundamental behavior of Vortex Self Induced Vibration (VSIV). *Applied Ocean Research*, Elsevier, v. 47, p. 183–191, Aug. 2014. ISSN 0141-1187. DOI: [10.1016/J.APOR.2014.04.003](https://doi.org/10.1016/J.APOR.2014.04.003).
- FERNANDES, A. C.; MIRZAEI SEFAT, S.; CASCÃO, L. V.; FRANCISS, R. Analysis of PIV Tests Results of the Vortex Self Induced Vibration (VSIV) of a Cylinder. In: PROCEEDINGS OF THE INTERNATIONAL CONFERENCE ON OFFSHORE MECHANICS AND ARCTIC ENGINEERING - OMAE. American Society of Mechanical Engineers Digital Collection, Aug. 2012. v. 5, p. 915–921. ISBN 978-0-7918-4492-2. DOI: [10.1115/OMAE2012-84021](https://doi.org/10.1115/OMAE2012-84021).
- FERNANDES, A. C.; SILVA, E. M. C.; FRANCISS, R.; COELHO, F. M.; NETO, S. F. S. VSIV (Vortex Self-Induced Vibration) Kinematics. In: VOLUME 5: MATERIALS TECHNOLOGY; CFD AND VIV. ASME, Jan. 2008. p. 847–854. ISBN 978-0-7918-4822-7. DOI: [10.1115/OMAE2008-57579](https://doi.org/10.1115/OMAE2008-57579).
- FERNANDES, A. C.; MIRZAEI SEFAT, S.; CASCÃO, L. V.; BOAS, P. V.; FRANCIS, R. Further Investigations on Vortex Self Induced Vibration (VSIV). In: VOLUME 7: CFD AND VIV; OFFSHORE GEOTECHNICS. ASME, Jan. 2011. p. 651–656. ISBN 978-0-7918-4439-7. DOI: [10.1115/OMAE2011-50187](https://doi.org/10.1115/OMAE2011-50187).
- FRANZINI, G. R.; FUJARRA, A. L. C.; MENEGHINI, J. R.; KORKISCHKO, I.; FRANCISS, R. Experimental investigation of vortex-induced vibration on rigid, smooth and inclined cylinders. *Journal of Fluids and Structures*, v. 25, n. 4, p. 742–750, 2009. DOI: [0.1016/j.jfluidstructs.2009.01.003](https://doi.org/10.1016/j.jfluidstructs.2009.01.003).
- FRANZINI, G. R.; GONÇALVES, R. T.; PESCE, C. P.; FUJARRA, A. L. C.; MAZZILLI, C. E. N.; MENEGHINI, J. R.; MENDES, P. Vortex-Induced Vibrations Experiments with a Very Flexible Cylinder under Tension Modulation: Fourier Transform and Hilbert-Huang Spectral Analysis. In: PROCEEDINGS OF THE 15TH (2013) INTERNATIONAL SYMPOSIUM ON DYNAMIC PROBLEMS OF MECHANICS (DINAME). Búzios-RJ, Brazil, 2013.
- FRANZINI, G. R.; PEREIRA, A. A. P.; FUJARRA, A. L. C.; PESCE, C. P. Experiments on VIV under frequency modulation and at constant Reynolds number. In: PRO-

- CEEDINGS OF THE 27RD (2008) INTERNATIONAL CONFERENCE ON OCEAN, OFFSHORE AND ARCTIC ENGINEERING. 2008. DOI: [10.1115/OMAE2008-57957](https://doi.org/10.1115/OMAE2008-57957).
- FRANZINI, G. R.; PESCE, C. P.; GONÇALVES, R. T.; FUJARRA, A. L. C.; MENDES, P. Experimental investigations on Vortex-Induced Vibrations with a long flexible cylinder. Part I: modal-amplitude analysis with a vertical configuration. In: PROCEEDINGS of the 11th International Conference on Flow-Induced Vibration-FIV2016. 2016. Last accessed: 05/20/2022. eprint: <http://sites.poli.usp.br/p/guilherme.franzini/Conferences/Experimental%20Investigation%20on%20VIV%20-%20Part%20I%20-%20Franzini%20et%20al.pdf>.
- FRANZINI, G. R.; PESCE, C. P.; GONÇALVES, R. T.; FUJARRA, A. L. C.; MENEGHINI, J. R. An experimental investigation on frequency modulated VIV in a water channel. In: IUTAM SYMPOSIUM ON BLUFF BODIES WAKES AND VORTEX-INDUCED VIBRATIONS CONFERENCE, BBVIV-6. Capri Island, 2010.
- FRANZINI, G. R.; PESCE, C. P.; GONÇALVES, R. T.; FUJARRA, A. L. C.; PEREIRA, A. A. P. Concomitant Vortex Induced Vibration Experiments: a Cantilevered Flexible Cylinder and a Rigid Cylinder Mounted on a Leaf-spring Apparatus. In: PROCEEDINGS OF THE 14TH (2011) INTERNATIONAL SYMPOSIUM ON DYNAMIC PROBLEMS OF MECHANICS (DINAME). São Sebastião-SP, Brazil, 2011. DOI: [10.1007/s40430-013-0095-x](https://doi.org/10.1007/s40430-013-0095-x).
- FRANZINI, G. R.; PESCE, C. P.; SALLES, R.; GONCALVES, R. T.; FUJARRA, A. L. C.; MENDES, P. Experimental Analysis of a Vertical and Flexible Cylinder in Water: Response to Top Motion Excitation and Parametric Resonance. *Journal of Vibration and Acoustics*, v. 137, 2015. doi 10.1115/1.4029265. DOI: [10.1115/1.4029265](https://doi.org/10.1115/1.4029265).
- FRANZINI, G. R.; PESCE, C. P.; SALLES, R.; GONÇALVES, R. T.; FUJARRA, A. L. C.; MENDES, P. Experimental analysis of a vertical and flexible cylinder in water: Response to top motion excitation and parametric resonance. In: INTERNATIONAL CONFERENCE ON OCEAN, OFFSHORE AND ARCTIC ENGINEERING (OMAE). PROCEEDINGS OF THE 33RD (2014) INTERNATIONAL CONFERENCE ON OCEAN, OFFSHORE AND ARCTIC ENGINEERING. San Francisco, USA, 2014. v. 2. ISBN 978-0-7918-4540-0. DOI: [10.1115/OMAE2014-24178](https://doi.org/10.1115/OMAE2014-24178).
- FRANZINI, G. R.; SANTOS, C. C. P.; PESCE, C. P.; MAZZILLI, C. E. N. Parametric excitation of an immersed, vertical and slender beam using reduced-order models: influence of hydrodynamic coefficients. *Marine Syst Ocean Technol*, 2016. DOI: [doi10.1007/s40868-016-0013-z](https://doi.org/10.1007/s40868-016-0013-z).

- FRANZINI, G. R.; PESCE, C. P.; GONÇALVES, R. T.; MENDES, P.; FUJARRA, A. L. C. Experimental investigations on Vortex-Induced Vibrations with a long flexible cylinder. Part II: effect of axial motion excitation in a vertical configuration. In: PROCEEDINGS of the 11th International Conference on Flow-Induced Vibration. 2016. Last accessed: 05/20/2022. eprint: <http://sites.poli.usp.br/p/guilherme.franzini/Conferences/Experimental%20Investigation%20on%20VIV%20-%20Part%20II%20-%20Franzini%20et%20al.pdf>.
- FU, B.; WAN, D.; HU, Z. Vortex-Induced Vibrations of a Flexible Cylinder Experiencing an Oscillatory Flow. In: ISOPE. PROCEEDINGS OF THE 27TH (2017) INTERNATIONAL OCEAN AND POLAR ENGINEERING CONFERENCE. San Francisco, California, USA: OnePetro, June 2017. p. 1264–1270. Last accessed: 01/20/2022. ISBN 978-1-880653-97-5. eprint: <https://onepetro.org/ISOPEIOPEC/proceedings-abstract/ISOPE17/All-ISOPE17/ISOPE-I-17-020/17129>.
- FU, S.; WANG, J.; BAARHOLM, R.; WU, J.; LARSEN, C. M. Features of Vortex-Induced Vibration in Oscillatory Flow. *Journal of Offshore Mechanics and Arctic Engineering*, v. 136, n. 1, p. 011801, Nov. 2013. ISSN 0892-7219. DOI: [10.1115/1.4025759](https://doi.org/10.1115/1.4025759).
- _____. VIV of Flexible Cylinder in Oscillatory Flow. In: PROCEEDINGS OF THE INTERNATIONAL CONFERENCE ON OFFSHORE MECHANICS AND ARCTIC ENGINEERING (OMAE). American Society of Mechanical Engineers Digital Collection, Nov. 2013. v. 7, v007t08a021. ISBN 978-0-7918-5541-6. DOI: [10.1115/OMAE2013-10348](https://doi.org/10.1115/OMAE2013-10348).
- FUJARRA, A. L. C. *Estudo em modelo reduzido de tubo flexível e liso, submetido ao fenômeno de vibração induzida por emissão de vórtices*. 1997. MA thesis – Escola Politécnica da Universidade de São Paulo, Escola Politécnica da Universidade de São Paulo, São Paulo, Brazil. In Portuguese.
- _____. *Estudos experimentais e analíticos das vibrações induzidas pela emissão de vórtices em cilindros flexíveis e rígidos*. 2002. PhD thesis – Universidade de São Paulo, São Paulo.
- FUJARRA, A. L. C.; PESCE, C. P.; FLEMMING, F.; WILLIAMSON, C. H. K. Vortex-induced Vibration of a Flexible Cantilever. *Journal of Fluids and Structures*, Academic Press, v. 15, n. 3-4, p. 651–658, Apr. 2001. ISSN 0889-9746. DOI: [10.1006/JFLS.2000.0368](https://doi.org/10.1006/JFLS.2000.0368).

- FUJARRA, A. L. C.; PESCE, C. P.; PARRA, P. P. H. Vortex induced vibrations experiments on a flexible cylinder. In: THE 8TH INTERNATIONAL OFFSHORE AND POLAR ENGINEERING CONFERENCE (OMAE). 1998. v. 3, p. 393–399. eprint: <https://onepetro.org/ISOPEIOPEC/proceedings-pdf/ISOPE98/All-ISOPE98/ISOPE-I-98-253/1938087/isope-i-98-253.pdf>.
- GONÇALVES, R. T.; C.P. PESCE, G. R. F. ans; FUJARRA, A. L. C.; MENDES, P. VIV experiments with a semi-immersed vertical flexible cylinder driven by top motion in a re-circulating water channel. In: THE 65TH ANNUAL MEETING OF THE APS DIVISION OF FLUID DYNAMICS. 2012. v. 57.
- GONÇALVES, R. T.; FRANZINI, G. R.; ROSETTI, G. F.; FUJARRA, A. L. C.; NISHIMOTO, K. Analysis methodology for vortex-induced motions (VIM) of a monocolumn platform applying the hilbert-huang transform method. *Journal of Offshore Mechanics and Arctic Engineering*, v. 134, n. 1, p. 011103-1–011103-7, 2012. DOI: [10.1115/1.4003493](https://doi.org/10.1115/1.4003493).
- GOPALKRISHNAN, R. *Vortex-Induced Forces on Oscillating Bluff Cylinders*. 1993. s. 1–248. PhD Thesis – MIT.
- GRANT, R.; LITTON, R.; FINN, L.; MAHER, J.; LAMBRAKOS, K. Highly Compliant Rigid Risers: Field Test Benchmarking a Time Domain VIV Algorithm. In: PROCEEDINGS OF THE ANNUAL OFFSHORE TECHNOLOGY CONFERENCE. OnePetro, May 2000. v. 2, p. 547–555. DOI: [10.4043/11995-MS](https://doi.org/10.4043/11995-MS).
- GRANT, R. G.; LITTON, R. W.; MAMIDIPUDI, P. Highly Compliant Rigid (HCR) Riser Model Tests and Analysis. In: PROCEEDINGS OF THE ANNUAL OFFSHORE TECHNOLOGY CONFERENCE. OnePetro, May 1999. v. 2. DOI: [10.4043/10973-MS](https://doi.org/10.4043/10973-MS).
- HOFFMAN, D.; ISMAIL, N. M.; NIELSEN, R.; CHANDWANI, R. The Design of Flexible Marine Risers in Deep and Shallow Water. In: (OTC Offshore Technology Conference). OTC-6724-MS. DOI: [10.4043/6724-MS](https://doi.org/10.4043/6724-MS).
- HOLOBORODKO, P. *Smooth Noise Robust Differentiators*. 2008. <http://www.holoborodko.com/pavel/numerical-methods/numerical-derivative/smooth-low-noise-differentiators/>. Last accessed: 11/15/2021.
- HUERA-HUARTE, F. J. *Multi-mode Vortex-Induced Vibrations of a Flexible Circular Cylinder*. 2006. PhD thesis – Imperial College, Imperial College, London, England.

- IZHIKEVICH, E. M.; KURAMOTO, Y. Weakly Coupled Oscillators. *Encyclopedia of Mathematical Physics*, Elsevier, v. 5, p. 448–453, 2006. Last Accessed: 03/17/2022. eprint: <https://www.izhikevich.org/publications/encwco.pdf>.
- KOZAKIEWICZ, A.; SUMER, B. M.; FREDSE, J. CrossFlow Vibrations of Cylinder in Irregular Oscillatory Flow. *Journal of Waterway, Port, Coastal, and Ocean Engineering*, American Society of Civil Engineers, v. 120, n. 6, p. 515–534, Nov. 1994. ISSN 0733-950X. DOI: [10.1061/\(ASCE\)0733-950X\(1994\)120:6\(515\)](https://doi.org/10.1061/(ASCE)0733-950X(1994)120:6(515)).
- LE CUNFF, C.; BIOLLEY, F.; DAMY, G. Experimental and Numerical Study of Heave-Induced Lateral Motion (HILM). In: 24TH INTERNATIONAL CONFERENCE ON OFFSHORE MECHANICS AND ARCTIC ENGINEERING. ASME, 2005. v. 3, p. 757–765. ISBN 0-7918-4197-9. DOI: [10.1115/OMAE2005-67019](https://doi.org/10.1115/OMAE2005-67019).
- LE CUNFF, C.; BONNISSEL, M.; SZYDLOWSKI, J.; DAMY, G. Modeling of Heave Induced Lateral Motion. In: POLAR AND ARCTIC SCIENCES AND TECHNOLOGY. ASME, 2009. v. 5. (CFD and VIV), p. 639–645. ISBN 978-0-7918-4345-1. DOI: [10.1115/OMAE2009-79652](https://doi.org/10.1115/OMAE2009-79652).
- LIFE&MO. *RT-1-M1. Dinâmica não-linear de Risers: Modelagem matemática da dinâmica de risers através de técnicas de redução fazendo uso de representação por modos não-lineares*. Technical Report. Escola Politécnica, Universidade de São Paulo. São Paulo, Brazil, 2011. Restricted Access. In Portuguese.
- _____. *RT-1-M2. Dinâmica não-linear de Risers: Modelagem no domínio do tempo com modelos fenomenológicos de VIV*. Technical Report. Escola Politécnica, Universidade de São Paulo. São Paulo, Brazil, 2011. Restricted Access. In Portuguese.
- _____. *RT-1-M4. Dinâmica Não-linear de Risers: experimentos hidroelásticos com cilindros flexíveis e modelos de risers. Concepção e técnicas experimentais*. Technical Report. Escola Politécnica, Universidade de São Paulo. São Paulo, Brazil, 2011. Restricted Access. In Portuguese.
- _____. *RT-2-M1. Dinâmica não-linear de Risers: Modelagem matemática da dinâmica de risers através de técnicas de redução fazendo uso de representação por modos não-lineares*. Technical Report. Escola Politécnica, Universidade de São Paulo. São Paulo, Brazil, 2011. Restricted Access. In Portuguese.
- _____. *RT-2-M4. Dinâmica Não-linear de Risers: experimentos hidro-elásticos com cilindros flexíveis e modelos reduzidos de risers: construção e caracterização de*

modelos e planejamento de ensaios. Technical Report. Escola Politécnica, Universidade de São Paulo. São Paulo, Brazil, 2011. Restricted Access. In Portuguese.

LIFE&MO. *RT-3.1-M4. Dinâmica Não-linear de Risers: Experimentos hidroelásticos com cilindros flexíveis verticais em canal de água recirculante (NDF)*. Technical Report. Escola Politécnica, Universidade de São Paulo. São Paulo, Brazil, 2012. Restricted Access. In Portuguese.

_____. *RT-3.2-M4. Dinâmica Não-linear de Risers: Experimentos hidroelásticos com modelo imerso de riser em catenária, sujeito à imposição de movimentos verticais no topo*. Technical Report. Escola Politécnica, Universidade de São Paulo. São Paulo, Brazil, 2012. Restricted Access. In Portuguese.

_____. *RT-3.3-M4. Dinâmica Não-linear de Risers: Experimentos hidroelásticos com modelo vertical de riser sujeito à correnteza uniforme e a imposição de movimentos verticais no topo (IPT)*. Technical Report. Escola Politécnica, Universidade de São Paulo. São Paulo, Brazil, 2012. Restricted Access. In Portuguese.

_____. *RT-3.4-M4. Dinâmica Não-linear de Risers: Experimentos hidroelásticos com modelo imerso de riser em catenária sujeito à correnteza uniforme e a imposição de movimentos verticais no topo (IPT)*. Technical Report. Escola Politécnica, Universidade de São Paulo. São Paulo, Brazil, 2012. Restricted Access. In Portuguese.

LIU, C.; FU, S.; ZHANG, M.; REN, H. Time varying hydrodynamics identification of a flexible riser under multi-frequency vortex-induced vibrations. In: PROCEEDINGS OF THE INTERNATIONAL CONFERENCE ON OFFSHORE MECHANICS AND ARCTIC ENGINEERING - OMAE. American Society of Mechanical Engineers (ASME), June 2017. v. 2. ISBN 978-0-7918-5764-9. DOI: [10.1115/OMAE2017-61261](https://doi.org/10.1115/OMAE2017-61261).

_____. Time-varying hydrodynamics of a flexible riser under multi-frequency vortex-induced vibrations. *Journal of Fluids and Structures*, Academic Press, v. 80, p. 217–244, July 2018. ISSN 10958622. DOI: [10.1016/j.jfluidstructs.2018.03.004](https://doi.org/10.1016/j.jfluidstructs.2018.03.004).

LIU, C.; FU, S.; ZHANG, M.; REN, H.; XU, Y. Hydrodynamics of a flexible cylinder under modulated vortex-induced vibrations. *Journal of Fluids and Structures*, Academic Press, v. 94, p. 102913, Apr. 2020. ISSN 10958622. DOI: [10.1016/j.jfluidstructs.2020.102913](https://doi.org/10.1016/j.jfluidstructs.2020.102913).

- LU, Z.; FU, S.; ZHANG, M.; REN, H. An efficient time-domain prediction model for vortex-induced vibration of flexible risers under unsteady flows. *Marine Structures*, Elsevier, v. 64, p. 492–519, Mar. 2019. ISSN 0951-8339. DOI: [10.1016/J.MARSTRU C.2018.12.005](https://doi.org/10.1016/J.MARSTRU C.2018.12.005).
- MA, L.; LIN, K.; FAN, D.; WANG, J.; TRIANTAFYLLOU, M. S. Flexible cylinder flow-induced vibration. *Phys. Fluids*, v. 34, p. 011302-1–011302-22, 2022. DOI: [10.1063/5.0078418](https://doi.org/10.1063/5.0078418).
- MARK CHANG, S. H.; ISHERWOOD, M. Vortex-Induced Vibrations of Steel Catenary Risers and Steel Offloading Lines due to Platform Heave Motions. In: PROCEEDINGS OF THE ANNUAL OFFSHORE TECHNOLOGY CONFERENCE. Houston, Texas: OnePetro, May 2003. 2003-May, p. 467–472. ISBN 978-1-55563-250-2. DOI: [10.4043/15106-MS](https://doi.org/10.4043/15106-MS).
- MEIROVITCH, L. *Computational methods in structural dynamics*. Alphen aan den Rijn, Netherlands: Sijthoff & Noordhoff International Publishers, 1980. ISBN 90-286-0580-0.
- MOROOKA, C.; TSUKADA, R.; SILVA, S. da; FRANCISS, R.; MATT, C. Model test of a steel catenary riser in a towing tank. In: THE 28TH INTERNATIONAL CONFERENCE ON OCEAN, OFFSHORE AND ARCTIC ENGINEERING. 2009. v. 3. (393-400). doi [10.1115/OMAE2009-79499](https://doi.org/10.1115/OMAE2009-79499).
- NESHAMAR, O. E.; VAN DER A, D. A.; O'DONOGHUE, T. Flow-induced vibration of a cantilevered cylinder in oscillatory flow at high KC. *Journal of Fluids and Structures*, Academic Press, v. 109, p. 103476, Feb. 2022. ISSN 0889-9746. DOI: [10.1016/J.JFLUIDSTRUCTS.2021.103476](https://doi.org/10.1016/J.JFLUIDSTRUCTS.2021.103476).
- PELLEGRINI, S. d. P. *Estimação dinâmica em tomografia por impedância elétrica com modelos adaptativos*. Mar. 2019. PhD thesis – Universidade de São Paulo, São Paulo. DOI: [10.11606/T.3.2019.TDE-29052019-085809](https://doi.org/10.11606/T.3.2019.TDE-29052019-085809).
- PESCE, C. P. *Mecânica de Cabos e Tubos Submersos Lançados em “Catenária”*: Uma Abordagem Analítica e Experimental. São Paulo, Brazil, 1997. Habilitation thesis. Escola Politécnica da Universidade de São Paulo, 1997. In Portuguese.
- _____. Riser Dynamics: experiments with small scale models. In: LABOCEANO - TEN-YEARS ANIVERSARY CELEBRATION WORKSHOP. Rio de Janeiro, Brazil, 2013. Rio de Janeiro, Brazil. Presentation.

- PESCE, C. P.; ARANHA, J. A. P.; MARTINS, C. A. *Modelo de análise da dinâmica de um SCR – Desenvolvimento de metodologia de projeto de risers rígidos em catenária*. 1996. Relatório Técnico, Escola Politécnica da Universidade de São Paulo - EPUSP. Projeto de Pesquisa para a Petrobras. In Portuguese.
- PESCE, C. P.; ARANHA, J. A. P.; MARTINS, C. A.; PINTO, M. M. O. *Análise preliminar de três risers rígidos em catenária para operação na Bacia de Campos*. 1994. Relatório Técnico, Escola Politécnica da Universidade de São Paulo - EPUSP. Projeto de Pesquisa para a Petrobras. In Portuguese.
- PESCE, C. P.; ARANHA, J. A. P.; MARTINS, C. A.; RICARDO, O. G. S.; SILVA, S. Dynamic curvature in catenary risers at the touch down point region: An experimental study and the analytical boundary-layer solution. *International Journal of Offshore and Polar Engineering*, v. 8, n. 4, p. 302–310, 1998. eprint: <https://onepetro.org/ISOPEIOPEC/proceedings-pdf/ISOPE97/A11-ISOPE97/ISOPE-I-97-252/1949059/isope-i-97-252.pdf>.
- PESCE, C. P.; FUJARRA, A. L. C. *Vibrações induzidas pela emissão de vórtices: Estimativa da vida Útil em um riser vertical*. 1997. Relatório Técnico, Escola Politécnica da Universidade de São Paulo – EPUSP. Projeto de Pesquisa para a Petrobras. In Portuguese.
- _____. Vortex-induced vibrations and jump phenomenon: experiments with a clamped flexible cylinder in water. *International Journal of Offshore and Polar Engineering*, v. 10, n. 1, p. 26–33, Mar. 2000. ISSN 1053-5381. eprint: <https://onepetro.org/IJOPE/article-pdf/2180424/isope-00-10-1-026.pdf>.
- PESCE, C. P.; FUJARRA, A. L. C.; KUBOTA, L. K. The Hilbert-Huang Spectral Analysis Method Applied to VIV. In: PROCEEDINGS OF THE 25TH (2006) INTERNATIONAL CONFERENCE ON OFFSHORE MECHANICS AND ARCTIC ENGINEERING. Hamburgo, Germany, 2006. DOI: [10.1115/OMAE2006-92119](https://doi.org/10.1115/OMAE2006-92119).
- PESCE, C. P.; FUJARRA, A. L. C.; SIMOS, A. N.; TANNURI, E. A. Analytical and closed form solutions for deep water riser-like eigenvalue problem. In: THE 9TH INTERNATIONAL OCEAN AND POLAR ENGINEERING CONFERENCE (ISOPE). 1999. eprint: <https://onepetro.org/ISOPEIOPEC/proceedings-pdf/ISOPE99/A11-ISOPE99/ISOPE-I-99-154/1927347/isope-i-99-154.pdf>.
- PESCE, C. P.; MARTINS, C. A. Numerical Computation of Riser Dynamics. In: CHAKRABARTI, S. K. (Ed.). *Numerical Methods in Fluid Structure Interaction, Advances in Fluid Mechanics*. 1. ed.: WIT Press, 2005. v. 42. (WIT Transactions on

State-of-the-art in Science and Engineering, 18). chap. 17, p. 253–309. ISBN 978-1-85312-837-0. DOI: [10.2495/978-1-85312-837-0/07](https://doi.org/10.2495/978-1-85312-837-0/07).

PESCE, C. P.; FRANZINI, G. R.; FUJARRA, A. L. C.; GONÇALVES, R. T.; SALLES, R.; MENDES, P. Further experimental investigations on vortex selfinduced vibrations (VSIV) with a small-scale catenary riser model. In: PROCEEDINGS OF THE INTERNATIONAL CONFERENCE ON OFFSHORE MECHANICS AND ARCTIC ENGINEERING - OMAE. Trondheim, Norway, June 2017. v. 2, v002t08a016. ISBN 978-0-7918-5764-9. DOI: [10.1115/OMAE2017-62100](https://doi.org/10.1115/OMAE2017-62100).

PIMENTA, P. M.; MAZZILLI, C. E. N. *Minima correctio methodi inveniendi lineas curvas elasticas*. 1986. Boletim técnico, No. BT/PEF/8613. Departamento de Estruturas e Fundações - Escola Politécnica, Universidade de São Paulo.

QUÉAU, L. M. *Estimating the fatigue damage of steel catenary risers in the touchdown zone*. 2015. PhD thesis – University of West Australia, Crawley, Australia. Last accessed: 01/05/22. eprint: https://research-repository.uwa.edu.au/files/4784095/Queau_Lucille_2015.pdf.

RAMOS, R.; PESCE, C. P. A stability analysis of risers subjected to dynamic compression coupled with twisting. *Journal of Offshore Mechanics and Arctic Engineering*, v. 125, n. 3, p. 183–189, 2003. DOI: [10.1115/1.1576819](https://doi.org/10.1115/1.1576819).

RATEIRO, F.; GONÇALVES, R. T.; PESCE, C. P.; FUJARRA, A. L. C.; FRANZINI, G. R.; MENDES, P. A Model Scale Experimental Investigation on Vortex-Self Induced Vibrations (VSIV) of Catenary Risers. In: OCEAN, OFFSHORE AND ARCTIC ENGINEERING DIVISION. ASME, June 2013. v. 7. (CFD and VIV), v007t08a029. ISBN 978-0-7918-5541-6. DOI: [10.1115/OMAE2013-10447](https://doi.org/10.1115/OMAE2013-10447).

RATEIRO, F.; PESCE, C. P.; GONÇALVES, R. T.; FRANZINI, G. R.; FUJARRA, A. L. C.; SALLES, R.; MENDES, P. Risers model tests: Scaling methodology and dynamic similarity. In: PROCEEDINGS of the 22nd (2012) International Society of Offshore and Polar Engineers. Rhodes, Greece, 2012. Last accessed: 02/12/2022. ISBN 978-1-880653-94-4. eprint: <https://onepetro.org/ISOPEIOPEC/proceedings-abstract/ISOPE12/All-ISOPE12/ISOPE-I-12-307/12587>.

SALLES, R. *Experimental analysis of fluid-structure interaction phenomena on a vertical flexible cylinder: modal coefficients and parametric resonance*. 2016. Universidade de São Paulo, São Paulo, Brazil. DOI: [10.11606/D.3.2016.TDE-25082016-085120](https://doi.org/10.11606/D.3.2016.TDE-25082016-085120).

- SALLES, R.; PESCE, C. P. Experimental Assessments of the Added Mass of Flexible Cylinders in Water: The Role of Modal Shape Representation. In: *Proceedings of DINAME 2017*. Ed. by Agenor de T. Fleury, Domingos A. Rade and Paulo R. G. Kurka. 1st. Cham: Springer International Publishing, 2019. chap. 15, p. 215–235. ISBN 978-3-319-91217-2. DOI: [10.1007/978-3-319-91217-2](https://doi.org/10.1007/978-3-319-91217-2).
- SARPKAYA, T. A critical review of the intrinsic nature of vortex-induced vibrations. *Journal of Fluids and Structures*, Academic Press, v. 19, n. 4, p. 389–447, May 2004. ISSN 0889-9746. DOI: [10.1016/J.JFLUIDSTRUCTS.2004.02.005](https://doi.org/10.1016/J.JFLUIDSTRUCTS.2004.02.005).
- _____. Force on a circular cylinder in viscous oscillatory flow at low Keulegan — Carpenter numbers. *Journal of Fluid Mechanics*, v. 165, p. 61, Apr. 1986. ISSN 0022-1120. DOI: [10.1017/S0022112086002999](https://doi.org/10.1017/S0022112086002999).
- _____. In - Line And Transverse Forces, On Cylinders In Oscillatory Flow At High Reynolds Numbers. In: OFFSHORE TECHNOLOGY CONFERENCE. Offshore Technology Conference, Apr. 1976. DOI: [10.4043/2533-MS](https://doi.org/10.4043/2533-MS).
- SARPKAYA, T.; RAJABI, F. Dynamic Response of Piles to Vortex Shedding in Oscillating Flows. In: PROCEEDINGS OF THE ANNUAL OFFSHORE TECHNOLOGY CONFERENCE. OnePetro, Apr. 1979. 1979-May, p. 2523–2528. ISBN 978-1-61399-062-9. DOI: [10.4043/3647-MS](https://doi.org/10.4043/3647-MS).
- SARPKAYA, T.; SCHOAFF, R. L. *A discrete-vortex analysis of flow about stationary and transversely oscillating circular cylinders*. Monterey, California, USA, 1979. DOI: [10945/29252](https://doi.org/10.10945/29252).
- SARPKAYA, T.; SCHOAFF, R. L. Inviscid Model of Two-Dimensional Vortex Shedding by a Circular Cylinder. *AIAA Journal*, v. 17, n. 11, p. 1193–1200, May 1979. ISSN 00011452. DOI: [10.2514/3.61300](https://doi.org/10.2514/3.61300).
- SILVEIRA, L. M. Y.; MARTINS, C. A.; CUNHA, L. D.; PESCE, C. P. An investigation on the effect of tension variation on VIV of risers. In: 267-275. THE 26TH INTERNATIONAL CONFERENCE ON OCEAN, OFFSHORE AND ARCTIC ENGINEERING (OMAE). San Diego, California, USA, 2007. v. 1. DOI: [10.1115/OMAE2007-29247](https://doi.org/10.1115/OMAE2007-29247).
- SRINIL, N.; REGA, G. Nonlinear longitudinal/transversal modal interactions in highly extensible suspended cables. *Journal of Sound and Vibration*, Academic Press, v. 310, n. 1-2, p. 230–242, Feb. 2008. ISSN 10958568. DOI: [10.1016/j.jsv.2007.07.056](https://doi.org/10.1016/j.jsv.2007.07.056).

- SRINIL, N.; REGA, G. Two-to-one resonant multi-modal dynamics of horizontal/inclined cables. Part II: Internal resonance activation, reduced-order models and nonlinear normal modes. *Nonlinear Dynamics*, Springer, v. 48, n. 3, p. 253–274, Dec. 2006. ISSN 1573-269X. DOI: [10.1007/S11071-006-9087-Z](https://doi.org/10.1007/S11071-006-9087-Z).
- SRINIL, N.; REGA, G.; CHUCHEEPSAKUL, S. Two-to-one resonant multi-modal dynamics of horizontal/inclined cables. Part I: Theoretical formulation and model validation. *Nonlinear Dynamics*, Springer, v. 48, n. 3, p. 231–252, Dec. 2006. ISSN 1573-269X. DOI: [10.1007/S11071-006-9086-0](https://doi.org/10.1007/S11071-006-9086-0).
- SUMER, B. M.; FREDSE, J. Effect of Reynolds Number on Vibrations of Cylinders. *Journal of Offshore Mechanics and Arctic Engineering*, American Society of Mechanical Engineers Digital Collection, v. 111, n. 2, p. 131–137, May 1989. ISSN 0892-7219. DOI: [10.1115/1.3257086](https://doi.org/10.1115/1.3257086).
- _____. Transverse Vibrations of an Elastically Mounted Cylinder Exposed to an Oscillating Flow. *Journal of Offshore Mechanics and Arctic Engineering*, American Society of Mechanical Engineers, v. 110, n. 4, p. 387, Nov. 1988. ISSN 08927219. DOI: [10.1115/1.3257077](https://doi.org/10.1115/1.3257077).
- THORSEN, M. J.; SÆVIK, S.; LARSEN, C. M. A simplified method for time domain simulation of cross-flow vortex-induced vibrations. *Journal of Fluids and Structures*, Academic Press, v. 49, p. 135–148, Aug. 2014. ISSN 0889-9746. DOI: [10.1016/J.JFLUIDSTRUCTS.2014.04.006](https://doi.org/10.1016/J.JFLUIDSTRUCTS.2014.04.006).
- _____. Fatigue damage from time domain simulation of combined in-line and cross-flow vortex-induced vibrations. *Marine Structures*, Elsevier, v. 41, p. 200–222, Apr. 2015. ISSN 0951-8339. DOI: [10.1016/J.MARSTRUC.2015.02.005](https://doi.org/10.1016/J.MARSTRUC.2015.02.005).
- _____. Non-linear time domain analysis of cross-flow vortex-induced vibrations. *Marine Structures*, Elsevier, v. 51, p. 134–151, Jan. 2017. ISSN 0951-8339. DOI: [10.1016/J.MARSTRUC.2016.10.007](https://doi.org/10.1016/J.MARSTRUC.2016.10.007).
- _____. Time Domain Simulation of Vortex-Induced Vibrations Based on Phase-Coupled Oscillator Synchronization. In: PROCEEDINGS OF THE INTERNATIONAL CONFERENCE ON OFFSHORE MECHANICS AND ARCTIC ENGINEERING - OMAE. ASME, May 2015. v002t08a029. ISBN 978-0-7918-5648-2. DOI: [10.1115/OMAE2015-41881](https://doi.org/10.1115/OMAE2015-41881).
- _____. Time domain simulation of vortex-induced vibrations in stationary and oscillating flows. *Journal of Fluids and Structures*, Academic Press, v. 61, p. 1–19, Feb. 2016. ISSN 0889-9746. DOI: [10.1016/J.JFLUIDSTRUCTS.2015.11.006](https://doi.org/10.1016/J.JFLUIDSTRUCTS.2015.11.006).

- TRIANAFYLLOU, M. S. Cable mechanics for moored floating systems. In: CHRYSOSTOMIDIS, C. (Ed.). *Proceedings of the 7th International Conference on the Behaviour of Offshore Structures (BOSS 1994)*. Massachusetts, USA: Pergamon, 1994. v. 2, p. 57–78. ISBN 978-0-08-041914-5.
- WANG, J.; FU, S.; BAARHOLM, R.; WU, J.; LARSEN, C. M. Fatigue damage of a steel catenary riser from vortex-induced vibration caused by vessel motions. *Marine Structures*, Elsevier, v. 39, p. 131–156, Dec. 2014. ISSN 0951-8339. DOI: [10.1016/J.MARSTRUC.2014.07.002](https://doi.org/10.1016/J.MARSTRUC.2014.07.002).
- _____. Out-of-plane vortex-induced vibration of a steel catenary riser caused by vessel motions. *Ocean Engineering*, Pergamon, v. 109, p. 389–400, Nov. 2015. ISSN 0029-8018. DOI: [10.1016/J.OCEANENG.2015.09.004](https://doi.org/10.1016/J.OCEANENG.2015.09.004).
- WANG, J.; FU, S.; BAARHOLM, R.; ZHANG, M.; LIU, C. Global motion reconstruction of a steel catenary riser under vessel motion. *Ships and Offshore Structures*, Taylor and Francis Ltd., v. 14, n. 5, p. 442–456, July 2019. ISSN 1744-5302. DOI: [10.1080/17445302.2018.1500785](https://doi.org/10.1080/17445302.2018.1500785).
- WANG, J.; FU, S.; MARTIN LARSEN, C.; BAARHOLM, R.; WU, J.; LIE, H. Dominant parameters for vortex-induced vibration of a steel catenary riser under vessel motion. *Ocean Engineering*, Pergamon, v. 136, p. 260–271, May 2017. ISSN 0029-8018. DOI: [10.1016/J.OCEANENG.2017.03.015](https://doi.org/10.1016/J.OCEANENG.2017.03.015).
- WILLIAMSON, C. H. K.; GOVARDHAN, R. Vortex-Induced Vibrations. *Annual Review of Fluid Mechanics*, Annual Reviews, v. 36, n. 1, p. 413–455, Jan. 2004. ISSN 0066-4189. DOI: [10.1146/annurev.fluid.36.050802.122128](https://doi.org/10.1146/annurev.fluid.36.050802.122128).
- WU, J.; LIE, H.; LARSEN, C. M.; BAARHOLM, R. J. An empirical heave induced VIV prediction model. In: PROCEEDINGS OF THE INTERNATIONAL CONFERENCE ON OFFSHORE MECHANICS AND ARCTIC ENGINEERING - OMAE. ASME, May 2015. v. 2, v002t08a031. ISBN 978-0-7918-5648-2. DOI: [10.1115/OMAE2015-42065](https://doi.org/10.1115/OMAE2015-42065).
- YUAN, Y.; XUE, H.; TANG, W. Numerical analysis of Vortex-Induced Vibration for flexible risers under steady and oscillatory flows. *Ocean Engineering*, Pergamon, v. 148, p. 548–562, Jan. 2018. ISSN 00298018. DOI: [10.1016/j.oceaneng.2017.11.047](https://doi.org/10.1016/j.oceaneng.2017.11.047).
- ZHANG, M.; FU, S.; LIU, C.; REN, H.; XU, Y. Experimental investigation on vortex-induced force of a Steel Catenary Riser under in-plane vessel motion. *Marine*

Structures, Elsevier Ltd, v. 78, p. 102882, July 2021. ISSN 09518339. DOI: [10.1016/j.marstruc.2020.102882](https://doi.org/10.1016/j.marstruc.2020.102882).

ZHANG, M.; FU, S.; REN, H.; MA, L.; XU, Y. A hybrid FEM-DNN-based vortex-induced Vibration Prediction Method for Flexible Pipes under oscillatory flow in the time domain. *Ocean Engineering*, v. 246, p. 110488, Feb. 2022. DOI: [10.1016/j.oceaneng.2021.110488](https://doi.org/10.1016/j.oceaneng.2021.110488).

A – TESTING MODEL DESIGN

The testing model designed is based on the Froude scale due to the action of gravitational waves on floating vessels, where risers and other structures are appended. Hence, risers hydroelastic response depends on the general sea wave behavior, which is studied using the Froude's parameter.

A.1 Froude scale

The Froude scaling technique is determined by equating the full scale model (m -superscript) and prototype (p -superscript) Froude numbers,

$$Fr = \frac{U}{\sqrt{gL}},$$

with

$$Fr^{(m)} = Fr^{(p)}, \quad (\text{A.1})$$

in which U is the heave velocity due to incident gravitational waves; g , the gravity; and L , a characteristic length. In addition, the Froude scale is based on a scaling factor, λ , acting upon the characteristic length, such as:

$$L^{(p)} = \lambda L^{(m)}. \quad (\text{A.2})$$

Consequently, the scaling factor for quantities of different physical units can assume power values of λ , which can be directly obtained using the equality of Froude numbers. Moreover, a model will be called small-scale model if the scaling factor is smaller than the unity, $\lambda < 1$.

For instance, assuming the gravity is constant for both model and prototype, the velocity can be scaled as

$$\frac{U^{(m)}}{\sqrt{gL^{(m)}}} = \frac{U^{(p)}}{\sqrt{gL^{(p)}}} = \frac{U^{(p)}}{\sqrt{g\lambda L^{(m)}}} \iff U^{(p)} = \sqrt{\lambda}U^{(m)}. \quad (\text{A.3})$$

Thus, obtaining the velocity scaling factor, $\sqrt{\lambda}$. More generally, the Froude scale factor for each basic SI unit (M , T , L) can be obtained in order to find the respective scaling factor for any other physical quantity; see Table A.1.

Table A.1: Scaling factor for selected physical quantities using the Froude scale.

Physical quantity	Physical dimension	Scale
Length	L	λ
Time	T	$\sqrt{\lambda}$
Mass	M	λ^3
Force per length	$M^1L^0T^{-1}$	λ^2
Axial stiffness, EA	$M^1L^1T^{-2}$	λ^3
Bending stiffness, EI	$M^1L^3T^{-2}$	λ^5
Torsion stiffness, GJ	$M^1L^3T^{-2}$	λ^5
Angle	$M^0L^0T^0$	1
Frequency	$M^0L^0T^{-1}$	$\sqrt{\frac{1}{\lambda}}$

Source: The author.

More importantly, the Froude scale has a direct impact in the general hydrodynamic for it is impossible to match both Froude's and Reynolds' numbers at the same time. Considering the Reynolds' number,

$$Re = \frac{UD}{\nu},$$

and assuming that both sea and regular water viscosities are equivalent, $\nu^{(m)} \cong \nu^{(p)}$, the Reynolds similarity can be simply written as:

$$Re^{(m)} = Re^{(p)}. \quad (\text{A.4})$$

Then, the velocity scaling factor would be

$$U^{(p)} = \frac{v^{(p)}}{v^{(m)}} \lambda U^{(m)} = \lambda U^{(m)}, \quad (\text{A.5})$$

which is incompatible to what was obtained before, as the velocity cannot be generally scaled simultaneously by $\sqrt{\lambda}$ and λ ; see Equation A.3.

Considering a small-scale prototype, $\lambda < 1$, the scaled velocity, obtained using Froude similarity, is greater than it should be to match the Reynolds' number in both full scale model and prototype. As a result, the scaled structure will be subjected to hydrodynamic loads that may differ to the real regime.

A.2 Riser scaling

The riser scaling procedure is fully described in [Rateiro et al. \(2012\)](#)¹ and here only a concise discussion on the subject will be provided.

The real riser has 8in of external diameter and it is considered to be filled with raw oil. In addition, using the scaling factor $\lambda = 1 : 100$, all mechanical properties are duly scaled as shown in Table A.2.

The scaled axial and bending stiffness are similar to polymeric materials, which agrees with the silicon hose chosen to construct the testing model. Although the relative weight in water of the silicon hose is negative, it is possible to increase its linear weight by filling the hose with a dense substance or solid material. Whilst the former cannot be toxic or unstable, the latter cannot change the structural axial and bending rigidity.

For that reason, the hose was filled up with stainless steel micro-spheres, $d = 1.5mm$, which provided enough distributed mass, achieving the desired scaled mass, m_s . The micro-spheres contribution on the axial and bending stiffness is far less than it would be if a metallic soul or internal hose were used.

The chosen instrumentation was a set of optical tracking cameras, measuring the structural displacement directly, working synchronously both above and under the water. Together with the cameras, a load cell was placed at the model upper top, providing a direct measure of the traction at the hang-off point. The reasoning behind this sensing system was to reduced as much as possible the interference on the hydroelastic

¹Although unlikely, should it be available to the reader, further details and a broader discussion on the riser scaling methodology could be obtained in [LIFE&MO \(2011c,e\)](#).

system, specially avoiding any mass lumps due to classical accelerometer techniques.

Table A.2: Mechanical properties of the chosen full scale riser and the scaled model.

Data	Full scale	Scaled (1:100)
Internal diameter (mm)	182.58	1.826
External diameter (mm)	219.10	2.191
Depth (m)	410.00	4.10
Angle ($^{\circ}$)	70	70
Mass per length, m_s (kg/m)	112.69	1.13E-02
Weight in air (filled with oil) (N/m)	1105.08	1.11E-01
Weight in water (filled with oil) (N/m)	726.12	7.26E-02
Axial rigidity, EA (kN)	2.60E+06	2.60
Bending stiffness, EI (Nm 2)	1.20E+07	1.20E-03
Flexural length, λ_f (mm)	7.14E+03	71.39
Displaced mass, m_d (kg/m)	38.65	3.86E-03
Reduced mass, $m^* = m_s/m_d$	28.60	28.60
Added mass coefficient, $C_a = m_a/m_d$	1.00	1.00
Added mass coefficient, $a = m_a/m_s$	0.035	0.035

Source: The author.

The external diameter obtained for the scaled model is a major obstacle, due to the model diameter be too small, $\mathcal{O}(D_e) \sim 1mm$, around the camera resolution limit. Hence, the testing model external diameter was distorted, augmented in 10 times, so the tracking cameras could work properly.

The augmented internal and external diameters acts directly on the scaled model linear distributed mass, m_s , increasing its weight. In the end, the designed model exhibits scaled parameters using two different scaling factors: $\lambda = 1 : 100$ is used to scale axial and bending rigidities, and flexural length; $\lambda' = 1 : 10$, in geometric and mass parameters.

Additionally, the designed external diameter also causes an increase in the overall Reynolds value to which the cylinder will be subjected. As exposed previously, the typ-

ical hydrodynamic loads that act on offshore structures tend to increase proportionally to the flow Reynolds' number. This is a limitation imposed both by the Froude scaling methodology and the structural diameter augmentation.

As the added mass in viscous fluid flow effect on the hydroelastic system mechanism is still an open researching field, it is only possible to assume the added mass coefficient, $C_a = 1$, typically used in offshore models.

Table A.3: Mechanical properties of the designed and “as-built” models.

Data	Designed	“As-built”
Internal diameter (mm)	15.80	15.80
External diameter (mm)	22.20	22.20
Depth (m)	3.50	3.50
Angle (°)	70	71.5
Mass per length, m_s (kg/m)	1.13	1.14
Weight in air (N/m)	11.08	11.18
Weight in water (N/m)	7.29	7.38
Axial rigidity, EA (kN)	1.91	1.0-1.6
Bending stiffness, EI (Nm ²)	8.86E-03	5.60E-02
Flexural length, λ_f (mm)	61	49
Displaced mass, m_d (kg/m)	0.387	0.387
Reduced mass, $m^* = m_s/m_d$	2.92	2.95
Added mass coefficient, $C_a = m_a/m_d$	1.00	1.00
Added mass coefficient, $a = m_a/m_s$	0.343	0.340

Source: The author.

The designed model mechanical properties are shown in Table A.3 and, as it was already discussed, there is little difference on the hydrodynamic parameters, such as reduced mass and added mass coefficient. In turn, other geometric and structural parameters, such as the axial and bending stiffness, and the flexural length, displayed substantial differences.

Rateiro et al. (2012) provides further details on the rationale behind the riser sim-

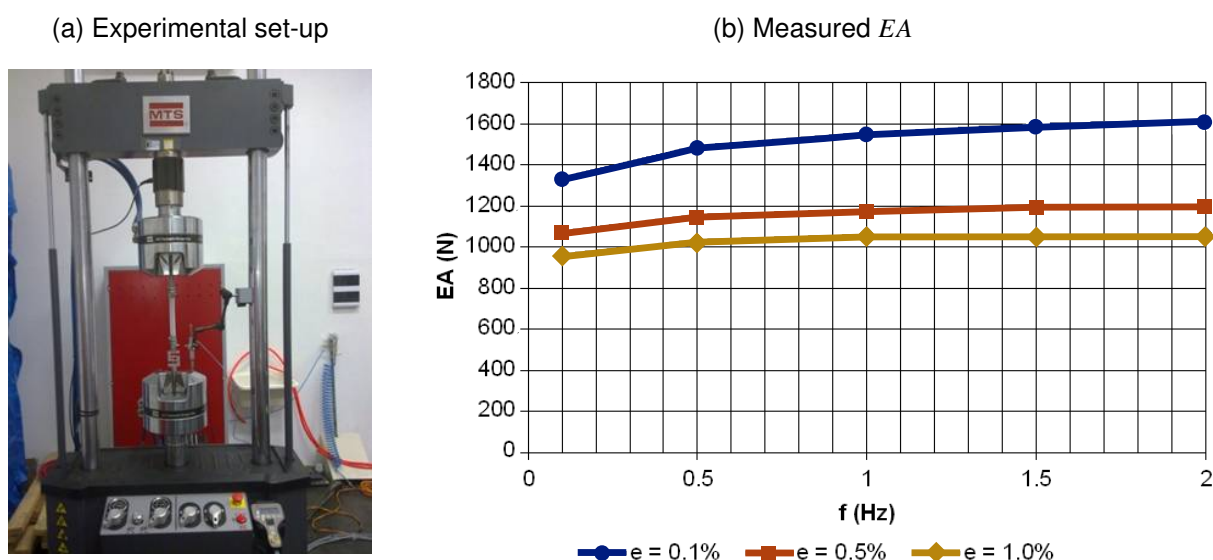
ilarity process, explaining the group of parameters chosen to characterize the testing model. The methodology is based on analytical and asymptotic dynamics solutions. Modal characterization, including natural frequencies and eigenfunctions, can be checked in [Pesce et al. \(2017\)](#).

A.3 Mechanical characterization

The first mechanical characterization was carried out at the Surface Phenomena Laboratory (LFS) where different sizes of stainless steel micro spheres were used in order to obtain linear mass equivalently to the scaled one; see Table A.3. The tests were executed by the present author and, unfortunately, there is no photos of the experimental tests.

Figure A.1 depicts the axial rigidity experimental assessment of the small-scale model. The tests were carried out at LIFE&MO facility, using a Material Test System MTS® that applied sinusoidal displacement in a testing tube. The monitoring system was composed of a Linear Variable Differential Transformer (LVDT) and load cell type 'S' in order to measure displacement and load, respectively; see Figure A.1a.

Figure A.1: Small-scale model axial stiffness experimental evaluation.



Source: Developed by the author.

The testing specimens were divided in two groups: the first was composed of empty tubes; and the second, of tubes filled with stainless steel micro spheres. The former

was used in order to experimentally evaluate the tube material rheology, which is viscoelastic.

The latter tests aimed at check if the filling composed of micro spheres contribute to the axial rigidity. It was shown that the filling only slightly contribute to the axial modulus due to the metallic material being incompressible, which provide a rigid internal wall that increased the axial stiffness by means of the Poisson's ratio.

Additionally, it was carried out imposed sinusoidal displacement in order to measure how much the velocity in which the load was applied would effect the axial stiffness due to the viscoelasticity rheology; see Figure A.2a.

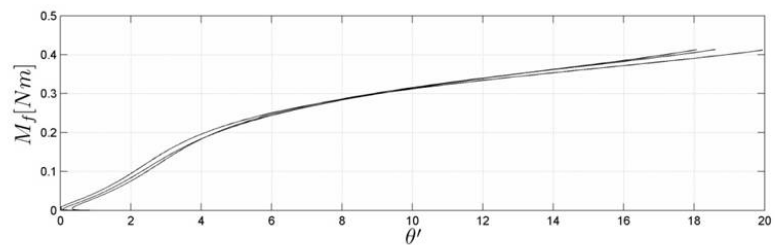
In turn, the bending stiffness experimental tests were executed at the TPN facility, using the analytic formulation reported in Pimenta and Mazzilli (1986). Figure A.2a displays the experimental set-up composed of the small-scale model in a cantilever arrangement.

Figure A.2: Small-scale model bending stiffness experimental evaluation.

(a) Experimental set-up



(b) Measured EI



Source: Extracted from Pesce (2013).

Figure A.2b presents the bending rigidity as a function of the angle variation with respect to the structural length.

B – EXPERIMENTAL ANALYSIS

METHODOLOGY: ALGORITHMS

B.1 Orthonormalization - Modified Gram-Schmidt

The Modified Gram-Schmidt (MGS) algorithm shows greater efficient implementation. In classical Gram-Schmidt (CGS), the orthonormalization is executed taking each vector, one at a time, and making it orthogonal to all previous vectors. In turn, the MGS evaluation takes each vector and modifies all forthcoming vectors to be orthogonal to it.

Listing B.1: Modified Gram-Schmidt's pseudo-code

```

5  % xj is vector so {x1,...,xn} is an arbitrary basis
   % vk is a vector so {v1,...,vn} is an orthogonal basis
   % qj is a vector so {q1,...,qn} is an orthonormal basis
   % norm is the Euclidean norm
   for j ← 1:n
       vj ← xj
   end
   for j ← 1:n
       qj ← vj/norm(vj)
10  for k ← j+1:n
           vk ← vk - (transpose(qj)*vk)*qj
       end
   end
end

```

B.2 Numerical differentiation

The numerical differentiation algorithms are selected depending if the data has a fixed step or not. Generally, experimental temporal series present a fixed step due to a constant sampling rate. In turn, the optical targets used to measure the structural displacement do not have a constant distribution on the model span.

B.2.1 Arbitrary step

In this case, the algorithm is based on a combination of forward, central and backwards differences. The data is segmented into three regions, whose size depends on the chosen precision.

This method is used due to the loss of a point every time a forward/backward differentiation is executed. Furthermore, the usage of a central difference increases the precision on the evaluation for it has a second order error.

For this example, one admits an arbitrary function $u(s)$ with respect to s . The function $u(s)$ is measured at different points, s_i , such that $s_{i+1} > s_i$ with $i = 1, \dots, N$. The step, δs , is irregularly spaced. Then, one wants to find the first derivative of $u(s)$ w.r.t s ,

$$u'(s) = \frac{du}{ds}, \quad (\text{B.1})$$

which is approximated as

$$u'(s) \approx \frac{\delta u}{\delta s}. \quad (\text{B.2})$$

Admitting that the forward and backward differences are of first order and the central one of second order, then:

Listing B.2: Arbitrary step differentiation pseudo-code

```

5  % u is 1-by-N vectors and s is N-by-1
   % u_s is also 1-by-N vector
   % Forward difference
   u_s [1] ← (u [2] - u [1]) / (s [2] - s [1])
   % Backward difference
   u_s [N] ← (u [N] - u [N-1]) / (s [N] - s [N-1])

```

10

```

% Remaining points - central differences
for i ← 2:N-1
    u_s[i+1] ← (u[i+1]-u[i])/(s[i+1]-s[i])
end

```

Higher order derivatives are evaluated likewise. Should the differentiated signal exhibit excessive noise, a simple Finite Impulsive Response (FIR) lowpass filter is used in order to cut high frequencies due to the differentiation process. The filter design is detailed in the following section.

B.2.2 Fixed step differentiation

This particular case is used only for temporal derivatives due to the constant sampling rate, F_s . The main issue with experimental temporal signals is the noise originated in the differentiation itself. Then, a different approach is adopted based on the smooth noise-robust differentiators derived in [Holoborodko \(2008\)](#). The differentiation algorithm is rather complex and only a concise idea is presented here.

The algorithm is based on a low-noise filter known as Lanczos differentiators, or Savitzky-Golay filters. Typical finite differences methods approximate the given function with a polynomial and, then, the differentiation depends on how close the exact value is from the approximation. In order to increase the precision, high order polynomials are used.

On the other hand, Lanczos filters also approximate the function with a polynomial, nonetheless, the coefficients are found using smooth least-squares optimization. The following steps are based on the fact that the differentiation filter is anti-symmetric of Type III, whose exact value is $H_d(\omega) = i\omega$.

One should admit the filter length as N (odd), whose coefficients are $\{c_k\}$. The function, $u(t)$, is sampled at N equidistant points around t^* with step h . Then,

$$f_k = f(t_k), \text{ with } t_k = t^* + kh, \quad (\text{B.3})$$

in which $k = -M, \dots, M$ and $M = \frac{N-1}{2}$. The numerical derivative can be written as

$$\dot{f}(t^*) \approx \frac{1}{h} \sum_{k=1}^M c_k (f_k - f_{-k}). \quad (\text{B.4})$$

The filter frequency response, considering $h = 1$ for now, is given as

$$H(\omega) = 2i \sum_{k=1}^M c_k \sin(k\omega), \quad (\text{B.5})$$

and the goal is to select the coefficients $\{c_k\}$ such that $H(\omega)$ is as close as possible to the differentiator filter, $H_d(\omega) = i\omega$ in low frequency region and smoothly tending to zero towards the Nyquist's frequency, $\omega = \pi$.

The chosen way to select such coefficients is to force both filters to exhibit high tangency order at $\omega = 0$ and $\omega = \pi$. Then,

$$\left. \frac{\partial^i H(\omega)}{\partial \omega^i} \right|_{\omega=0} = \left. \frac{\partial^i H_d(\omega)}{\partial \omega^i} \right|_{\omega=0} \quad (\text{B.6})$$

$$\left. \frac{\partial^j H(\omega)}{\partial \omega^j} \right|_{\omega=\pi} = 0, \quad (\text{B.7})$$

in which $i = 0, \dots, n$ and $j = 0, \dots, m$. Assuming that $n = 2$, $m = \frac{N-3}{2}$ and $M = \frac{N-1}{2}$, the coefficients are evaluated as

$$c_k = \frac{1}{2^{2m+1}} \left[\binom{2m}{m-k+1} - \binom{2m}{m-k-1} \right]. \quad (\text{B.8})$$

The lowest differentiator order, $N = 5$, assumes the following approximation:

$$\dot{f}(t^*) \approx \frac{2(f_1 - f_{-1}) + f_2 - f_{-2}}{8h} \quad (\text{B.9})$$

Once again, the forward and backward finite differences are used in the boundary layers, corresponding to two points at the beginning and end.

Listing B.3: Fixed step smooth noise-robust differentiation pseudo-code

```

5  % f(s,t) is 1-by-N vector and t is a N-by-1 vector
   % f_t is 1-by-N vector
   h ← t[2] - t[1]
   % Forward difference
   f_t[1] ← (f[2] - f[1]) / h
   f_t[2] ← (f[3] - f[2]) / h
   % Backward difference

```

```

f_t [N] ← (f [N] - f [N-1]) / h
f_t [N-1] ← (f [N-2] - f [N-1]) / h
10 % Smooth noise-robust filter
for i ← 3:N-2
    f_t [i] ← (2(f [i+1] - f [i-1]) + f [i+2] - f [i-2]) / (8h)
end

```

Inasmuch as the differentiation is smooth and noise-robust, high order derivatives can be obtained likewise. For instance, after obtaining the first derivative, the second is evaluated passing the first as input to the algorithm.

Although the method reduces noise and produces a smooth response, the beginning and last regions are still evaluated as forward and backward differences.

Thus, high order derivatives cause an increase at those boundary layers each time the method is iterated, *i.e.* these increasing regions exhibit lower precision and accuracy over time. An alternative is to discard $2 + 2$ points in the signal each time the method is iterated.

B.3 Filter design

A lowpass filter is used in several occasions so as to reduce high frequency noise due to the measuring system acquisition or other numerical analysis procedure. It is noteworthy that the acquisition system already has an anti-aliasing second order analog filter with fixed cut frequency, $f_{cut} = 3000Hz$.

In turn, the sampling frequency used in the experimental tests, $F_s = 60Hz$, is lower than the acquisition system one. The maximum observable frequency, $f_{obs,max} = 30Hz$, is given by the Nyquist-Shannon's theorem, which is suffice in the present tests due to the model natural frequencies are limited to the range $0.42 \leq f_N (Hz) \leq 4.53$.

Limiting the present analysis to the first 20 modes¹, which corresponds to 10 in-plane and 10 out-of-plane modes, the maximum natural frequency obtained in a numerical representation of the physical model² is $f_{N,b}^{(10)} = 4.53Hz \ll 30Hz$.

¹High in-plane and out-of-plane modes (from the eighth mode upwards) show small maximum modal amplitudes. For instance, the maximum modal amplitude evaluated in the tenth mode is $\mathcal{O}(A_{max}^{(10)*}) \sim 0.1$ in both directions. Thus, limiting the present analysis to the first 10 modes in each in-plane and out-of-plane directions is suffice.

²Using Orcaflex®.

In addition, the frequency bandwidth is large enough for the digital signal to be treated as a continuous one. This means that it is not necessary to consider the dynamic effect of a typical Zero-Order Hold (ZOH) block into the analysis.

Consequently, the filter is designed using MATLAB[®] Filter Design Toolbox, which is set to have the lowest possible order, to be equiripple with pass and stop frequencies of $f_{cut} = f_{pass} = 5Hz$ and $f_{stop} = 6Hz$, respectively.

Moreover, the filter is also set to exhibit pass and stop amplitude gains of $1dB$ and $80dB$, respectively. These gains are chosen so the filter does not add any gain to the response in low frequencies, whilst attenuating high frequency responses. The density factor is left with its default value.

C – VSIV: MODAL ANALYSIS COMPLEMENTARY RESULTS

C.1 $A_i = 105mm$

This section presents additional experimental results from the group $A_i = 105mm$. The testing case ID 06 will be used as to illustrate the dynamics in space of configuration, based on local reference frame measurements, that was reported in Figure 4.4.

Figure C.1 summarizes the space of configuration of the testing case ID 06. It is possible to observe the TDP variation in in Figure C.1a which occurs during the pushing-down and lifting-up phases of the imposed motion at the top (WANG et al., 2017).

The modal orbits evaluated using the normal and binormal displacements series for each testing case in the present group is exhibited in Figure C.2. The testing case ID 06 was selected due to its characteristic synchronization pattern in the second mode, displaying a amplitude peak and $N^{(2)} = 5$.

Table 4.2 reveals that the modal frequency ratio evaluated for this particular modal case is in the vicinity of $f^{(d,2)*} = 0.2$. Thus, the second mode peak responsible for the modal synchronization pattern described in Figure C.2 can be considered resonant.

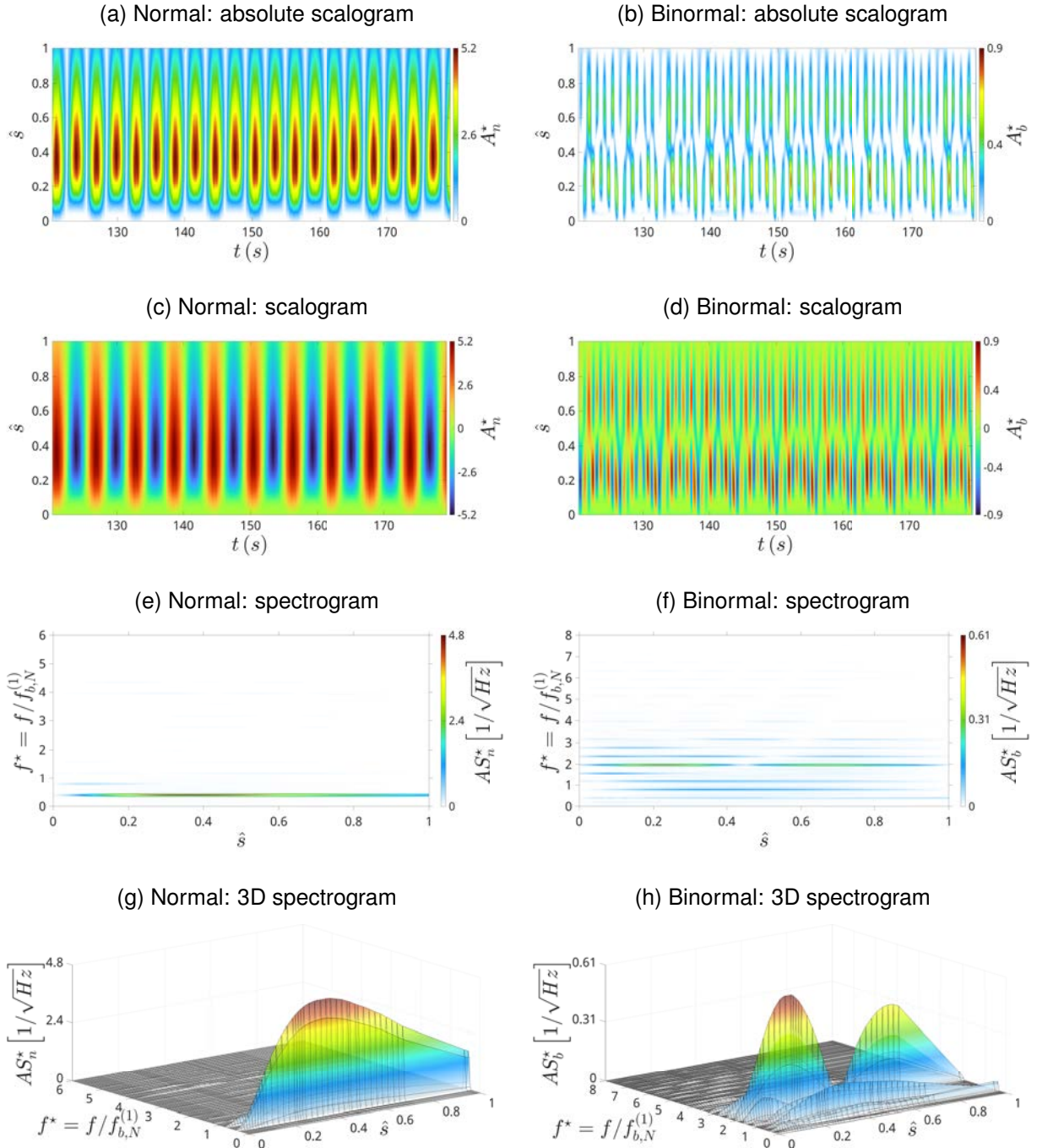
Modal resonant peaks can be predicted using Equation 4.3. Additionally, the space of configuration synchronization along the cylinder presented in Figure 4.4 displays a typical 5 lobes orbit in the middle-span.

The 5 lobes observed in Figure 4.4 contain some distortion, if compared to the second mode synchronization found in Figure C.2 (ID 06), due to small amplitude responses from the other modes.

Therefore, the modal decomposition assisted in retaining only relevant information

for each mode.

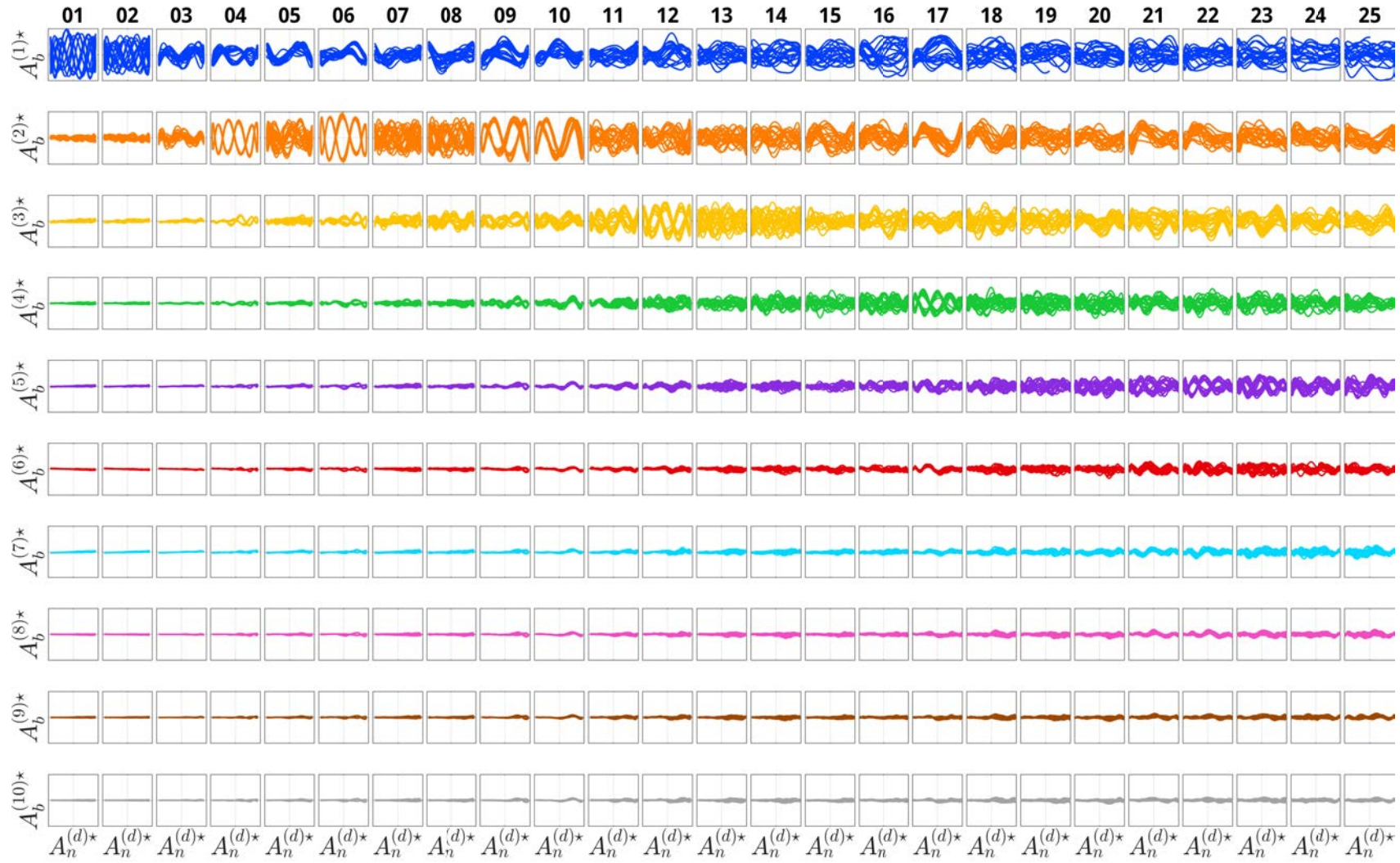
Figure C.1: Normal and binormal dynamics in the space of configuration obtained from the testing case ID 06 of the group $A_i = 105\text{mm}$.



Source: Developed by the author.

Table C.1 presents all modal KC evaluated from the present group. The testing case ID 06 exhibits $KC^{(d)} = 45.8$, obtained from the dominant in-plane mode, which is the first one. Higher modes present small modal KC.

Figure C.2: Modal orbits obtained from all testing cases in the group $A_i = 105\text{mm}$.



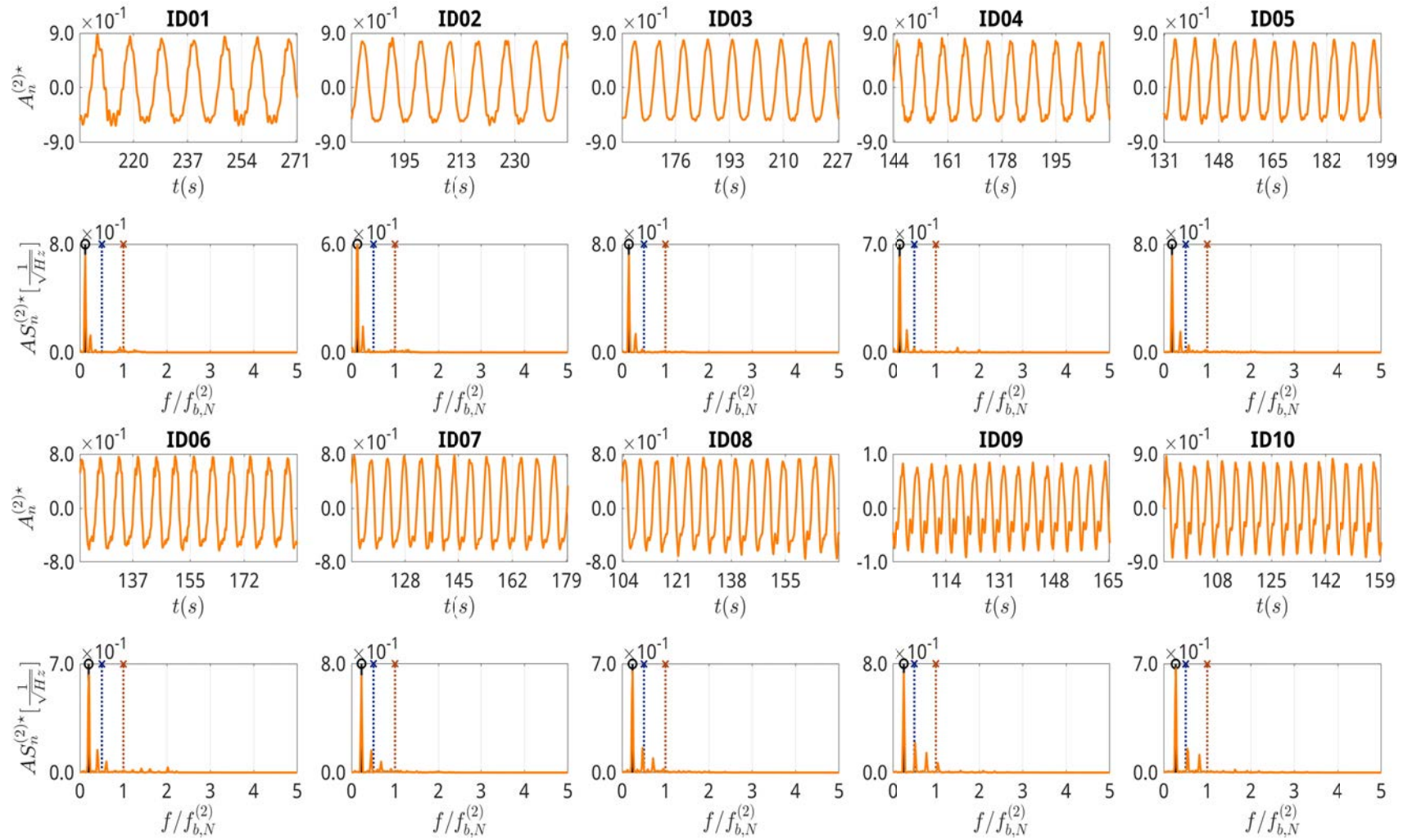
Source: Developed by the author.

Table C.1: Modal KC for imposed movement at the top $A_{top} = 105\text{mm}$. Dominant modal KC is colored with respect to the modal color scheme.

ID	Modal $KC^{(j)}$									
	1st	2nd	3rd	4th	5th	6th	7th	8th	9th	10th
01	45.33	4.35	4.74	0.72	4.12	3.75	4.60	1.36	1.53	0.42
02	45.22	4.34	4.73	0.70	4.12	3.72	4.59	1.34	1.54	0.43
03	45.26	4.29	4.66	0.73	4.09	3.72	4.56	1.35	1.52	0.42
04	45.30	4.29	4.70	0.75	4.10	3.72	4.56	1.34	1.53	0.42
05	45.60	4.27	4.63	0.77	4.09	3.74	4.56	1.36	1.52	0.42
06	45.77	4.26	4.69	0.91	4.12	3.76	4.58	1.36	1.53	0.42
07	45.96	4.28	4.61	0.81	4.09	3.75	4.56	1.37	1.52	0.41
08	46.05	4.33	4.64	0.82	4.10	3.75	4.57	1.36	1.52	0.42
09	46.11	4.51	4.64	0.88	4.09	3.75	4.56	1.36	1.52	0.42
10	46.07	4.41	4.59	0.86	4.08	3.75	4.55	1.36	1.51	0.42
11	46.61	4.39	4.59	0.93	4.07	3.78	4.56	1.38	1.51	0.41
12	46.48	4.58	4.76	1.08	4.09	3.75	4.53	1.38	1.51	0.43
13	46.96	4.57	4.64	1.04	4.06	3.79	4.53	1.40	1.50	0.41
14	47.20	4.73	4.65	1.11	4.05	3.80	4.53	1.41	1.50	0.42
15	47.37	4.83	4.58	1.17	4.03	3.81	4.52	1.43	1.50	0.42
16	47.49	5.13	4.75	1.24	4.02	3.82	4.51	1.43	1.50	0.42
17	47.65	5.74	4.87	1.38	3.99	3.84	4.50	1.46	1.49	0.43
18	47.58	5.70	4.95	1.39	4.02	3.83	4.49	1.45	1.49	0.44
19	47.97	6.17	5.29	1.52	4.01	3.88	4.49	1.47	1.49	0.45
20	47.88	6.43	5.46	1.60	4.02	3.86	4.49	1.46	1.49	0.46
21	47.95	7.45	5.68	1.76	4.00	3.91	4.47	1.50	1.48	0.47
22	47.65	7.91	5.97	1.92	3.98	3.91	4.43	1.50	1.47	0.49
23	47.59	8.69	6.47	2.05	4.00	3.92	4.43	1.53	1.48	0.52
24	47.76	8.65	6.52	2.08	4.01	3.94	4.42	1.53	1.48	0.52
25	47.94	8.95	6.73	2.16	4.00	3.96	4.41	1.55	1.48	0.53

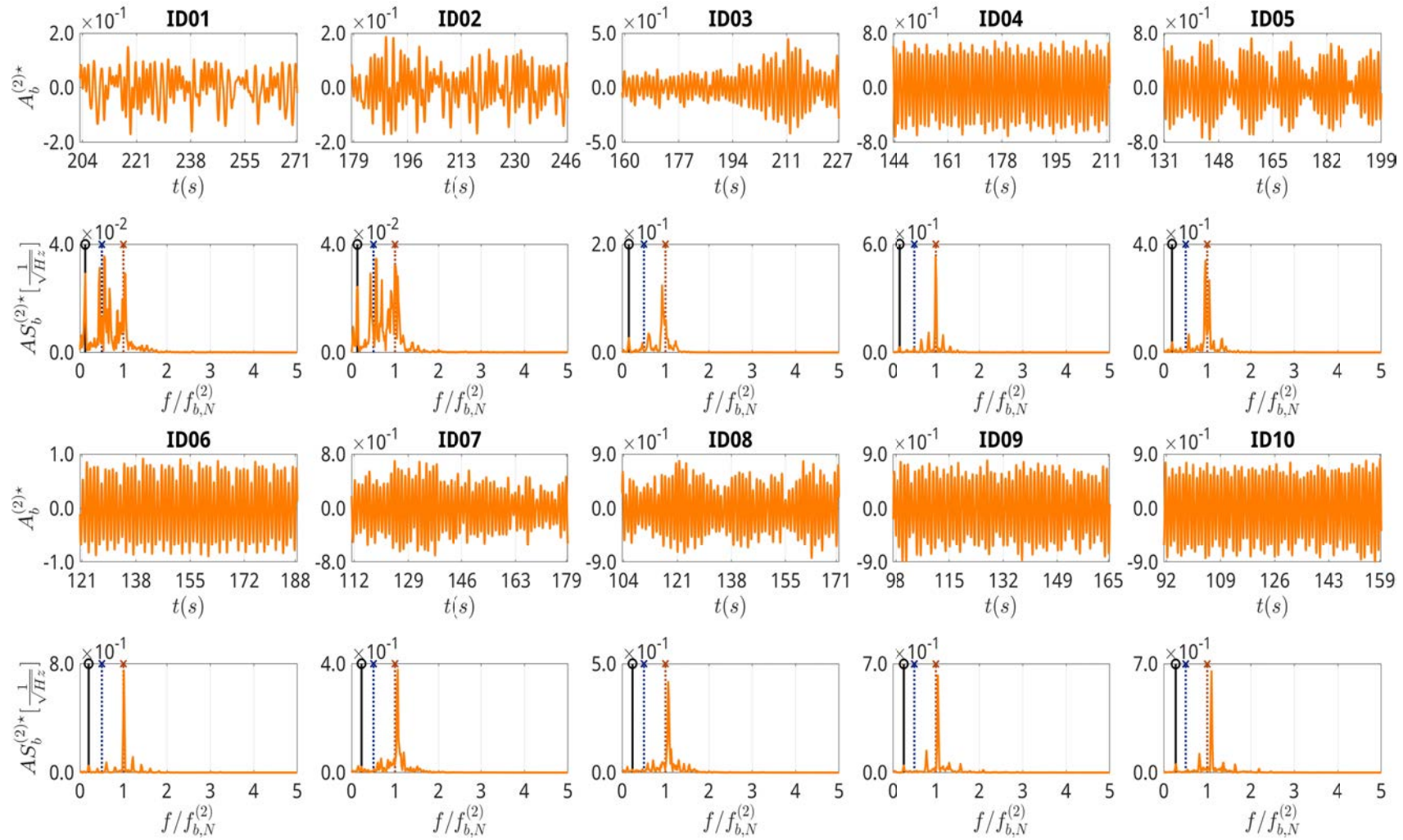
Figures C.3-C.4 exhibits the normal and binormal amplitude series, respectively, for the cases IDs 01 until 10. They also present the spectral content of each series.

Figure C.3: Second mode normal displacement series and correspondent spectral contents from testing cases IDs 01 until 10 in the group $A_i = 105\text{mm}$.



Source: Developed by the author.

Figure C.4: Second mode binormal displacement series and correspondent spectral contents from testing cases IDs 01 until 10 in the group $A_i = 105\text{mm}$.

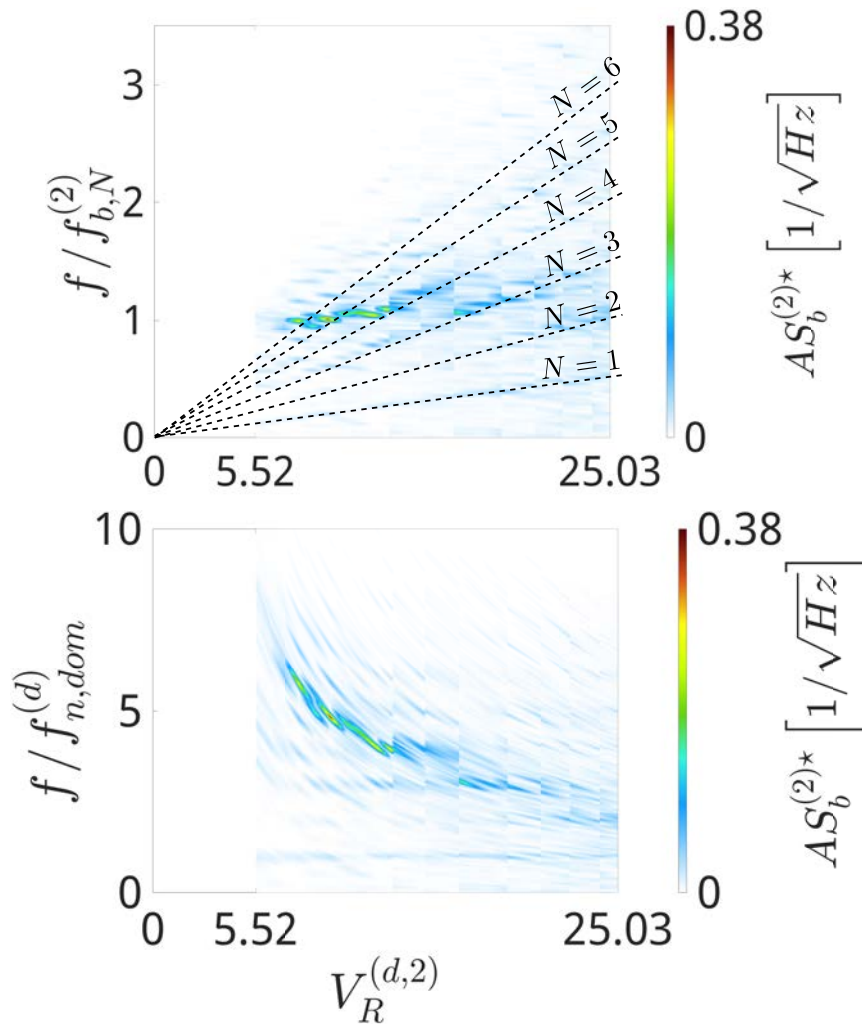


Source: Developed by the author.

The ID 06 is located in the first column of the second row in the charts presented in Figures C.3-C.4. The normal displacement series shows that its dominant frequency is equal to the driving frequency of the imposed vertical motion at the hang-off point.

Figure C.5 shows the second out-of-plane mode VSIV response with respect to the modal reduced velocity parameter, $V_R^{(d,k)}$. Note that, contrarily to the results in Figure 4.7, there is discontinuities in the frequency charts due to the modal KC not be fixed. Thus, reinforcing visually the adoption of modal frequency ratio parameter, $f^{(d,k)*}$, in the context of multi modal VSIV response.

Figure C.5: Modal frequency response of the second out-of-plane modes with respect to the modal reduced velocity parameter: $45.2 \leq KC^{(d)} \leq 48$.



Source: Developed by the author.

C.2 $A_i = 70\text{mm}$

This section presents additional experimental results from the group $A_i = 70\text{mm}$. The testing case ID 09 will be used as to illustrate the dynamics in space of configuration, based on local reference frame measurements, that was reported in Figure 4.10.

Figure C.6 summarizes the space of configuration of the testing case ID 09. It is possible to observe the TDP variation in in Figure C.6a which occurs during the pushing-down and lifting-up phases of the imposed motion at the top (WANG et al., 2017).

The modal orbits evaluated using the normal and binormal displacements series for each testing case in the present group is exhibited in Figure C.7. The testing case ID 09 was selected due to its characteristic synchronization pattern in the second mode, displaying a amplitude peak and $N^{(2)} = 3$.

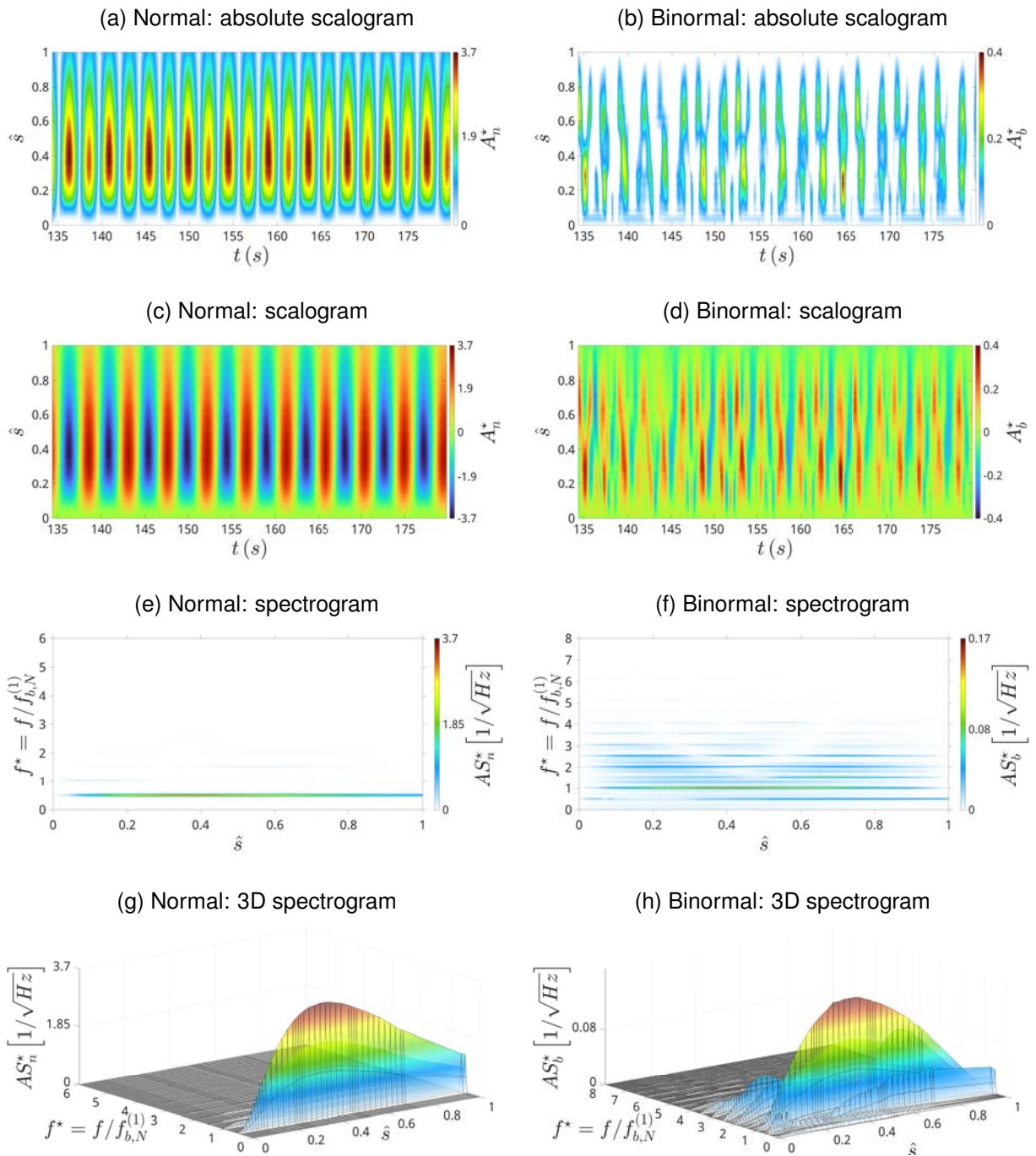
Table 4.4 reveals that the modal frequency ratio evaluated for this particular modal case is in the vicinity of $f^{(d,2)*} = 0.33$. Thus, the second mode peak responsible for the modal synchronization pattern described in Figure C.7 can be considered resonant.

Modal resonant peaks can be predicted using Equation 4.3. Additionally, the space of configuration synchronization along the cylinder presented in Figure 4.10 displays a typical 3 lobes orbit in the lower and upper quarter portion of the total span.

The 3 lobes observed in Figure 4.10 contain some distortion, if compared to the second mode synchronization found in Figure C.7 (ID 09), due to small amplitude responses from the other modes.

Therefore, the modal decomposition assisted in retaining only relevant information for each mode.

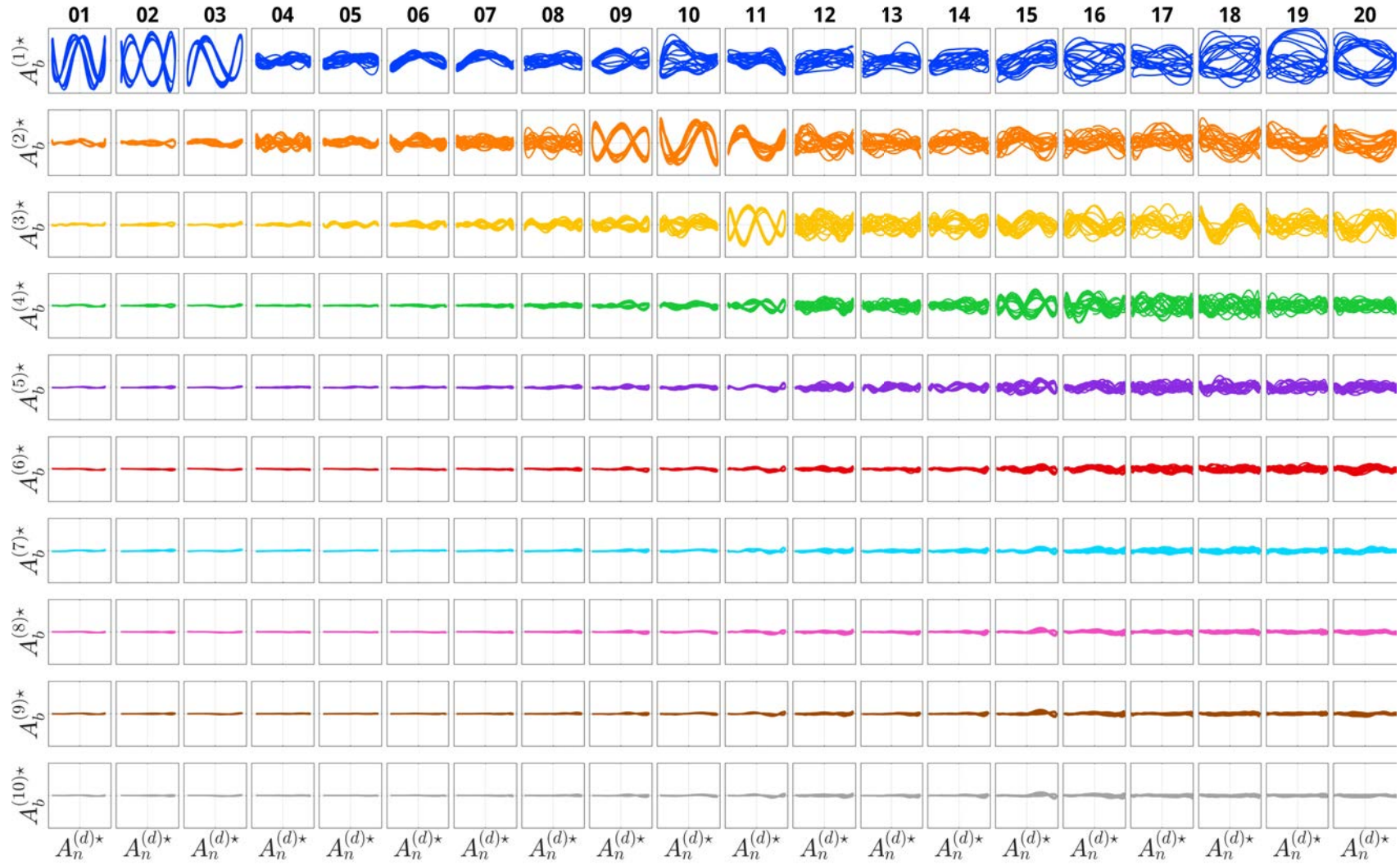
Figure C.6: Normal and binormal dynamics in the space of configuration obtained from the testing case ID 09 of the group $A_i = 70\text{mm}$.



Source: Developed by the author.

Table C.2 presents all modal KC evaluated from the present group. The testing case ID 09 exhibits $KC^{(d)} = 31.63$, obtained from the dominant in-plane mode, which is the first one. Higher modes present small modal KC.

Figure C.7: Modal orbits obtained from all testing cases in the group $A_i = 105\text{mm}$.



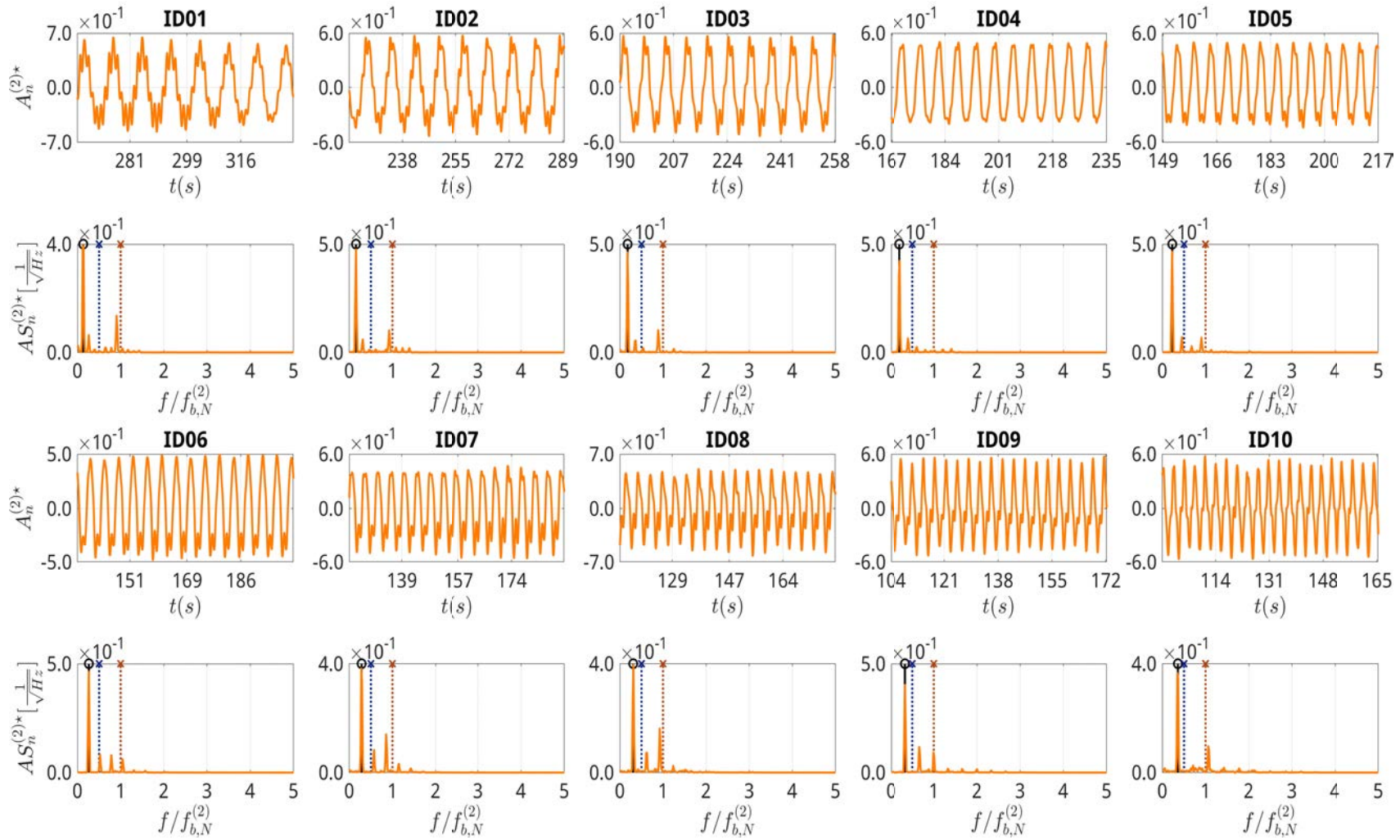
Source: Developed by the author.

Table C.2: Modal KC for imposed movement at the top $A_{top} = 70\text{mm}$. Dominant modal KC is highlighted in red.

ID	Modal $KC^{(j)}$									
	1st	2nd	3rd	4th	5th	6th	7th	8th	9th	10th
01	30.12	2.95	3.37	0.28	2.62	2.15	3.23	1.00	1.17	0.26
02	30.41	2.91	3.34	0.29	2.62	2.18	3.23	1.03	1.16	0.24
03	30.40	2.92	3.34	0.30	2.61	2.18	3.22	1.03	1.16	0.24
04	30.66	2.82	3.27	0.31	2.59	2.19	3.22	1.04	1.15	0.23
05	30.70	2.77	3.22	0.33	2.57	2.19	3.20	1.04	1.14	0.23
06	30.93	2.80	3.21	0.36	2.57	2.20	3.20	1.05	1.14	0.23
07	31.28	2.74	3.18	0.37	2.56	2.21	3.19	1.06	1.14	0.22
08	31.65	2.64	3.11	0.41	2.55	2.23	3.19	1.07	1.13	0.21
09	31.63	2.56	3.11	0.52	2.55	2.23	3.18	1.08	1.12	0.22
10	31.79	2.65	3.06	0.60	2.52	2.25	3.16	1.09	1.11	0.22
11	31.95	3.33	3.21	0.67	2.54	2.27	3.14	1.10	1.11	0.23
12	32.13	3.23	3.16	0.70	2.50	2.26	3.13	1.11	1.11	0.24
13	32.54	3.57	3.22	0.75	2.49	2.29	3.13	1.12	1.10	0.24
14	32.63	3.93	3.32	0.82	2.48	2.29	3.11	1.12	1.10	0.25
15	32.99	4.75	3.58	1.06	2.50	2.33	3.08	1.16	1.09	0.26
16	33.11	4.94	3.64	1.13	2.47	2.35	3.08	1.17	1.08	0.28
17	33.18	5.63	3.89	1.20	2.49	2.37	3.09	1.17	1.09	0.30
18	33.24	6.00	4.05	1.27	2.49	2.37	3.08	1.17	1.09	0.32
19	33.70	6.36	4.21	1.35	2.45	2.39	3.07	1.19	1.08	0.32
20	33.91	7.58	4.72	1.57	2.48	2.42	3.06	1.21	1.09	0.36

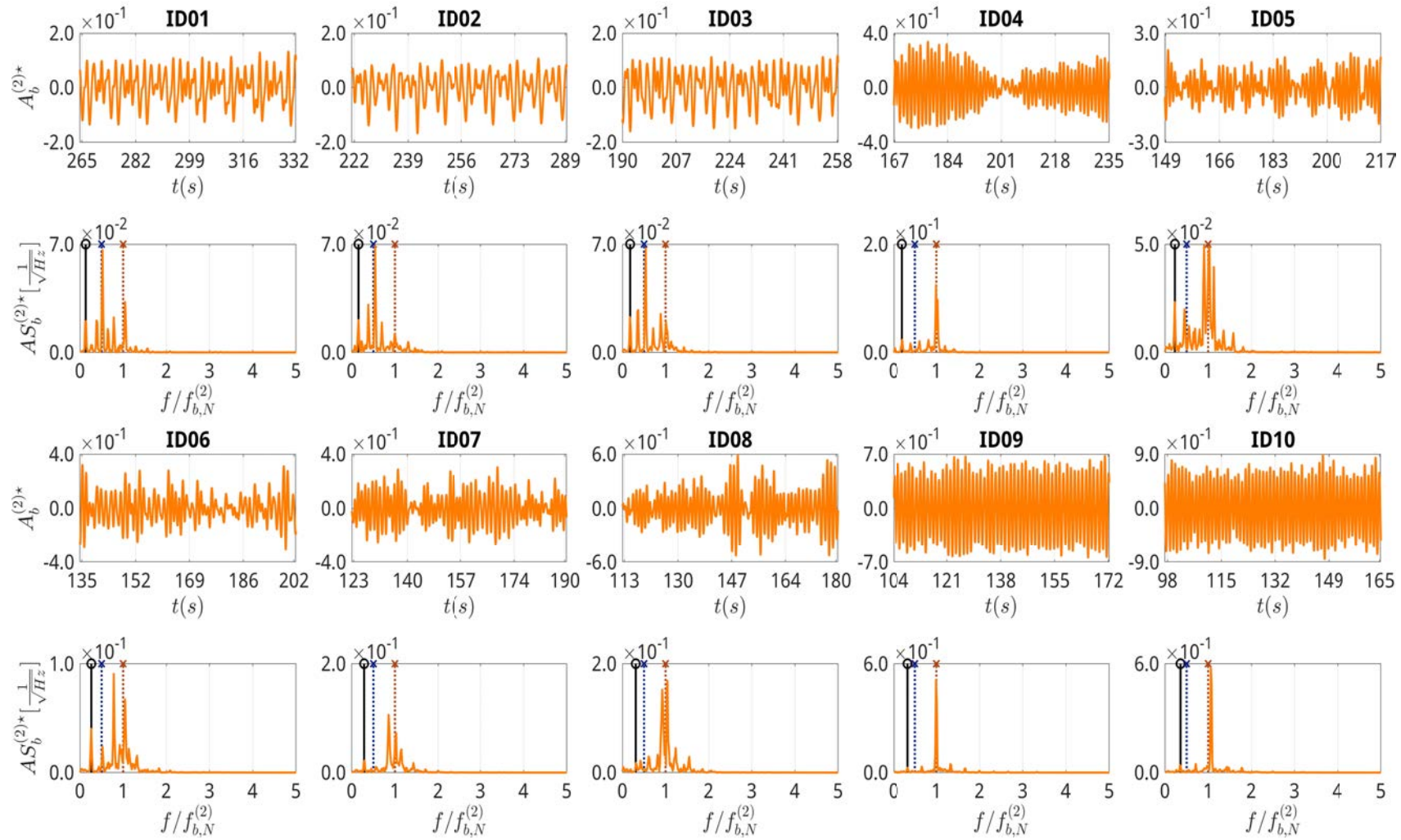
Figures C.8-C.9 exhibits the normal and binormal amplitude series, respectively, for the cases IDs 01 until 10. They also present the spectral content of each series.

Figure C.8: Second mode normal displacement series and correspondent spectral contents from testing cases IDs 01 until 10 in the group $A_i = 70\text{mm}$.



Source: Developed by the author.

Figure C.9: Second mode binormal displacement series and correspondent spectral contents from testing cases IDs 01 until 10 in the group $A_i = 70\text{mm}$.

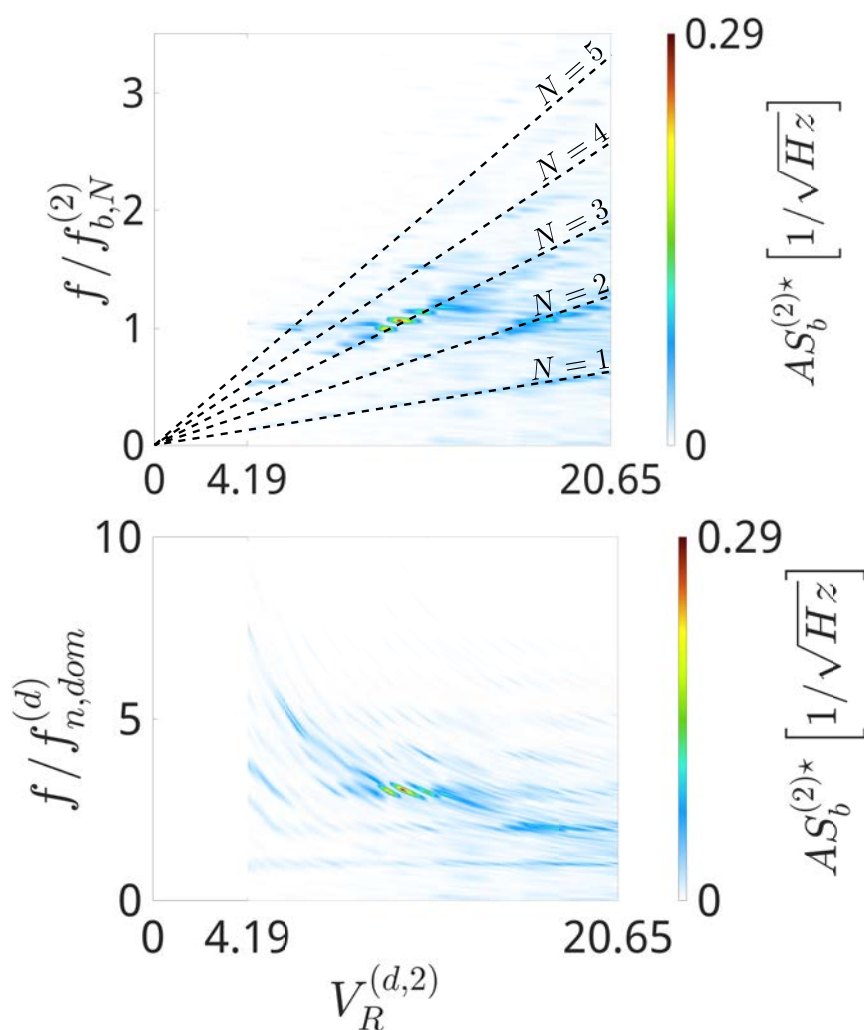


Source: Developed by the author.

The ID 09 is located in the fourth column of the second row in the charts presented in Figures C.8-C.9. The normal displacement series shows that its dominant frequency is equal to the driving frequency of the imposed vertical motion at the hang-off point.

Figure C.10 shows the second out-of-plane mode VSIV response with respect to the modal reduced velocity parameter, $V_R^{(d,k)}$.

Figure C.10: Modal frequency response of the second out-of-plane modes with respect to the modal reduced velocity parameter: $30.1 \leq KC^{(d)} \leq 33.9$.



Source: Developed by the author.

C.3 $A_i = 35mm$

This section presents additional experimental results from the group $A_i = 35mm$. The testing case ID 04 will be used as to illustrate the dynamics in space of configuration, based on local reference frame measurements, that was reported in Figure 4.16.

Figure C.11 summarizes the space of configuration of the testing case ID 04. It is possible to observe the TDP variation in in Figure C.11a which occurs during the pushing-down and lifting-up phases of the imposed motion at the top (WANG et al., 2017).

The modal orbits evaluated using the normal and binormal displacements series for each testing case in the present group is exhibited in Figure C.12. The testing case ID 04 was selected due to its characteristic synchronization pattern in the first mode, displaying a amplitude peak and $N^{(1)} = 2$.

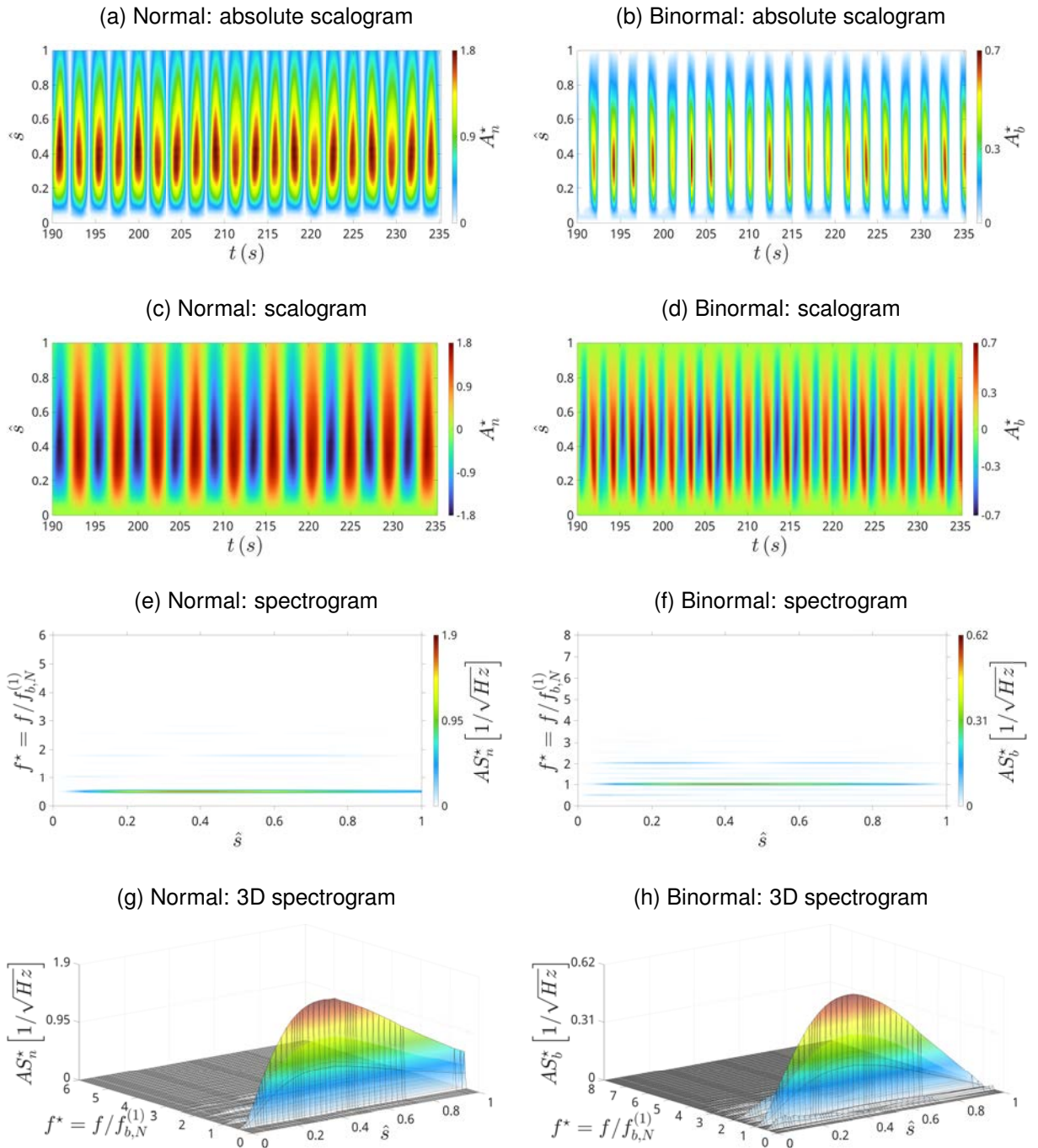
Table 4.6 reveals that the modal frequency ratio evaluated for this particular modal case is in the vicinity of $f^{(d,2)*} = 0.5$. Thus, the first mode peak responsible for the modal synchronization pattern described in Figure C.12 can be considered resonant.

Modal resonant peaks can be predicted using Equation 4.3. Additionally, the space of configuration synchronization along the cylinder presented in Figure 4.16 displays a typical 2 : 1 with $\pm 90^\circ$ phase.

The 2 : 1 observed in Figure 4.16 contain some distortion, if compared to the first mode synchronization found in Figure C.12 (ID 04), due to small amplitude responses from the other modes.

Therefore, the modal decomposition assisted in retaining only relevant information for each mode.

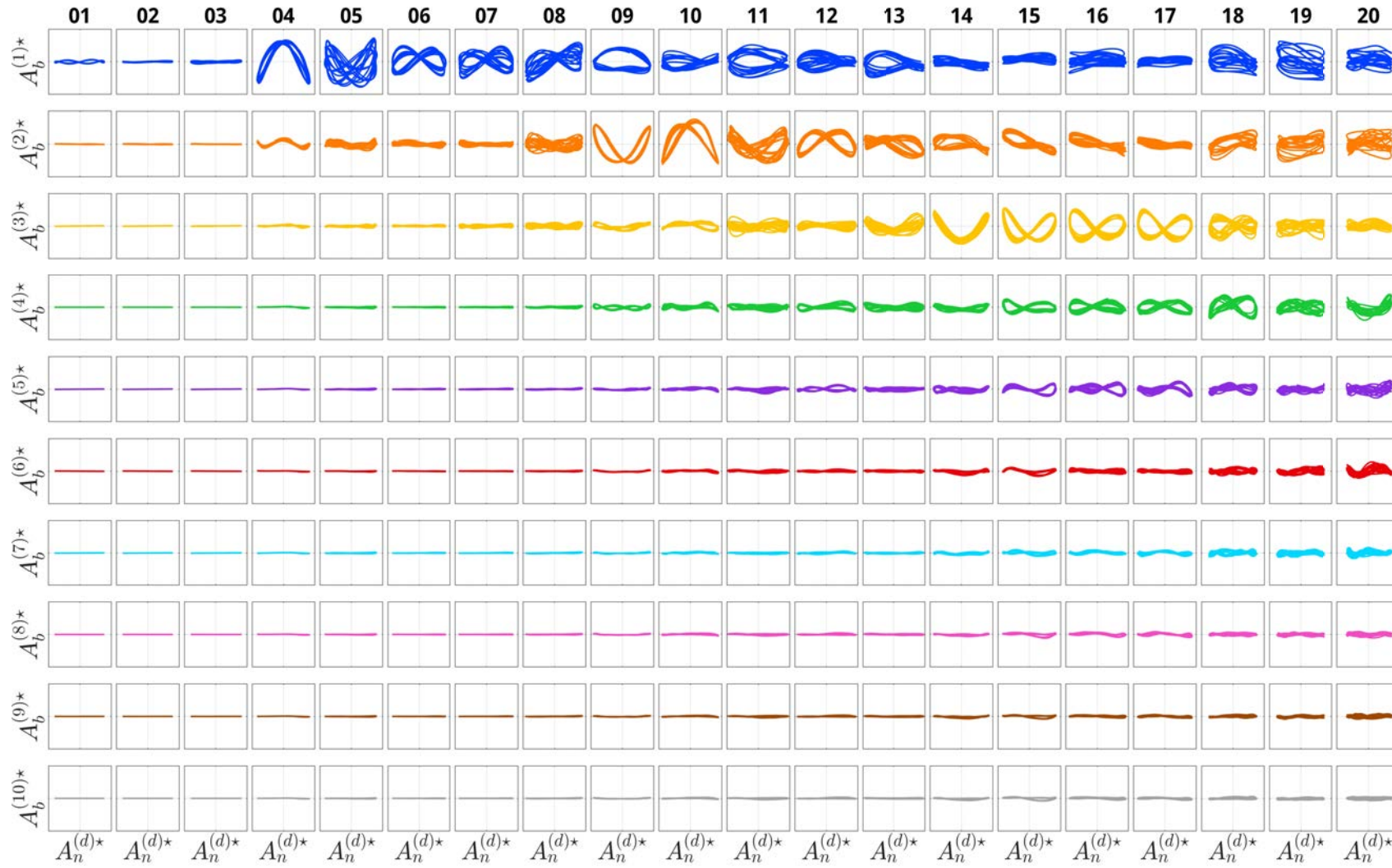
Figure C.11: Normal and binormal dynamics in the space of configuration obtained from the testing case ID 04 of the group $A_i = 105\text{mm}$.



Source: Developed by the author.

Table C.3 presents all modal KC evaluated from the present group. The testing case ID 04 exhibits $KC^{(d)} = 15.7$, obtained from the dominant in-plane mode, which is the first one. Higher modes present small modal KC.

Figure C.12: Modal orbits obtained from all testing cases in the group $A_i = 35\text{mm}$.



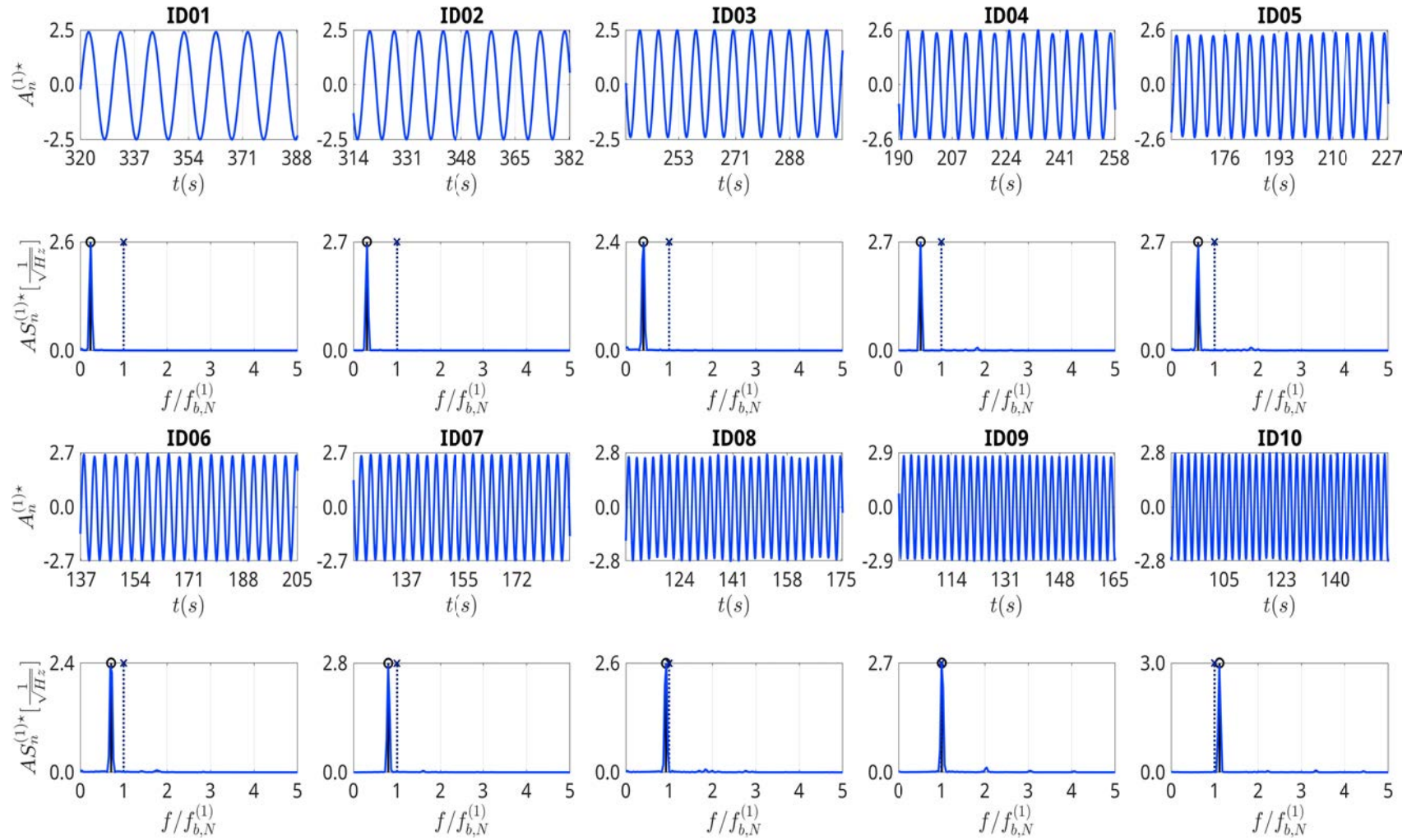
Source: Developed by the author.

Table C.3: Modal KC for imposed movement at the top $A_{top} = 35\text{mm}$. Dominant modal KC is highlighted in red.

ID	Modal $KC^{(j)}$									
	1st	2nd	3rd	4th	5th	6th	7th	8th	9th	10th
01	15.28	1.28	1.81	0.42	1.52	0.92	1.01	0.18	0.38	0.11
02	15.45	1.26	1.80	0.43	1.53	0.93	1.01	0.18	0.38	0.11
03	15.46	1.20	1.76	0.44	1.50	0.92	0.99	0.18	0.37	0.11
04	15.68	1.29	1.75	0.46	1.51	0.93	0.99	0.18	0.37	0.11
05	15.80	1.37	1.73	0.48	1.49	0.93	0.99	0.19	0.37	0.11
06	16.12	1.10	1.66	0.51	1.49	0.94	0.98	0.19	0.36	0.10
07	16.34	1.00	1.61	0.55	1.47	0.95	0.97	0.20	0.36	0.10
08	16.67	1.53	1.67	0.61	1.44	0.97	0.95	0.22	0.35	0.09
09	17.16	2.17	1.68	0.98	1.45	1.00	0.94	0.25	0.34	0.11
10	17.07	2.39	1.74	0.85	1.47	0.99	0.95	0.26	0.35	0.13
11	17.86	2.75	1.65	0.90	1.40	1.05	0.90	0.28	0.32	0.12
12	17.68	3.35	2.13	0.98	1.45	1.05	0.91	0.30	0.34	0.15
13	17.97	4.46	2.67	1.22	1.39	1.05	0.91	0.34	0.36	0.19
14	16.87	7.13	3.73	1.35	1.49	1.03	1.00	0.40	0.45	0.28
15	16.34	7.31	3.47	1.29	1.53	1.08	1.01	0.38	0.45	0.29
16	16.32	8.19	3.91	1.43	1.59	1.01	1.05	0.44	0.50	0.33
17	16.09	8.88	4.23	1.51	1.64	1.01	1.07	0.45	0.53	0.36
18	14.09	9.83	4.85	1.72	1.98	0.87	1.15	0.47	0.62	0.41
19	14.13	11.04	5.03	2.03	2.01	0.95	1.18	0.50	0.66	0.45
20	12.96	11.44	5.39	2.16	2.16	1.08	1.27	0.49	0.70	0.46

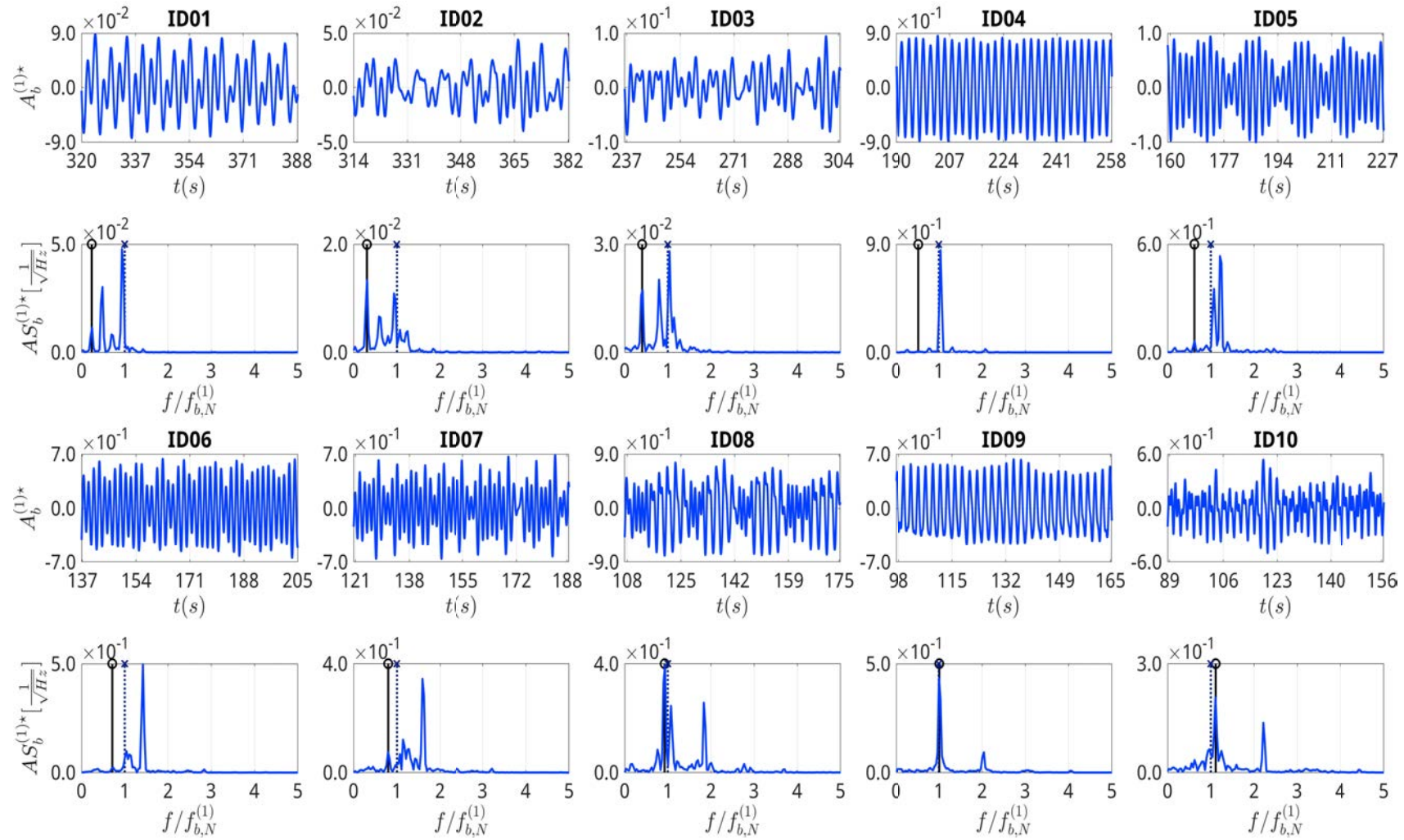
Figures C.13-C.14 exhibits the normal and binormal amplitude series, respectively, for the cases IDs 01 until 10. They also present the spectral content of each series.

Figure C.13: First mode normal displacement series and correspondent spectral contents from testing cases IDs 01 until 10 in the group $A_i = 35\text{mm}$.



Source: Developed by the author.

Figure C.14: First mode binormal displacement series and correspondent spectral contents from testing cases IDs 01 until 10 in the group $A_i = 35\text{mm}$.

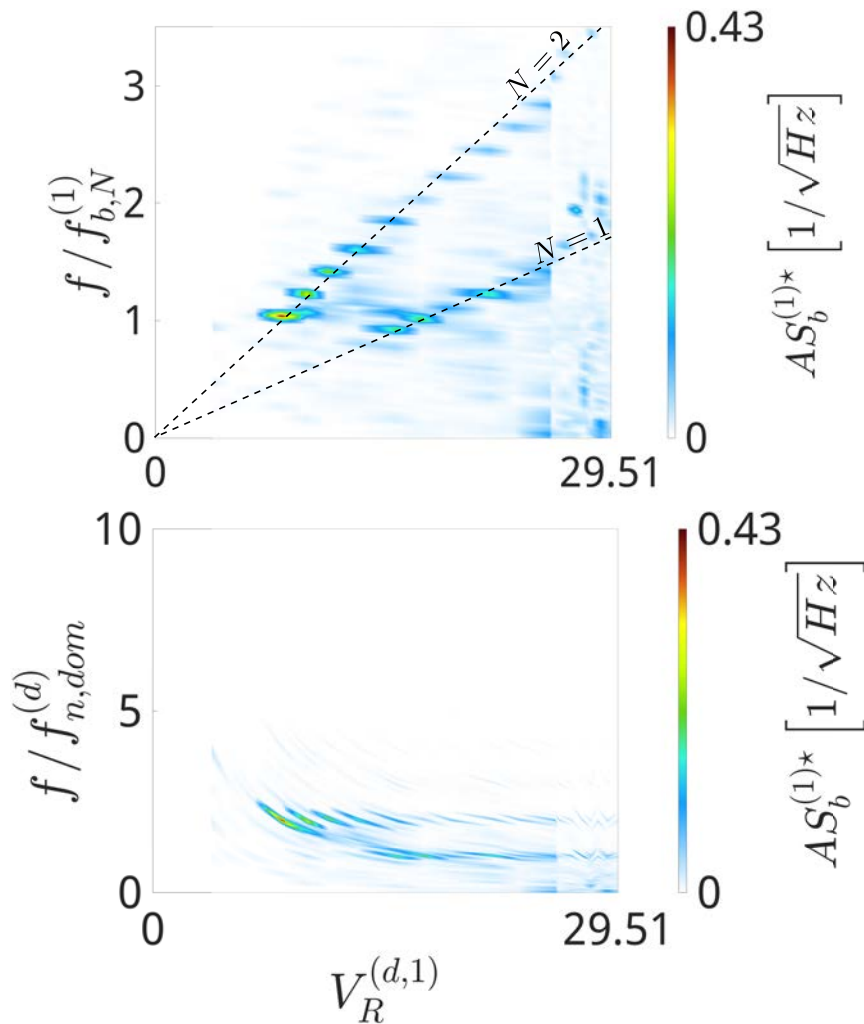


Source: Developed by the author.

The ID 04 is located in the fourth column of the first row in the charts presented in Figures C.13-C.14. The normal displacement series shows that its dominant frequency is equal to the driving frequency of the imposed vertical motion at the hang-off point.

Figure C.15 shows the first out-of-plane mode VSIV response with respect to the modal reduced velocity parameter, $V_R^{(d,k)}$. Note that, contrarily to the results in Figure 4.19, there is discontinuities in the frequency charts due to the modal KC not be fixed. Thus, reinforcing visually the adoption of modal frequency ratio parameter, $f^{(d,k)*}$, in the context of multi modal VSIV response.

Figure C.15: Modal frequency response of the first out-of-plane modes with respect to the modal reduced velocity parameter: $13 \leq KC^{(d)} \leq 18$.



Source: Developed by the author.

C.4 $A_i = 17.5mm$

This section presents additional experimental results from the group $A_i = 17.5mm$. The testing case ID 06 will be used as to illustrate the dynamics in space of configuration, based on local reference frame measurements, that was reported in Figure 4.23.

Figure C.16 summarizes the space of configuration of the testing case ID 06. It is possible to observe the TDP variation in in Figure C.16a which occurs during the pushing-down and lifting-up phases of the imposed motion at the top (WANG et al., 2017).

The modal orbits evaluated using the normal and binormal displacements series for each testing case in the present group is exhibited in Figure C.17. The testing case ID 06 was selected due to its characteristic synchronization pattern in the third mode, displaying a amplitude peak and $N^{(3)} = 2$.

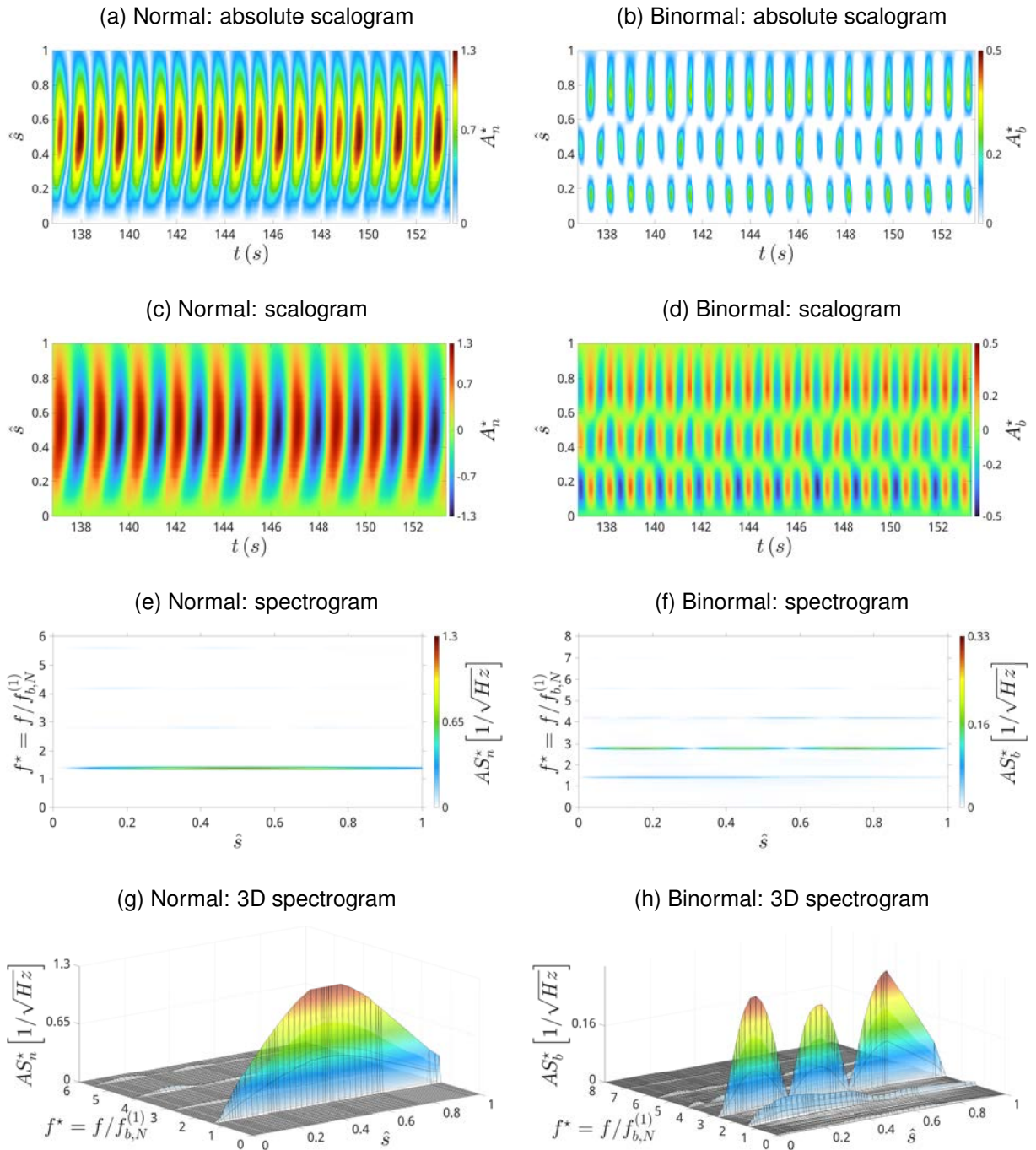
Table 4.8 reveals that the modal frequency ratio evaluated for this particular modal case is in the vicinity of $f^{(d,3)*} = 0.47$. Thus, the third mode peak responsible for the modal synchronization pattern described in Figure C.17 can be considered resonant.

Modal resonant peaks can be predicted using Equation 4.3. Additionally, the space of configuration synchronization along the cylinder presented in Figure 4.23 displays a typical 2 lobes in some parts of the structural span.

The 2 lobes observed in Figure 4.23 contain some distortion, if compared to the third mode synchronization found in Figure C.17 (ID 06), due to small amplitude responses from the other modes.

Therefore, the modal decomposition assisted in retaining only relevant information for each mode.

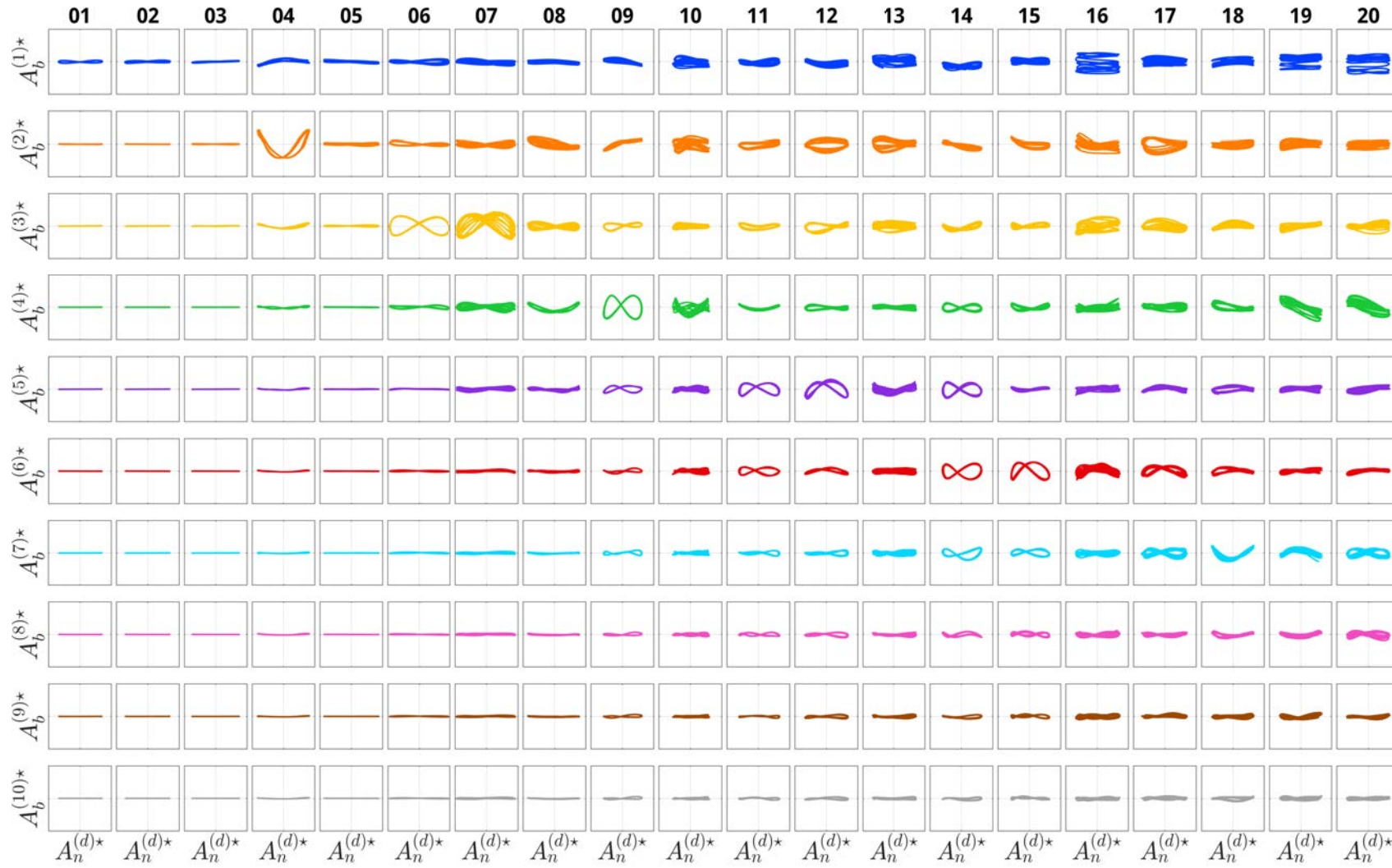
Figure C.16: Normal and binormal dynamics in the space of configuration obtained from the testing case ID 06 of the group $A_i = 17.5\text{mm}$.



Source: Developed by the author.

Table C.4 presents all modal KC evaluated from the present group. The testing case ID 06 exhibits $KC^{(d)} = 10.56$, obtained from the dominant in-plane mode, which is the first one. Higher modes present small modal KC.

Figure C.17: Modal orbits obtained from all testing cases in the group $A_i = 17.5\text{mm}$.



Source: Developed by the author.

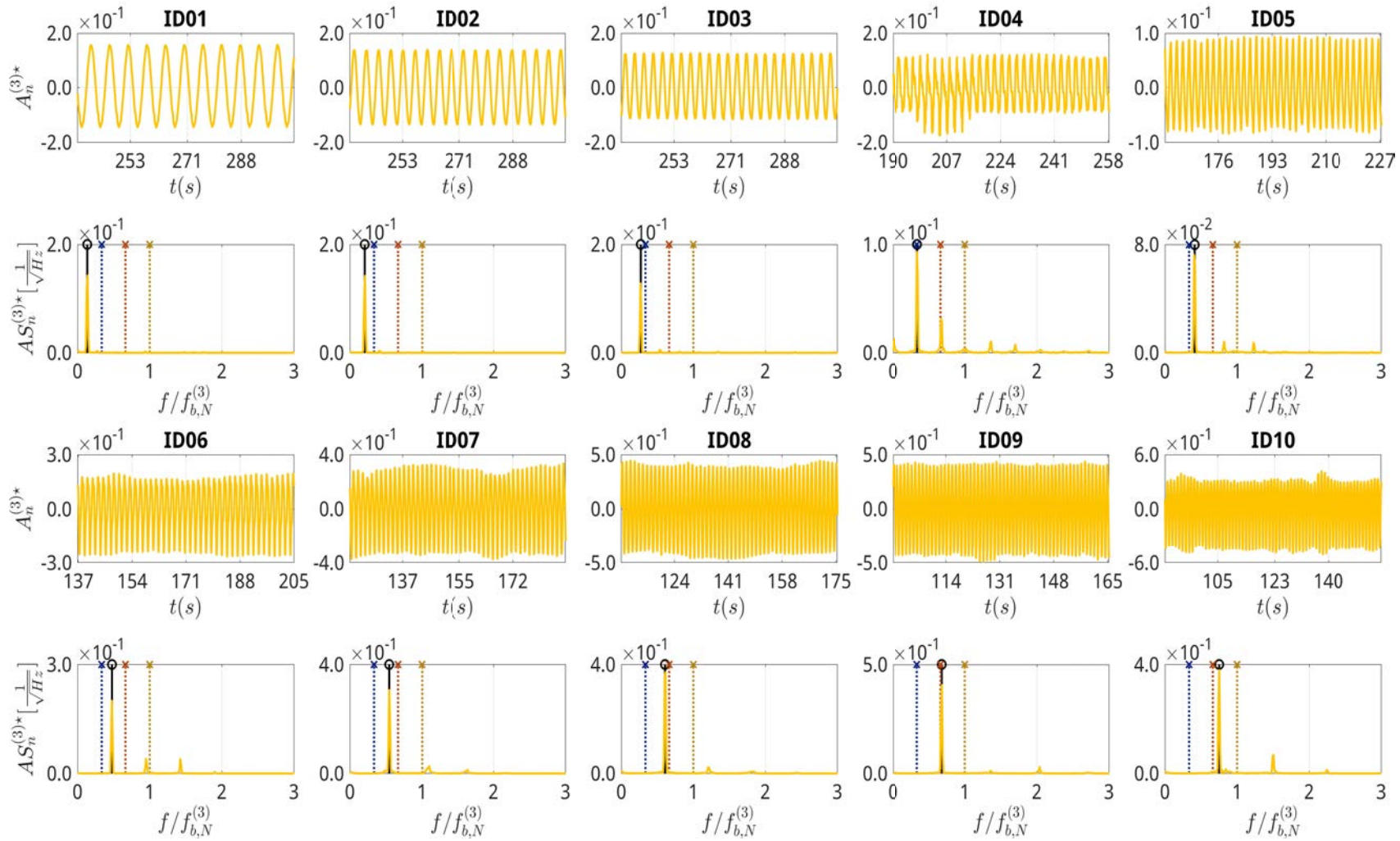
Table C.4: Modal KC for imposed movement at the top $A_{top} = 17.5\text{mm}$. Dominant modal KC is highlighted in red.

ID	Modal $KC^{(j)}$									
	1st	2nd	3rd	4th	5th	6th	7th	8th	9th	10th
01	7.82	0.58	0.93	0.13	0.72	0.39	0.55	0.08	0.22	0.07
02	8.07	0.46	0.86	0.16	0.70	0.41	0.54	0.09	0.22	0.06
03	8.42	0.29	0.76	0.20	0.68	0.43	0.53	0.10	0.21	0.05
04	8.90	0.86	0.65	0.34	0.64	0.47	0.54	0.22	0.22	0.06
05	9.76	1.07	0.49	0.39	0.57	0.52	0.45	0.18	0.16	0.04
06	10.56	3.06	1.23	0.60	0.58	0.56	0.43	0.25	0.17	0.12
07	10.45	5.11	1.90	0.78	0.65	0.59	0.47	0.30	0.24	0.20
08	9.17	8.28	2.60	0.89	0.93	0.54	0.56	0.36	0.35	0.28
09	6.47	7.55	2.57	0.89	1.10	0.46	0.63	0.29	0.38	0.28
10	6.15	8.13	2.38	1.24	1.09	0.40	0.61	0.22	0.35	0.23
11	7.09	6.85	3.73	1.35	1.26	0.51	0.72	0.32	0.39	0.25
12	7.58	5.39	5.62	1.51	1.49	0.55	0.91	0.39	0.49	0.30
13	7.62	5.07	7.18	1.73	1.84	0.71	0.96	0.46	0.55	0.37
14	7.02	3.74	8.08	1.63	1.58	0.88	1.10	0.55	0.65	0.44
15	6.80	3.14	8.14	1.45	1.57	1.18	1.17	0.50	0.66	0.40
16	7.25	3.12	8.24	1.45	1.70	1.29	1.17	0.55	0.70	0.41
17	7.32	3.21	7.17	1.66	1.79	0.93	1.56	0.79	0.64	0.50
18	7.39	3.37	6.29	2.59	2.03	0.73	1.70	0.78	0.62	0.67
19	7.32	3.31	5.64	3.1	2.14	0.75	1.79	0.68	0.73	0.57
20	7.25	3.07	5.42	3.13	2.14	0.76	1.23	1.13	0.82	0.46

Source: Developed by the author.

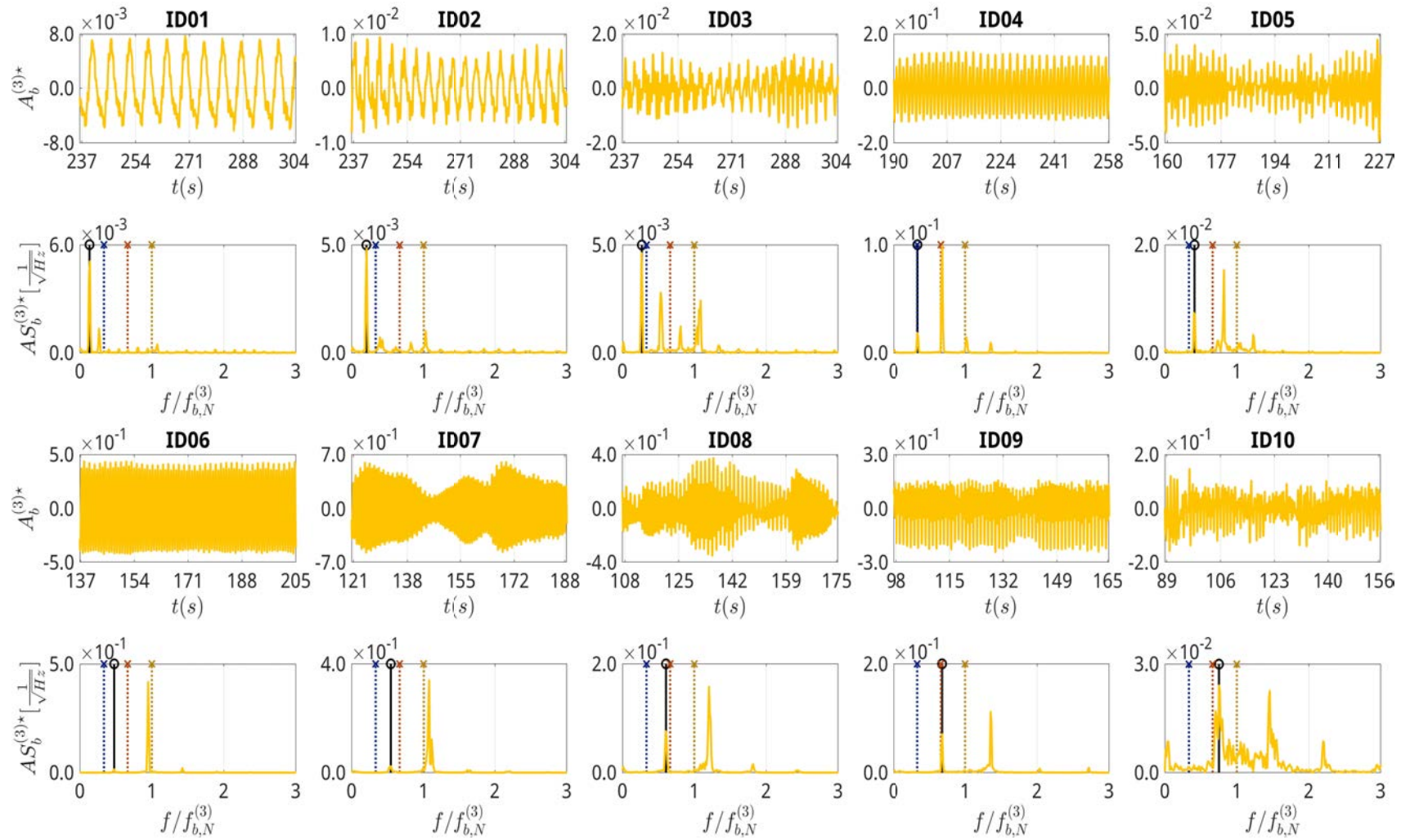
Figures C.18-C.19 exhibits the normal and binormal amplitude series, respectively, for the cases IDs 01 until 10. They also present the spectral content of each series.

Figure C.18: third mode normal displacement series and correspondent spectral contents from testing cases IDs 01 until 10 in the group $A_i = 17.5\text{mm}$.



Source: Developed by the author.

Figure C.19: third mode binormal displacement series and correspondent spectral contents from testing cases IDs 01 until 10 in the group $A_i = 17.5\text{mm}$.

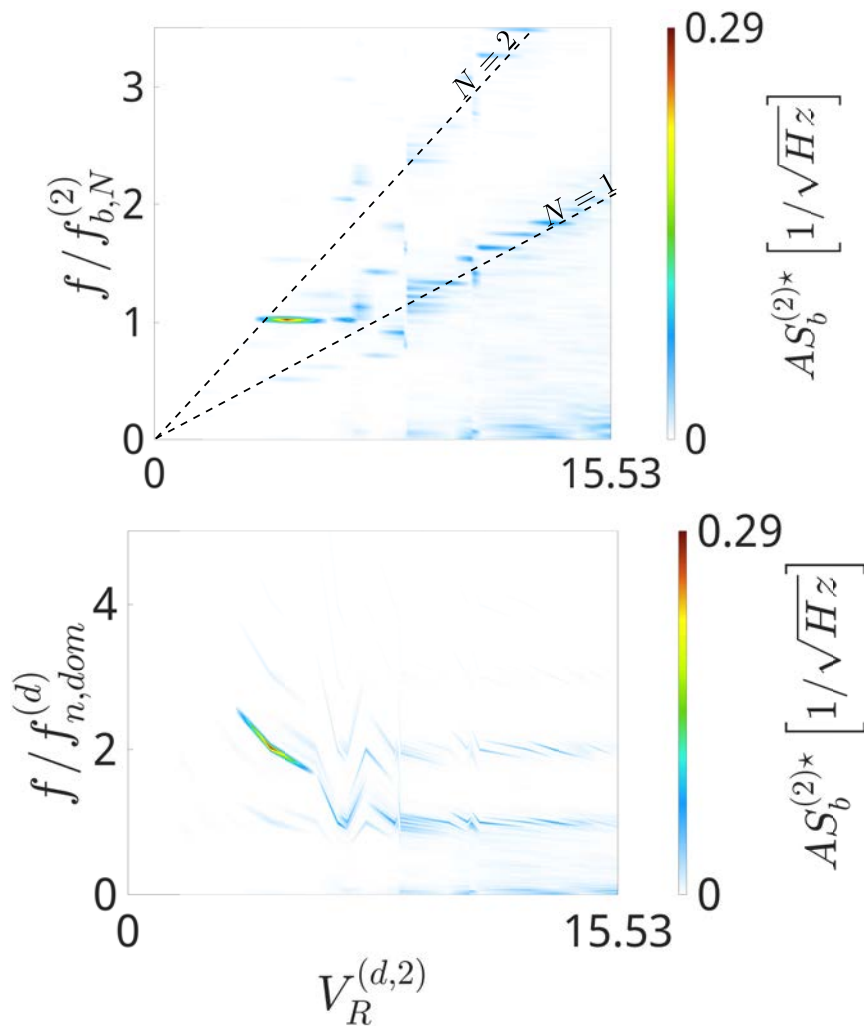


Source: Developed by the author.

The ID 06 is located in the third column of the first row in the charts presented in Figures C.18-C.19. The normal displacement series shows that its dominant frequency is equal to the driving frequency of the imposed vertical motion at the hang-off point.

Figure C.20 shows the third out-of-plane mode VSIV response with respect to the modal reduced velocity parameter, $V_R^{(d,k)}$. Note that, contrarily to the results in Figure 4.26, there is discontinuities in the frequency charts due to the modal KC not be fixed. Thus, reinforcing visually the adoption of modal frequency ratio parameter, $f^{(d,k)*}$, in the context of multi modal VSIV response.

Figure C.20: Modal frequency response of the third out-of-plane modes with respect to the modal reduced velocity parameter: $7 \leq KC^{(d)} \leq 10.6$.



Source: Developed by the author.